

# **Arrhythmogenesis in Pulmonary Hypertension**

A thesis submitted to the University of Manchester for the degree of Doctor  
of Philosophy in the Faculty of Medical and Human Sciences

2014

Dr Ian Peter Temple

Institute of Cardiovascular Sciences

School of Medicine

# Table of contents

---

<b>TABLE OF CONTENTS</b>	<b>2</b>
<b>ABSTRACT</b>	<b>7</b>
<b>Declaration</b>	<b>8</b>
<b>Copyright statement</b>	<b>9</b>
<b>Acknowledgements</b>	<b>10</b>
<b>List of abbreviations</b>	<b>11</b>
<b>List of tables</b>	<b>14</b>
<b>List of figures</b>	<b>18</b>
<b>The Author</b>	<b>32</b>
Qualifications	32
Prizes and awards	32
Publications	32
Abstracts presentations from current grant	32
Oral presentations from current grant	33
<b>1 GENERAL INTRODUCTION</b>	<b>34</b>
<b>1.1 Pulmonary hypertension: a clinical perspective</b>	<b>34</b>
1.1.1 Pulmonary arterial hypertension	34
1.1.2 Pulmonary hypertension due to left heart disease	34
1.1.3 Pulmonary hypertension due to lung diseases and or hypoxia	35
1.1.4 Chronic thromboembolic pulmonary hypertension	35
1.1.5 Multifactorial	35
<b>1.2 Pathological changes in the lungs leading to pulmonary arterial hypertension</b>	<b>35</b>
<b>1.3 Effects of pulmonary arterial hypertension on the heart</b>	<b>36</b>
1.3.1 Electrocardiographic changes in right ventricular hypertrophy	37
1.3.2 Pulmonary arterial hypertension and arrhythmias	38
1.3.3 Treatment in pulmonary arterial hypertension	41
<b>1.4 Cardiac physiology</b>	<b>42</b>

1.4.1	Ion channels in the heart	42
1.4.2	Membrane pumps and exchangers	43
1.4.3	The action potential	44
1.4.4	Impulse generation in pacemaking cells	46
1.4.5	Impulse propagation	47
<b>1.5</b>	<b>The cardiac conduction system</b>	<b>48</b>
1.5.1	The sinoatrial node	48
1.5.2	The atrioventricular node	49
1.5.2.1	Anatomy	50
1.5.2.2	Ionic currents in the atrioventricular node	50
1.5.2.3	Connexin expression in the atrioventricular node.	53
1.5.2.4	Dual atrioventricular nodal physiology	54
1.5.2.5	The Wenckebach phenomena and decremental conduction	55
<b>1.6</b>	<b>Arrhythmogenesis</b>	<b>57</b>
1.6.1	Cellular mechanisms	57
1.6.1.1	Abnormal automaticity	57
1.6.1.2	Triggered activity	57
1.6.1.2.1	Early after depolarisations	58
1.6.1.2.2	Delayed after depolarisations	58
1.6.2	Reentrant mechanisms	59
1.6.3	Arrhythmogenesis and ion channel remodelling	61
1.6.4	Arrhythmias and pulmonary hypertension in animal model studies	62
<b>1.7</b>	<b>Project aims</b>	<b>64</b>
<b>2</b>	<b>DEVELOPMENT OF THE MONOCROTALINE MODEL OF PULMONARY HYPERTENSION</b>	<b>65</b>
<b>2.1</b>	<b>Introduction</b>	<b>65</b>
2.1.1	Animal models of pulmonary hypertension	65
2.1.1.1	Chronic hypoxia model	65
2.1.1.2	Monocrotaline model	65
2.1.1.3	Sugen-Hypoxia model	66
2.1.1.4	Pulmonary artery banding	67
2.1.1.5	Left to right shunts	67
2.1.1.6	Choice of animal model	67
2.1.2	Differences between the human and rat heart	69
2.1.2.1	Ion channels in the rat heart	69
2.1.2.2	The action potential in the rat	70
2.1.2.3	The ECG in the rat	71

<b>2.2</b>	<b>Methods</b>	<b>72</b>
2.2.1	Development of the monocrotaline model	72
2.2.2	Monocrotaline preparation and injection	72
2.2.3	Animal monitoring	72
2.2.4	ECG recording	73
2.2.5	Echocardiography	73
<b>2.3</b>	<b>Results</b>	<b>76</b>
2.3.1	Demonstration of pulmonary hypertension in the MCT rats	81
<b>2.4</b>	<b>Experience with the monocrotaline model</b>	<b>82</b>
<b>2.5</b>	<b>Discussion</b>	<b>83</b>
<b>3</b>	<b>WHOLE HEART EXPERIMENTS IN THE MONOCROTALINE MODEL</b>	<b>85</b>
<b>3.1</b>	<b>Introduction</b>	<b>85</b>
<b>3.2</b>	<b>Methods</b>	<b>85</b>
3.2.1	Pacing protocols	86
<b>3.3</b>	<b>Results</b>	<b>90</b>
<b>3.4</b>	<b>Discussion</b>	<b>93</b>
<b>4</b>	<b>EXPERIMENTS ON THE ISOLATED SINOATRIAL/ATRIOVENTRICULAR NODAL PREPARATION IN THE MONOCROTALINE MODEL</b>	<b>96</b>
<b>4.1</b>	<b>Introduction</b>	<b>96</b>
<b>4.2</b>	<b>Methods</b>	<b>96</b>
4.2.1	Atrioventricular node preparation	96
4.2.2	Perfusion system	97
4.2.3	Bipolar electrode recording system	98
4.2.4	Measurement of distance	98
4.2.5	Conduction velocity	101
4.2.6	Mapping of earliest activation	101
4.2.7	Mapping of the His bundle	101
4.2.8	Pacing protocols	102
4.2.9	Optical mapping	105
<b>4.3</b>	<b>Results</b>	<b>105</b>
4.3.1	Mapping of the sinoatrial node	105
4.3.2	Atrial conduction velocity	107

4.3.3	Atrioventricular nodal functional measures	108
<b>4.4</b>	<b>Discussion</b>	<b>112</b>
<b>5</b>	<b>REMODELLING IN RESPONSE TO PULMONARY HYPERTENSION AT THE MRNA LEVEL</b>	<b>118</b>
<b>5.1</b>	<b>Introduction</b>	<b>118</b>
<b>5.2</b>	<b>Methods</b>	<b>118</b>
5.2.1	Mapping the AV node	119
5.2.2	Immunohistochemistry	119
5.2.3	Masson's trichrome staining	121
5.2.4	Identifying the regions of the AV node	122
5.2.5	Hand-assisted micro-dissection of the atrioventricular node	123
5.2.6	RNA extraction	126
5.2.6.1	Optimisation of RNA extraction technique	126
5.2.6.2	Final protocol for AV node dissection and RNA extraction	128
5.2.7	Reverse transcription	129
5.2.8	Quantitative polymerase chain reaction	130
5.2.9	The TaqMan microfluidic card system	130
5.2.10	Endogenous controls	131
5.2.11	Gene targets	132
5.2.12	Preamplification of cDNA	133
5.2.13	Preparation of the TaqMan Array Micro Fluidic Card	136
5.2.14	Final protocol for RT-qPCR	137
5.2.15	Control samples	137
5.2.16	Data analysis	138
<b>5.3</b>	<b>Results</b>	<b>142</b>
5.3.1	Assessment of preamplification	142
5.3.2	Normalisation strategy and interpretation of unamplified samples	143
5.3.3	Relative expression of mRNA targets	146
5.3.4	Regional specific expression of ion channels and connexions in the rat AV node.	149
5.3.5	Remodelling of ion channels in the monocrotaline model	160
5.3.5.1	Ventricular tissue	161
5.3.5.2	Atrial tissue	162
5.3.5.3	Remodelling within the atrioventricular node	163
<b>5.4</b>	<b>Discussion</b>	<b>171</b>
<b>6</b>	<b>REMODELLING IN RESPONSE TO PULMONARY HYPERTENSION AT THE PROTEIN LEVEL</b>	<b>175</b>

<b>6.1</b>	<b>Introduction</b>	<b>175</b>
<b>6.2</b>	<b>Methods</b>	<b>176</b>
<b>6.3</b>	<b>Results</b>	<b>177</b>
<b>6.4</b>	<b>Discussion</b>	<b>189</b>
<b>7</b>	<b>EFFECTS OF MACITENTAN ADMINISTRATION IN THE MONOCROTALINE MODEL</b>	<b>194</b>
<b>7.1</b>	<b>Introduction</b>	<b>194</b>
<b>7.2</b>	<b>Methods</b>	<b>195</b>
<b>7.3</b>	<b>Results</b>	<b>196</b>
<b>7.4</b>	<b>Discussion</b>	<b>202</b>
<b>8</b>	<b>SUMMARY AND FUTURE DIRECTIONS</b>	<b>207</b>
	<b>REFERENCES</b>	<b>213</b>
<b>A.</b>	<b>APPENDIX</b>	<b>230</b>

**WORD COUNT - 68571**

# Abstract

---

Submission for the degree of Doctor of Philosophy, The University of Manchester

Dr Ian Peter Temple

## Arrhythmogenesis in Pulmonary hypertension

February 2014

**Background:** Pulmonary arterial hypertension (PAH) is a condition with severe morbidity and mortality. It is associated with an increase in incidence of all forms of arrhythmias which further increase morbidity and mortality. The monocrotaline (MCT) model of pulmonary hypertension (PH) in the rat is analogous to PAH in humans and was used to study how PH causes arrhythmias.

**Methods:** A single injection of MCT or a volume matched saline injection (control) was given to the rats on day 0 of the protocol. The hearts of both groups of rats were studied *in vivo* with echocardiography (echo) and electrocardiogram (ECG). The rat's condition was monitored and they were electively sacrificed when they showed symptoms or on day 28. Live cardiac tissue was studied using the Langendorff preparation and a right atrial preparation that incorporated the sinoatrial (SA) and atrioventricular (AV) nodes. Molecular biology techniques including reverse transcription quantitative polymerase chain reaction (RT-qPCR) and immunohistochemistry were used identify changes in the heart caused by PH. The effects of macitentan, an endothelin receptor antagonist used in the treatment of PAH, on the MCT injected rats was assessed using echo and ECG

**Results:** Echo demonstrated that the MCT treated rats developed severe pulmonary hypertension with a decreased pulmonary artery acceleration time ( $P<0.005$ ) and an increased pulmonary artery deceleration ( $P<0.005$ ). The MCT treated rats also developed right ventricular hypertrophy ( $P<0.05$ ) and dilation ( $P<0.005$ ). The *in vivo* ECG demonstrated QT prolongation ( $P<0.005$ ). *Ex vivo* functional experiments demonstrated QT prolongation ( $P<0.005$ ) and prolonged ventricular effective refractory period ( $P<0.005$ ). AV node dysfunction was also seen in the *ex vivo* experiments with an increased AV effective refractory period ( $P<0.05$ ), AV functional refractory period ( $P<0.05$ ) and incidence of complete heart block ( $P<0.05$ ). RT-qPCR demonstrated significant changes in the mRNA expression of several ion channels and exchanges,  $Ca^{2+}$  handling proteins and autonomic receptors including a downregulation of HCN4 and  $Ca_v1.2$  in the AV nodal tissues ( $P<0.05$ ). Treatment of established pulmonary hypertension led to a reduction in the prolongation of the QT interval caused by MCT administration at day 21 ( $P<0.05$ ).

**Conclusions:** PH causes arrhythmogenic changes including prolonged repolarisation in the working myocardium and AV node dysfunction. These changes may be caused by dysregulation of ion channels and  $Ca^{2+}$  handling proteins. These ion channels and  $Ca^{2+}$  handling proteins may play a key role in both physiological and pathological processes within the AV node.

## Declaration

All the materials in this thesis were written and created by myself except where otherwise stated. The development of the monocrotaline model, ECG and echocardiographic data described in chapter 2 and the ECG and Langendorff experiments described in chapter 3 were performed jointly by Dr Gillian Quigley and myself. They form part of the work that was submitted for her thesis: *Inflammation of the Heart in Heart Disease*, The University of Manchester, 2013. All the work described in chapters 4-7 was performed by myself. The provisional data described in chapter 8 was created in collaboration with Dr Simon Castro and Dr Michael Coleman. No portion of the work in chapter 4-8 has been submitted in support of an application for another degree or qualification of this or any other university or other institute of learning.

## Copyright statement

- i.** The author of this thesis (including any appendices and/or schedules to this thesis) owns certain copyright or related rights in it (the “Copyright”) and s/he has given The University of Manchester certain rights to use such Copyright, including for administrative purposes.
- ii.** Copies of this thesis, either in full or in extracts and whether in hard or electronic copy, may be made only in accordance with the Copyright, Designs and Patents Act 1988 (as amended) and regulations issued under it or, where appropriate, in accordance with licensing agreements which the University has from time to time. This page must form part of any such copies made.
- iii.** The ownership of certain Copyright, patents, designs, trade marks and other intellectual property (the “Intellectual Property”) and any reproductions of copyright works in the thesis, for example graphs and tables (“Reproductions”), which may be described in this thesis, may not be owned by the author and may be owned by third parties. Such Intellectual Property and Reproductions cannot and must not be made available for use without the prior written permission of the owner(s) of the relevant Intellectual Property and/or Reproductions.
- iv.** Further information on the conditions under which disclosure, publication and commercialisation of this thesis, the Copyright and any Intellectual Property and/or Reproductions described in it may take place is available in the University IP Policy (see <http://www.campus.manchester.ac.uk/medialibrary/policies/intellectual-property.pdf>), in any relevant Thesis restriction declarations deposited in the University Library, The University Library’s regulations (see <http://www.manchester.ac.uk/library/aboutus/regulations>) and in The University’s policy on presentation of Theses

## Acknowledgements

It seems appropriate that the final act of preparing a thesis should be to thank the many people without whom there would have been nothing to write. I have been lucky to have a supervisory team of four inspirational figures whose attributes have combined to make the last three years immensely rewarding, productive and enjoyable. Professor Mark Boyett has a vast depth of knowledge, constant enthusiasm for new discoveries, and perhaps most importantly a seemingly unending reserve of patience that allows him to impart these gifts to those around him. Professor George Hart has always had friendly and helpful advice but has never lost the academic rigor and constant questioning of a true scientist. Dr Vaikom Mahadevan has the motivational skills to make sure that although deadlines were stretched they were never broken. Dr Halina Dobrzynski has offered both friendship and a wealth of experience that has more often than not been the key to experimental success.

I would also like to thank all of the team who ensure that the work gets done with the minimum of fuss and the maximum enjoyment. In particular I would like to thank Dr Oliver Monfredi who first introduced me to the team and found the funds to do the work, and Dr Gillian Quigley with whom I worked closely in creating the animal model that is the foundation for this project.

Straddling the world of science and home is Dr Heiko Schneider. He has been an indispensable colleague as together we have done our best to unravel the mysteries of ionic currents, exponentially replicating DNA and the dark arts of statistical analysis. He has also become a very close friend; indeed I think there can be no better description of him than that of the job he kindly helped me with at my wedding. Truly the best man.

My final word of thanks has to go to my family. To my parents, to whom no thank you will ever be enough, their support has been a constant in my life. To my wife, Hoda, whose knowledge and skill has been invaluable in completing this thesis. More importantly than this she instilled the belief in me that I needed before embarking on this project and who has supported me through the emotional highs and lows that research entails. Finally I would like to mention my unborn baby whom I will meet in just a matter of weeks. Motivation can be hard to come by but the joy I feel their arrival has pushed me over the finish line.

## List of abbreviations

AERP	Atrial effective refractory period
AF	Atrial fibrillation
AN cell	Atrio-nodal cell
ATP	Adenosine triphosphate
AV	Atrioventricular
AVERP	Atrioventricular effective refractory period
AVFRP	Atrioventricular functional refractory period
AVNRT	Atrioventricular nodal reentrant tachycardia
B2M	$\beta$ 2 microglobulin
BSA	Bovine serum albumin
cSNRT	Corrected sinus node recovery time
CTEPH	Chronic thromboembolic pulmonary hypertension
DAD	Delayed after depolarisation
DNA	Deoxyribonucleic acid
dsDNA	Double stranded deoxyribonucleic acid
EAD	Early after depolarisation
ECG	Electrocardiogram
Echo	Echocardiography
ERA	Endothelin receptor antagonist
ERG	Ether-related-a-go-go
FDR	False detection ratio

$I_{Ca,L}$	L-type $Ca^{2+}$ current
$I_{Ca,T}$	T-type $Ca^{2+}$ current
$I_f$	Funny current
$I_{K,ACh}$	Acetylcholine activated $K^+$ current
$I_{K,ATP}$	Adenosine triphosphate activated $K^+$ current
$I_{K,r}$	Rapid delayed rectifier $K^+$ current
$I_{K,s}$	Slow delayed rectifier $K^+$ current
$I_{K,ur}$	Ultra rapid $K^+$ current
$I_{K1}$	Inward rectifier $K^+$ current
$I_{Na}$	$Na^+$ current
$I_{NCX}$	$Na^+/Ca^{2+}$ exchanger current
ip	Intraperitoneal
$I_{to}$	Transient outward $K^+$ current
$I_{to,f}$	Fast transient outward $K^+$ current
$I_{to,s}$	Slow transient outward $K^+$ current
LV	Left ventricle
mRNA	Messenger ribonucleic acid
N cell	Nodal cell
NCX	$Na^+/Ca^{2+}$ exchanger
NH cell	Nodal-His Cell
NYHA	New York Heart Association
OCT	Optimal cutting temperature compound
PAAT	Pulmonary artery acceleration time

PAD	Pulmonary artery deceleration
PAH	Pulmonary arterial hypertension
PBS	Phosphate buffered saline
PH	Pulmonary hypertension
PV <sub>max</sub>	Maximum pulmonary velocity
qPCR	Quantitative polymerase chain reaction
QT <sub>c</sub>	Corrected QT interval (Bazett's formula)
RNA	Ribonucleic acid
RNase	Ribonuclease
RTqPCR	Reverse transcription quantitative polymerase chain reaction
RV	Right ventricle
RyR	Ryanodine receptor
SA	Sinoatrial
sc	Subcutaneous
SEM	Standard error of the mean
SR	Sarcoplasmic reticulum
TLDA	Taqman low density array
VEGF	Vascular endothelial growth factor
VERP	Ventricular effective refractory period
WHO	World Health Organisation

## List of tables

Table 1-1 Summary of some of the major ionic currents, $\alpha$ and $\beta$ subunits involved in the cardiac action potential. From Katz <sup>43</sup> and Nerbonne. <sup>52</sup> .....	44
Table 2-1. Weights at day 0, day 21 and immediately prior to termination. Mean $\pm$ standard error measurement (SEM). *The mean value is significantly different assessed by unpaired Student's <i>t</i> -test (P<0.05). **The mean value is significantly different assessed by unpaired Student's <i>t</i> -test (P<0.005). .....	76
Table 2-2. <i>In vivo</i> ECG parameters. Mean $\pm$ SEM. *The mean value is significantly different assessed by repeated measures ANNOVA with multiple comparisons (P<0.05). **The mean value is significantly different assessed by repeated measures ANNOVA with multiple comparisons (P<0.005). .....	77
Table 2-3. Echo parameters on day of termination. Mean $\pm$ SEM. *The mean value is significantly different assessed by repeated measures ANNOVA with multiple comparisons (P<0.05). **The mean value is significantly different assessed by repeated measures ANNOVA with multiple comparisons (P<0.005).....	78
Table 3-1. <i>In vivo</i> ECG results on the day of termination. Mean $\pm$ SEM. *Significantly different as assessed by unpaired Student's <i>t</i> -test (P<0.05). **Significantly different assessed by unpaired Student's <i>t</i> -test (P<0.005). .....	90
Table 3-2 Langendorff results. Mean $\pm$ SEM. *The mean value is significantly different assessed by Student's <i>t</i> -test (P<0.05). **The mean value is significantly different assessed by Student's <i>t</i> -test (P<0.005). .....	91
Table 3-3. Linear regression of Wenckebach cycle length against AVERP and AVFRP. * The correlation coefficient is non-zero (P<0.05), ** The correlation coefficient is non-zero (P<0.005).....	93
Table 4-1. Results from the conduction velocity experiment. Mean $\pm$ SEM. *Means significantly different as assessed by unpaired Student's <i>t</i> -test (P<0.05).....	108
Table 4-2 Results from the AV node pacing protocols. Mean $\pm$ SEM. *Means significantly different as assessed by unpaired Student's <i>t</i> -test (P<0.05), † Difference in proportion of animals with CHB significantly different assessed using Chi <sup>2</sup> test. ....	108

Table 4-3. Comparison of MCT treated Rats used in the Langendorff experiments and the MCT treated rats used in the isolated SA/AV node experiments. Mean $\pm$ SEM. There were no statistically significant differences between the two groups.....	114
Table 4-4 Comparison of the differences between the MCT Rats that had 1:1 conduction at the AV node and the MCT rats that had CHB in the isolated SA/AV node preparation. Mean $\pm$ SEM. There were no statistically significant differences between the two groups assessed by unpaired Student's <i>t</i> -test. ....	114
Table 5-1. Primary antibodies used in immunohistochemistry.....	120
Table 5-2 Secondary antibodies used in immunohistochemistry.....	120
Table 5-3. The gene names and proteins encoded by the 18 targets included on the endogenous control array. ....	131
Table 5-4. Sample numbers used in the rat endogenous control array experiments.....	132
Table 5-5. Viiia 7 Real-Time PCR settings for thermal cycling during PCR.....	132
Table 5-6. The genes of interest, the proteins they encode for and a brief description of their function. ....	134
Table 5-7. The genes of interest, the proteins they encode for and a brief description of their function. ....	135
Table 5-8. Veriti 96-Well Fast Thermal Cycler settings for preamplification.....	136
Table 5-9. n-numbers for all PCR experiments. ....	146
Table 5-10. Relative abundance (mean value) of RNA from six tissue regions of the AV node for both control and MCT rats. For each target, the relative quantification was normalised to the atrium of the control animal. ....	147
Table 6-1. Primary antibodies used for immunohistochemistry experiments.....	177
Table 6-2. Secondary antibodies used for immunohistochemistry experiments.....	177
Table 6-3. Results of protein quantification with epifluorescence. All values are means $\pm$ SEM and are in arbitrary fluorescence units. ....	187

Table 7-1. Body weights on day 21 and heart and lung weights on termination of the CON, MCT and MACI groups. Mean $\pm$ SEM. * P<0.05 MCT or MACI vs. CON assessed by unpaired Student's <i>t</i> -test; **P<0.005 MCT or MACI vs. CON assessed by unpaired Student's <i>t</i> -test.....	196
Table 7-2. Echo parameters of PH at day 7 post injection. Mean $\pm$ SEM. * P<0.05 MCT or MACI vs. CON assessed by two-way repeated measures ANNOVA with multiple comparisons; ** P<0.005 MCT or MACI vs. CON assessed by unpaired two-way repeated measures ANNOVA with multiple comparisons. ....	197
Table 7-3. Echo parameters of PH at day 14 post injection. Mean $\pm$ SEM. * P<0.05 MCT or MACI vs. CON assessed by two-way repeated measures ANNOVA with multiple comparisons; ** P<0.005 MCT or MACI vs. CON assessed by two-way repeated measures ANNOVA with multiple comparisons; †† P<0.005 MCT vs. MACI assessed by two-way repeated measures ANNOVA with multiple comparisons. ....	198
Table 7-4. Echo parameters of PH at day 21 post injection. Mean $\pm$ SEM. * P<0.05 MCT or MACI vs. CON assessed by two-way repeated measures ANNOVA with multiple comparisons; ** P<0.005 MCT or MACI vs. CON assessed by two-way repeated measures ANNOVA with multiple comparisons; † P<0.05 MCT vs. MACI assessed by two-way repeated measures ANNOVA with multiple comparisons; †† P<0.005 MCT vs. MACI assessed by two-way repeated measures ANNOVA with multiple comparisons. ....	198
Table 7-5. ECG measurements at day 7, day 14 and 21 post injection. Mean $\pm$ SEM. ** P<0.005 MCT or MACI vs. CON, † P<0.05 MCT vs. MACI. ....	200
Table A-1. Full list of targets included on TLDA qPCR card. ....	232
Table A-2. RNA concentrations of all samples (in ng/ $\mu$ l). For all samples with concentrations of greater than 1 were reverse transcribed using a total of 16ng of RNA. For samples with a concentration of less than 1ng/ $\mu$ l a total of 16 x sample concentration was used for reverse transcription (because the maximum volume for the reaction was 16 $\mu$ l). ....	233
Table A-3. Data used to model ion channel conductance and electrical coupling used in the computer modelling of the atrial cells in the MCT model in the AV node. Data is taken from the mRNA expression from the atrium. * p<0.05 for difference in control and MCT mRNA expression assessed by limma test. ....	234

Table A-4. Data used to model ion channel conductance and electrical coupling used in the computer modelling of the AN cells in the MCT model in the AV node. Data is taken from the mRNA expression from the inferior nodal extension. * $p < 0.05$ for difference in control and MCT mRNA expression assessed by limma test. ....	235
Table A-5. Data used to model ion channel conductance and electrical coupling used in the computer modelling of the N cells in the MCT model in the AV node. Data is taken from the mRNA expression from compact node. * $p < 0.05$ for difference in control and MCT mRNA expression assessed by limma test. ....	236
Table A-6. Data used to model ion channel conductance and electrical coupling used in the computer modelling of the NH cells in the MCT model in the AV node. Data is taken from the mRNA expression from the penetrating bundle. * $p < 0.05$ for difference in control and MCT mRNA expression assessed by limma test. ....	237
Table A-7. Data used to model ion channel conductance and electrical coupling used in the computer modelling of the ventricular cells in the MCT model in the AV node. Data is taken from the mRNA expression from the ventricle. * $p < 0.05$ for difference in control and MCT mRNA expression assessed by limma test. ....	238

## List of figures

- Figure 1-1. Ventricular action potential: A) schematic action potential identifying the 5 stages B) Individual currents underlying the action potential. From Nass *et al.*<sup>55</sup> .....46
- Figure 1-2. Modification of Courtemanche *et al.* model<sup>46</sup> using mRNA expression in the SA node and paranodal area to predict electrical activity in the SA node and paranodal area.<sup>47</sup> .....49
- Figure 1-3. Schematic diagram demonstrating the anatomy of the AV node A) Section of RA removed from the heart to reveal the location of the AV node in the interatrial septum along the tricuspid valve annulus B) An expanded version of the region of interest in A. The triangle of Koch (marked with a dashed red line marks the position of the AV node and is formed by the tricuspid valve annulus, tendon of Todaro and the coronary sinus. Within this region the atrium is in connection with the transitional tissue which in turn is in connection with the inferior nodal extension and compact node. As the AV node penetrates the central fibrous body it becomes the penetrating bundle which enters the ventricle before splitting into the left and right bundle branches. Ao – aorta, CFB – central fibrous body, CN – compact node, CS – coronary sinus, FO – fossa ovalis, INE – inferior nodal extension, IVC – inferior vena cava, LBB – left bundle branch, PA – pulmonary artery, PB – penetrating bundle, RA – right atrium, RBB – right bundle branch, RV – right ventricle, SVC – superior vena cava. From Temple *et al.*<sup>61</sup> .....51
- Figure 1-4. Schematic representation of Wenckebach conduction between two regions of excitable conduction separated by a region of delayed conduction. Region A is stimulated with a constant cycle length. The first impulse is not conducted from region A to region B which means that there is a long diastolic interval in region B (marked with a red arrow). The second impulse is conducted from region A to region B; because of the long diastolic interval there is no post repolarisation refractoriness. The third impulse is conducted from region A to region B after repolarisation has occurred, but because of the shorter diastolic interval there is some post repolarisation refractoriness and therefore a delay in excitation in region B (marked with a blue arrow). This effect increase for the fourth and fifth beat until the sixth beat is not conducted and the cycle starts again.....56
- Figure 1-5. ECG recordings showing examples of EADs and DADs. A) EADs can occur in phases 2 and 3. B) DADs occur during phase 4. If the EAD or DAD is of sufficient amplitude it can cause a triggered extrasystole. From Antzelevitch *et al.*<sup>116</sup> .....58

Figure 1-6. Classical re-entry around a fixed anatomical obstacle. The black region represents depolarised tissue, the white area represents repolarised/resting tissue, the stippled region represents repolarising tissue which is refractory to further stimulation A) Failure to initiate reentry due to a long wavelength. An initial impulse propagates with unidirectional block in the clockwise direction. The wavelength (conduction velocity x time for repolarisation) is greater than the length of the circuit and therefore the circuit terminates when the depolarising wavefront reaches the origin of the impulse which is still depolarised and therefore refractory to further stimulation. B) Successful reentry initiation with a reduced wavelength due to a decreased conduction velocity and time for repolarisation. The wavelength is less than the distance of the circuit and therefore the original site of stimulation has repolarised and therefore recovered excitability by the time the depolarising wavefront returns to its origin. The cycle can therefore repeat and a reentrant circuit is created. From Kleber *et al.*<sup>64</sup> .....59

Figure 1-7. Demonstration of reentry due to functional block in a rabbit left atrial preparation. A) Normal conduction (isochrones marked in ms). B) Premature beat with unidirectional block. Conduction occurs to the left of the stimulus but blocks to the right of the stimulus. C) First cycle of tachycardia. D) Map of the refractory periods of the tissue (the refractory periods are marked in ms). From Allesie *et al.*<sup>119</sup> .....60

Figure 2-1. Ventricular action potentials (APs) recorded in guinea-pig (square), rabbit (circle) and rat (triangle) demonstrating the short duration of the rat action potential due to the predominant effect of  $I_{to}$ . From Linz *et al.*<sup>167</sup> .....70

Figure 2-2. Schematic representation of a human and rat/mouse ECG demonstrating typical morphological differences with a shortened QT interval and lack of isoelectric baseline in the rat ECG. From Farraj *et al.*<sup>163</sup> .....71

Figure 2-3. Acquisition of anaesthetised rat ECG. The rat is first anaesthetised with 2% isoflurane then the electrodes connected to needles are inserted into the subcutaneous tissues. A three lead ECG with a configuration equivalent to lead I is taken. ....74

Figure 2-4. Pulsed wave Doppler recording through the pulmonary artery and measurement of PVmax, PAAT and PAD. The x axis measures time and the y axis measures velocity. PAAT is the time from the beginning of flow to the peak velocity, measured from the x axis. PV max is the maximum velocity measured from the y-axis. PAD is the gradient of the initial deceleration of the pulmonary velocity profile. ....75

Figure 2-5. Representative *in vivo* ECG recordings on day 0 and termination day from the control and MCT rats. There is a large increase in QT interval seen on termination day in the MCT rats. No significant difference is seen in the PR interval or the QRS duration. ..77

Figure 2-6. Representative pulmonary velocity profiles showing the development of raised pulmonary pressures in MCT treated rats, images taken from the same animal as Figure 2-7 and Figure 2-8. A) Both rats have a ‘rounded’ pulmonary velocity profile. B) On day 21 this has begun to alter in the MCT treated rat with a ‘transitional’ pattern. C) By day 23 (day of termination) these changes are very pronounced with a ‘spike and dome’ morphology giving a short PAAT and high PAD. ....79

Figure 2-7. Representative M-mode parasternal long axis views. The RV free wall and RV border of the septum are marked in dotted red lines. The RV thickness is demonstrated with blue arrows. The RV cavity is demonstrated with yellow arrows. A) Before injection both control and MCT have a thin RV wall which contracts well with a small RV cavity. B) By day 21 differences can be seen with the RV wall showing increasing thickness but continuing to contract well. The RV cavity is mildly enlarged. C) On day 23 (day of termination due to symptomatic endpoints being reached) the changes are very marked with a thickened RV which contracts poorly and an enlarged RV cavity. ....80

Figure 2-8. Representative parasternal short axis views in diastole showing the development of pulmonary hypertension. The LV is marked with a red dashed line and the RV is marked with a green dashed line. A) Before injection the LV cavity is circular in both animals and the RV is small. B) By day 21 the control animal still has a circular RV but the MCT rat’s septum is pushed over creating a ‘D-shape’; the RV is enlarged. C) More pronounced changes on day 23 immediately before termination. The RV is markedly enlarged and has ‘pushed’ the septum over creating a very pronounced ‘D-shape of the LV .....81

Figure 2-9. Kaplan-Meier graph to show the survival free from symptomatic endpoints. None of the control rats developed symptomatic endpoints. The earliest the MCT rats developed symptomatic endpoints was day 18. 79% of the rats had developed symptomatic endpoints by day 28. ....83

Figure 3-1. Diagram of Langendorff rig set up. The heart was perfused at a constant flow rate of 0.11 ml/min/g. After 20 min baseline ECG recordings were taken and pacing protocols applied to both the RA and RV outflow tract. ....87

Figure 3-2. Schematic diagram of pacing protocols. A) Wenckebach cycle length. At longer cycle lengths there was 1:1 conduction between the atrium and the ventricle. As the pacing cycle length decreased there was a gradual prolongation of the PR interval until conduction across the AV node failed and the cycle started again. B) S1-S2 protocol. A drive train of S1 stimuli with the same cycle length was delivered followed by an extrastimulus termed the S2. The protocol was repeated with a progressive reduction in the coupling interval of the extrastimulus, i.e. a shortening of the S1-S2 interval. Initially conduction across the AV node was maintained but there was progressive lengthening of the PR interval. At shorter intervals conduction across the AV node failed and there was atrial activation without ventricular activation. The longest S1-S2 interval at which conduction failed was termed the AVERP. Eventually, as the S1-S2 interval was reduced further the atrium was not captured. The longest S1-S2 interval at which the atrium was not captured is termed the AERP. ....89

Figure 3-3. AV node conduction curve. The S1-S2 interval (the ‘input’ to the AV node) is plotted against the R1-R2 interval (the ‘output’ of the AV node). The dotted line indicates the line that would be created if the AV node did not show decrementation (i.e. increasing delay with shorter coupling intervals, see section 2.9.5). A typical AV node conduction curve assumes a smooth ‘hockey-stick’ shape with no discontinuities. The AVERP is defined as the highest S1-S2 interval at which AV conduction fails and is read from the X-axis. The AVFRP is defined as the shortest R1-R1 interval that the AV node conducts and is read from the y-axis. ....90

Figure 3-4. Recordings from the widely spaced bipolar electrodes used in the Langendorff experiments. The recordings form a ‘pseudo-ECG’ pattern. There was a significant increase in the QT interval but no significant change in PR interval or QRS duration. ....91

Figure 3-5. AV node conduction curve for all control and MCT treated rats used in the Langendorff preparation. The mean AVERP and AVFRP were significantly increased. No discontinuities in the conduction curve were demonstrated. ....92

Figure 3-6. Graph showing Wenckebach cycle length plotted against both AVERP and AVFRP. ....93

Figure 4-1. Dissection to create the SA/AV node preparation. The lines of dissection are shown with dashed green lines (the dissection for all experiments was performed in oxygenated Tyrode’s solution but this dissection was performed a formalin fixed heart

without perfusing solution for clarity of the images). A-G are described in the text. H) Demonstration of the inferior vena cava. The blunt end of the dissecting pin was pushed through the inferior vena cava from the endocardial surface with no resistance demonstrating the wide lumen of the inferior vena cava which was severed during excision of the heart from the thorax. I) Demonstration of the coronary sinus. The blunt end of the dissecting pin was advanced into the ostium of the coronary sinus but could not pass further without resistance due to the narrow lumen of the coronary sinus which was not severed during removal of the heart from the thorax.....99

Figure 4-2. Diagram of the experimental setup for the isolated SA/AV node preparation. The perfusion circuit used two parallel inflows into the perfusion chamber to achieve a high flow rate and to direct the perfusion directly at the AV node as well as into the chamber. The outflow used two parallel tubes with the upper of the two tubes used to control the depth of fluid in the perfusion chamber. Initial experiments were performed using bipolar electrodes for pacing and recording signals. After the perfusion experiments were completed optical images were taken using optical dyes excited by the LEDs with signals recorded by the photodiode array. See text for further details.....100

Figure 4-3. Digital photograph of the AV node preparation. The anatomical landmarks were identified during dissection. For mapping the SA node a fixed electrode was positioned on the septum and used as a fiduciary point (marked in blue). A roving electrode was then used to map the point of earliest activation (marked in green). The conduction velocity was determined using a pacing electrode at the top of the crista terminalis (marked with a red star) and a recording electrode at the bottom of the crista terminalis (marked with a red dot). The position of the His signal was then determined by moving a bipolar electrode along the crista terminalis until a double signal was detected (marked with a yellow dot). CS – coronary sinus, FO – Fossa ovale, IVC – inferior vena cava. ....103

Figure 4-4. Bipolar recording from the SA/AV node preparation. A) Photograph of preparation. Once the His bundle had been identified (see Figure 4-3) the other three electrodes were positioned. Electrode 1 was positioned at the site of earliest activation (the SA node). Electrode 2 was positioned at the atrial septum, electrode 3 was at the His electrode and electrode 4 was positioned between the coronary sinus and the tricuspid valve annulus. B) Bipolar recordings from the 4 electrodes marked in A. Earliest activation was at electrode 1 and latest at electrodes 4. This represents rapid atrial

activation spreading from the SA node (marked with white dashed arrows). At the His signal (electrode 3) there was a discrete pause which was followed by a second smaller sharp deflection. This second deflection is the His signal. The time between the atrial and His signal is the AH interval. .... 104

Figure 4-5. Schematic diagram of the SA/AV node preparation with the earliest site of activation mapped. The coordinates have been transformed into an x value for distance from the crista terminalis and a y axis value for the proportion along the crista terminalis. See text for details. CS – coronary sinus, FO – fossa ovale, IVC – inferior vena cava.... 106

Figure 4-6. Comparison of bipolar electrode recording and optical mapping to identify the nodes. Ai) Photo of the preparation with Position of bipolar electrodes marked: earliest activation (marked in green) and location of the His signal (marked in yellow) shown. Aii) Bipolar electrode recording at the site of His signal. There was a clear atrial deflection followed by a discrete pause and then a His signal. Bi) Photo of the preparation with optical activation map superimposed. The activation map was created in Optiq using the time at which the optical signal was 90% from baseline to peak (Tact90\_Basic). Only signals with a clear upstroke were used with a ‘mask’ created to limit the map to the atrial tissue and the activation map was superimposed on a photo of the SA/AV node preparation. The earliest activation was defined as 0 ms and black on the scale bar. The position of earliest activation is marked with a 1 and is qualitatively similar to that seen in panel Ai. The colour scale bar indicates the time of activation from 0-10 ms with most of the atrial tissue activated in less than 5 ms. Bii) Example of optical action potentials taken from the sites shown in panel Bi. Despite the clear double deflection seen in panel Aii there is no second upstroke in region 3 to delineate the His signal on the optical action potential. .... 107

Figure 4-7. Optical mapping to assess conduction velocity. The activation maps were created as described in Figure 4-6. A) Control preparation. In the control rat the entire RA was activated in approximately 10ms. B) Preparation from MCT treated rat. In the MCT rat the entire RA was activated in approximately 15 ms. .... 109

Figure 4-8. Demonstration of CHB in a MCT treated rat. In a control rat every atrial signal (marked with a green arrow/A) was followed by a His signal (marked with a red arrow/H) with a fixed AH interval. In the MCT treated rat there was not a His signal following every atrial signal; instead the His signal is slower and independent of the His signal. This demonstrates CHB. .... 110

- Figure 4-9. AVERP and AVFRP mean and standard error for both S1-S1 drive trains...111
- Figure 4-10. AV node conduction curve for all control and MCT treated rats used in the isolated SA/AV node preparation. ....111
- Figure 4-11. Kaplan-Meier graph to show the survival free days from symptomatic endpoints for the MCT treated rats that were used for the Langendorff experiments and the isolated SA/AV node experiments. There was no difference assessed by the logrank test ( $P = 0.15$ ). ....113
- Figure 4-12. Optical mapping demonstrating ectopic activation from the AV node. Activation maps were created as described in Figure 4-6. A) Earliest activation at the expected site of the SA node (in the superior intercaval region). The entire atrium was activated in approximately 15 ms. This pattern accounted for the majority of impulses. B) Earliest activation at the AV node (along the tricuspid valve annulus near the coronary sinus). Activation propagated more slowly than in panel A, taking approximately 30 ms for the entire atrium to be activated. ....117
- Figure 5-1. Schematic diagram of double labelling of HCN4 and Cx43 with immunohistochemistry. See section 5.2.2 for details. BSA –bovine serum albumin. ....120
- Figure 5-2. Demonstration of the ‘AV node map’ to determine the locations of the regions within the AV node. Initially the slides were immunolabelled with Cx43 (red) and HCN4 (green). This identified nodal tissue and working myocardium. The slides then underwent Masson’s trichrome staining to delineate fibrous tissue (in blue). All the images were then reviewed sequentially to identify six different regions (see section 5.2.4 for details of the criteria for each region) .....124
- Figure 5-3. Images demonstrating hand assisted microdissection. A) AV node section double labelled for HCN4 (green) and Cx43 (red). The ringed area shows high levels of HCN4 and low levels of Cx43. B) Masson’s trichrome staining of a ‘sister section’. The area of interest demonstrated in A can be seen to be enclosed within the central fibrous body. The combination of high levels of HCN4, low levels of Cx43 and enclosure within the central fibrous body identifies this area as the penetrating bundle. C) Haematoxylin and Eosin stained section before microdissection. This reveals the area of interest identified from the ‘map’ created by A and B. D) The same slide as C post microdissection with the area of interest (in this case the penetrating bundle) removed. AS

– atrial septum, CFB – central fibrous body, CN – compact node, VS – ventricular septum.  
 ..... 125

Figure 5-4. Comparison of Qubit and Nanodrop to measure RNA concentration. The six tissue regions for a single AV node sample were assessed using both the Qubit and Nanodrop. At higher concentrations there is good agreement between the two techniques but at lower concentrations the Nanodrop reports higher concentrations than the Qubit. 127

Figure 5-5. Assessment of mRNA quality from the microdissected compact node samples. A) Sample before microdissection and RNA extraction were optimized. There are no clear peaks of mRNA for 18S and 28S indicating poor mRNA quality. B) Sample after microdissection and extraction were optimized. Clear peaks for 18S and 28S are seen. RIN - RNA integrity number; range 0- 10 with 10 indicating the best RNA quality. .... 128

Figure 5-6. qPCR amplification plots for all samples.  $\Delta R_n$  is the change in fluorescence due to the PCR reaction (current fluorescence – baseline fluorescence). A) Sample from the compact node showing good amplification with the majority of targets amplifying well. There are three targets which do not amplify which will have an undetermined  $C_q$  value which is replaced with 40. B) Sample from the compact node of a different rat. No targets have amplified indicating a failure of sample preparation; the entire sample was omitted from further analysis. .... 138

Figure 5-7. Determining  $C_q$  values for individual targets. With  $\log(\Delta R_n)$  plotted against cycle number there is a linear amplification phase. The green and red markers represent the beginning and end of the baseline. As long as the detection threshold is placed within this linear phase the difference in  $C_q$  between each sample will be the same (because the linear amplification plots are parallel to each other). A) Amplification curves Cx45. There is a relatively high abundance and therefore all samples cross the detection threshold and will have a relatively low  $C_q$ . B) Amplification curves for Cx30.2. There is a lower abundance and therefore the  $C_q$  values are higher. Some samples do not cross the detection threshold and will therefore not generate a  $C_q$  value, but this has been reported as 40 in this study. .... 139

Figure 5-8. Correlation of  $\Delta CT$  from preamplified and unamplified samples from the atrium and ventricle of all rats. Linear regression analysis showed a non-zero gradient of 0.84 ( $P < 0.001$ ),  $R^2 = 0.62$ . .... 143

Figure 5-9. Comparison of six different normalisation strategies for all six regions within the AV node. Each target is represented as a horizontal line. The FDR adjusted P value comparing control and MCT rats for significant differences is represented on a colour scale for each target with each normalisation strategy for each tissue region. The black boxes represent missing data due to the exclusion of targets with a CT of greater than 38. Within each tissue region there are qualitatively similar adjusted P values for the different targets demonstrated by a consistent colour bar, but, between tissue regions there are different colour bars. A) P values using B2M and HPRT and excluding  $C_q$  values of  $>38$ , B) P values using B2M and HPRT and including  $C_q$  values. C) P values using normalisation against all targets and excluding  $C_q$  values of  $>38$ , D) P values using normalisation against all targets and including all  $C_q$  values, E) P values using B2M and PKG1 and excluding  $C_q$  values of  $>38$ , F) P values using B2M and PKG-1 and including all  $C_q$  values.....145

Figure 5-10. Relative quantification of targets in the control atrium. All targets are normalised to the lowest expressing target (Cx30.2). The scale is logarithmic and therefore each marked interval is x10 greater than the last. A greater than x10 difference in the expression level allows tentative conclusions to be drawn regarding the expression levels (see section 5.2.16).....148

Figure 5-11. Relative quantification of mRNA for the six different regions of the AV node in control rats. Letters above the bar graphs denote a significant difference between that region and the region with the corresponding letter. Capital letters indicate significance with a corrected P value of  $<0.05$  and lower case letters indicate significance with a corrected P value of  $<0.20$  (using the limma test). Expression of  $\alpha$  and  $\beta$  subunits of inward current carrying ion channels. A - Atrium, TT - Transitional tissue, INE - Inferior nodal extension, CN - Compact node, PB - Penetrating bundle, V - Ventricle. ....150

Figure 5-12. Relative quantification of mRNA for the six different regions of the AV node in control rats. Letters above the bar graphs denote a significant difference between that region and the region with the corresponding letter. Capital letters indicate significance with a corrected P value of  $<0.05$  and lower case letters indicate significance with a corrected P value of  $<0.20$  (using the limma test). Expression of  $\alpha$  and  $\beta$  subunits of further inward current carrying ion channels. A - Atrium, TT - Transitional tissue, INE - Inferior nodal extension, CN - Compact node, PB - Penetrating bundle, V - Ventricle...151

Figure 5-13. Relative quantification of mRNA for the six different regions of the AV node in control rats. Letters above the bar graphs denote a significant difference between that region and the region with the corresponding letter. Capital letters indicate significance with a corrected P value of  $<0.05$  and lower case letters indicate significance with a corrected P value of  $<0.20$  (using the limma test). Expression of  $\alpha$  and  $\beta$  subunits of  $K^+$  channels. A - Atrium, TT - Transitional tissue, INE - Inferior nodal extension, CN - Compact node, PB - Penetrating bundle, V - Ventricle. .... 152

Figure 5-14. Relative quantification of mRNA for the six different regions of the AV node in control rats. Letters above the bar graphs denote a significant difference between that region and the region with the corresponding letter. Capital letters indicate significance with a corrected P value of  $<0.05$  and lower case letters indicate significance with a corrected P value of  $<0.20$  (using the limma test). Expression of  $\alpha$  and  $\beta$  subunits of further  $K^+$  channels. A - Atrium, TT - Transitional tissue, INE - Inferior nodal extension, CN - Compact node, PB - Penetrating bundle, V - Ventricle. .... 153

Figure 5-15. Relative quantification of mRNA for the six different regions of the AV node in control rats. Letters above the bar graphs denote a significant difference between that region and the region with the corresponding letter. Capital letters indicate significance with a corrected P value of  $<0.05$  and lower case letters indicate significance with a corrected P value of  $<0.20$  (using the limma test). A and B). Expression of  $Ca^{2+}$  handling proteins (A) and connexins (B). A - Atrium, TT - Transitional tissue, INE - Inferior nodal extension, CN - Compact node, PB - Penetrating bundle, V - Ventricle. .... 154

Figure 5-16. Relative quantification of mRNA for the six different regions of the AV node in control rats. Letters above the bar graphs denote a significant difference between that region and the region with the corresponding letter. Capital letters indicate significance with a corrected P value of  $<0.05$  and lower case letters indicate significance with a corrected P value of  $<0.20$  (using the limma test). A and B). Expression of ion exchangers (A) and autonomic receptors (B). A - Atrium, TT - Transitional tissue, INE - Inferior nodal extension, CN - Compact node, PB - Penetrating bundle. .... 155

Figure 5-17. Remodelling of ion channel expression in the atrium of the MCT treated rats. All the values are normalised to the corresponding control value for the target and tissue region. Therefore a value greater than 1 represents upregulation and a value less than 1 represents downregulation. .... 165

- Figure 5-18. Remodelling of ion channel expression in the transitional tissue of the MCT treated rats. All the values are normalised to the corresponding control value for the target and tissue region. Therefore a value greater than 1 represents upregulation and a value less than 1 represents downregulation. .... 166
- Figure 5-19. Remodelling of ion channel expression in the inferior nodal extension of the MCT treated rats. All the values are normalised to the corresponding control value for the target and tissue region. Therefore a value greater than 1 represents upregulation and a value less than 1 represents downregulation. .... 167
- Figure 5-20. Remodelling of ion channel expression in the compact node of the MCT treated rats. All the values are normalised to the corresponding control value for the target and tissue region. Therefore a value greater than 1 represents upregulation and a value less than 1 represents downregulation. .... 168
- Figure 5-21. Remodelling of ion channel expression in the penetrating bundle of the MCT treated rats. All the values are normalised to the corresponding control value for the target and tissue region. Therefore a value greater than 1 represents upregulation and a value less than 1 represents downregulation. .... 169
- Figure 5-22. Remodelling of ion channel expression in the ventricle of the MCT treated rats. All the values are normalised to the corresponding control value for the target and tissue region. Therefore a value greater than 1 represents upregulation and a value less than 1 represents downregulation. .... 170
- Figure 6-1. Images from the slidescanner for Masson's trichrome staining and immunohistochemistry in the control rat. A) Penetrating bundle. Ai-iii show identification of the penetrating bundle which is encased in the central fibrous body. Aiv) Immunostaining for Cx43 (red) and HCN4 (green) The penetrating bundle stains strongly for HCN4 but Cx43 is absent. The atrium and ventricle stain strongly for Cx43 but HCN4 is absent. Av) Immunostaining for RyR2 (red) and Cx 40 (green). RyR2 is expressed throughout all the myocardial tissues but Cx40 is only present in the penetrating bundle. B) Images as per section A demonstrating the compact node and transitional tissue. The compact node is bounded by the tricuspid valve annulus inferiorly and extends into the transitional tissue. The compact node stains strongly for HCN4; Cx43 is absent. The transitional tissue shows an intermediate staining pattern. RyR2 is expressed throughout the myocardial tissues; Cx40 is absent. C) Images as per section A demonstrating the

inferior nodal extension. The inferior nodal extension is a small area of tissue on the tricuspid annulus along the right atrial side of the atrial septum. It stains for HCN4 but Cx43 is absent. RyR2 is present throughout the myocardial tissues; Cx40 is absent. See section 5.2.4 for further details. LV – left ventricle, RA – right atrium, RV, right ventricle, VS – ventricular septum.....	179
Figure 6-2. Images from the slidescanner for Masson’s trichrome staining and immunohistochemistry in the MCT treated rat. All labels as per Figure 6-1. ....	180
Figure 6-3. Immunohistochemistry staining patterns for the atrium in control and MCT rats. In the left panel Cx40 is stained green and RyR2 is stained red, in the right panel HCN4 is stained green and Cx43 is stained red. ....	181
Figure 6-4. Immunohistochemistry staining patterns for the transitional tissue in control and MCT rats. In the left panel Cx40 is stained green and RyR2 is stained red, in the right panel HCN4 is stained green and Cx43 is stained red. ....	182
Figure 6-5. Immunohistochemistry staining patterns for the inferior nodal extension in control and MCT rats. In the left panel Cx40 is stained green and RyR2 is stained red, in the right panel HCN4 is stained green and Cx43 is stained red. ....	183
Figure 6-6. Immunohistochemistry staining patterns for the compact node in control and MCT rats. In the left panel Cx40 is stained green and RyR2 is stained red, in the right panel HCN4 is stained green and Cx43 is stained red. ....	184
Figure 6-7. Immunohistochemistry staining patterns for the penetrating bundle in control and MCT rats. In the left panel Cx40 is stained green and RyR2 is stained red, in the right panel HCN4 is stained green and Cx43 is stained red. ....	185
Figure 6-8. Immunohistochemistry staining patterns for the ventricle in control and MCT rats. In the left panel Cx40 is stained green and RyR2 is stained red, in the right panel HCN4 is stained green and Cx43 is stained red. ....	186
Figure 6-9. A) Protein expression level assessed by fluorescence for each region in control and MCT treated rats. The significant differences ( $P < 0.05$ using ANNOVA with multiple comparisons) are marked with letters above each region. There were no significant differences between control and MCT treated animals assessed by Student’s <i>t</i> -Test. B) Corresponding data from the RT-qPCR experiment (see Chapter 5). Letters	

correspond to significant differences between the control regions (lower case letters,  $P < 0.2$ , upper case letters,  $P < 0.05$ ; see section 5.2.16). The bars indicate significant differences between the control and MCT rats assessed by limma test (\*  $P < 0.2$ ; \*\*  $P < 0.05$  see section 5.2.16). A) Atrium; B) Transitional tissue; C) Inferior nodal extension; D) Compact node; E) Penetrating bundle F) Ventricle. ....188

Figure 6-10. HCN4 labelling in the compact node (green signal). A) The samples used for assessment of the quantity of HCN4 in the compact node are shown for all the control and MCT treated rats. One MCT treated rat showed very high levels of HCN4 staining (bottom right panel). B) Scatter plot of HCN4 protein expression in the compact node. Mean and standard error bars shown demonstrating the greater variability in the MCT rats. ....191

Figure 6-11 A) Protein expression level assessed by fluorescence for each region corrected by removing the value for regions with no specific staining (see text for details). The significant differences between regions ( $P < 0.05$  using ANNOVA with multiple comparisons) are marked with letters above each region. There were no significant differences between control and MCT treated animals assessed by Student's *t*-test. B) Corresponding data from the RT-qPCR experiment (see Chapter 5). Letters correspond to significant differences between the control regions (lower case letters,  $P < 0.2$ ; upper case letters,  $P < 0.05$ ; see section 5.2.16). The bars indicate significant differences between the control and MCT treated rats assessed by the limma test; \*  $P < 0.2$ , \*\*  $P < 0.05$  (see section 5.2.16). A) Atrium; B) Transitional tissue; C) Inferior nodal extension; D) Compact node; E) Penetrating bundle F) Ventricle. ....192

Figure 7-1. Echo images showing the development of PH assessed by the pulmonary velocity profile. The profile has a typical 'rounded' shape prior to injection. At day 21 no change is seen in the CON animal but the MCT animal shows a change to a typical 'spike and dome' morphology with a reduced PAAT and increased PAD. The MACI animal has an intermediate profile between the two groups. ....199

Figure 7-2. Development of PH. Mean and SEM plotted at each time point. The MACI group was compared with the MCT group and the CON group assessed by two-way repeated measures ANNOVA with multiple comparisons. Pulmonary hypertension developed in the MACI group by day 7 (i.e. before the initiation of macitentan) with a reduced PVmax. There is a significant improvement in the MACI group compared to the

MCT group at day 14 and day 21 with a reduced PAD, right ventricular internal dimension and QT interval and an increased pulmonary artery acceleration time.....201

Figure 7-3. Kaplan-Meier curves showing the freedom from symptomatic endpoints. The animals were sacrificed on the day they met their symptomatic endpoints. There is a significant difference between the CON and MACI treated groups ( $p=0.01$ ) but no difference between the MACI treated and MCT groups ( $p=0.50$ ).....202

Figure 8-1. Results of the computer simulation with incorporating the mRNA data. A Control and MCT action potential from AN cells. B Control and MCT action potential from N cells. C. 1D simulation for control AV node. The model is paced from the atrium at a cycle length of 330ms, there is 1:1 conduction through the from the atrium, through the AV node and into the ventricle. D. 1D simulation for MCT AV node. The model is paced from the atrium at a cycle length of 330ms. Block occurs in the region of the AN to N cells, corresponding to the anatomical compact node.....210

Figure A-1. Optical activation maps in the SA/AV node preparation. The activation map was created in Optiq using the time at which the optical signal was 90% from baseline to peak (Tact90\_Basic). All sequences are shown with a 20ms colour scale. A) Control rats. Conduction velocity in the atrium was rapid in all preparations. B) MCT treated rats. Some preparations showed slowed conduction velocity but others showed preserved conduction velocity. ....239

## The Author

### Qualifications

BSc (Hons.) 2-1 in Psychology intercalated degree	June 2000
MBChB (Hons)	June 2003
MRCP	March 2006
Cardiology Knowledge Based Assessment	May 2010
Heart Rhythm UK accreditation – Devices	May 2012
EHRA certified electrophysiology specialist level 1	August 2013

### Prizes and awards

BHF clinical research fellowship grant	Feb 2011 – Feb 2014
North West electrophysiology meeting	1 <sup>st</sup> prize case presentation Dec 2011
Boston Scientific electrophysiology traces course	2 <sup>nd</sup> prize case presentation Sept 2012

### Publications

- **Temple IP**, Fox DJ. Ventricular tachycardia and sudden cardiac death. In Khavandi A. eds: Essential revision notes for cardiology KBA. Oxford university press. In press.
- Dobrzynski H, Anderson RH, Atkinson A, Borbas Z, D'Souza A, Fraser JF, Inada S, Logantha SJRJ, Monfredi O, Morris GM, Moorman AFM, Nikolaidou T, Schneider H, Szuts V, **Temple IP**, Yanni J, Boyett MR. Structure, function and clinical relevance of the cardiac conduction system, including the atrioventricular ring and outflow tract tissues. *Pharmacol Ther.* 2013 (epub ahead of print)
- **Temple IP**, Schmitt M, Fox DJ. Feeling the squeeze: an unusual cause of atrial fibrillation, *Heart* 99:752 2013
- **Temple IP**, Inada S, Dobzynski H, Boyett MR. Connexins and the AV node. *Heart Rhythm.* 2013, 10:297-304
- **Temple IP**, Fitchet A, Fox DJ. Irregular narrow complex tachycardia: what is the mechanism? *Pacing Clin Electrophysiol.* 2012 35:1154-7
- McDowell G, **Temple IP**, Kirwan C, Bundred N, McCollum C, Burton I, Kumar S and Byrne G. Alteration of platelet function in patients with early breast cancer. *Anticancer research* 2005; 25:3963-6

### Abstracts presentations from current grant

- **Temple IP**, Quigley GM, Monfredi O, Schneider H, Mahadevan VS, Dobrzynski H, Hart G, Boyett MR. Pulmonary hypertension is a serious condition that is often fatal. Some of these fatalities are caused by heart rhythm disturbances. We studied why these heart rhythms disturbances occur. *CMFT Research and Innovation conference.* 2013
- **Temple IP**, Schneider H, Nicoll RAM, Griffiths L, Mahadevan VS. Heavy arrhythmia burden in adults with congenital heart disease and severe pulmonary hypertension. *Heart Rhythm Congress* 2013
- Quigley GM, **Temple IP**, Zi M, Cartwright E, Yamanushi TT, Dobrzynski H, Hart G, Boyett MR. Inflammation and fibrosis in the right side of the heart including the cardiac conduction system in pulmonary arterial hypertension. *European Society of Cardiology.* 2013
- **Temple IP** Quigley GM, Monfredi O, Zi M, Cartwright EJ, Yamanushi TT, Mahadevan VS, Boyett MR, Hart G. Arrhythmogenic profile of the atrium and

atrioventricular node in pulmonary arterial hypertension. Accepted abstract: *International Union of Physiological sciences*. 2013

- Quigley GM, **Temple IP**, Zi M, Cartwright E, Yamanushi TT, Cai X, Yanni JF, Dobrzynski H, Hart G, Boyett MR. Inflammation and fibrosis in right- and left-sided heart failure. Accepted abstract: *International Union of Physiological sciences*. 2013
- Schneider H, Logantha SJ, **Temple IP**, Boyett MR, Mahadevan VS, Monfredi O, Dobrzynski H. Right Ventricular Outflow Tract Arrhythmogenicity is Related to its Covert Pacemaking Phenotype. *Heart Rhythm Society* 2013
- **Temple IP**, Quigley GM, Monfredi O, Yamanushi1 TT, Mahadevan VS, Hart G, Boyett MR Atrioventricular nodal dysfunction in the monocrotaline rat model of pulmonary arterial hypertension. *Proc Physiol Soc* 2012, 28, PC34
- **Temple IP**, Mirjafari H, Griffiths L, Schneider H, Mahadevan VS. Significant Improvements in Patient Reported Outcomes in Eisenmenger Syndrome with Advanced Pulmonary Hypertension Therapies and Association with Objective Improvements in Exercise Tolerance. *Circulation*. 2011; 124:A10084

### Oral presentations from current grant

- Arrhythmogenic remodelling in pulmonary arterial hypertension: Significant alterations in the atrium and atrioventricular node. Europace/European Working Group on Cardiac Cellular Electrophysiology. **2013**
- Pulmonary hypertension & cardiac conduction system dysfunction. Northern Cardiovascular Research Group. **2012**

# 1 General introduction

---

## 1.1 Pulmonary hypertension: a clinical perspective

Pulmonary hypertension (PH) is a haemodynamic state defined as a mean pulmonary artery pressure greater than 25 mmHg whilst the patient is at rest. It is not a single entity and has multiple causes. The causes of PH are sub-classified into five diagnostic categories described below. These clinical groups are organised on the basis of shared pathological mechanisms and response to treatment. Within each group there may be multiple different diagnoses.<sup>1</sup> In this study I aim to characterise arrhythmogenesis caused by pulmonary arterial hypertension (PAH) which is the classification given to a specific set of diseases that lead to PH due to pathology within the pulmonary vasculature. Brief overviews of all the sub-classifications are given below.<sup>1</sup>

### 1.1.1 Pulmonary arterial hypertension

Patients with PAH have raised pulmonary pressures due to changes within the arterial vessel wall including vasoconstriction, proliferation, inflammation and thrombosis. The diagnosis of ‘idiopathic’ PAH is given if no cause can be found, and the diagnosis of ‘associated’ PAH is given if a disease known to cause PAH is found. The three most common diagnoses in the clinical group of PAH are idiopathic PAH, associated PAH due to connective tissue disease and associated PAH due to congenital heart disease.<sup>2</sup>

It is difficult to ascertain the true incidence of PAH because of the varying degrees of severity and the difficulty in excluding other causes of PH, especially as there can be an overlap between clinical groups.<sup>1,2</sup> In spite of this a study has suggested prevalence of 52 cases per million and an incidence of 7-8% per million per year in Scotland.<sup>2</sup> There was a female:male ratio of approximately 2-3:1 due to an increased prevalence of idiopathic PAH and PAH associated with connective tissue disease in females.<sup>2</sup> In 2007 there were 1499 patients on advanced therapies for PAH in the UK, which equates to 25 patients per million of the general population.<sup>3</sup>

### 1.1.2 Pulmonary hypertension due to left heart disease

Raised post capillary pressures in the lung imply that the increased pressure within the pulmonary artery is a result of increased pressure within the left heart. This may be as a

result of systolic or diastolic left ventricular dysfunction or valvular heart disease.<sup>1</sup> No specific therapies for the raised pulmonary pressures in these condition have been shown to be effective and treatment is aimed at the cause of the left sided heart disease.

### **1.1.3 Pulmonary hypertension due to lung diseases and or hypoxia**

Hypoxia leads to vasoconstriction within the pulmonary vasculature. There may also be a loss of capillaries associated with emphysema and an increased mechanical stress due to hyperinflated lungs.<sup>1,4,5</sup> No specific therapy is aimed at the raised pulmonary artery pressure and therapy is aimed at the underlying lung disease.

### **1.1.4 Chronic thromboembolic pulmonary hypertension**

A thrombus within the pulmonary vasculature can become organised into the vessel wall leading to mechanical obstruction and raised pressures.<sup>1</sup> The true incidence is not known, but approximately 3% of patients followed-up after pulmonary embolus were shown to have developed signs of chronic thrombo-embolic pulmonary hypertension (CTEPH). Despite this, only 37% of patients diagnosed with CTEPH had a previous clinical history of venous thromboembolism.<sup>6</sup> Surgical intervention to remove the thrombus can be curative and patients should receive lifelong anticoagulation. The CTEPH can be treated with the same pharmacological therapies as those used for PAH if surgery is not performed or if PAH recurs after surgery.<sup>1</sup>

### **1.1.5 Multifactorial**

Many other conditions including haematological and metabolic diseases can lead to pulmonary hypertension due to diverse mechanisms.<sup>1</sup>

## **1.2 Pathological changes in the lungs leading to pulmonary arterial hypertension**

As described above PAH may be due to many causes but the common factor is that the rise in pulmonary pressures is mediated by vascular remodelling within the vessel wall of the pulmonary artery.<sup>7</sup> There are multiple mechanisms underlying this remodelling. There may be dysregulation of vascular tone, with down-regulation of vasodilatory factors such as nitric oxide and prostaglandin I<sub>2</sub> and up-regulation of vasoconstrictors such as 5-hydroxytryptamine and endothelin.<sup>7</sup> There is also abnormal proliferation of the three

layers of the pulmonary artery; intima, media and adventia. This is mediated by many factors including; cytokines and chemokines controlling the inflammation pathways, growth factors, transcription factors and metabolic changes.<sup>7</sup> Some factors that promote vasoconstriction also promote cell proliferation e.g. 5-hydroxytryptamine and endothelin.<sup>7</sup>

There is a series of characteristic pathological lesions within the pulmonary vasculature in PAH. Initially there is eccentric thickening of the intima caused by fibrosis interspersed with fibroblasts.<sup>8</sup> In more advanced disease these lesions may form into concentric layers of either endothelial cells, myofibroblasts or smooth muscle cells forming an ‘onion-skin’ appearance. The hallmark of advanced PAH is the appearance of ‘plexiform lesions’.<sup>8</sup> These lesions typically occur at branching points within the pulmonary arteries and consist of an obstructive lesion consisting of myofibroblastic cells interspersed with ‘slit-like’ vascular channels lined with endothelial cells.<sup>8</sup> These lesions lead to a reduction of the luminal area of the pulmonary arteries, raise pulmonary pressures and increase afterload on the right ventricle.<sup>8</sup>

Given the multitude of different pathways leading to the formation of these characteristic lesions it is thought that, despite similar clinical phenotypes, there may be different mediators of PAH in different patient groups. Work is ongoing to try to understand the relevance of these mechanisms in different patients and tailor therapy accordingly.<sup>7</sup>

## 1.3 Effects of pulmonary arterial hypertension on the heart

In the general population the right ventricle (RV) is a thin-walled structure that is subjected to low resistance and can therefore generate high flow without generating high pressures. Despite generating the same flow as the left ventricle (LV), the RV has only one sixth the muscle mass and carries out only 25% of the stroke work.<sup>9</sup> The shape of the RV is more complex than that of the LV which has made morphological and functional assessment of the RV more difficult than for the LV.

In patients with PAH the RV needs to produce much higher pressures than in the general population in order to generate a pressure gradient across the pulmonary circulation and maintain adequate flow. This results in remodelling of both the RV and the LV. Initially there is compensatory RV hypertrophy with both the RV wall thickness and RV mass significantly increased.<sup>10-12</sup> In patients with more advanced PAH both systolic and

diastolic RV volumes are increased with a decrease in RV ejection fraction.<sup>9-11, 13</sup> In severe PAH both systolic and diastolic RV function is reduced and stroke volumes are significantly lower. These parameters have been shown to be independent poor prognostic indicators in PAH.<sup>9-11, 13</sup>

The changes seen in the RV in PAH are not only mediated by the increased afterload placed on the RV. Animal studies have been performed comparing the effects of PH with the effects of pulmonary artery banding, both of which placed an equivalent haemodynamic load on the RV.<sup>14</sup> These studies demonstrated that PH was associated with decompensated RV hypertrophy and right-sided heart failure; in contrast pulmonary artery banding led to compensated hypertrophy without heart failure. The mechanisms underlying heart failure in PAH were multifactorial but included a reduction in the RV capillary density, fibrosis and apoptosis.<sup>14</sup>

In contrast to the RV the LV is not subjected to an increased afterload in PH. There are however reduced left sided filling pressures as a result of the right sided heart dysfunction and also a reduction in LV cavity size as a result of 'bowing' of the interventricular septum secondary to the increased RV pressure. These changes mean that the LV diastolic diameter and stroke volume are significantly decreased although LV mass is unchanged.<sup>9, 11</sup>

### **1.3.1 Electrocardiographic changes in right ventricular hypertrophy**

Studies dating back to the 1940s have attempted to characterise the electrocardiogram (ECG) changes seen in patients who subsequently went on to have autopsy confirmed RV hypertrophy from any cause.<sup>15-17</sup> Several classification systems have been proposed to diagnose RV hypertrophy on the ECG but no single system has a high sensitivity and specificity and there is no single criterion that can be used to diagnose RV hypertrophy.<sup>18</sup>

The most prominent feature seen in RV hypertrophy is a large R wave and small S wave seen in lead V1 with a ratio of R:S of greater than 1. A small R wave and deep S wave in V5 and V6 is also seen.<sup>15-18</sup> Right axis deviation is commonly seen in both normal hearts and hearts with pulmonary hypertension, but the combination of right axis deviation and the changes in the V1 lead described above is more suggestive of RV hypertrophy.<sup>15-18</sup> Changes in the QRS complexes may be associated with ST segment depression and T wave inversion, particularly in leads V1 and V2 and in the inferior limb leads. These changes are not consistent however.<sup>15-18</sup>

In addition to changes in the amplitude of the QRS complexes there are also changes in QRS duration. The ventricular activation time defined as the time from the beginning of the QRS complex to the abrupt negative deflection of the downstroke of the R wave is increased in RV hypertrophy, with 42% of patients having values greater than the upper limit of normal (0.03 s).<sup>17</sup> In a series of 42 cases 9 (21.4%) patients were found to have incomplete right bundle branch block and 3 (7.1%) patients had complete right bundle branch block<sup>16</sup>. This can be compared with a suggested population incidence of 0.18–2% of complete right bundle branch block.<sup>19</sup>

The corrected QT interval (QT<sub>C</sub>) is prolonged in PAH and the degree of prolongation is correlated to both pulmonary pressures and RV function.<sup>20</sup> A QT<sub>C</sub> of greater than 480 ms is an independent predictor of mortality.<sup>20</sup> The difference between the longest and shortest QT interval (QT dispersion) has been shown to be increased in both men and women with PH and also asymptomatic patients with RV hypertrophy secondary to chronic altitude exposure.<sup>21, 22</sup>

Mapping of activation using monophasic activation potentials at the time of cardiac surgery for thromboembolism in CTEPH has shown delayed right ventricular activation with absence of epicardial breakthrough within the RV. Action potential duration was consistent across both the RV and LV meaning that repolarisation was delayed in the RV by the same amount as activation was delayed. This accounted for the negative T waves seen on the right side of the heart.<sup>23</sup>

The incidence of RV hypertrophy in PAH is estimated to be 87%, but the specificity of RV hypertrophy for PAH is poor due to multiple other causes.<sup>1</sup>

### **1.3.2 Pulmonary arterial hypertension and arrhythmias**

Cardiac arrhythmias are a major cause of morbidity and mortality in the general population. Virtually any condition that affects cardiac function is associated with an increase in arrhythmias. The incidence of arrhythmias in patients with PAH is high with reported figures of 11.7 to 26.7% depending on whether sinus tachycardia was classified as an arrhythmia.<sup>24-26</sup> Sinus tachycardia is found in around 10% of PAH patients and is thought to be related to sympathetic activation in response to decreased circulating volume. The presence of sinus tachycardia is associated with a poor prognosis.<sup>24</sup>

At the initial screening of a cohort of 51 untreated patients with PAH two patients had sinus bradycardia, and a further 6 patients had 1<sup>st</sup> degree atrioventricular (AV) heart block, with one patient requiring a dual chamber pacemaker for higher degree heart block. The mean PR duration in this cohort was  $180 \pm 50$  ms.<sup>24</sup>

Two studies have followed up a cohort of patients with PAH to look at the incidence and clinical significance of arrhythmias.<sup>26, 27</sup> In the first, a cohort of 231 patients with PAH and CTEPH were followed up for 6 years; 27 patients had a total of 31 episodes of supraventricular tachycardia (SVT) that consisted of atrial fibrillation (AF) (48%), atrial flutter (42%) and AV nodal reentrant tachycardia (AVNRT) (10%). This gave an annual risk of tachycardia of 2.8% per patient per year. The average time from diagnosis of PAH to arrhythmia was 3.5 years.<sup>26</sup> The second study included patients with PAH due to congenital heart disease and found similar rates of arrhythmias with 28 patients developing an SVT over a mean 5 year follow up. In this study AF (42%), atypical flutter (25%), typical flutter (18%) and AVNRT (14%) were observed.<sup>27</sup>

In 82-84% of patients the development of an SVT resulted in a clinical deterioration which was corrected by restoration of sinus rhythm.<sup>24-27</sup> To achieve restoration of sinus rhythm aggressive treatments were used with a combination of medical therapy, cardioversion and invasive ablation procedures.<sup>26</sup> Electrophysiological studies have demonstrated that flutter in PAH patients is often 'typical', i.e. related to a reentrant circuit in the right atrium (RA) which is dependent on conduction across the tricuspid isthmus and that these typical atrial flutters can be safely and effectively treated by ablation across the tricuspid valve isthmus.<sup>26-29</sup> In patients for whom it is not possible to restore sinus rhythm there is a significantly increased mortality.<sup>26</sup>

There is less evidence for ventricular arrhythmias in PAH.<sup>1</sup> In a limited study of 9 patients with PAH no serious ventricular arrhythmias were shown although there was an increase in the number of ventricular ectopic beats.<sup>30</sup> In a retrospective analysis of 3110 patients with PAH over 3 years in a multicentre study 513 patients died, and of these 17% were due to sudden and unexpected causes. Approximately one quarter of the patients who died underwent cardio-pulmonary resuscitation and of these patients ventricular fibrillation was seen in 8% of cases.<sup>31</sup>

Studies looking at arrhythmias in PAH have defined the incidence and prevalence of arrhythmias in a population of patients PAH but have not made a comparison with a matched cohort of apparently healthy individuals.<sup>25, 26</sup> The incidence and prevalence of

arrhythmias quoted from studies of the general population are not age and sex matched to studies of patients with PAH and may include people with other cardiac co-morbidities.<sup>32</sup>  
<sup>33</sup> This makes comparison of the rates of arrhythmias in PAH with apparently healthy individuals difficult and liable to underestimate the increase in arrhythmias due to the effect of PAH, but some inferences can be made.

There is evidence of AV node dysfunction with slowed conduction in the PAH population. The 14% incidence of 1<sup>st</sup> degree heart block and mean PR interval of 180±50 ms on initial screening in PAH patients discussed above is in contrast with an incidence of 1<sup>st</sup> degree heart block of 2.1% and mean PR interval of 160±22 ms for men and 153±22ms for women in the general population.<sup>34</sup>

As discussed above, there is strong evidence that all forms of SVT are more common in PAH with the cohort studies suggesting an incidence of around 3% per year and a prevalence of SVT of around 12%. This can be compared with general population studies suggesting an incidence of all forms of SVT of 0.04% and a prevalence of SVT of 0.23%.<sup>32</sup> It is also notable that there is a high proportion of AVNRT with no cases of accessory pathway mediated tachycardia (i.e. AV reentrant tachycardia) in the two cohort studies described above.<sup>26, 27</sup> Although reentry within the AV node results in a tachycardia, maintenance of the tachycardia is dependent on the balance between fast conduction, slow conduction and refractoriness within the AV node (see section 1.5.2.4).<sup>35</sup> There are no studies designed to elucidate which of these factors are affected in PAH.

A comparison can be made between the ratio of atrial flutter:AF cases. In the general population this is approximately 1:5 whereas in the PAH populations it is close to 1:1.<sup>26, 27</sup>  
<sup>33</sup> It is perhaps not surprising that typical flutter is disproportionately more prevalent in patients with PAH as the RA is exposed to raised pressures and the anatomical substrate for the flutter circuit is located within the RA.<sup>28</sup> Electrophysiological assessment of patients with PAH has shown slowing of conduction, fractionated signals and a trend towards an increase in right atrial effective refractory period in the in the RA in patients with PAH compared with controls. These changes may provide the substrate necessary for the maintenance of atrial flutter.<sup>28</sup>

The combination of bradycardia and tachycardia with involvement of the sinoatrial (SA) node, AV node, His-Purkinje system and atrial and ventricular myocardium demonstrates the impact of PAH on the cardiac conduction system at multiple sites and points to the possibility of multiple mechanisms.

### 1.3.3 Treatment in pulmonary arterial hypertension

Treatment in PAH has advanced rapidly over the past decade. In addition to supportive measures, specific therapy for PAH can be split into four broad categories: calcium channel blockers, prostanoids, endothelin receptor antagonists (ERAs) and phosphodiesterase inhibitors.<sup>1, 36-39</sup>

Calcium channel blockers act as vasodilating agents and their use should be restricted to patients who have shown a response to a vasodilating challenge assessed at right heart catheterisation which is estimated to be only around 15% of all PAH patients.<sup>1, 36, 39</sup>

Prostacyclin acts as a vasodilator. It also has antiplatelet and antiproliferative effects. Prostacyclin is down-regulated in PAH and therefore therapy with various forms of prostacyclins via inhaled, intravenous (iv), subcutaneous (sc) and oral routes can be used.<sup>36</sup> Benefits in terms of symptoms and haemodynamic parameters have been seen with all routes of administration of prostanoids.<sup>1, 36</sup> Prognostically significant benefits were seen with IV epoprostanol over a three month treatment period.<sup>40</sup>

The endothelin system is activated in PAH and leads to proliferation of vascular muscle cells and vasoconstriction.<sup>1, 37, 41</sup> ERAs have been shown to have beneficial effects on haemodynamic parameters, objective measurements of patients exercise capacity and subjective symptoms scores. No significant mortality benefit has been demonstrated with ERAs in randomised trials, but registry data suggest that there may be a mortality benefit.<sup>37</sup>

Phosphodiesterase inhibitors act by enhancing the effect of nitric oxide by inhibiting the inactivation of cGMP.<sup>38</sup> They were initially licensed for erectile dysfunction, but they are now used in the treatment of PAH. Clinical trials have demonstrated a benefit in patients with PAH showing an improved 6 minute walk test, New York Heart Association (NYHA) classification and subjective symptom assessment scores. They may be used in combination with prostacyclins and ERAs with improvement in functional status and haemodynamic parameters. There are no data to show prognostic benefit of phosphodiesterase inhibitors.<sup>38</sup>

Clinical trials with all four classes of drugs have focused on haemodynamic assessments, functional capacity and reduced symptom burden. There are limited data regarding

prognostic benefit and no studies have been performed to look at effect of treatment on the incidence of arrhythmias.

## 1.4 Cardiac physiology

### 1.4.1 Ion channels in the heart

Ion channels are transmembrane proteins that allow the passage of ions between the intra and extracellular space. They consist of an  $\alpha$  subunit which forms the pore that the ion passes through, and  $\beta$  subunits that regulate the function of the  $\alpha$  subunit.<sup>42, 43</sup>

The typical composition of an ion channel is of four  $\alpha$  subunits creating a central pore through the cell membrane. In the case of  $\text{Na}^+$  and  $\text{Ca}^{2+}$  channels these  $\alpha$  subunits have six transmembrane  $\alpha$  helices and are linked with covalent bonds. There is more variability in the  $\text{K}^+$  channels, with some consisting of four  $\alpha$  subunits that are similar to the  $\text{Ca}^{2+}$  and  $\text{Na}^+$  channels but are not covalently linked, and some of the  $\text{K}^+$  channels consisting of four smaller  $\alpha$  subunits or two  $\alpha$  subunits which have double the transmembrane  $\alpha$ -helices. Each of these  $\alpha$  and  $\beta$  subunit proteins is encoded by different genes.<sup>43</sup>

Flow of ions through ion channels is determined by the transmembrane electrochemical gradient and is a passive process. The flow of ions is controlled by opening and closing of the ion channels which for most of the ion channels involved in the action potential is controlled by voltage-dependent gates.<sup>43</sup>

The opening and closing of the  $\text{Na}^+$  channel for example is notionally controlled by two gates, one termed the m gate and one called the h gate. The m gate is formed by positively charged regions in the transmembrane  $\alpha$ -helices which undergo a conformational change in response to a change in the voltage across the cell membrane. The h gate is formed by intracellular peptide loops that form an 'inactivation particle' which occludes the intracellular opening of the pore.<sup>43</sup>

In the resting state the m gate is closed but the h gate is open and therefore there is no ionic flow. In response to a positive change in the transmembrane potential the m gate opens and the h gate remains open and hence both gates are open and ionic flow occurs. The change in voltage also causes the h gate to close but this happens more slowly. Once the h gate is closed the ionic current ceases; this process is called inactivation. In this state subsequent membrane depolarisation will not be able to reopen the ion channel as the h

gate will remain closed, and therefore the cell is said to be refractory. In the case of  $\text{Na}^+$  and  $\text{Ca}^{2+}$  channels, when the cell returns to its negative resting potential, the inactivation gate (h gate in the case of the  $\text{Na}^+$  channel) reopens and the activation gate (m gate in the case of the  $\text{Na}^+$  channel) closes meaning that the ion channel has returned to its resting state and can be activated by subsequent depolarisations; this process is called reactivation.<sup>43</sup> Detailed information regarding the activation and deactivation kinetics of individual ionic currents can be determined using the patch-clamp technique.<sup>44-47</sup>

Most ion channels are highly specific to a single ionic species due to ion binding sites within the pore of the ion channel.<sup>42, 46-49</sup> In addition to ion channels that are specific for an individual ion, the hyperpolarisation-activated cyclic nucleotide-gated (HCN) channels are permeable to both  $\text{K}^+$  and  $\text{Na}^+$ .<sup>42, 47-51</sup>

There are important differences in the distribution of these proteins between the different regions of the heart and also between species, which are thought to underlie the differences in the ionic currents seen.<sup>43, 52</sup> In particular there is substantial diversity in the repolarising  $\text{K}^+$  currents and considerable work has gone into determining the molecular basis of this diversity.<sup>52</sup> In part, the diversity is due to the considerable number of proteins that form the  $\alpha$  subunits, but it may also be attributable to either hetero- or homo-dimerization of the  $\alpha$ -subunits or regulation by the  $\beta$  subunits.<sup>52</sup> The currents and the  $\alpha$  subunits and  $\beta$  subunits responsible the currents within the heart are summarised in Table 1-1.<sup>43, 52</sup>

## 1.4.2 Membrane pumps and exchangers

In order for ion channels to function the ionic gradients across the cell membrane must be maintained and restored by the activity of membrane pumps and exchangers.

Membrane pumps such as the  $\text{Na}^+/\text{K}^+$  ATPase move ions against the electrochemical gradient across the membrane using intracellular stores of energy. The  $\text{Na}^+/\text{K}^+$  adenosine triphosphate(ATP)ase transports  $\text{Na}^+$  ions into the extracellular space in exchange for  $\text{K}^+$  ions into the intracellular space. The action of the  $\text{Na}^+/\text{K}^+$  ATPase leads to a high intracellular  $\text{K}^+$  concentration and a high extracellular  $\text{Na}^+$  concentration. This plays a crucial role in determining the negative intracellular resting potential of the myocytes due to the selective permeability of the cell membrane to  $\text{K}^+$  at typical resting membrane potential voltages. The permeability of the cell membrane to  $\text{K}^+$  is mainly due to the 'inward rectifier  $\text{K}^+$  current' current  $I_{K1}$ . In addition to this the  $\text{Na}^+/\text{K}^+$  ATPase moves

three  $\text{Na}^+$  ions to the extracellular space in exchange for two  $\text{K}^+$  ions into the intracellular space contributing further, by a few mV only, to the negative resting membrane potential of cardiac myocytes.<sup>42, 46, 53</sup>

Membrane exchangers use the electrochemical gradient across the cell membrane created by one ion to transport a different ion across the cell membrane in a passive manner. The  $\text{Na}^+-\text{Ca}^{2+}$  exchanger utilizes the gradient created by the  $\text{Na}^+-\text{K}^+$  ATPase to move one  $\text{Ca}^{2+}$  ion out of the cell in exchange for three  $\text{Na}^+$  ions into the cell.<sup>54</sup>

<b>Current</b>	<b>Ion selectivity</b>	<b><math>\alpha</math> subunit</b>	<b><math>\beta</math> subunit</b>
$I_f$ (funny current)	$\text{Na}^+$ and $\text{K}^+$	HCN1 HCN2 HCN4	
$I_{\text{Na}}$	$\text{Na}^+$	Nav1.1 Nav1.5 Nav1.8	Nav $\beta$ 1
$I_{\text{Ca,L}}$ (L-type $\text{Ca}^{2+}$ current)	$\text{Ca}^{2+}$	Cav1.2 Cav1.3	
$I_{\text{Ca,T}}$ (T-type $\text{Ca}^{2+}$ current)	$\text{Ca}^{2+}$	Cav3.1 Cav3.2	
$I_{\text{to}}$ (transient outward $\text{K}^+$ current)	$\text{K}^+$	Kv1.2 Kv1.4 Kv4.2 Kv4.3	KChIP2
$I_{\text{K,r}}$ (rapid delayed rectifier $\text{K}^+$ current)	$\text{K}^+$	ERG	minK
$I_{\text{K,s}}$ (slow delayed rectifier $\text{K}^+$ current)	$\text{K}^+$	KvLQT1	minK
$I_{\text{K1}}$ (inward rectifier $\text{K}^+$ current)	$\text{K}^+$	Kir2.1 Kir2.2 Kir2.4	

**Table 1-1 Summary of some of the major ionic currents,  $\alpha$  and  $\beta$  subunits involved in the cardiac action potential. From Katz<sup>43</sup> and Nerbonne.<sup>52</sup>**

### 1.4.3 The action potential

The action potential is a change in voltage across the cell membrane over time, and its morphology is created by the net inward and outward flux of ions across the cell membrane.<sup>46, 47</sup> The principal three ions involved in impulse generation and propagation are  $\text{Na}^+$ ,  $\text{Ca}^{2+}$  and  $\text{K}^+$ .

The characteristics of an individual current in terms of both voltage and time dependent activation and inactivation have been determined experimentally. However, the action

potential of the whole cell involves multiple individual currents acting simultaneously and therefore the action of each current can have an effect on the other currents. The action potential is the net result of the complex interactions of these different currents. Computer modelling has been used in order to synthesise the information about the kinetics of individual ion channels into a description of the action potential of the cell. The Courtmanche *et al.* model<sup>40</sup> is based on data for ionic currents in human atrial cells. This information has been integrated to generate a model of the action potential in a human atrial cell.<sup>46</sup> The model generates action potentials that show remarkable similarity to experimentally recorded data in human atrial cells. The simulated cell has a stable resting potential of -80 mV and when stimulation is modelled it generates an action potential that has the typical morphology recorded from human atrial cells.

The typical action potential morphology seen in atrial and ventricular cells has been classified into 5 distinct phases and the major ionic currents underlying them have been described (Figure 1-1):<sup>55</sup>

Phase 0: Rapid depolarisation caused by activation of the fast  $\text{Na}^+$  current ( $I_{\text{Na}}$ )

Phase 1: Rapid early repolarisation caused by the transient outward  $\text{K}^+$  current ( $I_{\text{to}}$ )

Phase 2: Plateau phase, a relatively prolonged period during which there is a balance of inward  $\text{Ca}^{2+}$  currents and outward  $\text{K}^+$  currents, predominantly  $I_{\text{K,r}}$  and  $I_{\text{K,s}}$

Phase 3: Inactivation of inward  $\text{Ca}^{2+}$  currents leads to repolarisation via outward  $\text{K}^+$  currents

Phase 4: The membrane is held at its negative resting potential by the inward rectifying  $\text{K}^+$  current,  $I_{\text{K1}}$

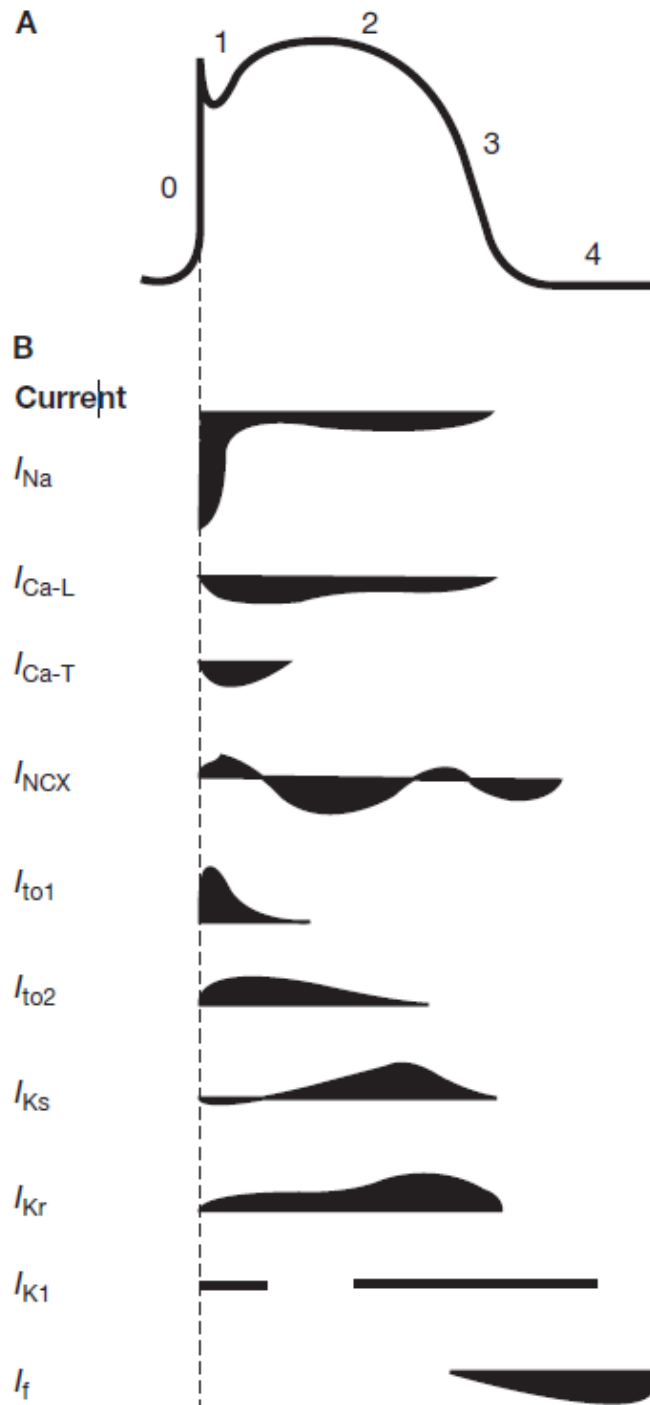


**Figure 1-1. Ventricular action potential: A) schematic action potential identifying the 5 stages B) Individual currents underlying the action potential. From Nass *et al.*<sup>55</sup>**

#### 1.4.4 Impulse generation in pacemaking cells

There is still considerable debate as to the cellular mechanisms that underlie the generation of an action potential in pacemaking cells. Current debate has focused on the concepts of the ‘membrane-clock’ and the ‘calcium clock’.<sup>56</sup> In the membrane clock hypothesis the funny current ( $I_f$ ) is thought to be the key current initiating the heartbeat. Support for this comes from the fact that the HCN channels that underlie the funny current

are highly abundant within the sinoatrial (SA) node.<sup>47</sup> The kinetics of  $I_f$  are also appropriate for pacemaking within the SA node with activation occurring at around  $-45$  mV with full activation at approximately  $-100$  mV. At these voltages there is a net inward current due to influx of  $\text{Na}^+$  ions into the cell which is thought to account for the early phase of diastolic depolarisation.<sup>50, 56</sup> Further evidence for the role of  $I_f$  in pacemaking comes from the demonstration that blockade of  $I_f$  leads to a slowing of the sinus rate with a drug (ivabradine) that blocks  $I_f$  licensed for clinical practice in heart failure and angina.<sup>56, 57</sup>

A competing hypothesis comes in the form of the ‘calcium-clock’. In this theory pacemaking is due to the cycling of  $\text{Ca}^{2+}$  into and out of the sarcoplasmic reticulum. In this hypothesis the initiating event for each beat is localised  $\text{Ca}^{2+}$  release events from the sarcoplasmic reticulum via the ryanodine receptor. These  $\text{Ca}^{2+}$  release events cause depolarisation by the activation of the  $\text{Na}^+/\text{Ca}^{2+}$  exchanger (NCX).<sup>56</sup>

The degree to which both the ‘membrane clock’ and the ‘calcium clock’ may both be relevant, with the possibility of one mechanism ‘entraining’ or regulating the other is currently debated.<sup>56</sup>

### 1.4.5 Impulse propagation

In order for the impulse generated in the pacemaking cells to propagate through the heart myocardial cells are electrically coupled to each other *via* gap junctions. These are channels that allow the electrical impulse to be conducted between cells via electrotonic flow.<sup>58, 59</sup> The channels are created by connexins which form two joined hemichannels, one from each cell. The hemichannels are present on adjacent areas of the two coupled cells and are composed of six connexins creating central pore forming units.<sup>58-60</sup> Four connexin isoforms have been described in the heart: Cx40, with the highest conductance (200 pS); Cx43, with a medium conductance (60-100 pS); Cx45 with a small-conductance (20-40 pS); and Cx31.9 with an ultra-small conductance (9 pS). In the working myocardium Cx43 is the predominant isoform expressed.<sup>61-63</sup>

In order for the action potential to be propagated the ‘source’ current delivered from the upstream cells must be sufficient to depolarise the down-stream cells to the point where  $I_{\text{Na}}$  is activated and an action potential is generated. Once the action potential is generated the cell becomes positively charged relative to the downstream cells which are still at their negative potential; these cells act as a ‘sink’ drawing current from the depolarised cell.<sup>64</sup>

The velocity of conduction in working myocardium is dependent on both  $\text{Na}^+$  influx during phase 0 of the action potential and the coupling of cells via gap junctions.<sup>64</sup> For conduction to continue the charge generated by each cell must equal or exceed the charge consumed by each cell. The charge generated is the sum of the current provided by the cell. The charge consumed is the sum of the current necessary to bring the downstream cell to threshold.<sup>64</sup> This concept has been expressed as a ratio of charge generated:charge consumed termed the safety factor, whereby a safety factor of greater than 1 implies that conduction will continue. When the safety factor drops below 1 conduction fails due to ‘source-sink’ mismatch.<sup>64</sup>

## 1.5 The cardiac conduction system

The cardiac conduction system comprises the SA node, the AV node and the His-Purkinje system. These are areas of specialised cells within the heart that have distinct functional differences from the working myocardium.<sup>48</sup>

### 1.5.1 The sinoatrial node

The SA node has been known to be the initiating source of the heartbeat for over 100 years since its discovery by Keith and Flack in 1907. The SA node lies in the posterior RA in a region termed the intercaval region that lies between the superior and inferior vena cava. It is bordered on the lateral side by a thick ridge of muscle called the crista terminalis.<sup>47, 48</sup>

The relative abundance of mRNA of the genes known to encode for the proteins that make up the ion channels, membrane pumps and exchangers have been quantified in the SA node. Low levels of the genes encoding the proteins that generate the current  $I_{K1}$  have been demonstrated.  $I_{K1}$  is responsible for the negative resting potential of cells in the working myocardium as described in section 1.4.2 and therefore a reduction in this current leads to a less negative resting membrane potential in the SA node of around -60 mV (compared with approximately -84mV in working myocardium).<sup>47, 48</sup> There are also high levels of the HCN genes that are responsible for  $I_f$  which leads to the phase 4 diastolic depolarisation in the pacemaker cells due to a flow of cations (predominantly  $\text{Na}^+$ ) into the cell as described in section 1.4.1.<sup>47, 48</sup>

Using a mathematical model for  $I_f$  and using the relative abundance of mRNA for the ion channels, membrane pumps and exchangers to alter the relative magnitude of the currents

seen in the Courtmanche *et al.* model<sup>46</sup> an action potential for the atrial muscle, SA node and paranodal area ( the area surrounding the SA node) was generated which showed a marked similarity to that seen in experimental data (Figure 1-2).<sup>47-49</sup>

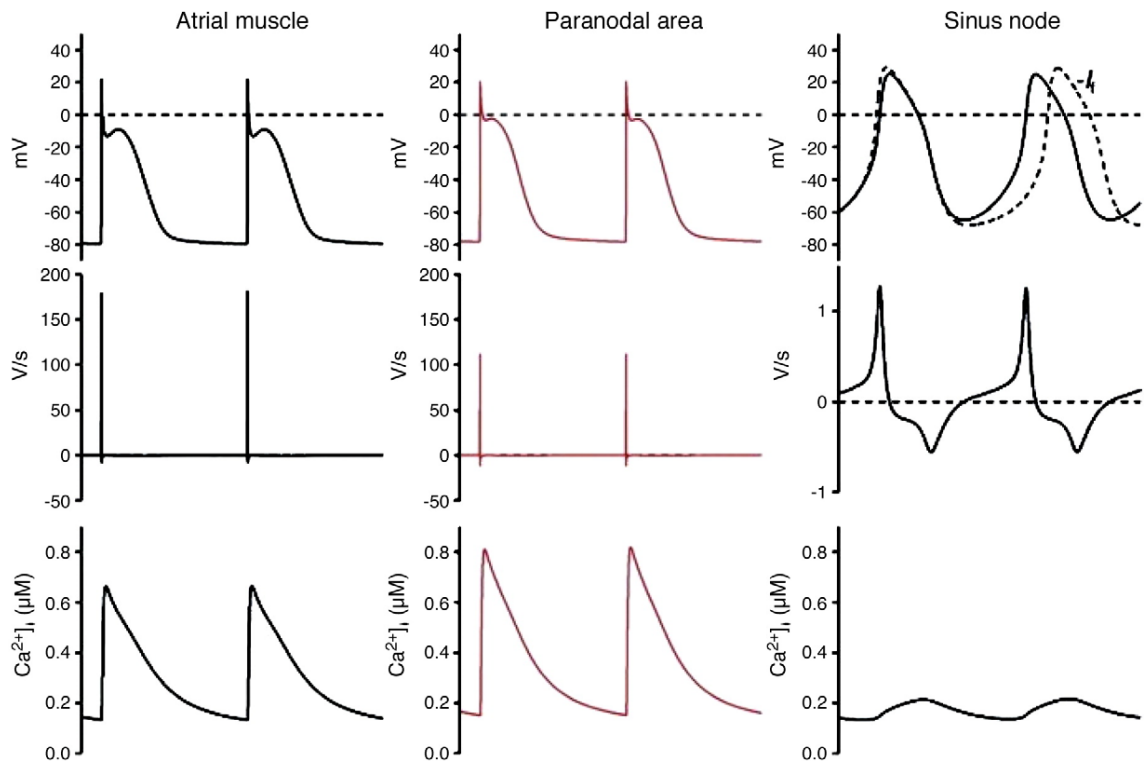


**Figure 1-2.** Modification of Courtmanche *et al.* model<sup>46</sup> using mRNA expression in the SA node and paranodal area to predict electrical activity in the SA node and paranodal area.<sup>47</sup>

## 1.5.2 The atrioventricular node

Under normal conditions the AV node is the only connection between the atria and the ventricles. Its primary function is to conduct the action potential to ensure each atrial contraction is followed at an appropriate interval by a ventricular contraction. The AV node delays conduction from the atrium to the ventricle to allow atrial contraction to complete before ventricular contraction begins and hence optimise cardiac output. In addition to this basic function the AV node protects the ventricle by limiting the maximum rate of conduction in conditions of rapid atrial activation such as AF. In sinus bradycardia it may also act as a ‘backup’ pacemaker. In contrast to these beneficial roles dysfunction of the AV node may lead to AV block and the need for pacemaker implantation. The AV node may also provide part of the substrate for the reentrant arrhythmia, AVNRT.<sup>61, 65</sup>

### 1.5.2.1 Anatomy

There is considerable structural heterogeneity within the relatively small region of tissue defined as the AV node and this has led to some variation in the terms used to describe the different regions within the AV node.<sup>61, 65, 66</sup> The term AV node is defined as the tissue contained within the triangle of Koch, which in turn is defined as the region between the tendon of Todaro, ostium of the coronary sinus and the tricuspid valve annulus at the base of the RA. This is in contrast to the tissue enclosed within the central fibrous body for which the term ‘penetrating bundle’ is reserved.<sup>66</sup> The working atrial myocardium is connected to an area within the AV node termed the transitional tissue, which in turn is connected to a tract of specialised nodal and nodal-like myocytes that extend along the tricuspid valve annulus in the RA called the inferior nodal extension. The inferior nodal extension forms a continuum with the compact node located at the apex of the triangle of Koch at the point at which the AV node becomes the penetrating bundle.<sup>61, 66</sup> The penetrating bundle passes through the central fibrous body emerging into the ventricle where it becomes the His bundle. The His bundle bifurcates into the left and right bundle branches which then branch further to become the Purkinje fibres. The Purkinje fibres are in contact with the endocardial aspect of the working ventricular myocardium and allow rapid synchronous conduction of the action potential to the working myocardium (Figure 1-3).<sup>65</sup>

### 1.5.2.2 Ionic currents in the atrioventricular node

Studies on the functional characteristics of the cells of the AV node have defined three different types of cell: AN cells, which have an action potential similar to that of atrial cells, with a rapid upstroke; N cells, which have an action potential with a slow upstroke and diastolic depolarisation; and NH cells, with a fast action potential upstroke and prolonged action potential duration.<sup>67, 68</sup> Despite the description of three distinct subtypes of cell the transition from one region to the next is gradual. Correlation of the anatomical regions described above with single cell recordings taken using sharp electrodes in the rabbit have demonstrated that there was heterogeneity and overlap of cell types within each region. However, the AN cell type was largely localised to the region of the transitional tissue, the N cell type was largely localised to the region of the compact node and inferior nodal extension and the NH cell type were largely localised to the penetrating bundle.<sup>69-72</sup>

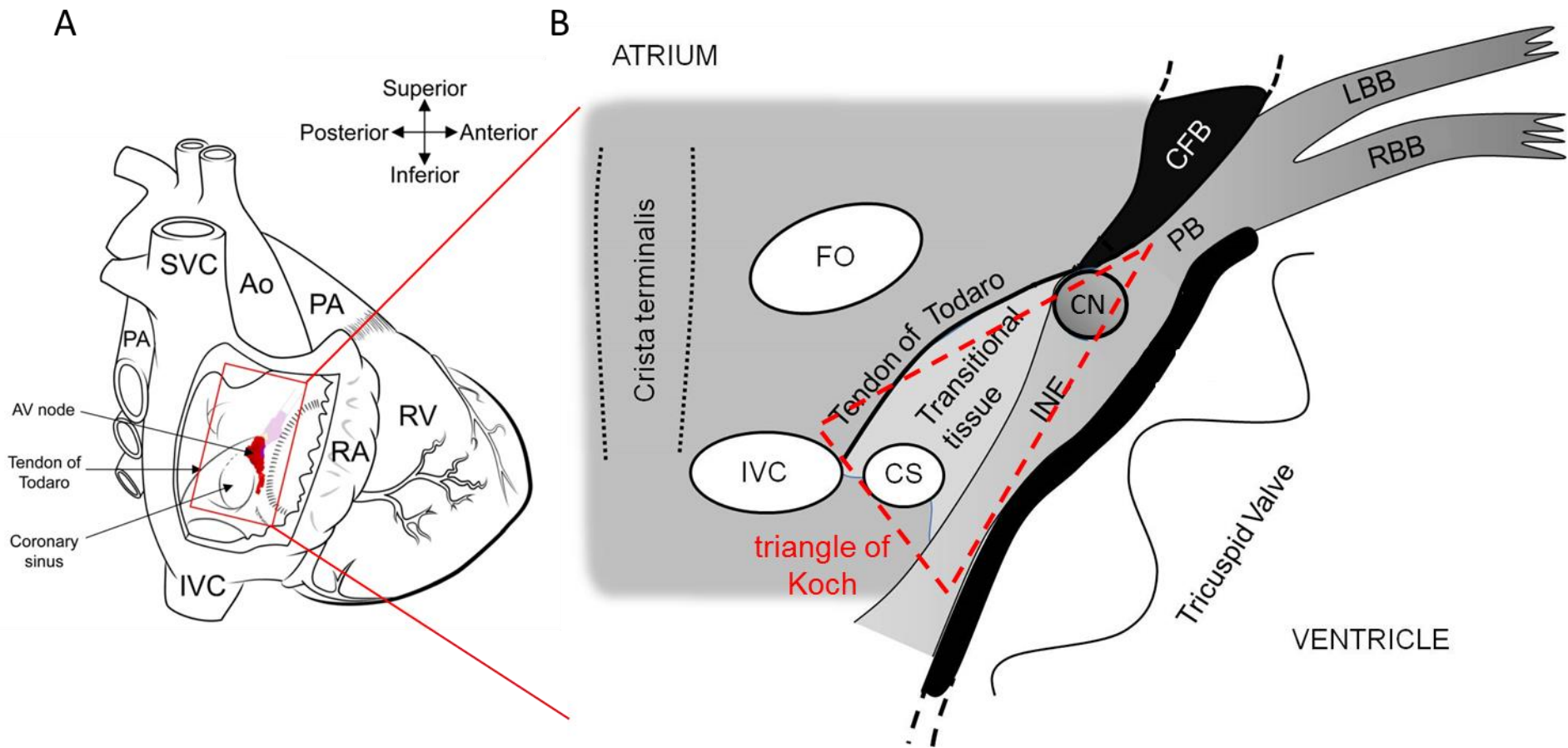


**Figure 1-3.** Schematic diagram demonstrating the anatomy of the AV node A) Section of RA removed from the heart to reveal the location of the AV node in the interatrial septum along the tricuspid valve annulus B) An expanded version of the region of interest in A The triangle of Koch (marked with a dashed red line marks the position of the AV node and is formed by the tricuspid valve annulus, tendon of Todaro and the coronary sinus. Within this region the atrium is in connection with the transitional tissue which in turn is in connection with the inferior nodal extension and compact node. As the AV node penetrates the central fibrous body it becomes the penetrating bundle which enters the ventricle before splitting into the left and right bundle branches. Ao – aorta, CFB – central fibrous body, CN – compact node, CS – coronary sinus, FO – fossa ovalis, INE – inferior nodal extension, IVC – inferior vena cava, LBB – left bundle branch, PA – pulmonary artery, PB – penetrating bundle, RA – right atrium, RBB – right bundle branch, RV – right ventricle, SVC – superior vena cava. From Temple *et al.*<sup>61</sup>

Studies on isolated cells from the AV node suggest that the cells corresponding to the AN, N and NH action potential types are morphologically distinct with smaller spindle shaped or ovoid cells corresponding to N or NH cells and larger (although still smaller than atrial cells) rod shaped cells corresponding to AN cells.<sup>67, 73</sup> Patch-clamp studies using these single cells have been performed to determine which of the ionic currents described above are important in the AV node. In the N cells the  $I_{Na}$  current is dramatically reduced, consistent with the slow upstroke of the N cell action potential.<sup>68, 73, 74</sup>  $I_{Na}$  is present in the AN and NH cells consistent with their rapid upstroke.<sup>68, 73, 74</sup> Support for these findings comes from low expression of SCN5A and  $Na_v1.5$  (the gene and protein that form the channel responsible for  $I_{Na}$ ) in the inferior nodal extension and compact node.<sup>71, 72, 75, 76</sup>

Both  $I_{Ca,L}$  and  $I_{Ca,T}$  have been demonstrated in the N cells of the AV node and are responsible for the action potential upstroke.<sup>77-81</sup> Mouse studies using knockout of both  $Ca_v1.3$  (which underlies  $I_{Ca,L}$ ) and  $Ca_v3.1$  (which underlies  $I_{Ca,T}$ ) demonstrate impaired AV nodal conduction with an additive effect of double knockout causing higher grades of AV node disruption and AV block. In addition to being important for AV nodal conduction, block of  $I_{Ca,L}$  and  $I_{Ca,T}$  leads to a decrease in the rate of spontaneous activity of the N-cells.<sup>79, 82</sup> The relative contributions of the different proteins that underlie both  $Ca^{2+}$  currents is species specific; in the mouse  $Ca_v1.3$  is the protein that accounts for the majority of  $I_{Ca,L}$  in the AV node with only a small residual effect of  $Ca_v1.2$  seen in  $Ca_v1.3$  knockout.<sup>79, 80</sup> In the rat, mRNA for  $Ca_v1.3$  is expressed in low quantities with mRNA for  $Ca_v1.2$  expressed in much greater quantities. However, the functional consequences of this difference has not been assessed.<sup>83</sup>

The HCN channels underlying the funny current  $I_f$  are highly expressed in the compact node and inferior nodal extension compared with the working myocardium, and  $I_f$  has been shown to play a role in the pacemaker activity of the AV node.<sup>71, 72, 76, 84-86</sup> In mice there are regional differences in the expression of the HCN isoforms in different regions of the heart; HCN4 is mainly expressed in nodal tissue whereas HCN1 is expressed in the atrial and nodal tissue and HCN2 is predominantly expressed in the ventricular myocardium.<sup>87</sup> A recent study using a conditional cardiac specific knockout of HCN4 in mice demonstrated significant sinus bradycardia but the most serious consequences were seen in the AV node with sudden death around the 5<sup>th</sup> day after conditional knockout of HCN4 due to AV block.<sup>84</sup> These intriguing findings were unexpected but suggest that  $I_f$  may play an important role in both pacemaking and conduction in the AV node.

As described in section 1.4.1,  $I_{K1}$  is important for maintaining the negative resting potential of the cardiac cells in the working myocardium.  $I_{K1}$  is greatly reduced in the AV nodal cells resulting in a negative resting potential of approximately  $-60\text{mV}$  similar to that of the SA node.<sup>48, 68, 88, 89</sup> In keeping with absence of  $I_{K1}$ , very low levels of mRNA and protein expression for  $K_{ir2.1}$ ,  $K_{ir2.2}$  and  $K_{ir2.3}$  (which underlie  $I_{K1}$ ) have been shown in the compact node and inferior nodal extension in the rat, rabbit and human.<sup>72, 74, 76, 83</sup>

In the AV nodal cells  $I_{K,r}$  but not  $I_{K,s}$  has been shown to play an important role in repolarisation in contrast with the working myocardium where both  $I_{K,r}$  and  $I_{K,s}$  are important.<sup>81, 90, 91</sup> Consistent with this is the finding that rat hearts exhibit prolonged AH intervals and increased AV effective refractory period (AVERP) when exposed to pharmacological agents that block  $I_{K,r}$ , but not  $I_{K,s}$ .<sup>92</sup> Considerably higher levels of ether-related-a-go-go (ERG) (the protein that underlies  $I_{K,r}$ ) compared with  $K_vLQT1$  (the protein that underlies  $I_{K,s}$ ) have been seen in both rabbit and human hearts.<sup>72, 74, 76</sup>

The transient outward current  $I_{to}$  has also been shown to be present in the nodal myocytes, albeit reduced compared with the working myocardium.<sup>67, 74, 88</sup> Despite this the levels of  $K_v4.2$  expression was increased in the nodal tissues in rabbits and humans,  $K_v1.4$  was decreased in nodal tissues in rabbits but increased in humans, and  $K_v4.3$  was unchanged in humans and not studied in rabbits ( $K_v1.4$ ,  $K_v4.2$  and  $K_v4.3$  are the proteins that underlie  $I_{to}$ ).<sup>72, 76</sup> Gene knockout studies using mice deficient in either  $K_v1.4$  or  $K_v4.2$  showed minimal alterations in AV node function. However, a combination of knockout of both  $K_v1.4$  and  $K_v4.2$  caused complete heart block.<sup>93</sup>

Vagal stimulation causes decreased conduction at the AV node. This is due to release of acetylcholine which activates the current  $I_{K,ACh}$  leading to an outward potassium current which hyperpolarises the AV nodal cells.<sup>94</sup> Interestingly a similar current has recently been shown to be activated in nodal myocytes by endothelin 1.<sup>90</sup>

### **1.5.2.3 Connexin expression in the atrioventricular node.**

Studies of the AV node have all shown that the compact nodal region shows very low expression of the medium conductance Cx43 but preserved expression of the low conductance Cx45.<sup>72, 75, 76, 95-97</sup> This means that the cells of the AV node have poor electrical coupling, which is consistent with the role of the AV node in delaying conduction from the atria to the ventricles.

The transitional tissues do express Cx43 but at reduced levels compared to the atrial myocardium.<sup>72, 76, 95, 96</sup> Most studies have shown low levels of Cx43 at the origin of the inferior nodal extension near the coronary sinus with increasing Cx43 levels as the inferior nodal extension approaches the compact node region, but one study has demonstrated high levels of Cx43 in the inferior nodal extension in humans.<sup>76, 95, 98</sup> As the conduction system continues distally through the central fibrous body to become the penetrating bundle the expression of Cx43 continues to increase in the rabbit; in the rat and human node Cx43 levels remain low but expression levels of the high conductance Cx40 rise.<sup>75, 76, 95, 98</sup>

As the penetrating bundle continues distally it splits into the right and left bundle branches. Both branches have been shown to have high levels of Cx40 in the mouse, rat, rabbit and human heart consistent with their role in fast conduction to the ventricles.<sup>75, 97, 99</sup>

The functional consequences of the connexins in the AV node have been investigated using gene knockout studies in the mouse. These studies have demonstrated the importance of Cx30.2, Cx40 and Cx45 but not Cx43 to AV node conduction.<sup>100</sup> These investigations have been limited by the lethality of homozygous knockout of either Cx43 or Cx45.<sup>101, 102</sup> Homozygous Cx40 knockout mice demonstrate an increased PR interval which is due to slowing of conduction in both the AV node and the His-Purkinje system.<sup>103, 104</sup> Knocking out Cx30.2 in mice leads to a paradoxical increase in conduction velocity across the AV node which can be normalised by knocking out Cx40 in addition to Cx30.2.<sup>105</sup> The reason for these changes in conduction across the AV node are not clear. It is possible that they are due to Cx30.2 forming heterotypic gap junctions with Cx40. Another possibility is that the Cx30.2 and Cx40 are expressed in different regions of the AV node and that the increased conduction velocity induced by knockout of Cx30.2 is balanced by the reduced conduction velocity induced by knockout of Cx40.<sup>105</sup> Despite this the human equivalent of Cx30.2 is Cx31.9 and only very low levels of Cx31.9 have been shown in all areas of cardiac tissue. Therefore, the relevance of mouse knockout studies to human physiology is questionable.<sup>72, 100, 106</sup> Heterozygous knockout of Cx45 in addition to homozygous knockout of Cx40 has been shown to lead to further increases in PR interval, but the site at which conduction is slowed has not been investigated.<sup>107</sup>

#### ***1.5.2.4 Dual atrioventricular nodal physiology***

Both clinical and experimental electrophysiology has demonstrated that there are two pathways for impulse propagation through the AV node, termed the fast and slow pathways.<sup>35, 108</sup> The fast pathway provides the quickest route through the AV node and is

the route for action potential conduction at normal heart rates. The slow pathway is ‘bypassed’ at longer coupling intervals (i.e. normal heart rates) but it may be the route for impulse propagation with shorter coupling intervals because the slow pathway has a shorter refractory period than the fast pathway and is therefore still excitable when conduction along the fast pathway has failed.<sup>74</sup> This concept has been called ‘dual nodal physiology’.<sup>74</sup> Intracellular recordings, optical recordings and computer models of AV node action potentials have been used to investigate the functional consequences of dual nodal physiology and all have shown that the dual pathways form the substrate of AVNRT (see section 1.6.2).<sup>74, 108, 109</sup> Correlation of the functional recordings with histological images has demonstrated that the region within the AV node corresponding to the fast pathway is the transitional tissue and that the region corresponding with the slow pathway is the inferior nodal extension.<sup>95</sup> Support for these findings comes from the fact that catheter ablation for AVNRT targets the slow pathway at a region between the coronary sinus os and the tricuspid valve, i.e. the location of the inferior nodal extension.<sup>110</sup> The ‘fast’ and ‘slow’ conduction properties of the two regions are in accordance with both their ion channel and connexin distribution, i.e. higher levels of Cx43 and  $I_{Na}$  in the transitional tissues and lower levels of Cx43 and  $I_{Na}$  in the inferior nodal extension.<sup>72</sup>

#### ***1.5.2.5 The Wenckebach phenomena and decremental conduction***

Wenckebach described an intermittent block in conduction over 100 years ago on the basis of arterial pressure tracings before the existence of ECG recordings.<sup>111</sup> Subsequent work has further classified Wenckebach conduction using the ECG and the term is most often applied to describe block across the AV node where it can be used interchangeably with the term Mobitz 2<sup>nd</sup> degree block, type I.<sup>111</sup> In Wenckebach conduction the PR interval progressively increases until conduction blocks and therefore there is no ventricular beat following the atrial beat. The next atrial beat conducts to the ventricle with a short PR interval and the cycle then repeats.<sup>111</sup>

Wenckebach type conduction has been shown to occur in several experimental situations including in single cells from the AV node and working ventricular myocardium and also in larger tissue preparations where two areas of excitable tissue are connected by a region of poor conduction.<sup>112-114</sup> If one area of excitable tissue was stimulated at an appropriate short cycle length the second region of excitable tissue had not regained full excitability and therefore the second region of tissue took longer to activate and subsequently repolarise. This meant that the diastolic interval of the second region was reduced before

the next beat. The shorter diastolic interval led to further delay in conduction and therefore further shortening of the diastolic interval for each subsequent beat until the impulse is not conducted from the first region to the second region and there is a long diastolic interval in the second region. The cycle restarts on the next beat (Figure 1-4).<sup>112-114</sup> The ionic currents underlying the delay in conduction have been studied using single myocytes from nodal tissues and ventricular myocardium demonstrating that cardiac myocytes can continue to be refractory after the action potential has completed, so called ‘post repolarisation refractoriness’. This is thought to be due to an incomplete inactivation of the voltage and time dependent slow repolarising  $K^+$  currents which were activated by the preceding action potential (named  $I_K$  in the study, but presumably corresponding to  $I_{K,r}$  and  $I_{K,s}$ ).<sup>112</sup> This post repolarisation refractoriness caused a ‘step delay’ in activation before the rapid upstroke of the next action potential which led to further shortening of the diastolic interval until failure of conduction occurs. After failure of conduction there is a prolonged diastolic interval which allows the myocytes to recover full excitability. The next beat therefore occurs without a ‘step delay’ and the cycle repeats.<sup>112, 113</sup> In addition to the ionic mechanisms demonstrated in single cells the fast and slow pathways play a role in the Wenckebach phenomenon with a transition from activation propagating via the fast pathway in the initial cycles and switching to the slow pathway towards the end of the Wenckebach sequence until finally block occurs and the sequence repeats.<sup>61, 114</sup> Destruction of the slow pathway increases the Wenckebach cycle length but Wenckebach conduction still occurs demonstrating the complexity of the phenomenon.<sup>114</sup>

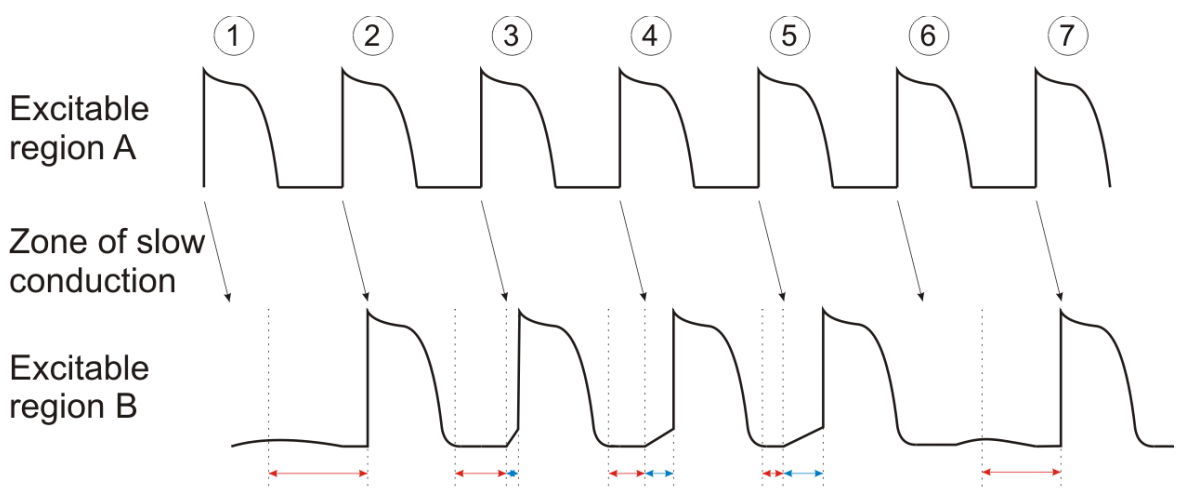


**Figure 1-4. Schematic representation of Wenckebach conduction between two regions of excitable conduction separated by a region of delayed conduction. Region A is stimulated with a constant cycle length. The first impulse is not conducted from region A to region B which means that there is a long diastolic interval in region B (marked with a red arrow). The second impulse is conducted from region A to region B; because of the long diastolic interval there is no post repolarisation refractoriness. The third impulse is conducted from region A to region B after repolarisation has occurred, but because of the shorter diastolic interval there is some post**

repolarisation refractoriness and therefore a delay in excitation in region B (marked with a blue arrow). This effect increase for the fourth and fifth beat until the sixth beat is not conducted and the cycle starts again.

The term decremental conduction is used to describe the slowing of conduction across the AV node with progressively shorter-coupled stimuli which generates a characteristic AV node conduction curve. Modelling studies have taken the data from these conduction curves for individual human subjects and then used them to predict AV nodal conduction at different atrial rates. These models accurately predict both the atrial rate at which Wenckebach conduction occurs and the pattern of Wenckebach conduction across the AV node, suggesting that both decremental conduction and the Wenckebach phenomenon are due to similar mechanisms.<sup>115</sup>

## 1.6 Arrhythmogenesis

### 1.6.1 Cellular mechanisms

#### 1.6.1.1 Abnormal automaticity

The SA node is the leading site of pacemaker formation under normal conditions (see sections 1.4.4 and 1.5.1). In contrast the atrial and ventricular muscle display a stable and more negative resting membrane potential than the cells of the sinus node. This negative potential inhibits normal pacemaking activity.<sup>116, 117</sup>

Under certain pathological conditions such as ischaemia, hypokalaemia, hyperkalaemia and stretch, the resting membrane potential of atrial and ventricular myocytes becomes less negative, and abnormal automaticity mediated by  $I_f$ ,  $I_{Na}$  and  $I_{Ca,L}$  can occur.<sup>116, 117</sup>

#### 1.6.1.2 Triggered activity

Depolarisations that depend on the preceding impulse for their formation are termed triggered potentials. They are split into early afterdepolarisations (EADs) and delayed afterdepolarisations (DADs) (Figure 1-5).<sup>116</sup>

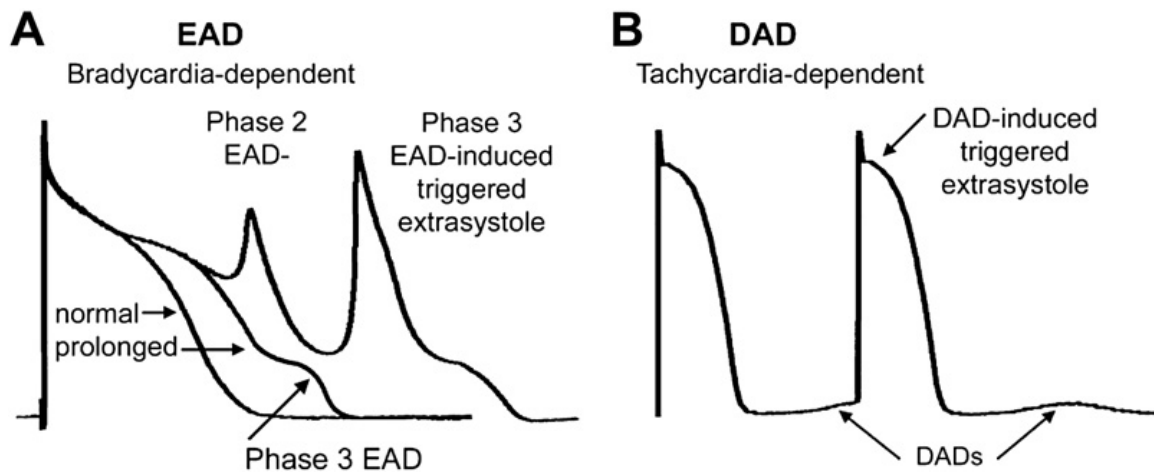


Figure 1-5. ECG recordings showing examples of EADs and DADs. A) EADs can occur in phases 2 and 3. B) DADs occur during phase 4. If the EAD or DAD is of sufficient amplitude it can cause a triggered extrasystole. From Antzelevitch *et al.*<sup>116</sup>

#### 1.6.1.2.1 Early after depolarisations

EADs occur during phase 2 and phase 3 of the action potential. They are caused when the balance of repolarising  $K^+$  currents and depolarising currents (predominantly  $I_{Ca,L}$  and  $I_{NCX}$ ) are altered to favour depolarisation rather than repolarisation. This can cause the membrane potential to remain between the voltage at which steady state activation and steady state inactivation of  $I_{Ca,L}$  overlap (i.e. the 'window current') which further promotes  $I_{Ca,L}$  and the depolarising current generated by NCX ( $I_{NCX}$ ). The combination of these factors can lead to time- and voltage-dependent reactivation of  $I_{Ca,L}$  which can generate sufficient inward current to initiate a second action potential.<sup>116-118</sup>

Conditions favouring the formation of EADs can be related to a reduction of the repolarising outward  $K^+$  currents. This is seen in bradycardia, with drugs that block the  $K^+$  currents and genetic conditions such as the long QT syndrome. They can also be caused by a gain in function of the inward  $Na^+$  current such as in the long QT III syndrome.<sup>116-118</sup> Triggered activity can then lead to torsades des pointes, polymorphic ventricular tachycardia (VT), and ventricular fibrillation (VF) via a combination of focal activity and reentrant mechanisms.<sup>118</sup>

#### 1.6.1.2.2 Delayed after depolarisations

In contrast to EADs, DADs occur during phase 4 of the action potential. Spontaneous release of  $Ca^{2+}$  from the sarcoplasmic reticulum (SR) leads to further activation of

depolarising currents including  $I_{NCX}$  and the  $Ca^{2+}$  activated  $Cl^-$  channel. If the amplitude of the inward current is sufficient a spontaneous action potential occurs leading to a triggered premature beat. A combination of factors including a reduced  $I_{K1}$ , enhanced NCX and adrenergic stimulation promote the formation of DADs.<sup>116-118</sup>

### 1.6.2 Reentrant mechanisms

Classical reentry has been described for over one hundred years. It requires a fixed anatomical obstacle with a circuit of conducting tissue around it and unidirectional block of conduction.<sup>64, 116, 117</sup> The fixed anatomical obstruction gives a distance for the circuit. The wavelength of the circuit  $\lambda$  is defined as the conduction velocity ( $\theta$ ) multiplied by the time for repolarisation  $t_r$ .

$$\text{i.e. } \lambda = \theta t_r$$

If an appropriately timed stimulus results in unidirectional conduction block the impulse blocks in one direction but is able to propagate in the other direction.<sup>64, 116, 117</sup>

Looking at the formula above it can be seen that if the length of the circuit is greater than the wavelength then the tissue will have recovered excitability before the impulse returns to its original position and hence can be reactivated. This leads to an active wavefront that is able to propagate in a continuous repeating pattern. This is termed reentry or circus movement (Figure 1-6).<sup>64, 116, 117</sup>

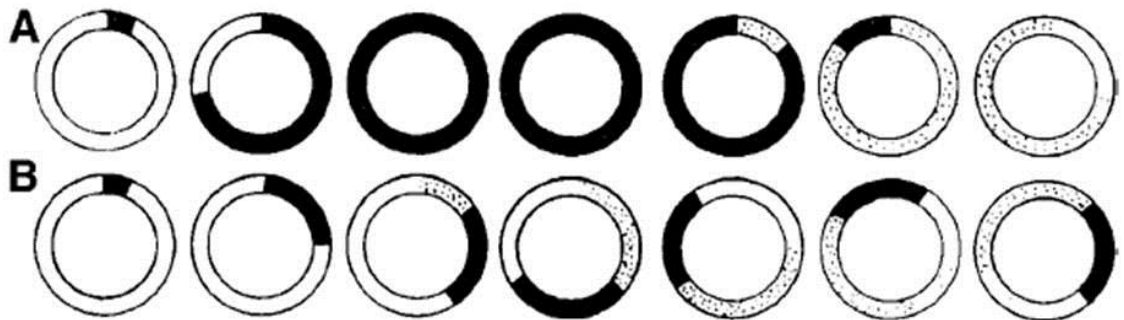


**Figure 1-6. Classical re-entry around a fixed anatomical obstacle.** The black region represents depolarised tissue, the white area represents repolarised/resting tissue, the stippled region represents repolarising tissue which is refractory to further stimulation. A) Failure to initiate reentry due to a long wavelength. An initial impulse propagates with unidirectional block in the clockwise direction. The wavelength (conduction velocity  $\times$  time for repolarisation) is greater than the length of the circuit and therefore the circuit terminates when the depolarising wavefront reaches the origin of the impulse which is still depolarised and therefore refractory to further stimulation. B) Successful reentry initiation with a reduced wavelength due to a decreased conduction velocity and time for repolarisation. The wavelength is less than the distance of the circuit and therefore the original site of stimulation has repolarised and therefore recovered excitability by the time the depolarising wavefront returns to its origin. The cycle can therefore repeat and a reentrant circuit is created. From Kleber *et al.*<sup>64</sup>

In this model there is an area of excitable tissue between the head of the active wavefront and the tail of the depolarised tissue from the previous circuit of activation. This is termed the excitable gap.<sup>64, 116, 117</sup>

This classical mechanism of reentry has been used to understand many clinical tachycardias including atrial flutter, AVNRT, atrioventricular reentrant tachycardia (AVRT) and monomorphic VT.<sup>64, 116, 117</sup> The commonest form of AVNRT is ‘slow-fast’ in which the circus movement propagates anterogradely along the slow pathway, then retrogradely back up the fast pathway, although atypical AVNRT in which the circuit is reversed is also described (see section 1.5.2.4).

More recent studies have looked at mechanisms of reentry where no fixed anatomical obstruction exists. Alteration in the functional characteristics of cells can give rise to unidirectional block with appropriately early extrastimuli, for example where there is a variation in refractory period in the tissue. This block is described as ‘functional’ and excitability can recover by the time the wavefront has circumvented the area leading to retrograde activation, which can then result in ongoing continuous activation in a manner similar to anatomical block (Figure 1-7).<sup>64, 116, 117</sup>

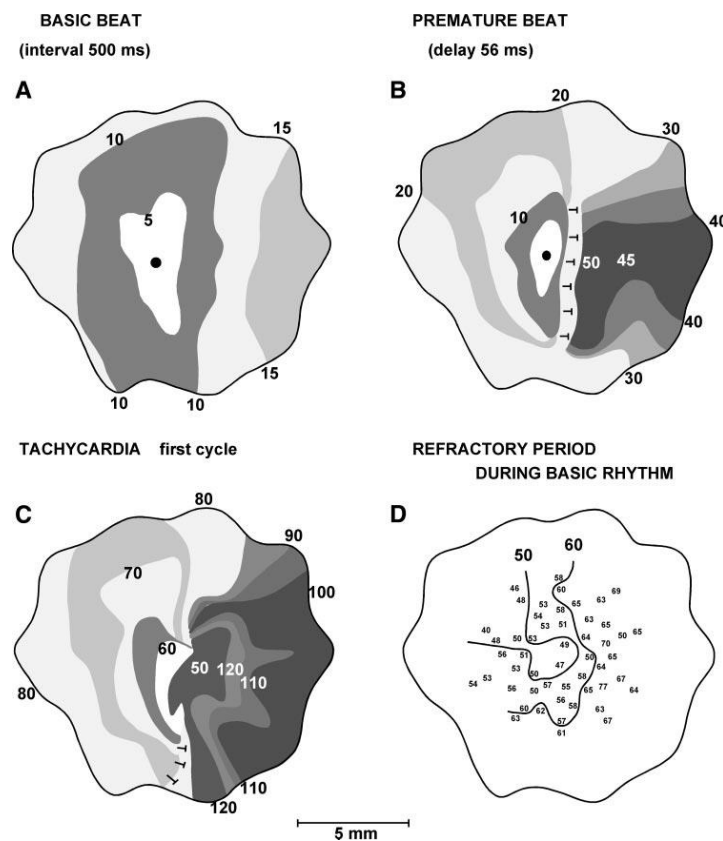


**Figure 1-7. Demonstration of reentry due to functional block in a rabbit left atrial preparation. A) Normal conduction (isochrones marked in ms). B) Premature beat with unidirectional block. Conduction occurs to the left of the stimulus but blocks to the right of the stimulus. C) First cycle of tachycardia. D) Map of the refractory periods of the tissue (the refractory periods are marked in ms). From Allesie *et al.*<sup>119</sup>**

The areas of ‘functional’ block do not need to be fixed and could be related to areas of relative refractoriness resulting from premature extra stimuli. Computer simulations of these waveforms have generated self-sustaining areas of functional reentry in the absence of anatomical boundaries described as ‘rotors’ that give rise to spiral wavefront activations.<sup>64, 116, 117</sup> These rotors may be fixed in the myocardium or ‘wandering’ depending on the kinetics of the wavefront. These rotors are thought to be central to the development of both atrial and ventricular fibrillation and have been implicated in the progression from monomorphic VT to polymorphic VT and VF.<sup>64, 116, 117</sup>

### 1.6.3 Arrhythmogenesis and ion channel remodelling

Ion channels, intracellular  $\text{Ca}^{2+}$ -handling proteins and connexins are key determinants of the both action potential shape and conduction velocity. Both the shape of the action potential and conduction velocity are critical to the generation of arrhythmias. Many disease processes including dilated cardiomyopathy, myocardial infarction, atrial fibrillation and pulmonary hypertension are associated with an increased incidence of arrhythmias.<sup>49</sup> Changes in ion channels, intracellular  $\text{Ca}^{2+}$ -handling proteins and connexins have been demonstrated in response to these disease processes, and are thought to play a critical role in the generation of arrhythmias.<sup>49, 120-122</sup>

Studies have been performed in both animal models and humans. Within each different disease process there are different changes in the action potential which are due to remodelling of different ion channels, intracellular  $\text{Ca}^{2+}$ -handling proteins and connexins. For example, in dilated cardiomyopathy there is an increase in action potential duration, which is thought to be due to down-regulation of several  $\text{K}^+$  currents ( $I_{to}$ ,  $I_{K,s}$  and  $I_{K1}$ ) and up-regulation in NCX, which promotes the generation of both EADs and DADs. However, in atrial fibrillation there is reduced action potential duration due an up-regulation of  $I_{K1}$ , which may reduce the formation of EADs but shortens the wavelength of potential reentrant circuits promoting the formation of multiple circuit reentry.<sup>120</sup> Connexin dysregulation with increased proportion of laterally distributed connexins has been shown in dilated cardiomyopathy, myocardial infarction and atrial fibrillation, which prolongs conduction velocity and promotes the formation of reentrant arrhythmias.<sup>120</sup>

Information is more limited regarding the remodelling in the cardiac conduction system compared with working myocardium. No studies have reported on ion channel remodelling within the AV node. However, the SA node however has been studied and

there is evidence of widespread changes in ion channels,  $\text{Ca}^{2+}$  handling proteins and connexins in response to both ageing and myocardial infarction.<sup>121, 122</sup>

#### 1.6.4 Arrhythmias and pulmonary hypertension in animal model studies

Most studies investigating arrhythmogenesis in PAH have been performed in the monocrotaline (MCT) model. They have shown a reduced resting heart rate in the anaesthetised MCT animals although when telemetry has been used an increased heart rate has been demonstrated.<sup>123-125</sup> The tachycardia seen in active animals could be because of increase sympathetic drive or because of a compensatory increase in rate in the failing heart with a reduced cardiac output. It is possible that anaesthesia reveals an intrinsic underlying sinus bradycardia, by diminishing the effects of the autonomic nervous system on heart rate. There is marked prolongation of the QT interval of the MCT-treated rat ECG, and T wave alternans.<sup>125-130</sup> No change in the PR interval has been shown.<sup>125-129</sup>

Reduced conduction velocity has been demonstrated in the ventricle in the MCT model, with more marked effects at higher stimulation rates.<sup>130, 131</sup> Despite the reduction in conduction velocity no change was demonstrated in  $I_{\text{Na}}$ .<sup>132</sup> Changes in connexin expression have been demonstrated with Cx43 showing more lateral distribution in the RV myocytes, another study reported a reduction of total Cx43 in the RV myocytes.<sup>131, 132</sup> Fibrosis can also interfere with cardiac conduction and has been shown to be an important substrate in the maintenance of arrhythmias.<sup>49</sup> Increased fibrosis and myocytes fibre disarray have been demonstrated in the MCT model, although the contribution of this to reduced conduction velocity is uncertain.<sup>130, 133-135</sup>

There is an increase in the monophasic action potential duration in PH which is greatest in the RV but also occurs in the LV.<sup>131, 132</sup> Prolongation of the action potential is due to a combination of an increase in  $\text{Ca}^{2+}$  currents and a decrease in  $\text{K}^{+}$  currents, predominantly  $I_{\text{K1}}$  and  $I_{\text{to}}$ .<sup>128, 130, 136, 137</sup> The prolonged action potential was demonstrated in both isolated hearts and single cells, with dynamic changes at different cycle lengths indicated by a steeper restitution curve. This promoted the development of discordant action potential duration alternans, a risk factor for the development of reentrant ventricular arrhythmias.<sup>130</sup> In addition to action potential alternans  $\text{Ca}^{2+}$  transient alternans was also seen. However, this was not due to an alteration of  $I_{\text{Ca,L}}$  but was instead due to alterations of intracellular  $\text{Ca}^{2+}$  handling with a reduction in SERCA function and increased SR  $\text{Ca}^{2+}$  load and SR  $\text{Ca}^{2+}$  release fraction. Increased SR  $\text{Ca}^{2+}$  load also promoted spontaneous  $\text{Ca}^{2+}$  release events.<sup>129</sup>

The prolonged action potential and increased cytosolic  $\text{Ca}^{2+}$  release promote the formation of EADs and triggered activity.<sup>129</sup> In Langendorff perfused hearts from MCT treated rats triggered activity was demonstrated in the right ventricular outflow tract which then initiated spontaneous polymorphic VT. This was sustained by a combination of focal and reentrant mechanisms within the right ventricle.<sup>129</sup>

Despite the demonstration of arrhythmia susceptibility *ex vivo* there is less data regarding spontaneous arrhythmias *in vivo*. Telemetry recordings from MCT treated rats that were sacrificed when they became symptomatic have shown only T wave alternans and occasional ventricular extrasystoles.<sup>130</sup> A separate study monitored MCT treated rats with telemetry and invasive RV pressure traces for up to 62 days without sacrificing rats when they became symptomatic.<sup>138</sup> In this cohort there was a 69% mortality before the end of the monitoring period. All the rats that died had arrhythmias prior to death; 55% showed progressive AV block, 36% had sinus arrest and 9% had torsade's de points degenerating into ventricular fibrillation.<sup>138</sup> All the arrhythmic events occurred minutes prior to death.<sup>138</sup> An interesting study was performed to look at the effects of air pollution on spontaneous arrhythmias in rats monitored with telemetry.<sup>139</sup> In addition to simply exposing rats to pollution the study also looked at MCT treated rats exposed to pollution.<sup>139</sup> These rats were studied at up to 90 days post MCT injection. Increased numbers of atrial and ventricular ectopic beats were seen in the MCT group before exposure to pollution and this was greatly exacerbated by pollution exposure.<sup>139</sup> There was a high mortality in the MCT rats when they were exposed to pollution (approximately 50%) compared with 0% mortality in those exposed to pollution but not treated with MCT.<sup>139</sup> The fatal events were split evenly between a gradual progression and a sudden deterioration.<sup>139</sup> The gradual changes seen were ST depression, bradycardia and peaked T waves before eventual asystole, which was thought to represent hypoxia related mortality due to a combination of RV failure and pollution exposure.<sup>139</sup> A second group showed sudden bradycardia with high degrees of AV block and bundle branch block. None of the mortalities were related to ventricular tachyarrhythmias.<sup>139</sup> All the mortality events occurred with the combination of MCT and pollution exposure, nevertheless these findings point to AV node dysfunction in PH.<sup>139</sup> These monitoring studies demonstrate that MCT treated rats do develop spontaneous arrhythmias with a high incidence of AV block and SA node dysfunction, but that these events occur late in the disease progression. The pollution study suggests a 'double-hit' may provoke arrhythmias earlier in the disease progression.

There are limited data on using treatments to reverse the substrate for arrhythmias.

Treatment of the MCT injected rats with both bosentan or a combination of sildenafil and beraprost reduced the dysregulation of Cx43 seen with MCT administration.<sup>140, 141</sup>

Treatment with sildenafil alone has been demonstrated to reduce the dysregulation of the Ca<sup>2+</sup> handling proteins.<sup>142</sup>

## 1.7 Project aims

The aims of this work were as follows:

- i To use the MCT model to generate rats with severe PH
- ii To characterise the potentially arrhythmogenic changes seen in the MCT model of PH with specific reference to the atria and cardiac conduction system
- iii To study impulse propagation in the AV node along both the fast and slow pathway and therefore to localise functional changes in AV node conduction seen in the MCT model to the different regions of the AV node
- iv To characterise changes in the molecular substrate of the AV node in the MCT model and to understand how molecular changes could lead to functional changes
- v To attempt to reverse the arrhythmogenic changes seen in the MCT model using putative treatments for PH

# 2 Development of the monocrotaline model of pulmonary hypertension

---

## 2.1 Introduction

Animal models have been used extensively to study all aspects of physiology and pathology. There are clear benefits compared to studying humans in terms of the availability of tissue and the ability to induce pathology, and therefore many aspects of pathology can be studied only in animal models. Several animal models have been used which generate PH in a manner analogous to PAH.<sup>4, 5, 143-146</sup> This information has yielded significant advances in understanding that has led to novel drug therapies, which have been tested in the animal model before progressing to become mainstream treatment in patients with PAH.<sup>4, 5, 143-146</sup>

### 2.1.1 Animal models of pulmonary hypertension

#### 2.1.1.1 *Chronic hypoxia model*

The pulmonary circulation undergoes vasoconstriction in response to hypoxia as a result of autoregulation to match pulmonary ventilation and perfusion.<sup>4, 5</sup> The constriction is a result of contraction of pulmonary artery smooth muscle cells and is well preserved across species. Chronic hypoxia has been used as a stimulus to create animal models of PH in both rats and mice. The phenotype that it produces is of mild PH. Smooth muscle artery cells proliferate and the media thickens; however these changes are reversible on return to normoxia. This model is analogous in part to PH secondary to hypoxia or lung diseases.<sup>4,</sup>

<sup>146</sup>

#### 2.1.1.2 *Monocrotaline model*

Oral ingestion of *Crotalaria spectabilis* seeds by rats produced an increase in the medial thickness of the pulmonary artery which was associated with PH with pulmonary artery pressures in the range of 62-122 mmHg (compared with control values of 22-36 mmHg). RV mass was also increased.<sup>147</sup>

Monocrotaline (MCT) is an extract from *Crotalaria spectabilis*. Sequential histological analysis of Sprague Dawley rats treated with MCT revealed an initial inflammatory infiltrate consisting of mononuclear cells, which occurs within the first 24 hours, and leads to oedema within the adventitia. This happens in the smaller pulmonary arteries and veins initially then progresses into the larger pulmonary arteries over the next 4-8 days.<sup>148</sup> Over the next 15 days there is proliferation of the smooth muscle cells within the media that leads to the obstruction and raised right heart pressures.<sup>148</sup> The MCT model induces a severe phenotype with progressively increasing right heart pressures, right ventricular hypertrophy, right ventricular dilation, tricuspid regurgitation and death such that mortality rates in Wistar rats at 4 weeks post injection were 53%.<sup>149, 150</sup> Animal studies using the MCT model have shown the benefit of several treatments which have gone on to become standard clinical therapies including bosentan, sildenafil and prostacyclin.<sup>146, 149</sup> The MCT model has been criticised because the lung vasculature does not show plexiform lesion formation. However, the combination of MCT injection and pneumonectomy has given rise to the development of plexiform lesions.<sup>4, 151</sup>

### 2.1.1.3 *Sugen-Hypoxia model*

A combination of administration of the synthetic vascular endothelial growth factor (VEGF) receptor inhibitor, Sugen 5416, and exposure to three weeks of hypoxia has been shown to cause severe PH in rats, although neither factor in isolation generates raised pulmonary pressures.<sup>152, 153</sup> The rats have subsequently been exposed to normoxia for up to 11 weeks, but continue to develop PH. The pathogenesis is still incompletely understood but it is thought that VEGF may play a role in maintaining the vascular endothelium in conditions of hypoxia.<sup>152, 153</sup> Block of VEGF in conjunction with hypoxia may lead to apoptosis of endothelial cells that would normally have been preserved, leading to a preferential survival of an apoptosis-resistant population of endothelial cells with subsequent unrestricted proliferation.<sup>152</sup>

This model has been given particular interest because the lungs of the affected rats show lesions similar to the plexiform lesions seen in patients with PAH. However there has been limited study of the cardiac effects of this model, in particular whether the combination of Sugen 5416 or 3 week period of hypoxia may have direct effects on the heart unrelated to the development of PH.

#### ***2.1.1.4 Pulmonary artery banding***

Surgical banding of the pulmonary arteries in mice has been shown to generate raised pulmonary pressures. This is not a model of PH but does allow the study of chronic pressure overload on the right ventricle. Interestingly, animals with pulmonary artery banding do not develop right ventricular failure despite a similar increase in pulmonary pressures, suggesting that the effects of PH on the heart may not be due solely to the mechanical effects of raised right ventricular pressures.<sup>154</sup>

#### ***2.1.1.5 Left to right shunts***

Models of PH in congenital heart disease have been created with surgical shunts from the systemic to pulmonary circulation including the anastomosis of the left subclavian artery to the pulmonary trunk in pigs, left upper pulmonary artery to aorta in sheep and aorta to vena cava in rats.<sup>4, 143-145</sup> These models require considerable technical expertise and take approximately three months or more to induce relatively mild increases in pulmonary pressures, because shunts large enough to induce more severe PH are fatal on table or early post operatively.<sup>4, 143-146</sup>

#### ***2.1.1.6 Choice of animal model***

Pulmonary arterial hypertension is a multifactorial disease and although several animal models generate PH no single ideal model of PAH exists or ever will. Although the MCT model is widely used there remain some concerns over its representativeness as a model of PAH.<sup>4</sup> Histological examination of the lungs of MCT injected rats shows medial thickening and muscular hypertrophy but not the characteristic plexiform lesions that are seen in patients with PAH. Further concerns are raised that many pharmacological agents that are highly effective in the MCT model have much more equivocal benefits in clinical practice.<sup>4</sup> In our study we are interested in the effects of PH on the heart and therefore these concerns seem less relevant given the known increases in pulmonary pressure with the MCT model.

A greater concern for our study is the possibility that MCT may have a direct effect on the heart and therefore any changes seen in cardiac function may be attributable to MCT and not PH. Published studies offer conflicting data on this subject with one study demonstrating inflammation in RV free wall, septum and posterior LV wall in response to MCT injection with some evidence of inflammation in the posterior LV wall prior to the

development of PH. The authors argue that this demonstrates a direct toxic effect of MCT on the heart.<sup>155</sup> In contrast to this another study using both *in vivo* single-photon emission computed tomography imaging and *ex vivo* histological and PCR techniques demonstrated that inflammation was largely confined to the RV and interventricular septum. The authors argue that inflammation is part of the pathogenesis of right heart failure secondary to PH rather than a direct MCT effect.<sup>156</sup> Support for this view comes from the finding of right ventricular inflammation in a rat model of pulmonary embolism and PH.<sup>157</sup> The conflicting findings regarding left ventricular involvement in the MCT model may in part be explained by which areas of the left ventricle were studied; the study reporting inflammation in the left ventricle looked at the posterior wall which is in close proximity to the septum and posterior attachment of the RV.<sup>155</sup>

There are conflicting reports of the effects of MCT on the coronary arteries with some studies reporting medial arterial thickening but others reporting no change.<sup>155</sup> With regards to the study of the effects of PH on the heart it should be noted that the classification of PAH subdivides into a number of different categories including patients with connective tissue disease and associated with HIV. Both of these conditions have an inflammatory component and are associated with accelerated rates of atherosclerosis of the large coronary arteries and alterations in the microvascular circulation, suggesting that some extra-pulmonary effects of MCT do not invalidate the findings of the model.<sup>158, 159</sup> Further support for the validity of the MCT model to investigate the cardiac effects of PH comes from the success of several pharmacological therapies showing beneficial on cardiac function in both the MCT model and in humans. This would not be expected if the deleterious effects on cardiac function seen in the MCT model were purely due to a direct toxic effect of MCT.<sup>147,168-171</sup>

It is important that the model used to study PAH and arrhythmogenesis induces a severe PH phenotype with significant RV hypertrophy, RV dilation and dysfunction. The MCT model has the benefit of being relatively inexpensive and less technically challenging than the surgical models of PH. It provides the required severe PH phenotype in only 3 weeks. The MCT model has been well characterised and has previously been used to investigate arrhythmogenesis. This allows comparison of our findings with previous work. In light of these benefits MCT model was chosen to study arrhythmias in PH.<sup>4, 146</sup>

## 2.1.2 Differences between the human and rat heart

Larger animals may have greater similarities to humans than rat. Despite these differences rat models have several advantages over large animal models when it comes to studying cardiac physiology. Due to the small size and low cost of rats it is possible to use greater numbers of animals than in studies than when larger animals are used, this allows for more statistical power. The rat genome is known allowing for the use of commercially available reagents to be used in experiments.

Knowledge of rat physiology has led to many rat models being generated to gain insight into many aspects of disease including arrhythmias in conditions including myocardial infarction, heart failure, hypertension and PH.<sup>4, 5, 143-146, 160</sup>

### 2.1.2.1 Ion channels in the rat heart

Patch-clamp recordings in rat ventricular myocytes have demonstrated several different voltage-dependent repolarising  $K^+$  currents. There are two rapidly-activating transient outward currents:  $I_{to,fast}$  ( $I_{to,f}$ ) and  $I_{to,slow}$  ( $I_{to,s}$ ).  $I_{to,f}$  is rapidly activated and inactivated, it also recovers from steady-state inactivation rapidly.  $I_{to,s}$  is rapidly-activating but has slower inactivation and recovery from inactivation.<sup>161</sup>

In rats the dominant delayed rectifier current is termed  $I_K$  and is slowly activating and deactivating, making it responsible for repolarisation later in the action potential.<sup>161-164</sup>  $I_K$  activates and deactivates much more slowly than both  $I_{to,f}$  and  $I_{to,s}$ , and in addition to this undergoes steady-state inactivation at all potentials positive to  $-120mV$ , in contrast to  $I_{to}$  which undergoes steady-state inactivation at potentials positive to  $-50mV$ .<sup>161-164</sup> These factors combined mean that  $I_{to}$  is the dominant repolarising current in the rat.<sup>161-164</sup>

In humans there are two delayed rectifier currents ( $I_{K,r}$  and  $I_{K,s}$ ) that play an important role in repolarisation; however these currents appear to be less important in the rat. A current similar to  $I_{K,r}$  has been demonstrated in rat ventricular myocytes and is associated with the protein ERG, similar to in humans.<sup>165</sup> However experiments blocking  $I_{K,r}$  have shown only limited effects *in vivo*.<sup>92</sup> The gene which is thought to underlie the protein that generates  $I_{K,s}$  (KCNQ1) has been demonstrated in the rat ventricular myocardium but despite this, a current similar to  $I_{K,s}$  has not been demonstrated in the rat, and pharmacological agents blocking  $I_{K,s}$  only have minimal effects at high concentrations, which may be due to non-selective effects.<sup>52, 92</sup>

In addition to the differences in currents in the myocytes the rat also has a higher resting heart rate than the human which further favours the dominance of  $I_{to,f}$  in rats due to its rapid activation and recovery from inactivation.<sup>52</sup>

There are also important differences in the  $Ca^{2+}$  handling mechanisms. In humans and other large mammal the proportion of cytosolic calcium influx is approximately 23% due to  $I_{Ca,L}$  and 77% due to  $Ca^{2+}$  release from the SR, in the rat is approximately 8% due to  $I_{Ca,L}$  and 92% due to  $Ca^{2+}$  release from the SR. Correspondingly, in humans  $Ca^{2+}$  extrusion from the cytosol during diastole is approximately 70% due to SERCA and 28% due to NCX whereas, in the rat  $Ca^{2+}$  extrusion from the cytosol is approximately 92% due to SERCA and only 7% due to NCX. The increased heart rate in the rat also promotes high SR  $Ca^{2+}$  concentrations (by reduced time for recovery of ryanodine receptors and decreasing the time for NCX activity).<sup>166</sup>

#### 2.1.2.2 The action potential in the rat

The action potential in both rats and mice are similar but are considerably shorter in duration than in humans and large mammals (Figure 2-1). This is due to the predominant effect of  $I_{to}$  as the repolarising current and the alteration in intracellular calcium handling (described above).

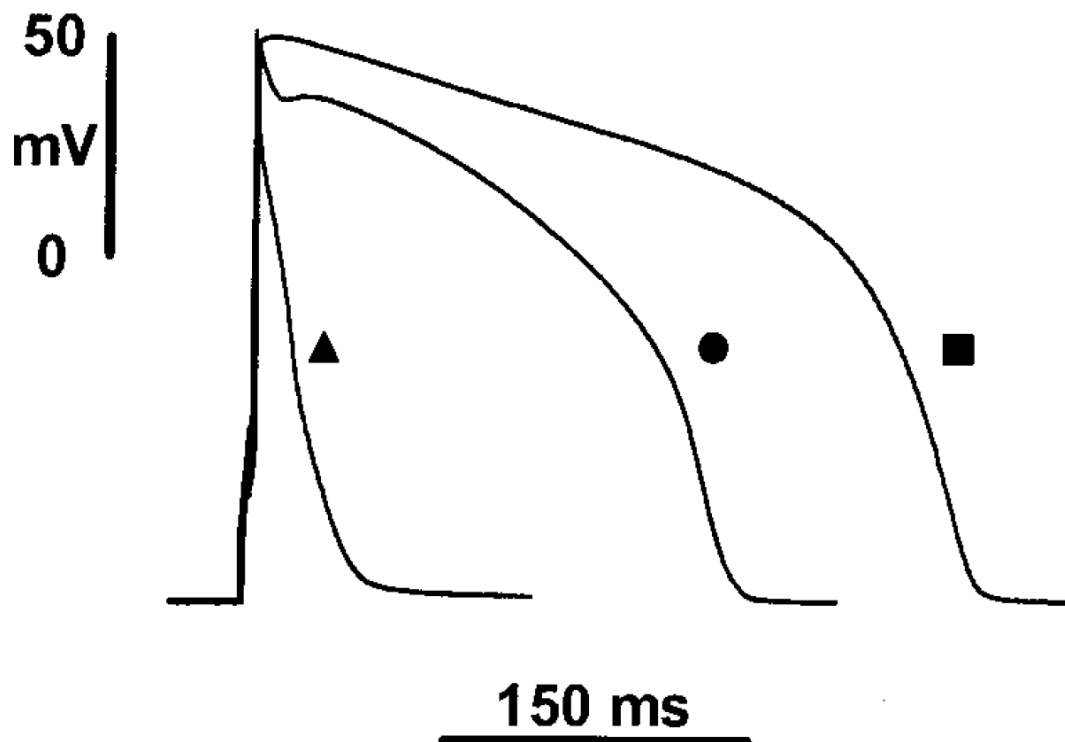


Figure 2-1. Ventricular action potentials (APs) recorded in guinea-pig (square), rabbit (circle) and rat (triangle) demonstrating the short duration of the rat action potential due to the predominant effect of  $I_{to}$ . From Linz *et al.*<sup>167</sup>

The action potentials are not uniform throughout the ventricular myocardium with longer action potentials in the endocardium as compared with the epicardium due to a larger  $I_{to}$  in the epicardial cells.<sup>167, 168</sup>

### 2.1.2.3 The ECG in the rat

The differences described in ion current flows and subsequent action potential morphology mean that the rat ECG has consistent differences from that of a human. The most striking of these is an absent isoelectric baseline between the QRS complex and the T wave due to the superimposition of these two features. The T wave may have an indistinct tail making accurate measurement of intervals difficult. Q waves are absent in most leads (Figure 2-2).<sup>163, 169</sup>

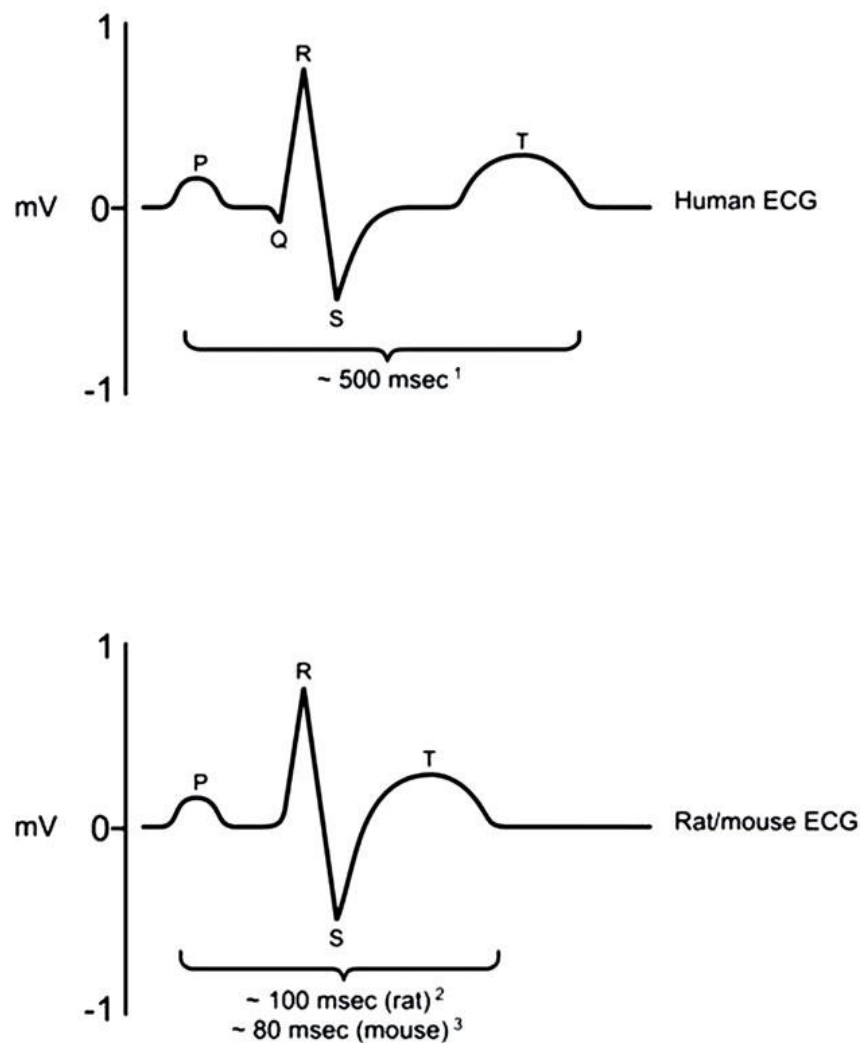


Figure 2-2. Schematic representation of a human and rat/mouse ECG demonstrating typical morphological differences with a shortened QT interval and lack of isoelectric baseline in the rat ECG. From Farraj *et al.*<sup>163</sup>

## 2.2 Methods

All procedures were carried out under the appropriate Home Office Project licence by appropriately trained staff with a Home Office personal license at the University of Manchester Biomedical Service Facility.

### 2.2.1 Development of the monocrotaline model

The MCT model has been used for several decades using a variety of strains of rats with varying doses of oral, subcutaneous (sc) and intraperitoneal (ip) routes of injections used. There has been shown to be a high mortality as early as three weeks.<sup>132, 137, 149, 155</sup> In our early experimentation with the model Sprague Dawley rats weighing 250 g were administered a sc injection of MCT and monitored for 18 days. The results were disappointing with no evidence of PH on echocardiography (echo). The protocol was altered such that Wistar rats (Charles river, UK) weighing 200g with ip injections and a 28 day monitoring period were used as described below. The final methodology for generation of the MCT rats is described below.

### 2.2.2 Monocrotaline preparation and injection

Wistar rats weighing 125-150g (Charles River, UK) were habituated in the biomedical service facility for 10 days prior to commencing the protocol. On the day of injection 200mg MCT (Sigma chemicals, UK) was dissolved in 2ml of 1M HCL and 7ml of 0.9% Na<sup>+</sup>Cl<sup>-</sup> was added. The pH was measured with a pH meter and adjusted with addition of 4M NaOH in 10-20 $\mu$ L increments until a pH of 7.35-7.45 was achieved. Any 'overshoot' in pH was corrected with 10-20 $\mu$ L increments of 1M HCL to achieve a pH of 7.35-7.45. The volume was made up to 10ml giving a concentration of 20mg/ml. The rats were weighed and then *anaesthetised* with 2% isoflurane. A single injection of MCT at a dose of 60mg/kg (i.e. a volume of 3ml/kg) was given to the MCT group via the ip route. Rats in the control group were injected with normal saline with a volume of 3ml/kg ip.

### 2.2.3 Animal monitoring

The rat's physical condition and weight were monitored 3 times a week for the first 21 days then daily from day 21 to day 28. Symptomatic endpoints were; development of symptomatic heart failure with tachypnoea, reduced movement, piloerection, distress, and weight loss greater than 10g over a 48 hour period.

If symptomatic endpoints were reached the rat was sacrificed on that day. If symptomatic endpoints were not reached the rats were sacrificed on day 28. A matched control or MCT rat was sacrificed within 24 hours of any rat that developed the symptomatic endpoint.

#### 2.2.4 ECG recording

Rats were anaesthetised with 2% isoflurane and ECGs were recorded with the in the left lateral position. A three lead configuration with the negative electrode in the right foreleg and the positive electrode in the left foreleg was used (Figure 2-3). The ground electrode was placed in the right hind leg. This gave a signal equivalent to lead I in a human ECG. The electrodes were inserted subcutaneously and connected to a PowerLab A/D converter (AD Instruments, New Zealand). The signal was recorded and RR, PR and QT intervals were measured from an average of 100 beats using Labchart software (AD Instruments, New Zealand). For the first 8 animals ECG was performed on day 0, day 21 and termination day. For subsequent animals ECG was performed on termination day only.

Rats have a much faster heart rate than large mammals and there is concern that formula's used to generate the corrected QT (QT<sub>c</sub>) interval may not be applicable. The most commonly used formula for QT<sub>c</sub> in clinical situations is Bazett's formula:

$$QT_c = \frac{QT}{\sqrt{RR}}$$

Both QT<sub>c</sub> and uncorrected QT intervals were recorded.

#### 2.2.5 Echocardiography

Both direct cannulation of the RV and echo have been used to monitor the progression of increasing RV pressures in the MCT model.<sup>150, 170</sup> Echo has the advantages of being non-invasive, repeatable and has a high sensitivity and specificity when compared with invasive cannulation.<sup>123, 150, 170</sup>

Echo images were acquired on an ACUSON Sequoia™ (Acuson Universal Diagnostics Solution, USA) with a 15 MHz 15L8 transducer on animals anaesthetised with 2% isoflurane. All images were stored on optical media disks and analysed at a later date.

M-mode recordings were taken in the parasternal short axis allowing recording of LV septal and posterior wall thickness and the internal diameter of the LV in both systole and

diastole. RV wall thickness was measured from M-mode recordings in the parasternal long axis position.

Pulsed-wave Doppler through the pulmonary artery was used to assess the pulmonary velocity profile. The maximum pulmonary velocity (PVmax), time from the onset of pulmonary outflow to maximal flow (pulmonary artery acceleration time (PAAT)) and the rate of deceleration of pulmonary flow (pulmonary artery deceleration time (PAD)) were measured (Figure 2-4).<sup>123, 150</sup>

For the first 8 animals echo was performed at day 0, day 21 and termination day. For subsequent animals the clinical condition and ECG were assessed and echo was performed only if there was uncertainty over whether the animal had developed pulmonary hypertension.

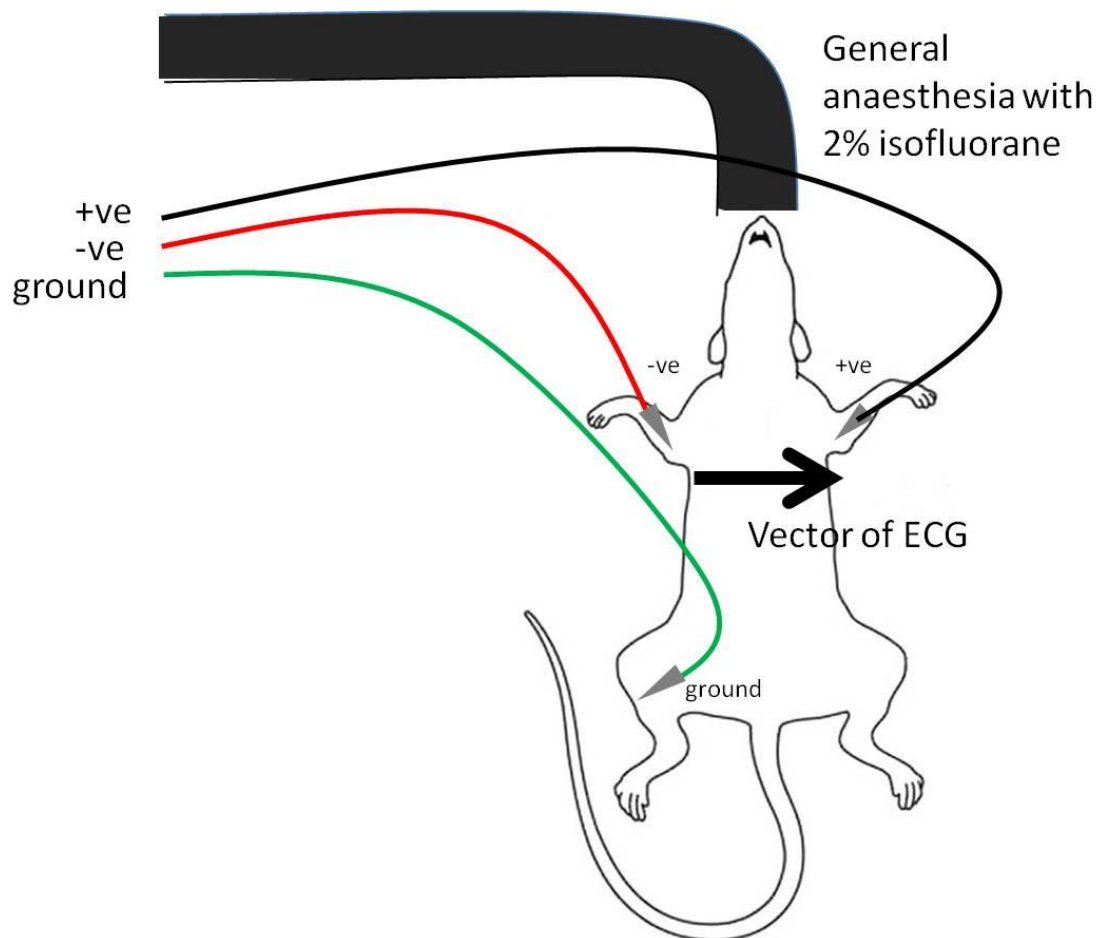


**Figure 2-3. Acquisition of anaesthetised rat ECG.** The rat is first anaesthetised with 2% isoflurane then the electrodes connected to needles are inserted into the subcutaneous tissues. A three lead ECG with a configuration equivalent to lead I is taken.

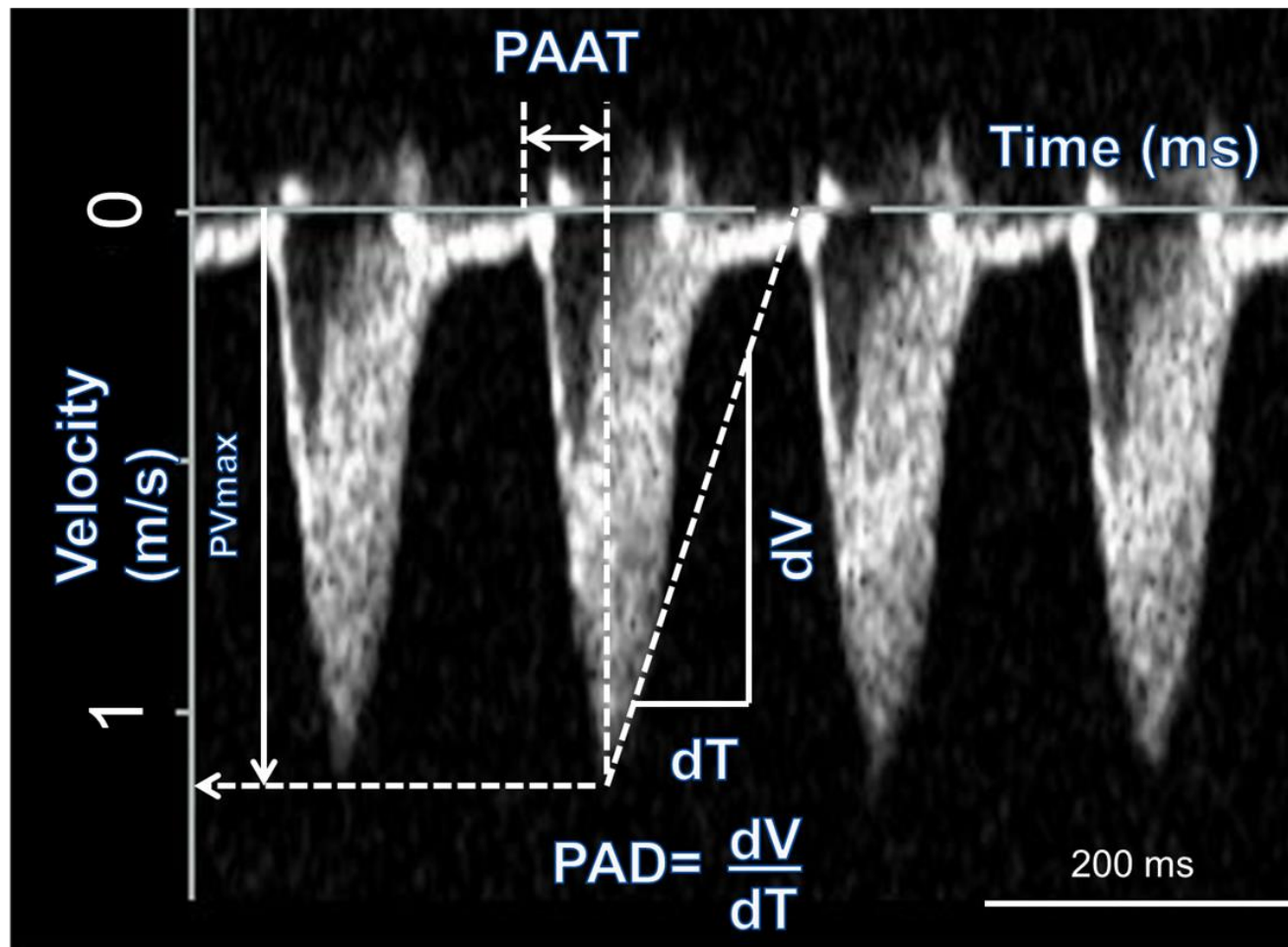


Figure 2-4. Pulsed wave Doppler recording through the pulmonary artery and measurement of PVmax, PAAT and PAD. The x axis measures time and the y axis measures velocity. PAAT is the time from the beginning of flow to the peak velocity, measured from the x axis. PV max is the maximum velocity measured from the y-axis. PAD is the gradient of the initial deceleration of the pulmonary velocity profile.

## 2.3 Results

	Control (n=8 rats)	MCT (n=8 rats)
Mean body weight at day 0 (g)	208.0 ± 8.53	207.9 ± 4.59
Mean weight at day 21 (g)	298.8 ± 12.68	276.8 ± 7.48
Mean weight on day of termination (g)	308.1 ± 15.33	269.7 ± 8.25 *
Heart weight (mg)	1.55 ± 0.09 (n=6)	1.90 ± 0.09 *
Lung weight (mg)	1.43 ± 0.07	2.69 ± 0.20 **

**Table 2-1. Weights at day 0, day 21 and immediately prior to termination. Mean ± standard error measurement (SEM). \*The mean value is significantly different assessed by unpaired Student's *t*-test (P<0.05). \*\*The mean value is significantly different assessed by unpaired Student's *t*-test (P<0.005).**

The mean ± SEM day of termination was day 26 ± 0.8 for the control group and 26 ± 0.9 for the MCT group. The median (interquartile range) day of termination was day 26 (24 - 28) for the control group and day 27 (24-28) for the MCT rats. There was no significant difference in the day of termination between the two groups assessed by Student's T-test.

There was no significant difference in the body weight of the control and MCT rats on the day of injection. During the experimental protocol the MCT treated rats gained significantly less weight such that they weighed 12% less than the control rats by the day of termination. Despite the decrease in body weight they also had a 23% increase in heart weight and an 88% increase in lung weight compared to the control group (Table 2-1).

There were no significant differences between the control and MCT rats demonstrated in *in vivo* ECG intervals pre-injection. By day 21 post injection the MCT treated rats had significant changes compared with the control group on *in vivo* ECG with a prolonged QT and QT<sub>C</sub> interval and a relative bradycardia in the MCT rats. By termination there was further QT interval prolongation and bradycardia in the MCT rats. No change in PR interval or QRS duration was noted (Table 2-2, Figure 2-5).

The *in vivo* echo recordings demonstrated no differences between the control and MCT rats pre-injection. By day 21 post injection the *in vivo* echo demonstrates that MCT rats had developed PH with a 56% reduction in PAAT and a 157% increase in PAD (Figure 2-6). The MCT animals also showed evidence of RV hypertrophy with a diastolic wall thickness increase of 57%. There was also evidence of RV dysfunction assessed with a 35% reduction in RV fractional shortening. Further evidence of worsening PH came from the finding of a reduced LV internal diameter in diastole due to a direct effect of the raised RV pressure displacing the LV septum (Table 2-3, Figure 2-7, Figure 2-8).

	Control (n=8)	MCT (n=8)
<b>Day 0</b>		
RR (ms)	133.7 ± 2.35	138.9 ± 2.94
PR (ms)	46.88 ± 1.28	44.47 ± 1.47
QRS duration (ms)	13.33 ± 0.62	14.71 ± 0.33
QT Interval duration (ms)	44.67 ± 4.35	55.09 ± 2.75
QTc (ms)	120.0 ± 11.33	148.3 ± 6.74
<b>Day 21</b>		
RR (ms)	145.4 ± 2.57	148.6 ± 4.69 *
PR (ms)	48.12 ± 1.55	43.68 ± 2.24
QRS duration (ms)	14.88 ± 0.66	15.12 ± 0.39
QT Interval duration (ms)	52.86 ± 3.00	84.14 ± 7.22 **
QTc (ms)	138.4 ± 5.541	217.3 ± 16.27 **
<b>Day of termination</b>		
RR (ms)	141.9 ± 2.70	157.1 ± 3.08 **
PR (ms)	46.81 ± 1.69	47.47 ± 1.64
QRS duration (ms)	14.95 ± 0.73	14.00 ± 0.98
QT Interval duration (ms)	50.06 ± 2.54	104.4 ± 1.89 **
QTc (ms)	132.7 ± 5.76	263.6 ± 3.22 **

Table 2-2. *In vivo* ECG parameters. Mean ± SEM. \*The mean value is significantly different assessed by repeated measures ANNOVA with multiple comparisons ( $P < 0.05$ ). \*\*The mean value is significantly different assessed by repeated measures ANNOVA with multiple comparisons ( $P < 0.005$ ).

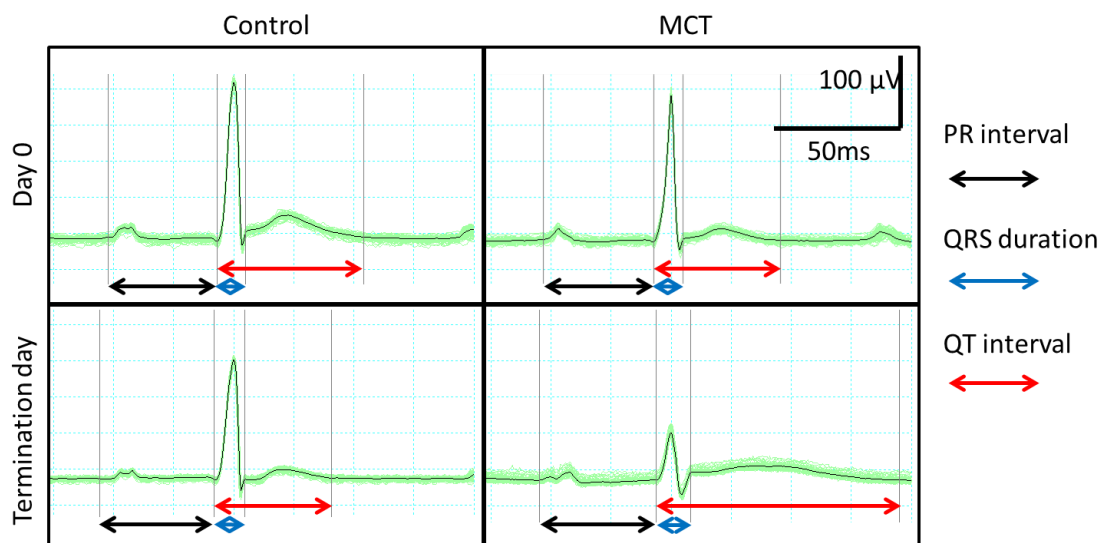


Figure 2-5. Representative *in vivo* ECG recordings on day 0 and termination day from the control and MCT rats. There is a large increase in QT interval seen on termination day in the MCT rats. No significant difference is seen in the PR interval or the QRS duration.

On the day of termination there was still evidence of PH and RV hypertrophy with a raised PAD, reduced PAAT and increased diastolic wall thickness (Figure 2-6). The RV was dilated with a 41% increase in the RV internal dimension during diastole and RV function was impaired with a 36% reduction in RV fractional shortening. The LV internal diameter was reduced during diastole and systole (Table 2-3, Figure 2-7, Figure 2-8)

	Control (n=8)	MCT (n=8)
<b>Day 0</b>		
LV septal wall thickness, diastole (cm)	0.17 ± 0.019	0.17 ± 0.012
LV internal diameter, diastole (cm)	0.63 ± 0.026	0.63 ± 0.013
LV posterior wall, diastole (cm)	0.15 ± 0.013	0.17 ± 0.010
LV septal wall thickness, systole (cm)	0.30 ± 0.019	0.26 ± 0.011
LV internal diameter, systole (cm)	0.28 ± 0.026	0.29 ± 0.019
LV posterior wall, systole thickness (cm)	0.26 ± 0.015	0.26 ± 0.013
PAAT (ms)	32.13 ± 2.90	33.00 ± 0.97
PAD (m/s)	8.92 ± 0.75	11.02 ± 1.11
PVmax (m/s)	0.94 ± 0.029	0.955 ± 0.044
Right ventricular wall thickness, diastole (mm)	0.064 ± 0.0071	0.064 ± 0.0043
Right ventricular internal dimension, diastole (mm)	0.26 ± 0.018	0.30 ± 0.016
Right ventricular wall thickness, systole (mm)	0.11 ± 0.015	0.11 ± 0.012
Right ventricular internal dimension, systole (mm)	0.10 ± 0.014	0.14 ± 0.016
RV fractional shortening (%)	59.64 ± 3.92	54.61 ± 4.99
<b>Day 21</b>		
LV septal wall thickness, diastole (cm)	0.16 ± 0.014	0.18 ± 0.009
LV internal diameter, diastole (cm)	0.73 ± 0.030	0.61 ± 0.055 *
LV posterior wall, diastole thickness (cm)	0.17 ± 0.014	0.18 ± 0.016
LV septal wall thickness, systole (cm)	0.31 ± 0.016	0.29 ± 0.015
LV internal diameter, systole (cm)	0.32 ± 0.035	0.26 ± 0.050
LV posterior wall, systole thickness (cm)	0.29 ± 0.016	0.28 ± 0.020
PAAT (ms)	33.75 ± 3.88	19.00 ± 2.35**
PAD (m/s)	12.11 ± 1.71	31.10 ± 5.31**
PVmax (m/s)	0.99 ± 0.046	0.88 ± 0.047
Right ventricular wall thickness, diastole (mm)	0.07 ± 0.0061	0.11 ± 0.0132 **
Right ventricular internal dimension, diastole (mm)	0.28 ± 0.017	0.30 ± 0.019
Right ventricular wall thickness, systole (mm)	0.12 ± 0.010	0.14 ± 0.018
Right ventricular internal dimension, systole (mm)	0.12 ± 0.015	0.20 ± 0.047
RV fractional shortening (%)	56.38 ± 5.22	36.51 ± 12.91 *
<b>Day of termination</b>		
LV septal wall thickness, diastole (cm)	0.15 ± 0.012	0.18 ± 0.012
LV internal diameter, diastole (cm)	0.71 ± 0.031	0.44 ± 0.045 **
LV posterior wall, diastole thickness (cm)	0.18 ± 0.013	0.20 ± 0.012
LV septal wall thickness, systole (cm)	0.26 ± 0.023	0.30 ± 0.017
LV internal diameter, systole (cm)	0.36 ± 0.030	0.17 ± 0.027**
LV posterior wall, systole thickness (cm)	0.27 ± 0.012	0.29 ± 0.024
PAAT (ms)	33.00 ± 3.55	14.25 ± 0.62 **
PAD (m/s)	14.93 ± 1.74	33.58 ± 3.48 **
PVmax (m/s)	1.09 ± 0.051	0.70 ± 0.046 **
Right ventricular wall thickness, diastole (mm)	0.087 ± 0.0080	0.14 ± 0.0066 **
Right ventricular internal dimension, diastole (mm)	0.27 ± 0.022	0.38 ± 0.051 **
Right ventricular wall thickness, systole (mm)	0.13 ± 0.009	0.16 ± 0.014
Right ventricular internal dimension, systole (mm)	0.12 ± 0.016	0.25 ± 0.037 **
RV fractional shortening (%)	54.44 ± 4.86	34.38 ± 5.12 *

**Table 2-3. Echo parameters on day of termination. Mean ± SEM. \*The mean value is significantly different assessed by repeated measures ANNOVA with multiple comparisons (P<0.05). \*\*The mean value is significantly different assessed by repeated measures ANNOVA with multiple comparisons (P<0.005).**



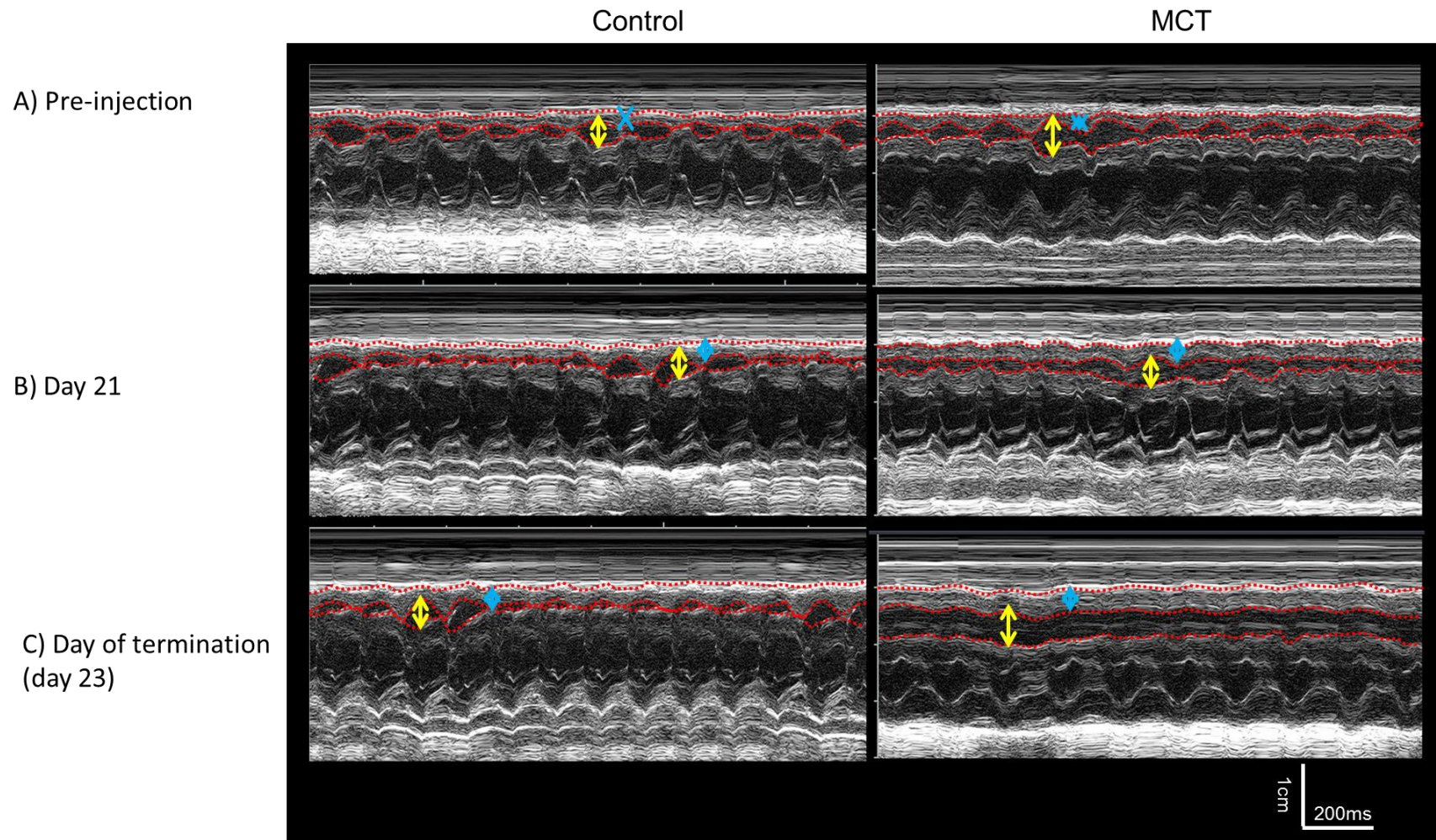


**Figure 2-7.** Representative M-mode parasternal long axis views. The RV free wall and RV border of the septum are marked in dotted red lines. The RV thickness is demonstrated with blue arrows. The RV cavity is demonstrated with yellow arrows. **A)** Before injection both control and MCT have a thin RV wall which contracts well with a small RV cavity. **B)** By day 21 differences can be seen with the RV wall showing increasing thickness but continuing to contract well. The RV cavity is mildly enlarged. **C)** On day 23 (day of termination due to symptomatic endpoints being reached) the changes are very marked with a thickened RV which contracts poorly and an enlarged RV cavity.

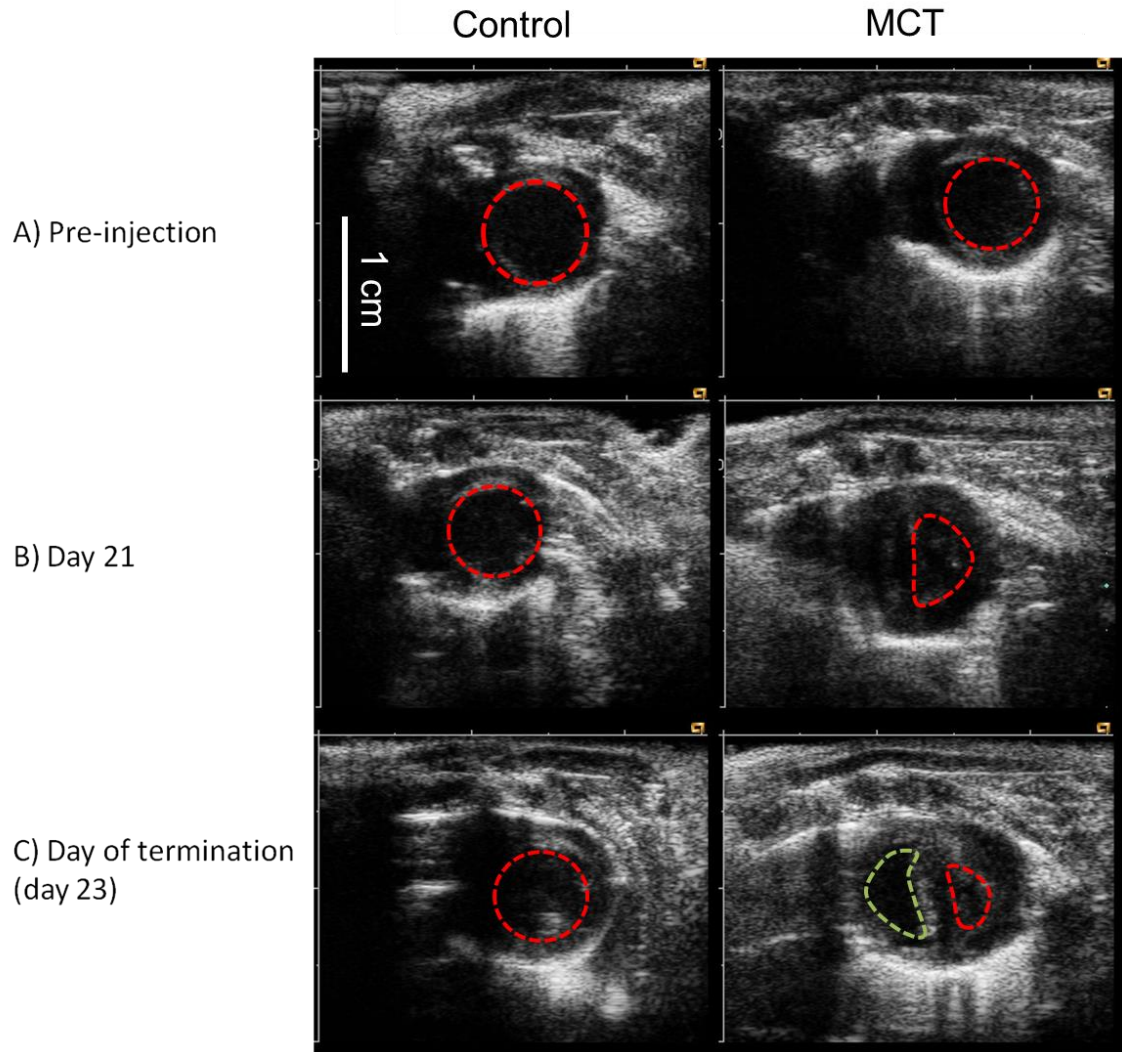


**Figure 2-8. Representative parasternal short axis views in diastole showing the development of pulmonary hypertension. The LV is marked with a red dashed line and the RV is marked with a green dashed line. A) Before injection the LV cavity is circular in both animals and the RV is small. B) By day 21 the control animal still has a circular RV but the MCT rat's septum is pushed over creating a 'D-shape'; the RV is enlarged. C) More pronounced changes on day 23 immediately before termination. The RV is markedly enlarged and has 'pushed' the septum over creating a very pronounced 'D-shape' of the LV**

### 2.3.1 Demonstration of pulmonary hypertension in the MCT rats

Echo was used to assess the pulmonary pressures for the first 8 control and MCT animals as described above. The increase in PAD and reduction in PAAT in the MCT treated rats compared with the control rats replicate previous findings in the MCT model. These studies have shown that these changes correlate well with invasive measures of pulmonary artery pressure.<sup>150, 170</sup> The echo also demonstrated RV hypertrophy with an increased RV wall thickness in diastole and RV systolic dysfunction with a reduced fractional shortening. In addition to the numerical values generated by the echo there were also clear qualitative

change in the echo images. The pulmonary velocity profile in the MCT rats changed from a rounded profile before MCT injection to a 'spike and dome' morphology at 21 days post injection which became more exaggerated by the day of termination, this is consistent with previous findings in PH. Further qualitative changes were seen in the parasternal short axis views. The MCT rats showed a typical circular LV prior to MCT injection but by the day of termination this was altered such that septum was displaced towards the LV cavity forming a characteristic 'D-shape'. This is due to the raised pressures in the RV having a direct effect on the septum and is a characteristic finding in PH. Neither of these two qualitative changes was seen in any of the control rats. These findings demonstrate that the MCT rats had developed PH by day 21 post injection with MCT and had progressive worsening of PH until the day of termination.

## 2.4 Experience with the monocrotaline model

Once the model had been validated in the first eight MCT rats echo and ECG were no longer performed at each of the time points described and instead the animals were monitored for clinical deterioration and weight loss. ECG was performed prior to termination. If the ECG demonstrated the marked QT prolongation seen with the previous MCT rats no further investigations were performed. If the ECG was equivocal echo was performed to see if the rats had developed PH. In total; 37 out of 38 rats injected with MCT using the protocol above displayed clear signs of PH on ECG or echo. The rat that did not show PH was excluded from further analysis.

The mean  $\pm$  SEM day of termination was day  $25 \pm 0.4$  for the control group and  $24 \pm 0.4$  for the MCT group. The median (interquartile range) day of termination was day 25 (24-27) for the control group and day 24 (23-27) for the MCT rats. There was no significant difference in the day of termination between the two groups assessed by Student's T-test.

In the control group no animals met the specified symptomatic endpoints, in the MCT group 30 out of 38 animals met the specified symptomatic endpoints requiring sacrifice before day 28. The difference in meeting symptomatic endpoints was assessed by the logrank test and was significant ( $P < 0.0001$ ) (Figure 2-9).

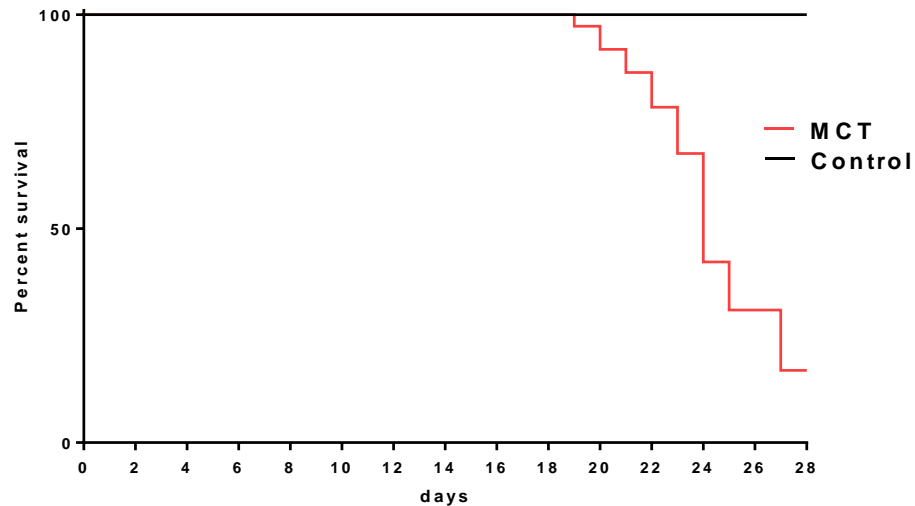


**Figure 2-9. Kaplan-Meier graph to show the survival free from symptomatic endpoints. None of the control rats developed symptomatic endpoints. The earliest the MCT rats developed symptomatic endpoints was day 18. 79% of the rats had developed symptomatic endpoints by day 28.**

## 2.5 Discussion

A single injection of MCT reliably induced a pulmonary hypertension phenotype within 28 days. The progression of PH was somewhat variable with some animals developing clear symptoms and weight loss by as early as day 21 and others with no symptoms and only echo confirmation of PH by day 28 (Figure 2-9). There was no difference in the day of termination between the two groups but this was anticipated on the basis that the timing of the sacrifice of the rats was paired so that when an animal from the MCT group reached the symptomatic endpoints the paired rat from the control group was sacrificed within 24 hours. There was a rapid progression of PH with 79% of the MCT injected animals developing weight loss and clinical deterioration within 28 days of injection. The severity of the model was confirmed by echo which showed PH by day 21 with progressive RV and failure by the day of termination. The ECG showed that this model was potentially arrhythmogenic with a bradycardia and QT prolongation.

The hearts and lungs of the MCT injected animals have been studied by other researchers in our group. Dr. Gillian Quigley has looked at the differences between the RV and LV of the rat's heart using a combination of histology, immunohistochemistry and qPCR techniques. She found that whilst there was marked inflammation in the right side of the heart there were only minimal changes in the LV.<sup>171</sup> No changes were seen in the coronary arteries of the MCT-injected rats.

Dr. Basma Eid studied the rats' lung histology and showed muscular hypertrophy of the pulmonary arteries which is characteristic of the MCT model. In order to assess the selectivity of MCT on the pulmonary vasculature the contractility of the pulmonary arteries and systemic arteries from the mesentery was assessed using wire myography. Increased contractility was seen in the pulmonary vessels of the MCT animals but not in the mesenteric arteries from the same animals.<sup>172</sup>

Although other animal models of PH are available, none combine the relative ease of model generation with the required severe phenotype of PH. The published work using the MCT model and our unpublished findings support the theory that the cardiac effects seen in the MCT model are due to the development of PH and not due to a direct toxic effect of MCT. All the subsequent experiments described in this thesis has been performed using the MCT model to study the effects of PH on the heart.

# 3 Whole heart experiments in the monocrotaline model

---

## 3.1 Introduction

The Langendorff preparation has been used for over 100 years to study many aspects of cardiac physiology.<sup>173</sup> The heart is retrogradely cannulated via the ascending aorta allowing perfusion of the coronary arteries maintaining viability of the myocardium whilst experiments are performed. It allows the intact heart to be studied and rapid characterisation of many key electrophysiological parameters. It is therefore the preparation that has been used for the first set of functional experiments on the hearts of the MCT rats to investigate the atrium, ventricle, SA node and AV node.

## 3.2 Methods

The animals were generated as described in section 2.2.2. Prior to termination *in vivo* ECG was performed and PH was confirmed in all the MCT animals as described in section 2.4.

Tyrode's solution ( NaCl – 120 mM, CaCl – 1.2 mM, KCl – 4mM, MgSO<sub>4</sub>.7H<sub>2</sub>O – 1.3 mM, NaH<sub>2</sub>PO<sub>4</sub>.2H<sub>2</sub>O 1.2 mM, NaHCO<sub>3</sub> – 25.2 mM, glucose – 5.8 mM) was generated on the day of the experiment and bubbled with 95% O<sub>2</sub>/5% CO<sub>2</sub>.

Heparin (1000 U) was administered by sc injection 30 min prior to sacrifice. The animal was sacrificed by stunning and cervical dislocation and the heart was excised from the thorax and retrogradely perfused with oxygenated Tyrode's solution chilled to 4°C.

The heart was mounted on a Langendorff column and retrogradely perfused with oxygenated Tyrode's solution at a temperature of 36.5°C with a fixed flow rate of 0.11 ml/g/s.<sup>137</sup> The heart was left to stabilize for 20 minutes. Widely spaced extracellular bipolar electrodes were placed on the RA and LV to record a signal including atrial and ventricular components. The bipolar electrodes were connected via a headstage (NL100AK, Digitimer, UK) to an amplifier (NL104A, Digitimer, UK) with a gain of 5000. The signal was then filtered between 50 – 500 Hz (NL125/6, Digitimer, UK). The amplified and filtered signal was then converted to a digital signal using a data acquisition

unit (Micro 1401, Cambridge Electronic Design, UK) and recorded and analysed using the Spike 2 software (Cambridge Electronic Design, UK) (Figure 3-1).

The bipolar electrodes record a 'pseudo-ECG' from the Langendorff perfused heart which is equivalent to the *in vivo* ECG (Figure 3-4). The recording from 19-20 min (i.e. immediately prior to stimulation) were exported and analysed using Chart software. This allowed an averaged ECG of the last 100 beats before stimulation to be inspected. The RR, PR and QT intervals and the QRS duration were measured.

### 3.2.1 Pacing protocols

The heart was then stimulated at the RA with a bipolar pacing electrode connected to a DS2A Isolated Constant Voltage Stimulator (Digitimer, UK). The voltage stimulator was connected to the computer via the data acquisition unit which allowed pacing protocols programmed in Spike 2 to be executed.

Threshold was determined using a fixed S1-S1 protocol with an interval of 180 ms. A square pulse of duration 2 ms was gradually increased from 0 to 99 V. The minimum voltage required to capture the atrium was determined. This minimum voltage was then doubled and the output was kept constant for all subsequent pacing protocols.

SA node recovery time (SNRT) was determined using a S1-S1 protocol with a cycle length of 150 ms for 30 s. The time taken for the first spontaneous atrial beat after cessation of pacing was defined as the SNRT. This protocol was repeated three times and the longest value was recorded. Corrected SNRT (cSNRT) was calculated by subtracting the RR interval from the SNRT.

Wenckebach cycle length was determined using a S1-S1 protocol. The atrium was paced with a fixed cycle length of 200ms for 30 s. If 1:1 atrial to ventricular conduction occurred the S1-S1 protocol was repeated with a 10 ms reduction in coupling interval until Wenckebach conduction was seen. A further set of 30 s S1-S1 pacing protocols was undertaken starting at 11 ms longer than the cycle length at which Wenckebach conduction had occurred. If 1:1 atrial to ventricular conduction occurred the protocol was repeated with a 1 ms reduction in the cycle length of the S1-S1 protocol. The cycle length at which 1:1 atrial to ventricular conduction failed and Wenckebach conduction occurred using 1 ms reductions in cycle length was recorded as the Wenckebach cycle length (Figure 3-2).

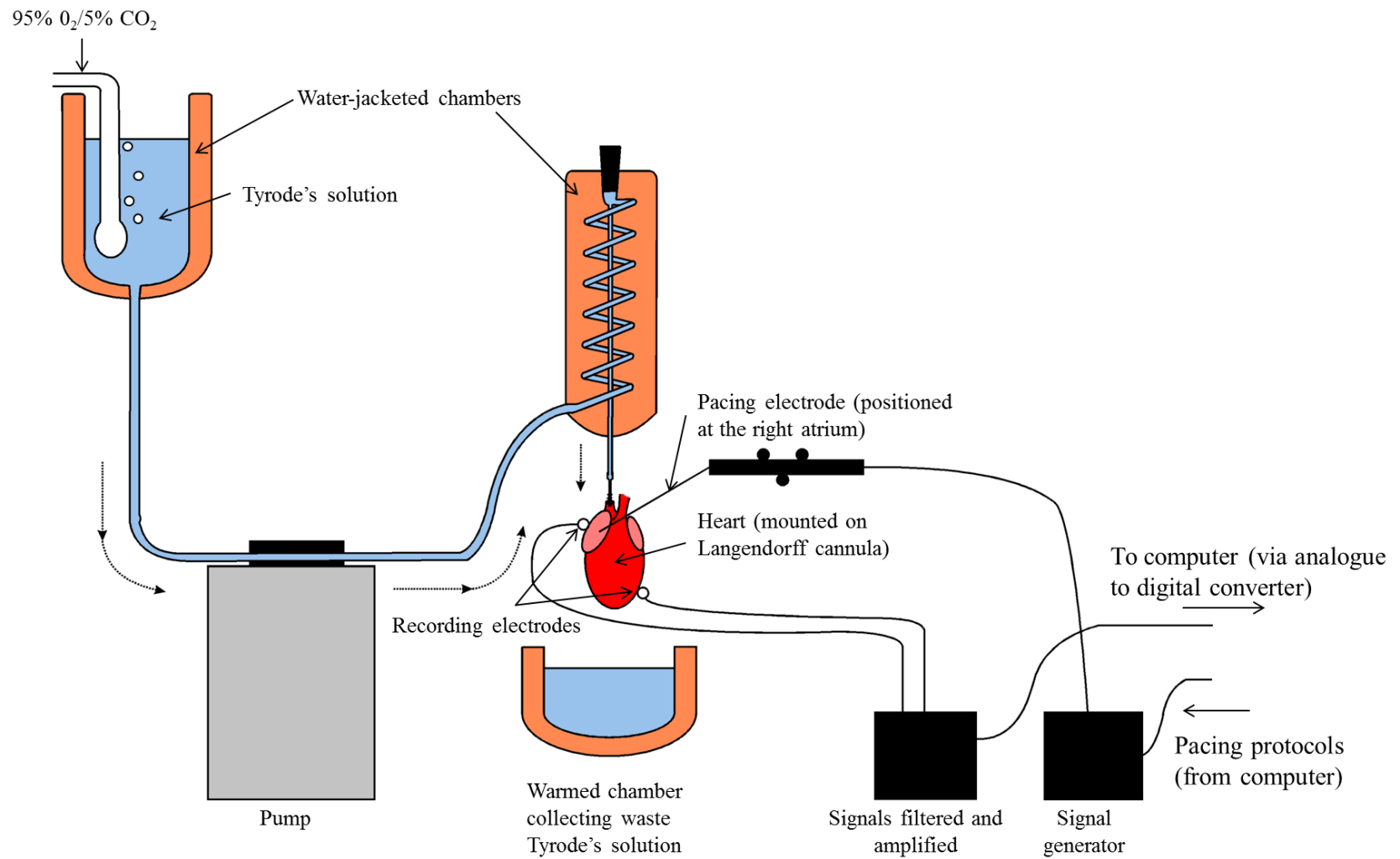


**Figure 3-1. Diagram of Langendorff rig set up. The heart was perfused at a constant flow rate of 0.11 ml/min/g. After 20 min baseline ECG recordings were taken and pacing protocols applied to both the RA and RV outflow tract.**

AV node effective refractory period (AVERP) was determined using an S1-S2 protocol. There was an initial drive train of S1 beats (S1-S1, 180 ms) for 8 beats. The initial S1-S2 coupling interval was 170 ms. If the extrastimuli captured the atrium and was conducted to the ventricle the protocol was repeated with a 10 ms reduction in the S1-S2 coupling interval. This was repeated until AV conduction was lost. A new set of protocols was run again with the S1-S2 coupling interval starting at 10 ms greater than the S1-S2 coupling interval at which AV node conduction had failed. If this extrastimulus was conducted successfully from the atrium to the ventricle the protocol was repeated with the S1-S2 coupling interval reduced by 1 ms until AV conduction was lost. The greatest S1-S2 coupling interval that did not conduct after a 1 ms decrement was defined as the AVERP (Figure 3-2).

Atrial effective refractory period (AERP) was determined using the same an S1-S2 protocol as described above for AVERP. For AERP the protocol was continued until atrial capture was lost.<sup>86, 174</sup>

Atrioventricular node functional refractory period (AVFRP) was determined using the protocol described for AVERP. The RR interval between the QRS of the last of the paced beats in the drive train and the QRS elicited by the S2 stimulus, i.e. the R1-R2 interval, was measured and plotted as an AV node conduction curve (Figure 3-3). The lowest R-R interval represents the fastest conduction across the AV node and was defined as the AVFRP.

The stimulating electrode was then moved onto the RV at the right ventricular outflow tract and the threshold for the ventricle was determined in the same manner as that described for atrial threshold. Ventricular effective refractory period (VERP) was determined in the same manner the AERP with the protocol continued until ventricular capture was lost.

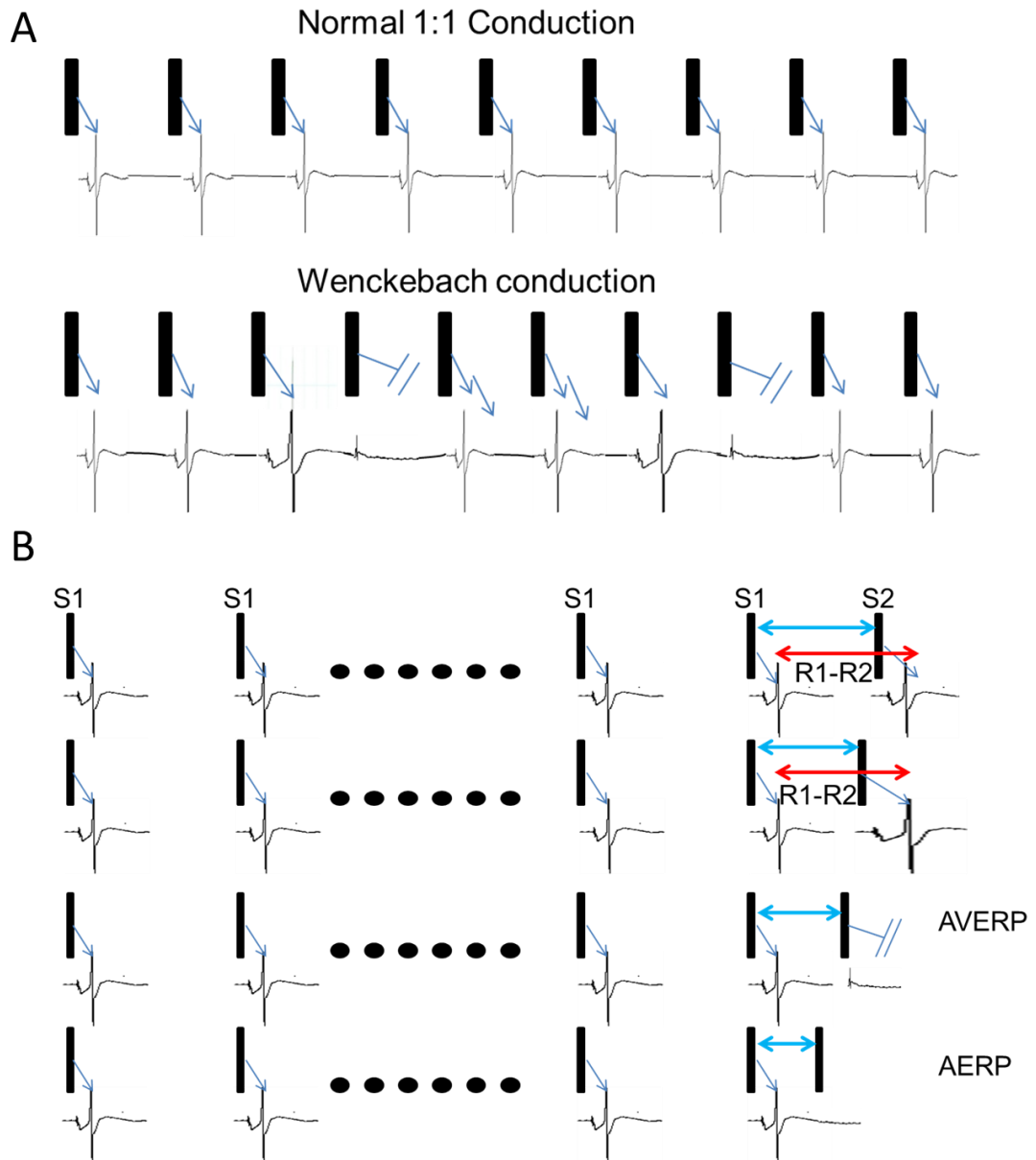


**Figure 3-2. Schematic diagram of pacing protocols. A) Wenckebach cycle length. At longer cycle lengths there was 1:1 conduction between the atrium and the ventricle. As the pacing cycle length decreased there was a gradual prolongation of the PR interval until conduction across the AV node failed and the cycle started again. B) S1-S2 protocol. A drive train of S1 stimuli with the same cycle length was delivered followed by an extrastimulus termed the S2. The protocol was repeated with a progressive reduction in the coupling interval of the extrastimulus, i.e. a shortening of the S1-S2 interval. Initially conduction across the AV node was maintained but there was progressive lengthening of the PR interval. At shorter intervals conduction across the AV node failed and there was atrial activation without ventricular activation. The longest S1-S2 interval at which conduction failed was termed the AVERP. Eventually, as the S1-S2 interval was reduced further the atrium was not captured. The longest S1-S2 interval at which the atrium was not captured is termed the AERP.**

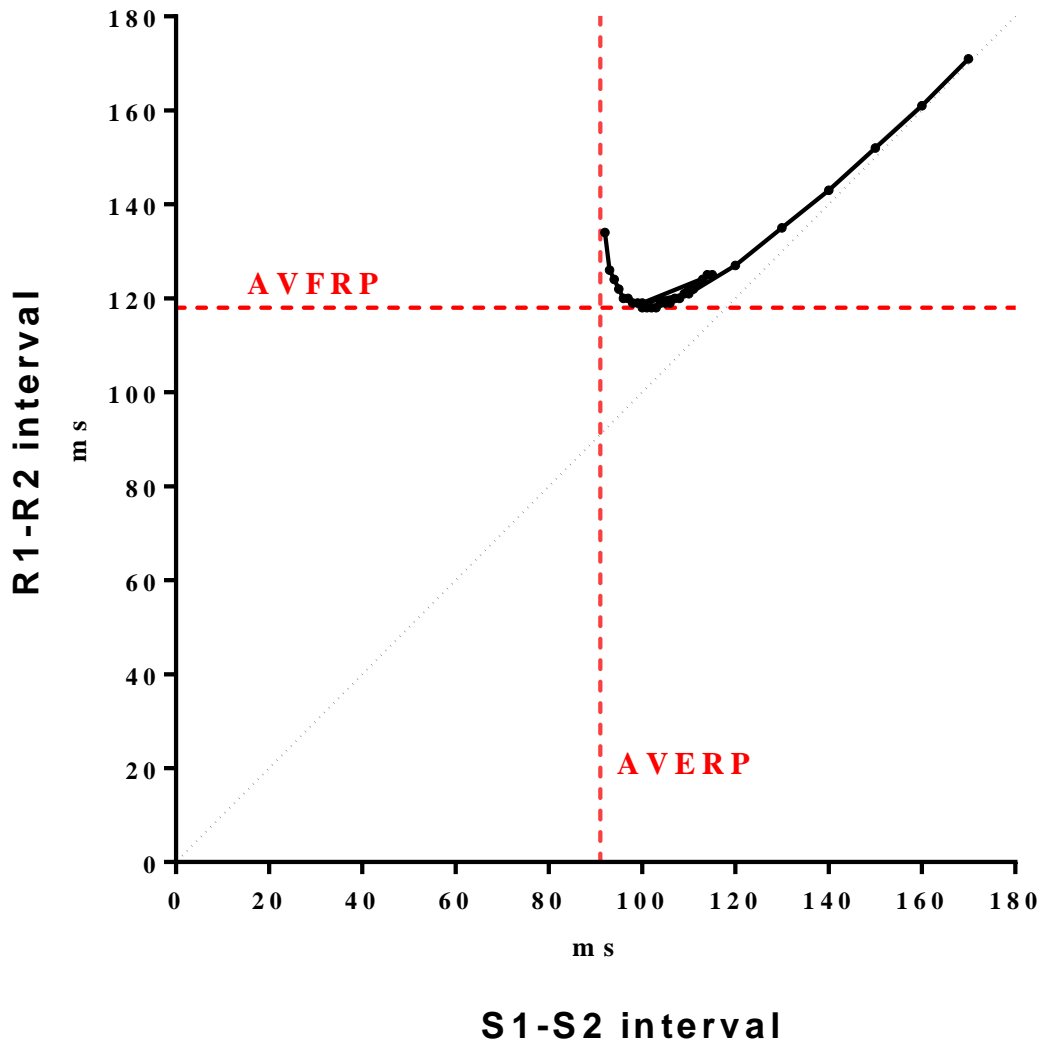


Figure 3-3. AV node conduction curve. The S1-S2 interval (the ‘input’ to the AV node) is plotted against the R1-R2 interval (the ‘output’ of the AV node). The dotted line indicates the line that would be created if the AV node did not show decrementation (i.e. increasing delay with shorter coupling intervals, see section 2.9.5). A typical AV node conduction curve assumes a smooth ‘hockey-stick’ shape with no discontinuities. The AVERP is defined as the highest S1-S2 interval at which AV conduction fails and is read from the X-axis. The AVFRP is defined as the shortest R1-R1 interval that the AV node conducts and is read from the y-axis.

### 3.3 Results

	Control (n=27)	MCT (n=28)
RR interval (ms)	144.6 ± 1.83	158.1 ± 2.00**
PR interval (ms)	46.12 ± 0.73	45.76 ± 0.73
QT interval (ms)	52.06 ± 1.75	103.1 ± 3.04**
QTc interval (ms)	136.7 ± 4.09	259.3 ± 6.90 **
QRS duration (ms)	15.47 ± 0.52	14.68 ± 0.39

Table 3-1. *In vivo* ECG results on the day of termination. Mean ± SEM. \*Significantly different as assessed by unpaired Student’s *t*-test (P<0.05). \*\*Significantly different assessed by unpaired Student’s *t*-test (P<0.005).

The *in vivo* ECG data show a 98% increase in the QT interval and a 90% increase in the QTc interval and a 9% increase in the RR interval, equivalent to a 9% decrease in heart rate, in the MCT treated rats (Table 3-1 and Figure 2-5). No changes were seen in the PR interval or QRS duration.

	Control	MCT
RR interval (ms)	236.7 ± 7.71 (n=9)	244.31 ± 13.72 (n=11)
PR interval (ms)	42.78 ± 1.53 (n=9)	43.65 ± 1.51 (n=11)
QT interval (ms)	56.05 ± 4.77 (n=9)	135.20 ± 9.51 (n=11) **
QTc interval (ms)	115.62 ± 9.97 (n=9)	274.80 ± 18.18 (n=11) **
QRS duration (ms)	13.19 ± 0.75 (n=9)	15.87 ± 2.73 (n=11)
SNRT (ms)	298.70 ± 20.09 (n=9)	309.4 ± 21.05 (n=11)
cSNRT (ms)	62.03 ± 20.26(n=9)	65.15 ± 14.96 (n=11)
Wenckebach cycle length (ms)	111.1 ± 2.72 (n=10)	117.0 ± 3.00 (n=11)
AVERP (ms)	87.50 ± 1.40 (n=10)	94.3 ± 2.66 (n=10) *
AVFRP (ms)	114.9 ± 1.87 (n=10)	122.3 ± 1.89 (n=10) *
AERP (ms)	34.44 ± 2.23 (n=9)	42.56 ± 4.89 (n=9)
VERP (ms)	40.33 ± 3.02 (n=6)	98.25 ± 10.94 (n=5) **

Table 3-2 Langendorff results. Mean ± SEM. \*The mean value is significantly different assessed by Student's *t*-test (P<0.05). \*\*The mean value is significantly different assessed by Student's *t*-test (P<0.005).

Table 3-2 and Figure 3-4 show the results from the Langendorff experiments. There was evidence of prolonged ventricular repolarisation with a 141% increase in the QT interval, a 138% increase in QTc interval and a 144% increase in the VERP in the MCT treated rats compared with the control group. The AERP showed a 24% increase in the MCT animals but this was not significant (P=0.15).

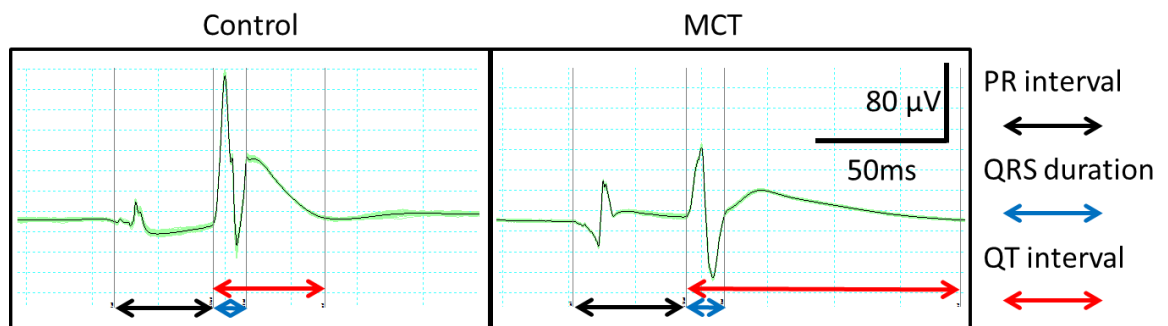
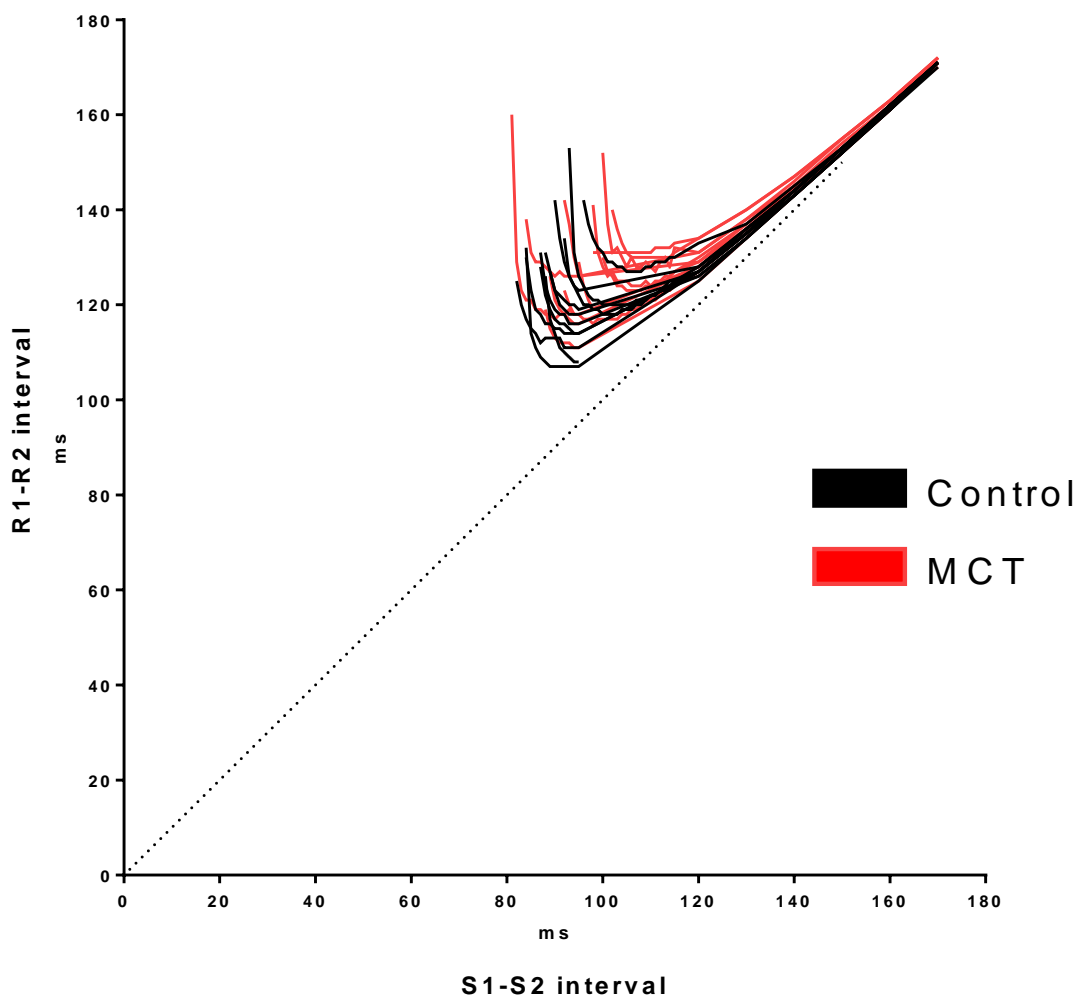


Figure 3-4. Recordings from the widely spaced bipolar electrodes used in the Langendorff experiments. The recordings form a 'pseudo-ECG' pattern. There was a significant increase in the QT interval but no significant change in PR interval or QRS duration.

There was no significant change in RR interval although there was an absolute increase of 3% ( $P=0.65$ ) in the MCT treated rats compared with the control group rats. No changes were seen in SNRT or cSNRT, the other measures of SA node function.

No difference was seen in the PR interval on the Langendorff ECG in the MCT treated rats compared with the control rats. There was an absolute increase in Wenckebach cycle length of 5% in the MCT treated group that was not significant ( $P=0.16$ ). The AVERP showed a significant 8% increase ( $P=0.04$ ) and the AVFRP showed a significant 6% increase ( $P=0.01$ ). Examination of the conduction curves for both the control and MCT treated rats revealed the typical 'hockey-stick' shape expected of AV node conduction (Figure 3-3 and Figure 3-5). There curve was not entirely smooth with a small degree of variation in the R1-R2 interval as the S1-S2 interval shortened but there was no clear discontinuity in the conduction curve for either the control or MCT treated rats, i.e. dual nodal physiology was not demonstrated in either the control or MCT treated rats.



**Figure 3-5.** AV node conduction curve for all control and MCT treated rats used in the Langendorff preparation. The mean AVERP and AVFRP were significantly increased. No discontinuities in the conduction curve were demonstrated.

Linear regression showed the Wenckebach cycle length to be significantly correlated with both the AVERP and AVFRP for both control and MCT treated rats (Table 3-3,

Figure 3-6). This suggests that the MCT treatment does tend to prolong the Wenckebach cycle length.

	Control	MCT
Wenckebach cycle length v AVERP	Correlation coefficient: 0.31 $\pm 0.13$ , $R^2 = 0.36$ *	Correlation coefficient: 0.71 $\pm 0.13$ , $R^2 = 0.77$ **
Wenckebach cycle length v AVFRP	Correlation coefficient: 0.56 $\pm 0.12$ , $R^2 = 0.67$ , **	Correlation coefficient: 0.52 $\pm 0.10$ , $R^2 = 0.76$ **

Table 3-3. Linear regression of Wenckebach cycle length against AVERP and AVFRP. \* The correlation coefficient is non-zero ( $P < 0.05$ ), \*\* The correlation coefficient is non-zero ( $P < 0.005$ )

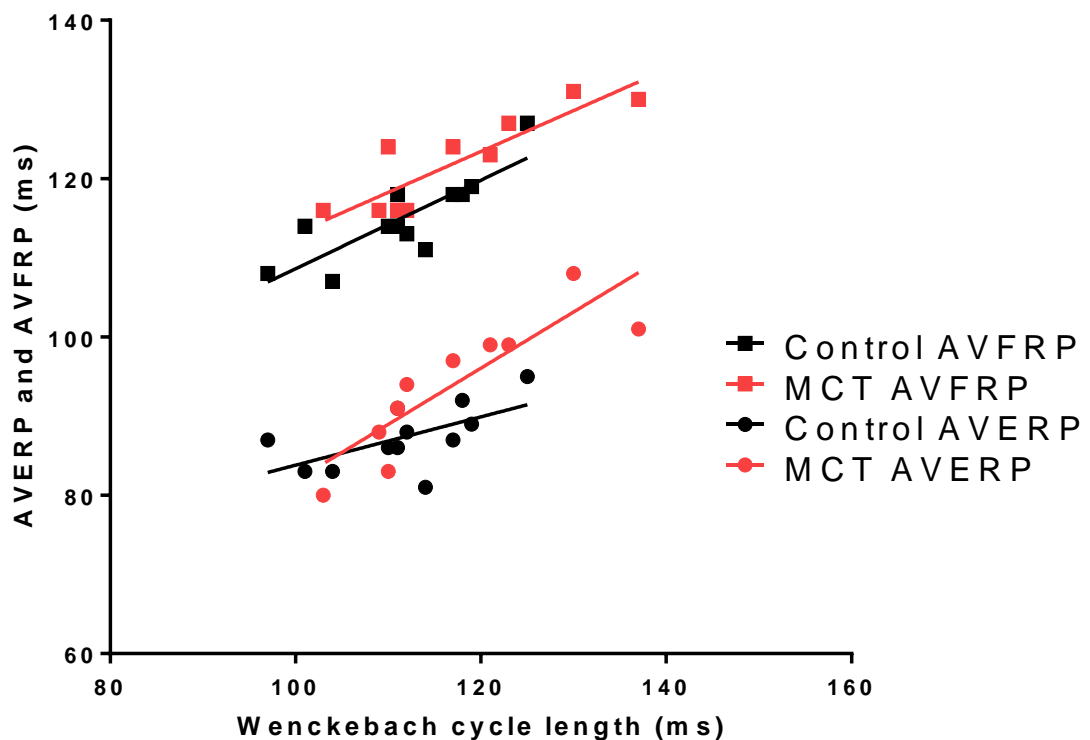


Figure 3-6. Graph showing Wenckebach cycle length plotted against both AVERP and AVFRP.

### 3.4 Discussion

There was no evidence of AV node dysfunction seen in either the *in vivo* or *ex vivo* ECG in the MCT treated rats, in keeping with previous studies in which no change in the PR interval was detected.<sup>125-128</sup> However, the pacing protocols did demonstrate AV node

dysfunction with a prolonged AVERP and AVFRP (Table 3-2). Although the Wenckebach cycle length was not significantly prolonged, the absolute value was increased in the MCT animals and the Wenckebach cycle length was highly significantly correlated with both the AVERP and AVFRP suggesting that the lack of statistical significance may be due to an inadequate number of experimental rats (

Figure 3-6). There was no evidence of dual nodal physiology in either the control or MCT animals (Figure 3-5). There is evidence of AV node dysfunction with both heart block and AVNRT in clinical studies (see section 1.3.2). As described in section 1.6.4 studies with ECG telemetry have demonstrated severe AV node dysfunction in MCT treated rats, but this is only detectable late in model progression, shortly before death. The results of this chapter demonstrate that AV node dysfunction is beginning to develop earlier in the model progression, before it is manifest in *in vivo* ECG recordings. AV node dysfunction has been seen in both clinical studies and animal models of other forms of heart failure and has been shown to be a predictor of morbidity and mortality in these conditions.<sup>175</sup>

Both the *in vivo* ECG and the Langendorff data show marked prolongation of the QT interval and the Langendorff experiments showed a prolonged VERP. These findings suggest delayed repolarisation in the ventricle and are consistent with previous studies which have shown a prolonged ventricular action potential in both animal models and human studies in PAH.<sup>20, 129, 130, 137</sup> Previous studies have demonstrated that in patients with PAH the QTc is prolonged and a QTc of greater than 480 ms is an independent predictor of mortality.<sup>20</sup> In addition to this the QTc is correlated to pulmonary pressures and RV dilation and inversely correlated to RV function.<sup>20</sup> Previous studies with the MCT model have shown that prolongation of QT interval is correlated with an increase in the action potential duration of the right but not the left ventricle, increasing the dispersion of repolarisation.<sup>129, 130, 137</sup> The restitution curve of the prolonged action potential is also steeper in the right ventricle and both of these factors may form a potential substrate for ventricular arrhythmias. The prolonged action potential duration in the right ventricle has been shown to be due to a reduction in repolarising K<sup>+</sup> currents leading to triggered activity, which can initiate VF.<sup>129, 130, 137</sup>

The *in vivo* ECG data shows a relative bradycardia in the anaesthetised rats (Table 3-2). However, this was not replicated in the Langendorff preparation, in which bradycardia was not demonstrated. Previous studies have shown conflicting results with regard to heart rate in the MCT model. Bradycardia was seen in MCT rats anaesthetised with

phenobarbital and isoflurane but a tachycardia was seen in MCT animals with telemetry and no anaesthesia.<sup>123-125, 137</sup> This study with telemetry looked at heart rate variability and suggested reduced parasympathetic activity in the MCT treated rats. When treated with atropine there was a greater increase in the heart rate of the control rats than the MCT rats but no significant differences were seen with propranolol.<sup>125</sup>

In this study no change has been noted in QRS duration whereas previous reports have demonstrated QRS prolongation.<sup>125-128</sup> It is notable that these studies tended to use older rats with a longer duration of PH which may explain the discordant findings.<sup>125-128</sup>

Another explanation for the conflicting findings from this study and previous studies is that some previous studies have used more than a single lead configuration to monitor the ECG. Using this technique it has been demonstrated that there is a significant shift in the QRS axis as PH develops.<sup>125</sup> A study specifically looking at the change in QRS axis as PH developed suggested that new bundle branch block did not develop, although the QRS duration was not compared with controls.

The whole heart experiments have confirmed that the MCT model results in potentially arrhythmogenic changes in the rat heart which will be investigated in more detail in subsequent chapters.

# 4 Experiments on the isolated sinoatrial/atrioventricular nodal preparation in the monocrotaline model

---

## 4.1 Introduction

Despite a normal PR interval in the *in vivo* ECG, AV node dysfunction was demonstrated in the Langendorff experiments described in chapter 3 with a prolonged AVERP and AVFRP and some evidence pointing towards a prolonged Wenckebach cycle length. In the rabbit it has been suggested that the determinants of AVFRP are in the more distal portions of the AV node near the His bundle whereas the determinants of the AVERP are in the more proximal AV node near the inputs from the atrium.<sup>69</sup> This suggests there may be widespread changes in the AV node in response to PH in the MCT model. In order to investigate which areas of the AV node were affected a series of functional experiments were performed on an isolated SA/AV node preparation.

## 4.2 Methods

### 4.2.1 Atrioventricular node preparation

The animals were generated as described in section 2.2.2. Prior to termination PH was confirmed in all the MCT treated rats as described in section 2.4.

Tyrode's solution ( NaCl – 120 mM, CaCl – 1.2 mM, KCl – 4mM, MgSO<sub>4</sub>.7H<sub>2</sub>O – 1.3 mM, NaH<sub>2</sub>PO<sub>4</sub>.2H<sub>2</sub>O 1.2 mM, NaHCO<sub>3</sub> – 25.2 mM, glucose – 5.8 mM) was generated on the day of the experiment and bubbled with 95% O<sub>2</sub>/5% CO<sub>2</sub>.

Heparin (1000 U) was administered by sc injection 30 min prior to sacrifice. Rats were sacrificed by stunning and cervical dislocation and the heart was excised from the thorax and retrogradely perfused with oxygenated Tyrode's solution chilled to 4°C. The heart

underwent dissection in a dissection chamber whilst being constantly superfused with oxygenated Tyrode's solution at 4 °C

The dissection is illustrated in Figure 4-1. The heart was pinned with the RV facing forwards and the bottom of both ventricles was removed (Figure 4-1 A). The left atrial appendage was removed creating a hole in the left atrium (Figure 4-1 B and C). An incision was made from the free wall of the LV into the hole created by removal of the left atrial appendage (Figure 4-1 D). The LV was opened and pinned with the endocardial surface of the LV pinned facing leaving the free wall of the RV facing upwards (Figure 4-1 E). An incision was made from the exposed surface of the RV free wall to the tricuspid annulus (Figure 4-1 E). An incision was made from the tricuspid annulus into the right atrial appendage extending up to the SVC Figure 4-1 F). A second incision was made from the RV free wall into the pulmonary artery Figure 4-1 F). These two incisions allowed the RA and RV to be opened and pinned exposing the endocardial surface of the RA and the AV node whilst avoiding any incisions being created near the AV node (Figure 4-1 G)

On completion of dissection the heart was transferred to the perfusion system (see below). The preparation was left in the perfusion chamber with recirculating warmed and oxygenated Tyrode's solution for 20 min before recordings were taken.

#### **4.2.2 Perfusion system**

The perfusion system incorporated glass chambers, perfusion cylinders and a perfusion bath which were 'jacketed' in order to allow warmed water to be pumped through them via a waterbath. The temperature of the waterbath was adjusted to ensure a temperature of  $36.5 \pm 0.5^{\circ}\text{C}$  of the Tyrode's solution within the perfusion system.

Fluid was recirculated in the system using the Gilson Minipuls 3 pump (Gilson, USA) with a four way adaptor to control both inflow and outflow. Initial experiments whilst designing the perfusion system demonstrated a high incidence of complete AV block in healthy rats whilst using relatively low flow rates (10 ml/min) to the perfusion chamber. Improved AV conduction was noted by increasing the flow rate and directing the perfusion solution directly at the AV node. The final design of the perfusion system incorporated two parallel inflow circuits with equal flow rates each supplying 25 ml/min giving a total perfusion flow of 50ml/min. One inflow was directed at the AV node and the other supplied the whole chamber. Two outflow circuits were also used to match the

inflow circuits. They were arranged so that one outflow circuit was positioned at the bottom of the chamber and the other was elevated to the of desired perfusion fluid level. The efficiency of the pump was altered by adjusting the pressure applied to the perfusion tubing so that the return circuits were able to pump greater volumes than the perfusion circuits. In this way a 'feedback' loop was created so that the chamber was filled to a desired level but would not exceed the desired level. With the final perfusion system AV node conduction parameters were stable over several hours (Figure 4-2).

### **4.2.3 Bipolar electrode recording system**

Bipolar electrodes were made using 0.25 mm silver wire coated with 0.04 mm Teflon (Advent Research Materials, Oxford). The Teflon coating was removed from the tip along approximately 0.5 mm of the length of two wires. At the other end these wires were soldered onto dual core shielded copper wires. The two Teflon wires were then twisted around each other and held in a supporting case made using a 1 mm syringe and PVC tubing. The distance between the two poles of the electrodes was approximately 0.2 mm.

The bipolar electrodes were connected via a headstage (NL100AK, Digitimer, UK) to an amplifier (NL104A, Digitimer, UK) with a gain of 5000 and filtered between 50 – 500 Hz (NL125/6, Digitimer, UK). The amplified and filtered signal was then converted to a digital signal using a data acquisition unit (Micro 1401, Cambridge Electronic Design, UK) and recorded and analysed using the Spike 2 software (Cambridge Electronic Design, UK) (Figure 4-2).

### **4.2.4 Measurement of distance**

A digital camera (Scion, USA) with a fixed focal length was mounted above the perfusion chamber and the height of the perfusion chamber was adjusted until that the camera recorded an in focus image of the preparation. A micromanipulator (Narishige®, Japan) was used to position the bipolar electrode and a picture recorded. The micromanipulator was then used to move the electrode to a position 5 mm away (the micromanipulator was accurate to 0.1 mm) and a second image recorded. These images were used to calibrate all future measurements of distance.

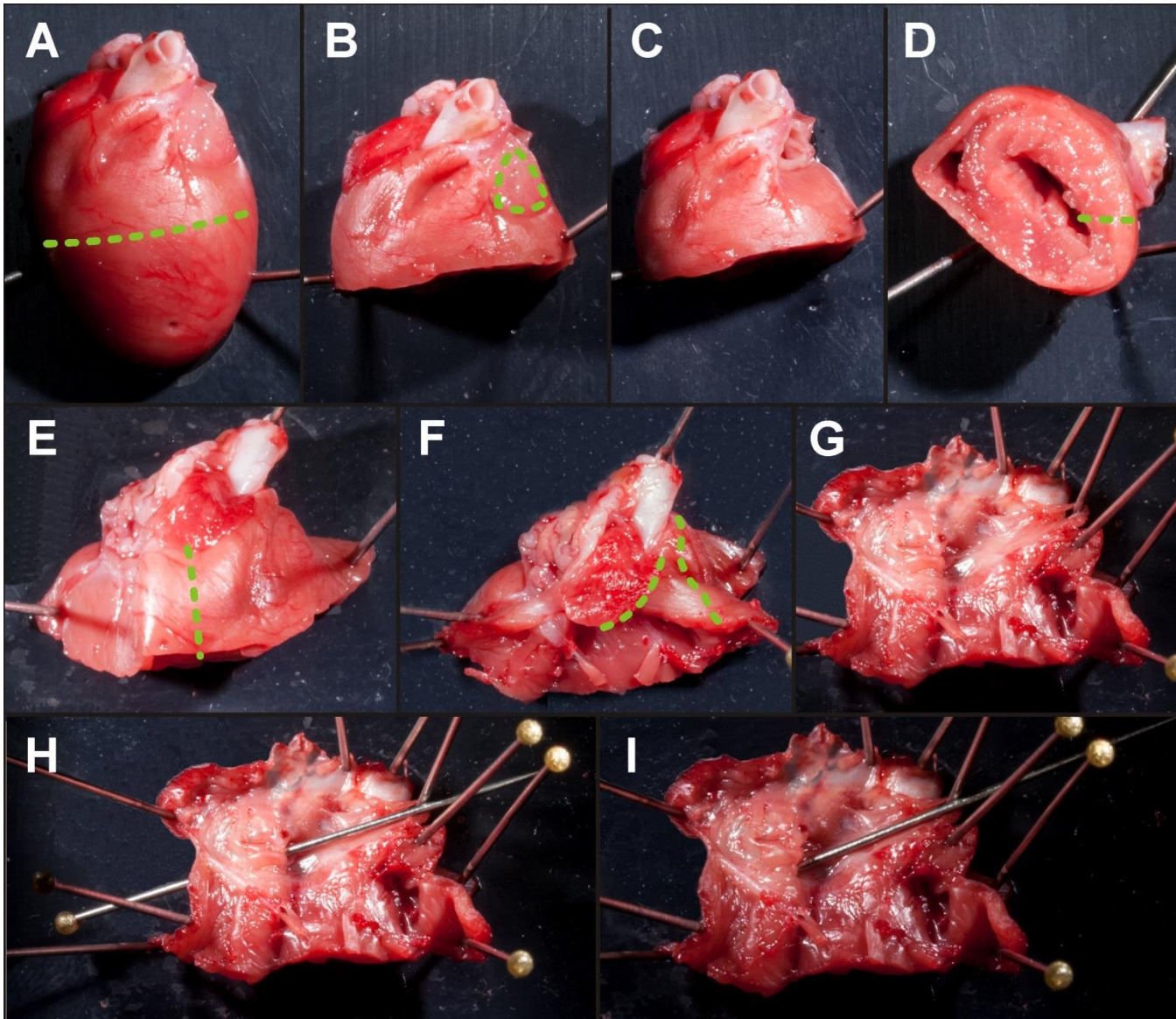


**Figure 4-1. Dissection to create the SA/AV node preparation.** The lines of dissection are shown with dashed green lines (the dissection for all experiments was performed in oxygenated Tyrode's solution but this dissection was performed a formalin fixed heart without perfusing solution for clarity of the images). A-G are described in the text. H) Demonstration of the inferior vena cava. The blunt end of the dissecting pin was pushed through the inferior vena cava from the endocardial surface with no resistance demonstrating the wide lumen of the inferior vena cava which was severed during excision of the heart from the thorax. I) Demonstration of the coronary sinus. The blunt end of the dissecting pin was advances into the ostium of the coronary sinus but could not pass further without resistance due to the narrow lumen of the coronary sinus which was not severed during removal of the heart from the thorax.

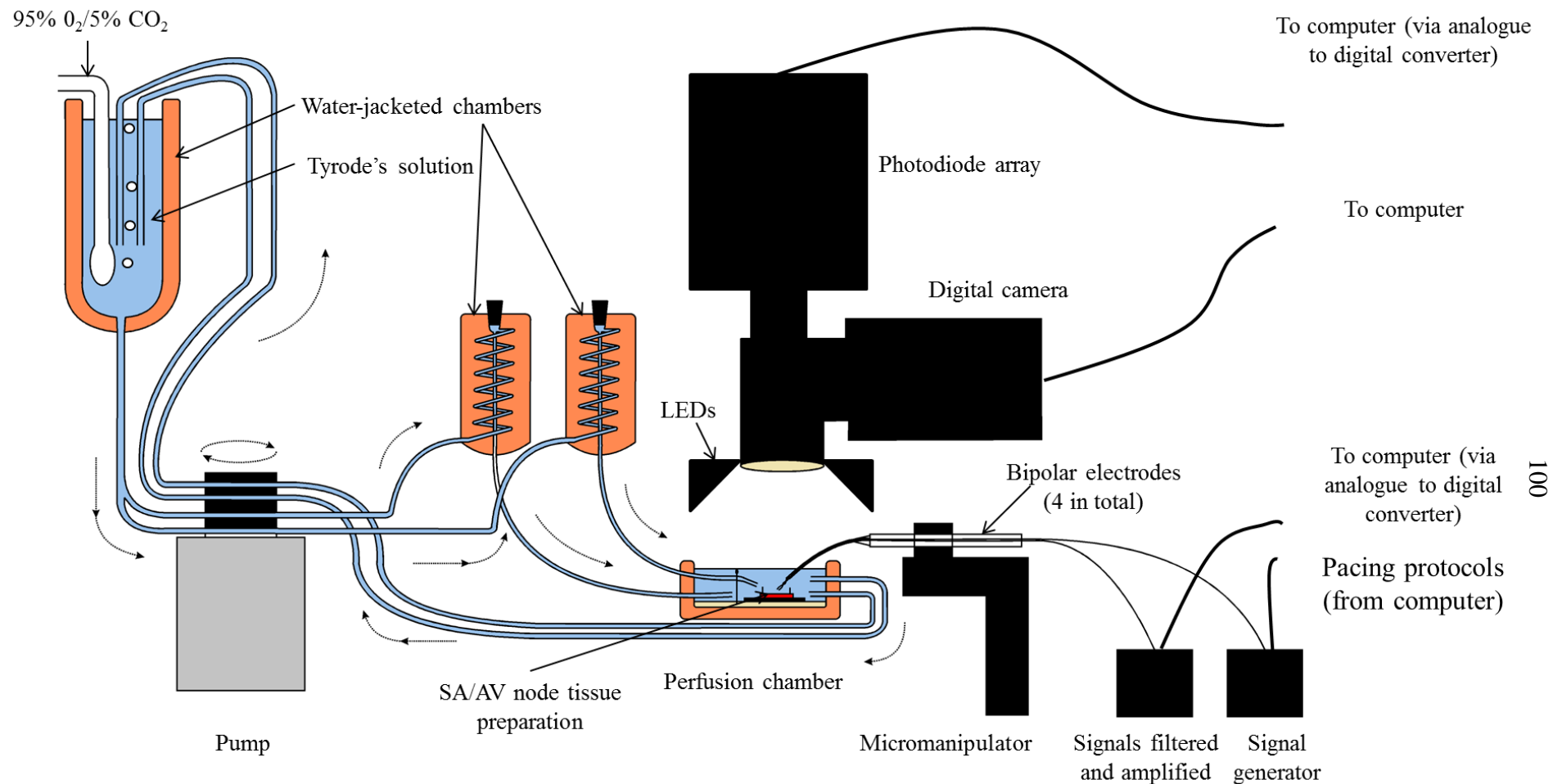


**Figure 4-2. Diagram of the experimental setup for the isolated SA/AV node preparation.** The perfusion circuit used two parallel inflows into the perfusion chamber to achieve a high flow rate and to direct the perfusion directly at the AV node as well as into the chamber. The outflow used two parallel tubes with the upper of the two tubes used to control the depth of fluid in the perfusion chamber. Initial experiments were performed using bipolar electrodes for pacing and recording signals. After the perfusion experiments were completed optical images were taken using optical dyes excited by the LEDs with signals recorded by the photodiode array. See text for further details.

#### 4.2.5 Conduction velocity

Using micromanipulators the pacing electrode was positioned at the superior end of the crista terminalis and a recording electrode was used to record the timing of the signal at the inferior end of the crista terminalis.

The threshold of activation for the pacing electrode was determined using a S1-S1 protocol pacing at a cycle length of 180 ms using a 2 ms square pulse by gradually increasing output from 0-99 V until capture of the tissue was confirmed. The output was increased to double the threshold and pacing continued at a 180 ms cycle length. The time taken for activation to reach the inferior electrode was recorded. A picture of the pacing and recording electrode positions was taken allowing measurement of distance and therefore calculation of velocity to be performed (Figure 4-3).

#### 4.2.6 Mapping of earliest activation

Mapping of earliest activation was performed using two bipolar electrodes which were positioned using the micromanipulators. The first bipolar electrode was positioned on the septal aspect of the RA. Once a good atrial signal was obtained this electrode was no longer moved and was used as a 'fiduciary point' for subsequent mapping.

The second electrode was moved across the surface of the RA. At each point the timing of atrial activation relative to the fiduciary point was recorded until the roving electrode recorded the earliest activity compared with that of the fiduciary point. A photograph was taken and the position of the roving electrode was used to mark the position of the SA node (Figure 4-3).

#### 4.2.7 Mapping of the His bundle

A bipolar electrode was positioned along the tricuspid valve annulus and moved using the micromanipulator until both an atrial and a second discrete sharp signal was recorded, i.e. an atrial and His signal. Another electrode was positioned at the point of the earliest activation determined as described above. A third electrode was positioned on the septal aspect of the atrium between the fossa ovalis and the tricuspid valve annulus in a position near the 'fast pathway'. A fourth electrode was positioned between the coronary sinus and the tricuspid valve annulus in a location near the 'slow pathway' (Figure 4-4).

#### 4.2.8 Pacing protocols

One of the 'electrodes' created contained two bipolar electrodes. One of the bipolar electrodes was used to record signals as above. The other bipolar electrode was connected to a DS2A Isolated Constant Voltage Stimulator (Digitimer, UK) which provided a square pulse of controllable voltage and duration. The voltage stimulator was connected to the computer via the data acquisition unit (Micro 1401, Cambridge Electronic Design, UK) which allowed pacing protocols programmed in Spike 2 (Cambridge Electronic Design, UK) to be performed.

Similar protocols were used to those described in section 3.2.1. Threshold was determined as described previously. SNRT, cSNRT and Wenckebach cycle length were determined as described previously. Some modifications were required for the protocol to determine AVERP and AVFRP. It was noted that for some preparations the S1 drive train of eight beats at 180 ms was inadequate because the intrinsic cycle length of the preparation was less than 180 ms (i.e. the preparation was 'competing for rate'). In order to counteract this a drive train consisting of 15 S1 beats with a cycle length of 150 ms was used (with the S2 extrastimuli starting at 140 ms). Using this protocol it was noted that some preparations demonstrated Wenckebach conduction between the atrium and His bundle during the 15 beat drive train and therefore a second protocol using 15 S1 beats with a cycle length of 200 ms was used (with the S2 extrastimuli starting at 190 ms). The reductions in S1-S2 coupling intervals were otherwise the same as those described in section 3.2.1. Where possible both S1-S2 protocols were run. However if this was not possible only the S1-S2 protocol that could generate reproducible data was performed. AVFRP was determined as described previously for both S1-S2 protocols described above.

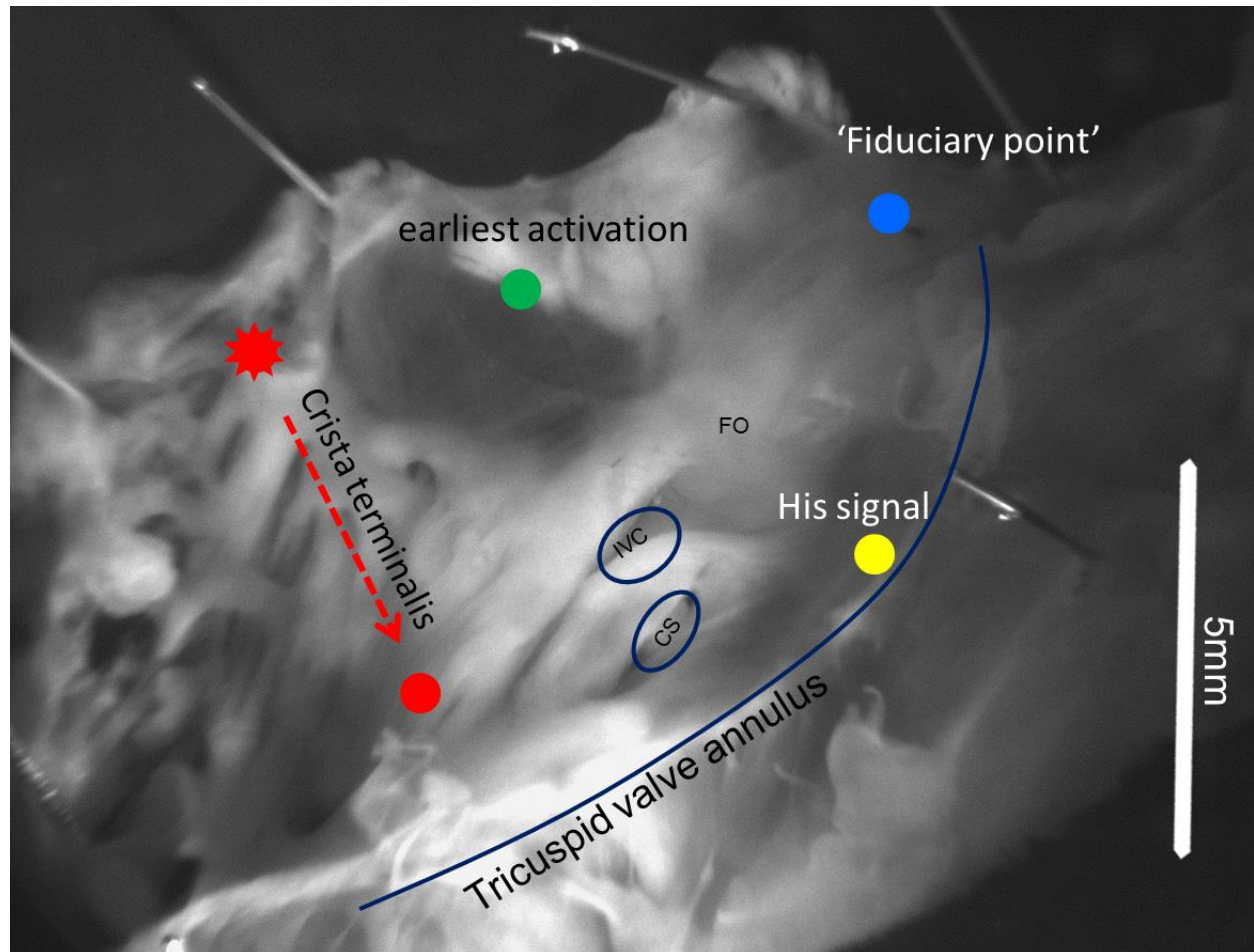
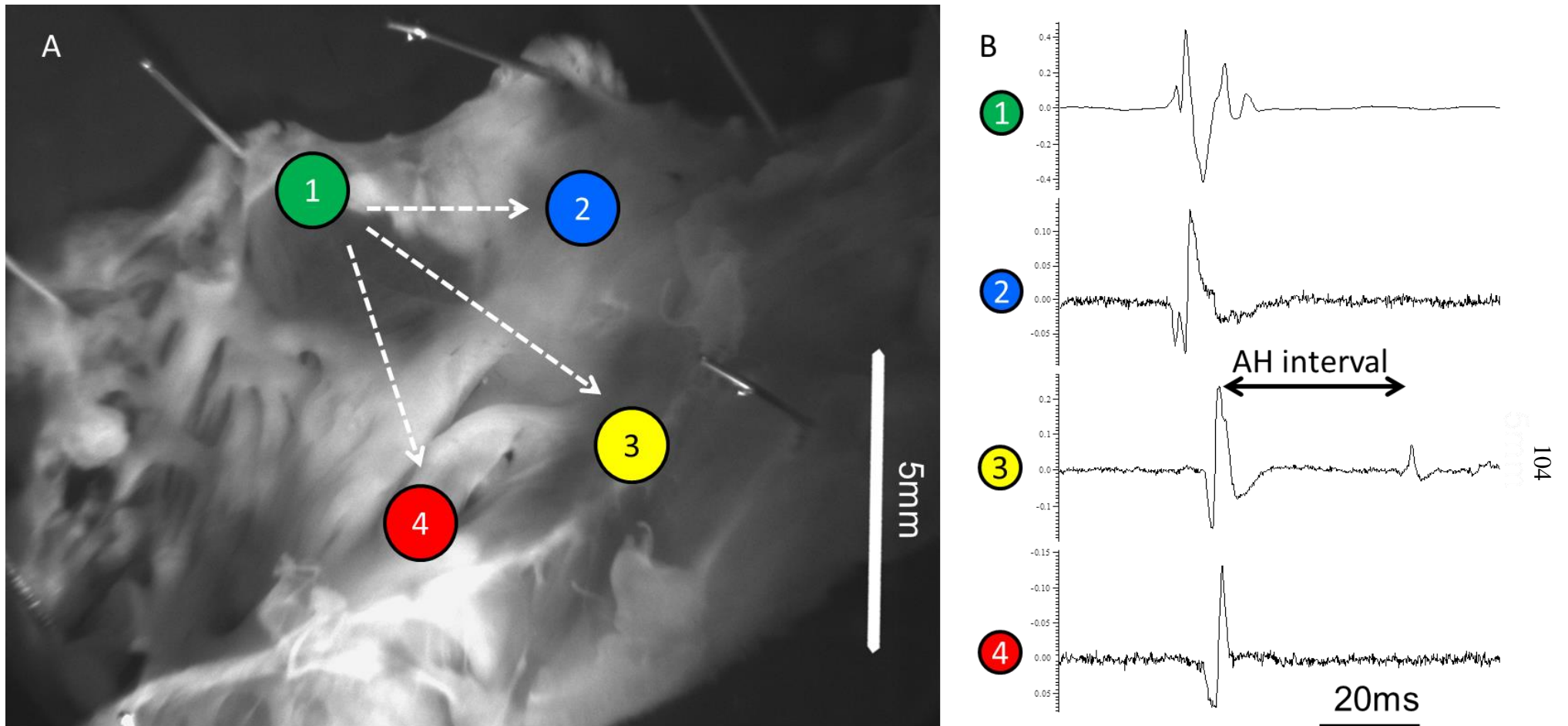


Figure 4-3. Digital photograph of the AV node preparation. The anatomical landmarks were identified during dissection. For mapping the SA node a fixed electrode was positioned on the septum and used as a fiduciary point (marked in blue). A roving electrode was then used to map the point of earliest activation (marked in green). The conduction velocity was determined using a pacing electrode at the top of the crista terminalis (marked with a red star) and a recording electrode at the bottom of the crista terminalis (marked with a red dot). The position of the His signal was then determined by moving a bipolar electrode along the crista terminalis until a double signal was detected (marked with a yellow dot). CS – coronary sinus, FO – Fossa ovale, IVC – inferior vena cava.



**Figure 4-4. Bipolar recording from the SA/AV node preparation. A) Photograph of preparation. Once the His bundle had been identified (see Figure 4-3) the other three electrodes were positioned. Electrode 1 was positioned at the site of earliest activation (the SA node). Electrode 2 was positioned at the atrial septum, electrode 3 was at the His electrode and electrode 4 was positioned between the coronary sinus and the tricuspid valve annulus. B) Bipolar recordings from the 4 electrodes marked in A. Earliest activation was at electrode 1 and latest at electrodes 4. This represents rapid atrial activation spreading from the SA node (marked with white dashed arrows). At the His signal (electrode 3) there was a discrete pause which was followed by a second smaller sharp deflection. This second deflection is the His signal. The time between the atrial and His signal is the AH interval.**

### 4.2.9 Optical mapping

Optical mapping experiments were performed after all the data generated from the pacing protocols was collected. The optical dye RH 237 was dissolved in DMSO to a concentration of 2 $\mu$ M. The excitation-contraction uncoupler blebbistatin was dissolved to a concentration of 17 $\mu$ M. The tissue preparation was loaded with the RH 237 via a slow direct application of 0.4  $\mu$ mol (final concentration in recirculating perfusate 0.8  $\mu$ M) into the perfusion chamber followed by loading with slow application of 5  $\mu$ mol blebbistatin directly into the perfusion chamber (final concentration in recirculating perfusate 10  $\mu$ M).

Four LED arrays with an emission wavelength of 530 nm were used to excite the tissue preparation. The resulting signal was passed through a dichroic mirror and recorded by a 16  $\times$  16 element photodiode array (C4675-302, Hamamatsu, Japan) connected to an analogue to digital converter (NI PX1-1042, National Instruments, UK) sampling at 1000 Hz. The spatial resolution of the system was such that each pixel of the photodiode array represented 0.6 mm. The optical signals were recorded using Qrecord software (National instruments, Newbury, UK) (Figure 4-2). The dichroic mirror was designed to be used with RH 237 although the wavelength filtered by the mirror was not specified, typically in experiments with RH 237 the mirror is designed to filter out wavelengths below 630 nm.<sup>176</sup> The tracings were analysed using Optiq software (Cairn, Faversham, UK). Optical signals were filtered with a Gaussian filter and activation time was calculated using the time at which the optical signal was 90% from baseline to peak (defined as Tact90\_Basic within Optiq).

## 4.3 Results

### 4.3.1 Mapping of the sinoatrial node

No marked changes between the control and MCT group were noted in terms of the earliest atrial activation. Standardisation of recording of the position of the nodes was difficult due to the variations in the dissection process as well as biological variability between animals. In order to compare the position of the SA node between rats the photographs of SA and AV node position were superimposed onto a single image of the preparation using GIMP software. The x/y coordinates of SA node (site of earliest activation), the top of the crista terminalis, bottom of the crista terminalis (by the tricuspid annulus) and His bundle and node position were recorded. These values were transformed

into the ‘height of the SA node’ which was the fractional distance along the crista terminalis (0 at the tricuspid annulus, 1 at top of the crista terminalis) at which the SA node was located and ‘distance from the crista terminalis’ which was proportion along the tricuspid annulus (from 0 at the crista terminalis to 1 at the AV node) at which the SA node was located. There was no difference seen in either the height of the SA node or the distance from the CT of the SA node in the MCT treated rats. These values were mapped onto a schematic diagram of the SA/AV node preparation to display the positions of the site of earliest activation for both the control and MCT animals (Figure 4-5).

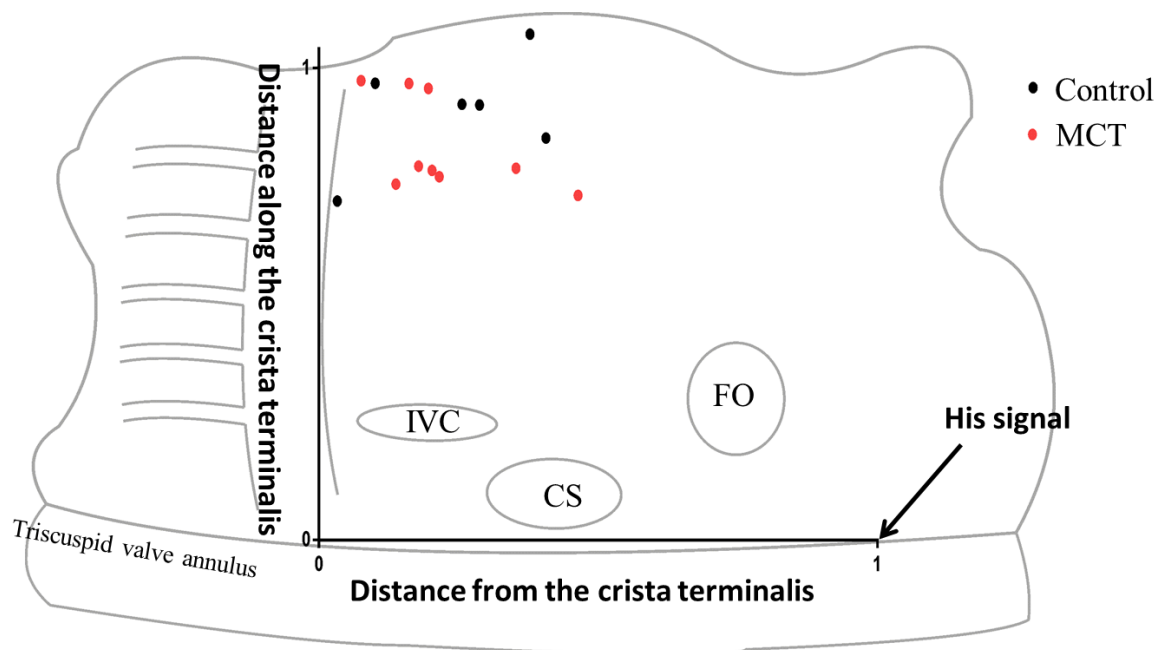


**Figure 4-5.** Schematic diagram of the SA/AV node preparation with the earliest site of activation mapped. The coordinates have been transformed into an x value for distance from the crista terminalis and a y axis value for the proportion along the crista terminalis. See text for details. CS – coronary sinus, FO – fossa ovale, IVC – inferior vena cava.

The optical activation patterns were superimposed on images of the atrial preparations to determine the earliest site of activation by optical mapping and were compared with the position of the SA node as determined by the bipolar electrodes. The positions were qualitatively similar although precise determination of the site of earliest activation was made difficult due to the poor spatial resolution of the 16x16 array used in the optical mapping system and therefore no further analysis of the position of the SA node was performed using the optical signals (Figure 4-6).

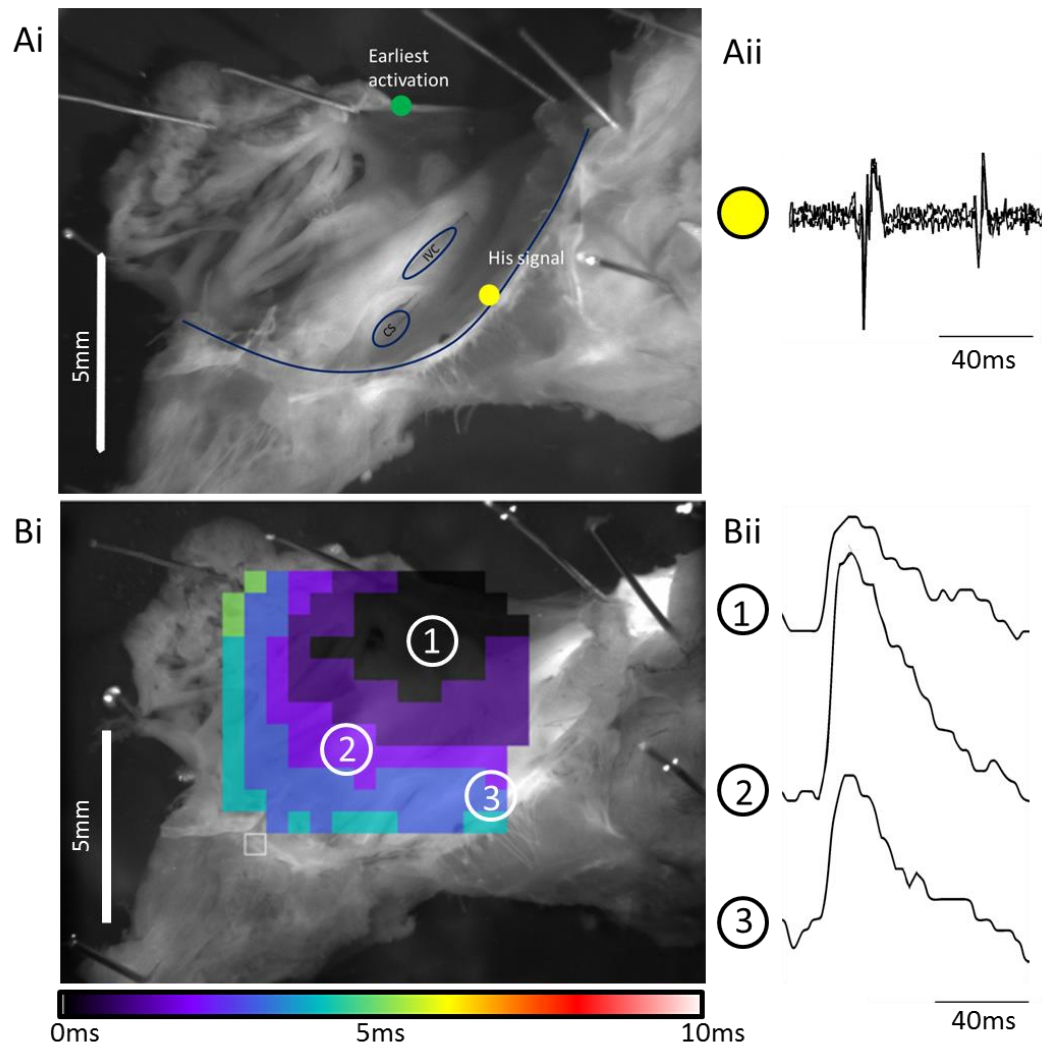


**Figure 4-6.** Comparison of bipolar electrode recording and optical mapping to identify the nodes. **Ai)** Photo of the preparation with Position of bipolar electrodes marked: earliest activation (marked in green) and location of the His signal (marked in yellow) shown. **Aii)** Bipolar electrode recording at the site of His signal. There was a clear atrial deflection followed by a discrete pause and then a His signal. **Bi)** Photo of the preparation with optical activation map superimposed. The activation map was created in Optiq using the time at which the optical signal was 90% from baseline to peak (Tact90\_Basic). Only signals with a clear upstroke were used with a ‘mask’ created to limit the map to the atrial tissue and the activation map was superimposed on a photo of the SA/AV node preparation. The earliest activation was defined as 0 ms and black on the scale bar. The position of earliest activation is marked with a 1 and is qualitatively similar to that seen in panel Ai. The colour scale bar indicates the time of activation from 0-10 ms with most of the atrial tissue activated in less than 5 ms. **Bii)** Example of optical action potentials taken from the sites shown in panel Bi. Despite the clear double deflection seen in panel Aii there is no second upstroke in region 3 to delineate the His signal on the optical action potential.

### 4.3.2 Atrial conduction velocity

Table 4-1 shows the results from the recording of conduction velocity along the crista terminalis. No differences were observed in the length of the crista terminalis or the time for the propagation of the paced impulse from the top of the crista terminalis to the bottom (Table 4-1). Despite this there was a 24% reduction in the conduction velocity along the crista terminalis in the MCT treated rats.

	<b>Control</b>	<b>Monocrotaline</b>
Distance (mm)	4.9 ± 0.3 (n=10)	5.1 ± 0.3 (n=11)
Time (ms)	11.7 ± 1.1 (n=10)	14.8 ± 1.6 (n=11)
Velocity (m/s)	0.49 ± 0.04 (n=9)	0.37 ± 0.03 (n=11) *

**Table 4-1. Results from the conduction velocity experiment. Mean ± SEM. \*Means significantly different as assessed by unpaired Student's *t*-test (P<0.05).**

The impulse propagation maps generated by the optical signals allow an assessment of conduction in the two dimensional plane. This has the advantage of allowing assessment of anisotropic conduction through the atrial myocardium. However, comparison of propagation among animals is difficult, particularly given the biological variability in anatomy and technical variability due to the dissection. The activation maps suggested a slowing of velocity in some of the MCT treated rats compared with the controls although this was not consistent across all the MCT treated rats. Example of the control and MCT rats are shown in (Figure 4-7) and the activation maps for all rats are included in the Appendix (Figure A-1).

### 4.3.3 Atrioventricular nodal functional measures

Table 4-2 shows the results from the isolated RA/AV node preparation once all four recording electrodes were in position. There was a 50% incidence of complete heart block (CHB) in the MCT treated rats compared to 0% in the control group which was statistically significant using the Chi<sup>2</sup> test (P=0.009) (Figure 4-8).

	<b>Control</b>	<b>MCT</b>
RR interval (ms)	215.9 ± 9.601 (n=9)	211.5 ± 7.079 (n=11)
AH interval (ms)	40.7 ± 5.323 (n=10)	53.0 ± 6 (n=6)
Wenckebach cycle length (ms)	129.3 ± 7.472 (n=9)	138.6 ± 11.42 (n=5)
AVERP (200 ms cycle length drive)	109.6 ± 12.96 (n=5)	114.3 ± 13.28 (n=4)
AVERP (150 ms cycle length drive)	95.00 ± 3.697 (n=6)	102.0 ± 15.00 (n=2)
AVFRP (200 ms cycle length drive)	132.5 ± 0.5000 (n=2)	137.5 ± 10.94 (n=4)
AVFRP (150 ms cycle length drive)	117.0 ± 4.933 (n=7)	127.0 ± 6.000 (n=2)
Incidence of CHB n(%)	0% (n=10)	50% † (n=12)
AV node spontaneous cycle length (ms)	913.7 ± 147.4 (n=5)	424.8 ± 84.40 (n=5) *

**Table 4-2 Results from the AV node pacing protocols. Mean ± SEM. \*Means significantly different as assessed by unpaired Student's *t*-test (P<0.05), † Difference in proportion of animals with CHB significantly different assessed using Chi<sup>2</sup> test.**

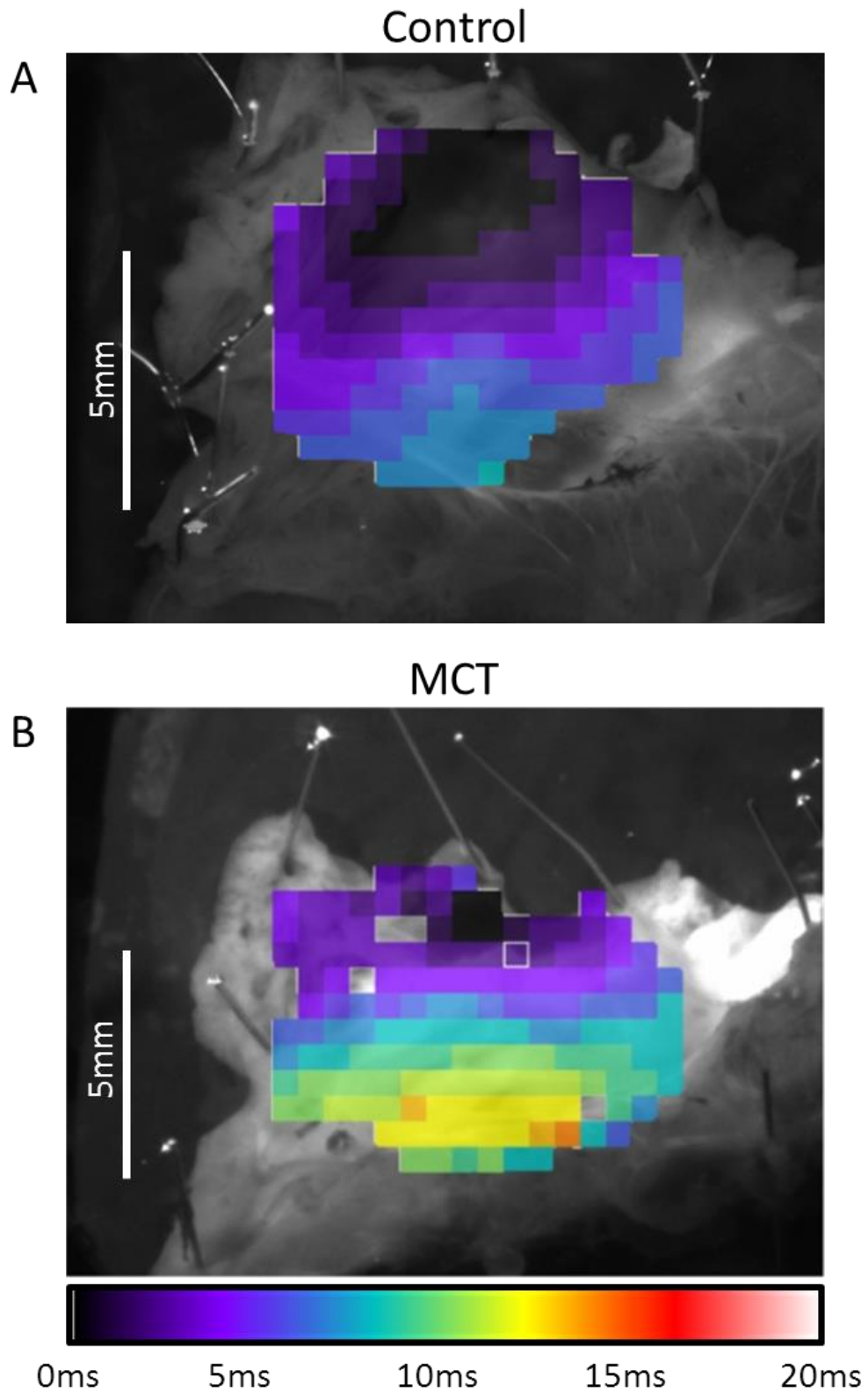


**Figure 4-7. Optical mapping to assess conduction velocity. The activation maps were created as described in Figure 4-6. A) Control preparation. In the control rat the entire RA was activated in approximately 10ms. B) Preparation from MCT treated rat. In the MCT rat the entire RA was activated in approximately 15 ms.**

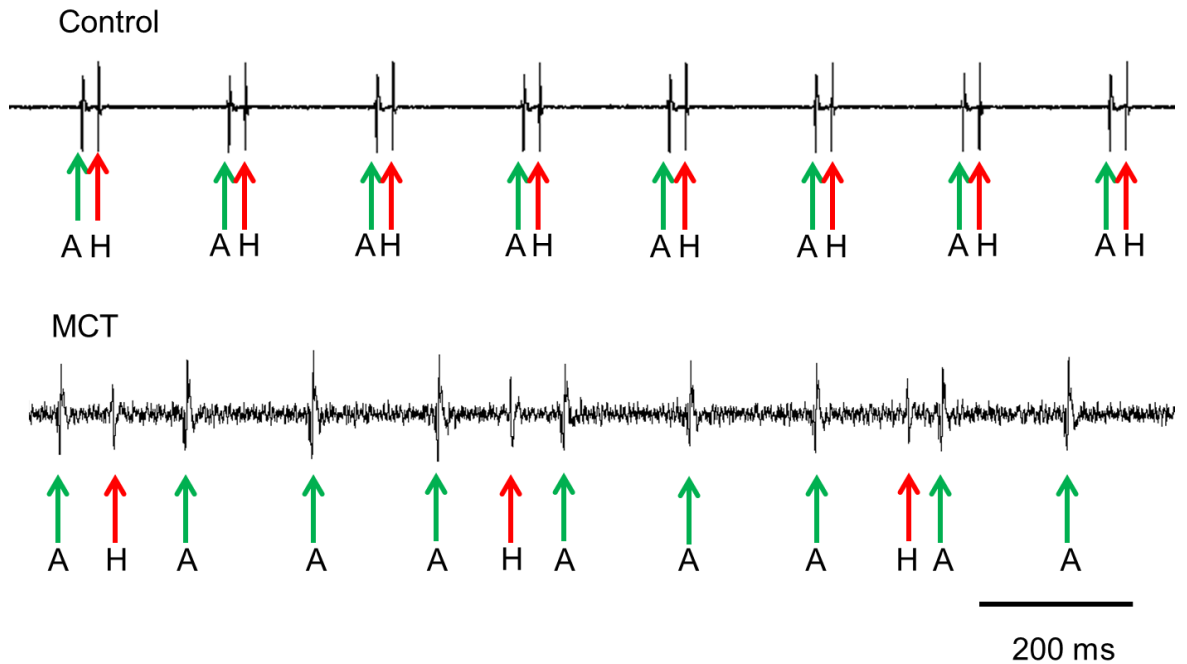


**Figure 4-8. Demonstration of CHB in a MCT treated rat. In a control rat every atrial signal (marked with a green arrow/A) was followed by a His signal (marked with a red arrow/H) with a fixed AH interval. In the MCT treated rat there was not a His signal following every atrial signal; instead the His signal is slower and independent of the His signal. This demonstrates CHB.**

No significant difference was seen in the AH interval although the value was increased by 30% ( $P=0.16$ ) in the MCT rats. Similarly although the differences between the means for the control and MCT groups were not significant the absolute values for the Wenckebach cycle length, AVERP, and AVFRP at both drive train cycle lengths were greater in the MCT rats than the control rats (Figure 4-9). There was a greater variability in the AV node conduction curves for both the control and MCT treated rats compared with the AV node conduction curves described in chapter 3. There was a small degree of variation in the H1-H2 interval as the S1-S2 interval shortened with the individual SA/AV node preparations but there was no clear discontinuity in the conduction curve for either the control or MCT treated rats i.e. dual nodal physiology was not demonstrated in either the control or MCT treated rats (Figure 4-10).

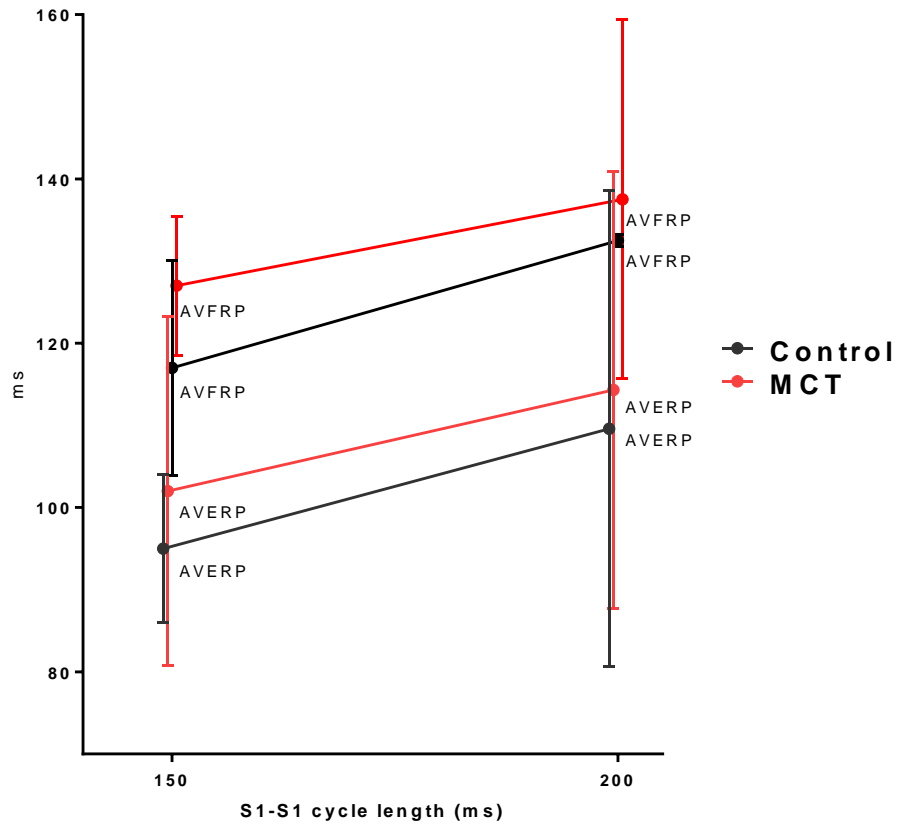


Figure 4-9. AVERP and AVFRP mean and standard error for both S1-S1 drive trains.

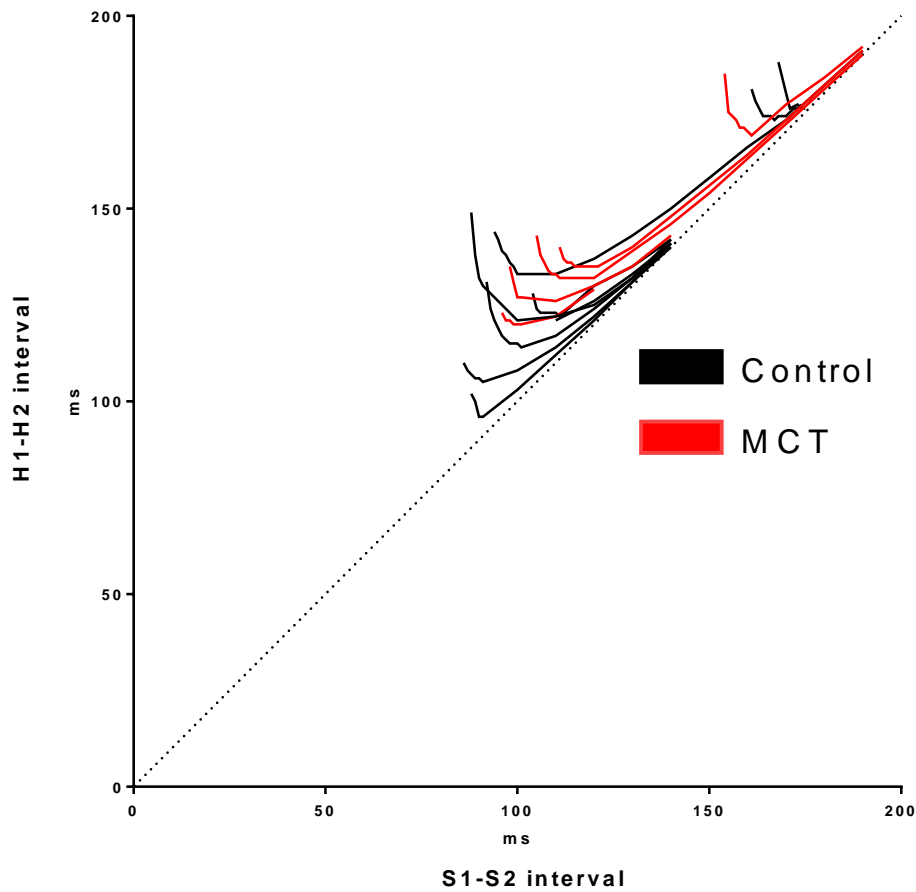


Figure 4-10. AV node conduction curve for all control and MCT treated rats used in the isolated SA/AV node preparation.

It had been hoped that the optical signals would be able to distinguish the atrial signals from that of the fast pathway, slow pathway and His bundle in order to demonstrate at which anatomical location the AV node dysfunction had occurred and allow a more detailed analysis of dual nodal physiology. Despite careful analysis of the signals recorded from the triangle of Koch it was not possible to distinguish these separate signals and therefore optical mapping was not able to provide further information regarding the location of AV node dysfunction and the relevance of dual nodal physiology (Figure 4-6).

Similar to the Langendorff findings there was no difference in sinus rate seen between the control and MCT groups (Table 4-2). The spontaneous cycle length of the isolated AV node preparation was reduced by 46 % in the MCT treated rats, i.e. the pacemaker activity of the AV node was faster. Both the control and the MCT treated rats showed a slower intrinsic rate after removal of the SA node, i.e. the intrinsic rate of the AV node was lower than that of the sinus node (Table 4-2).

## 4.4 Discussion

The isolated SA/AV nodal preparation showed AV nodal dysfunction with a 50% incidence of complete AV block in the MCT treated rats (Table 4-2 and Figure 4-8). This supports the findings from the Langendorff preparation which showed a normal RR and PR interval but demonstrated AV node dysfunction with the pacing protocols (Table 3-1 and Table 3-2). The other measures of AV node function showed no significant difference between the MCT treated and control rats in contrast to the findings from the Langendorff preparations although the absolute values suggest AV node dysfunction in all cases (Table 4-2 and Figure 4-9). The lack of significance of these parameters is likely due to the high incidence of CHB in the MCT treated rats. CHB is the most severe form of AV node dysfunction; but in rats with CHB it is not possible to generate values for AH interval, Wenckebach cycle length, AVERP and AVFRP as these numbers all rely on 1:1 AV conduction. This will lead to a systematic underestimation of the mean AH interval, Wenckebach cycle length, AVERP and AVFRP in the MCT group as the most severely affected rats are excluded from the analysis.

In addition to CHB there was a further reduction in the experimental rat numbers for AVERP and AVFRP in the MCT treated rats. This is because in order to generate a valid number for both these measurements it is essential that a drive train be delivered that is slower than the Wenckebach cycle length of the AV node (in order for stable AV node

conduction to be maintained during the drive) but faster than the intrinsic rate of the preparation (in order to ensure the preparation is only stimulated by the drive train and not the intrinsic sinus rate). In some preparations this meant that only slower drive trains could be delivered (hence the use of a 200 ms drive train). However, in some preparations only the faster drive train of 150ms could be used because of faster intrinsic heart rates.

Although AV node dysfunction was anticipated as a result of the Langendorff experiments CHB was not seen in the Langendorff experiments and it is difficult to explain the difference between these two sets of experiments. As described in section 1.6.4, *in vivo* telemetry monitoring has demonstrated that AV node dysfunction is only seen in the ECG with advanced PH in the MCT model<sup>138</sup> and therefore it is possible that the animals with CHB represented a cohort with more severe PH than the Langendorff animals. The survival curves of the MCT rats used for the Langendorff experiments and the isolated SA/AV node preparation experiments suggest that the animals used for the AV node experiments met their symptomatic endpoints earlier with a greater mortality at day 28; however, this was not statistically significant as assessed by a logrank test ( $P=0.15$ ) (Figure 4-11). Similarly if the rats in the isolated SA/AV node preparation are split into those with 1:1 conduction and those with CHB the mortality is greater in the rats with CHB but this is not statistically significant as assessed by a logrank test ( $P=0.45$ ) (Figure 4-11).

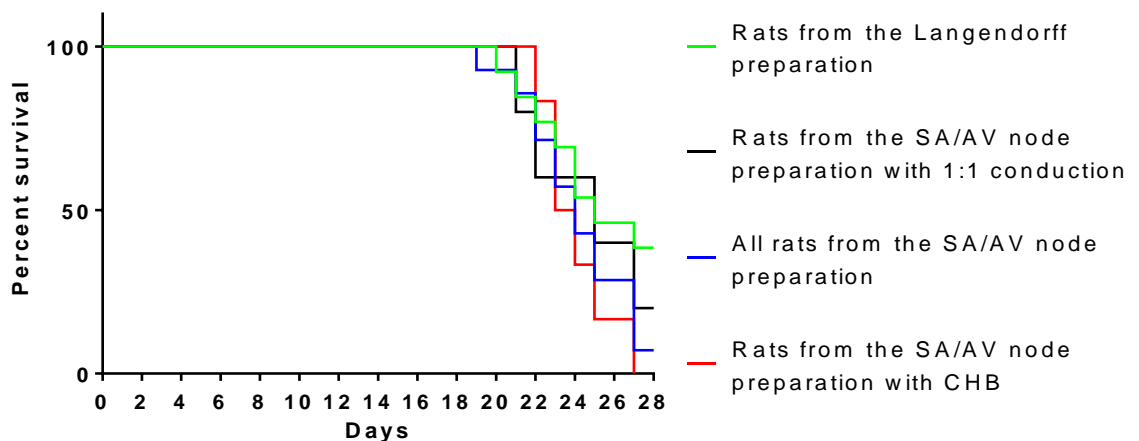


**Figure 4-11.** Kaplan-Meier graph to show the survival free days from symptomatic endpoints for the MCT treated rats that were used for the Langendorff experiments and the isolated SA/AV node experiments. There was no difference assessed by the logrank test ( $P = 0.15$ ).

The severity of disease assessed by either weight change from baseline or weight change in the 48 hours prior to termination also suggested that the cohort investigated in

the isolated SA/AV node experiments may have been more severely affected by the MCT but again this was not statistically significant (Table 4-3). Similarly, splitting the MCT treated animals that used for the isolated SA/AV node experiments into those that had 1:1 conduction, and those displaying CHB shows greater absolute values for weight loss in the animals that displayed CHB but these differences did not approach statistical significance (Table 4-4).

	<b>MCT rats used in the Langendorff experiments</b>	<b>MCT rats used in the SA/AV node prep experiments</b>
Weight change in the 48 hours before termination (g)	-8.7 ± 2.8 (n=13)	-11.7 ± 1.6 (n=13) (p=0.37)
Weight change from day 0 on day of termination (g)	68.4 ± 4.8 (n=14)	58.3 ± 2.2 (n=14) (p=0.06)

**Table 4-3. Comparison of MCT treated Rats used in the Langendorff experiments and the MCT treated rats used in the isolated SA/AV node experiments. Mean ± SEM. There were no statistically significant differences between the two groups**

	<b>MCT rats with 1:1 conduction in the AV node prep experiments</b>	<b>MCT rats with CHB in the AV node prep experiments</b>
Weight change in the 48 hours before termination (g)	-10.5 ± 3.2 (n=6)	-13.1 ± 1.4 (n=6) (p=0.48)
Weight change from day 0 on day of termination (g)	58.4 ± 4.2 (n=6)	60.4 ± 2.0 (n=6) (p=0.69)

**Table 4-4 Comparison of the differences between the MCT Rats that had 1:1 conduction at the AV node and the MCT rats that had CHB in the isolated SA/AV node preparation. Mean ± SEM. There were no statistically significant differences between the two groups assessed by unpaired Student's *t*-test.**

Another possibility is that the difference between the two sets of experiments is due to technical factors associated with the dissection of the AV node preparation or its viability with the perfusion system. Serial sections and staining of the SA/AV node dissection in both the control and MCT animals are shown in Chapter 6. The histology and immunohistochemistry demonstrates that the anatomy of the AV node is intact after the dissection. Although these are different hearts to those used in the functional experiments this finding coupled with a 50% incidence of CHB in the MCT animals versus 0% in the control animals suggests that cause of CHB is not a simple 'severing' of the AV node or the nodal inputs during the dissection.

Initial experience during development of the perfusion system demonstrated that adequate perfusion was essential for good AV node conduction; therefore it is possible that a 'threshold' effect could have existed with the AV node of the control animals just above the threshold of perfusion at which 1:1 conduction was possible and the MCT animals just below this threshold. In order to look at this possibility one of the control SA/AV node preparations was further investigated after completing all the pacing protocols but before loading with optical dyes. This experiment showed that despite dramatic reductions in perfusion rate 1:1 conduction continued throughout with minimal changes in AH interval until there was a greater than 80% reduction in perfusion rate (from 50 to 9 ml/min). The values for RR interval, AH interval, AVERP and Wenckebach cycle length were similar for before and after the perfusion experiment when the flow rate had been put back to the original 50 ml/min. The Wenckebach cycle length was checked while the perfusion was running at 9 ml/min and showed a marked increase from 110 to 180 ms. The results from this preparation suggest that perfusion is important for AV nodal conduction, but that the flow rate in the control preparations is well above the level at CHB would occur. The perfusion experiment was performed over 60 min which also demonstrates the stability of AV node conduction during this period. Although it is possible that 1:1 conduction could have been restored in the MCT treated SA/AV node preparations with CHB by increasing the perfusion rate it is unlikely given the experience with the control rat. Another possibility is that the dissection may have had some effect on autonomic function within the heart. It would have been interesting to perform both autonomic blockade and autonomic stimulation on the SA/AV node preparations to see if 1:1 conduction could have been restored and also to see if differences between the control and MCT treated groups were maintained. Irrespective of whether 1:1 conduction could have been restored by either of these methods the results from this experiment reinforce the idea that there is a significant impairment of intrinsic AV node function in the MCT animals.

The aim of the optical mapping was to localise the site of dysfunction to a more specific region within the AV node, particularly with a view to examining the fast and slow pathways and the penetrating bundle, but unfortunately this was not possible with these experiments (Figure 4-6). The AV node is a transmural structure which means that the atrial and AV nodal tissues overlie each other: therefore, the optical signals from the AV node show two signals, the first from the atrium and the second from the nodal tissue.<sup>71, 86, 108, 174</sup> The ability to distinguish these two signals requires a high signal to noise ratio and

good spatial resolution and it is likely that it is a combination of these two factors that meant that it was not possible to record AV nodal optical signals.

The finding of a reduced cycle length and therefore faster rate in the isolated AV node preparation is an interesting finding. It is possible that the faster intrinsic rate of the AV node may dispose to ectopic beats. Support for this comes from the optical images in which one of the MCT treated rat showed spontaneous ectopy coming from the region of the AV node before the SA node was removed. This was only seen in one of the preparation from the MCT treated rats and was not seen in any of the preparations from the control rats (Figure 4-12). As described in section 1.3.2 there are increased numbers of ectopic beats seen in PAH patients which is in keeping with these findings. Appropriately timed ectopic beats may initiate AVNRT and therefore increased ectopic beats may promote the generation of AVNRT. No changes in SA node function in terms of rate and location of the leading pacemaker site were seen in the MCT treated rats compared with the control rats.

A further finding from these experiments is that of a reduced conduction velocity along the crista terminalis. The reduction in conduction velocity seen is comparable with the reduction in conduction velocity in the ventricle seen in animal studies using the MCT model and reduced conduction velocity in the atrium seen in human studies in patients with PAH.<sup>28, 131</sup> The reduction in conduction velocity may be implicated in the pathogenesis of atrial flutter in which there is a fixed anatomical circuit in the RA which includes the crista terminalis.<sup>177</sup> A decrease in conduction velocity along the crista terminalis will reduce the wavelength of the circuit and hence promote the maintenance of reentrant arrhythmias (see section 1.6.2). The optical mapping data were more difficult to interpret due to the structural heterogeneity and anisotropic conduction of the preparation. The propagation maps were taken during spontaneous sinus rhythm which means that there was variation in the site of the original impulse and also the possibility of different breakthrough sites from the SA node into the atrium affecting conduction patterns.<sup>178</sup> However there was some evidence of conduction slowing in the MCT treated rats.

The isolated SA/AV node preparation experiments have provided several insights into arrhythmogenesis in PH showing reduced atrial conduction velocity, an increased spontaneous rate of non SA node tissue and intrinsic AV node dysfunction. Despite this they have been unable to define the anatomical and functional correlates that underlie these changes.

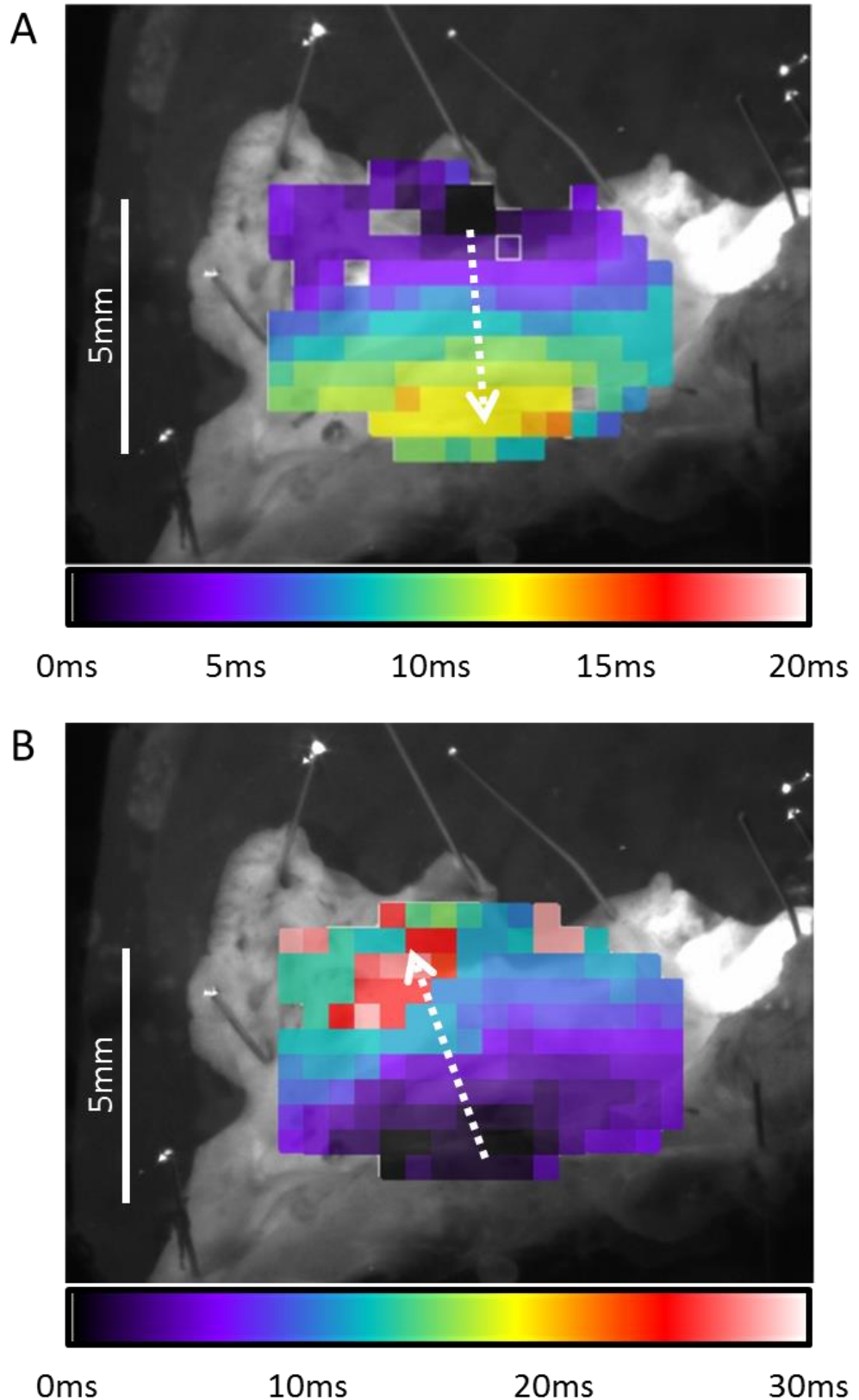


**Figure 4-12.** Optical mapping demonstrating ectopic activation from the AV node. Activation maps were created as described in Figure 4-6. **A)** Earliest activation at the expected site of the SA node (in the superior intercaval region). The entire atrium was activated in approximately 15 ms. This pattern accounted for the majority of impulses. **B)** Earliest activation at the AV node (along the tricuspid valve annulus near the coronary sinus). Activation propagated more slowly than in panel A, taking approximately 30 ms for the entire atrium to be activated.

# 5 Remodelling in response to pulmonary hypertension at the mRNA level

---

## 5.1 Introduction

As described in section 1.5.2 the AV node is a complex structure that is defined by both its anatomy and functional characteristics with considerable heterogeneity among the myocardial cells that compose it. This heterogeneity means that studies investigating the molecular biology of the AV node must first define which region of the AV node the cells come from. As previously discussed the AV node and surrounding structures can be divided into six different regions; the atrial septum, transitional tissue, inferior nodal extension, compact node, penetrating bundle and ventricular septum. The aim of this study was to identify and isolate these six different tissue regions of the AV node from both the control and MCT treated rats and then investigate them using reverse transcription quantitative polymerase chain reaction (RT-qPCR) to look at the expression of messenger RNA (mRNA) transcripts for ion channels and transporters, connexins, intracellular Ca<sup>2+</sup> handling proteins, and the receptors of the autonomic nervous system.

## 5.2 Methods

The control and MCT treated animals were created and monitored as previously described in Chapter 2. On the day of termination the animals were administered 1000 U heparin and then after 30 min they were sacrificed and the hearts excised.

Tyrode's solution ( NaCl – 120 mM, CaCl – 1.2 mM, KCl – 4mM, MgSO<sub>4</sub>.7H<sub>2</sub>O – 1.3 mM, NaH<sub>2</sub>PO<sub>4</sub>.2H<sub>2</sub>O 1.2 mM, NaHCO<sub>3</sub> – 25.2 mM, glucose – 5.8 mM) was generated on the day of the experiment and bubbled with 95% O<sub>2</sub>/5% CO<sub>2</sub>.

The aorta was perfused retrogradely with oxygenated Tyrode's solution and the hearts were immersed in the oxygenated Tyrode's solution. The hearts were dissected into the isolated SA/AV node preparation as previously described in section 4.2.1. The Tyrode's solution was removed and the SA/AV node preparation was immersed in optimal cutting

temperature compound (OCT) mounting medium and then rapidly frozen by immersion in isopentane chilled in liquid nitrogen. This encased the SA/AV node preparation in solid OCT and therefore the dissecting pins were removed without disrupting the tissue preparation. The OCT was then cut into a rectangle containing the entire tissue preparation. This sample was stored at -80 °C for processing at a later date.<sup>179</sup>

The AV node tissue preparation encased in OCT was cryosectioned into sections of 50 µm thickness with two sections per slide onto Superfrost Plus (Fisher Scientific, USA) slides at -18°C. The slides were stored at -80°C for processing at a later date.

### 5.2.1 Mapping the AV node

### 5.2.2 Immunohistochemistry

Immunohistochemistry relies on using antibodies that bind to specific proteins within a cell in combination with a means of visualising the antibody that has bound. Within this study this has been achieved using protein specific primary antibodies in combination with species specific secondary antibodies conjugated with a fluorescent tag. The principle is demonstrated in Figure 5-1. Two primary antibodies against specific proteins are demonstrated which are raised in two species other than the rat. Two secondary antibodies are used to bind to the primary antibodies, but because each primary antibody is raised in a different species each of the secondary antibodies is specific for one of the primary antibodies. Both of the secondary antibodies are labelled with a fluorescent tag with specific absorption and emission spectra which can therefore be measured separately. Theoretically a single tissue can be stained with multiple different primary antibodies, provided that they are each from a different species and can be labelled with a secondary antibody specific for the species that the primary antibody was raised in and provided that each secondary antibody is labelled with a fluorescent tag with unique absorption and emission spectra. The practicalities of using commercially available primary and secondary antibodies has limited all the sections to dual labelling (i.e. two primary antibodies and two secondary antibodies) for all the sections in this study.<sup>179</sup> The primary and secondary antibodies used are shown in Table 5-1 and Table 5-2.

Antibody	Manufacturer	Species antibody raised in	Monoclonal/ Polyclonal	Concentration used
HCN4	Alomone, Israel (ACC-052)	Rabbit	Polyclonal	1:100
Cx43	Millipore, Germany (MAB3068)	Mouse	Monoclonal	1:100

Table 5-1. Primary antibodies used in immunohistochemistry.

Antibody	Manufacturer	Species antibody raised in	Concentration used	Fluorescent tag	Primary antibodies bound
Anti-Mouse (IgG)	Millipore, Germany (AP192 C)	Donkey	1:400	Cy3	RyR2 and Cx43
Anti-Rabbit (IgG)	Millipore, Germany (AP 182F)	Donkey	1:100	FitC	HCN4

Table 5-2 Secondary antibodies used in immunohistochemistry.

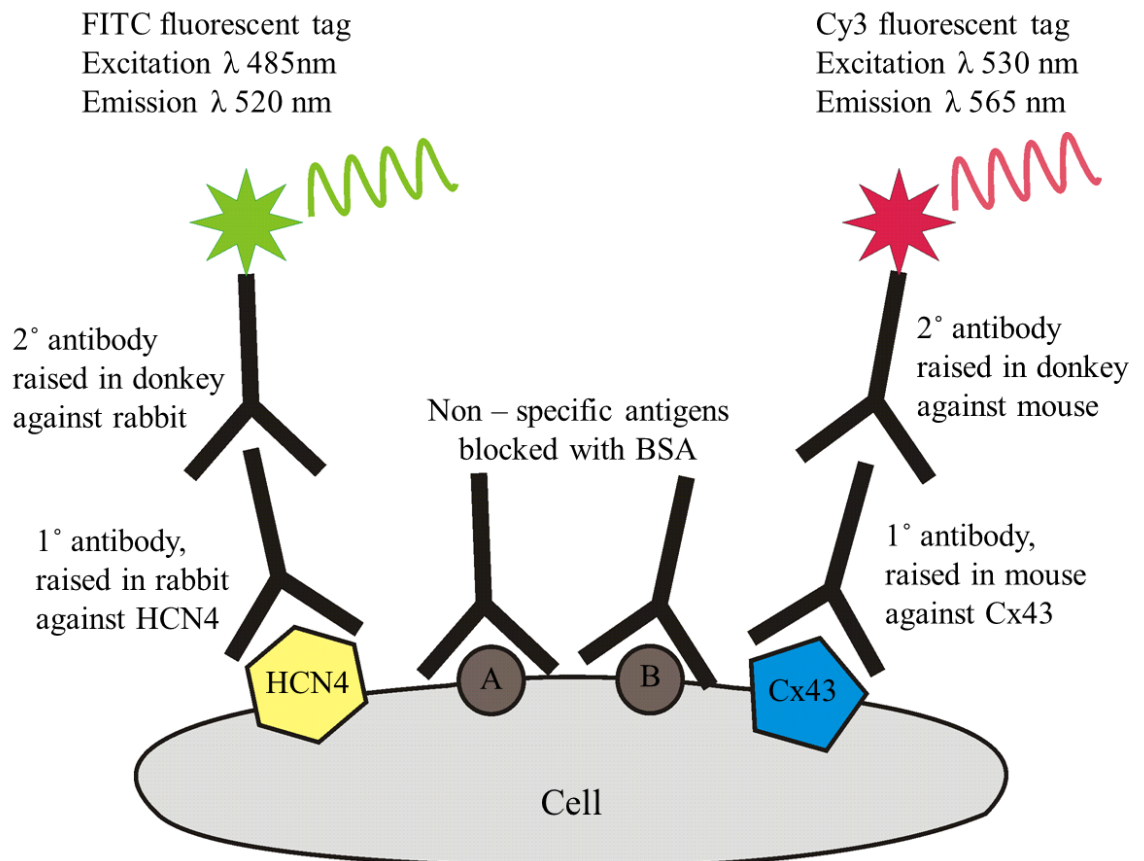


Figure 5-1. Schematic diagram of double labelling of HCN4 and Cx43 with immunohistochemistry. See section 5.2.2 for details. BSA –bovine serum albumin.

In order to create a 'map' of the AV node every fourth slide per animal was removed from the freezer and underwent immunolabelling for HCN4 and Cx43 using the following protocol described in Morris *et al.*<sup>179</sup>

The slides were immersed in 10% buffered formalin for 30 min to fix the tissue sections. Each tissue section was outlined with a water repellent pen, this allowed each tissue section to be treated individually. From this point on all solutions were added via pipette to the individual tissue sections and removed using aspiration. Tissue sections were washed in phosphate buffered saline (PBS) for 10 min, three times, in order to remove formalin. 0.1% Triton-X100 was applied to each tissue section for 30 min to permeabilise the cell membrane, allowing the antibodies to reach the cytoplasmic epitopes. Tissue sections were washed in PBS for 10 min, three times, to remove any residual 0.1% Triton-X100. Tissue sections were treated with bovine serum albumin (BSA) (Sigma, USA) for 60 min. The BSA is used as a blocking agent, the antibodies in the BSA bind to non-specific binding sites; this stops the primary antibodies binding to these non-specific sites. Tissue sections were incubated in primary antibody overnight at 4°C; during this time the primary antibodies bound to the proteins of interest. Tissue sections were washed in PBS for 10 min, three times, to remove residual primary antibody. Tissue sections were incubated with secondary antibody for 120 min; during this time the secondary antibody bound to the primary antibodies. Tissue sections were washed in PBS for 10 min, three times, to remove residual secondary antibody. Each slide was mounted in H-1000 VECTASHIELD (Vector laboratories, UK), a coverslip was applied, and the edges of the coverslip were sealed with nail varnish. The VECTASHIELD avoided photo-bleaching of the sections pending imaging. The sections were imaged using the Leica DM500 microscope (Leica, Germany) using epifluorescence.

### 5.2.3 Masson's trichrome staining

After imaging the immune stained sections the coverslip was removed and the sections underwent Masson's trichrome staining. Each slide was removed from -80 °C freezer, placed in Bouin's fluid and left overnight for fixation. Next day the slides were washed in 70% alcohol for 10 min, three times. The slides were then; stained with celestine blue for 5 min, rinsed in distilled water for 15 min, stained with Cole's alum haematoxylin for 10 min, washed in tap water for 15 min, stained in acid fuchsin for 3 min, washed in distilled water for 15 min, stained with phosphomolybdic acid for 5 min, drained, stained in methyl

blue for 5 min, rinsed in distilled water for 15 min and immersed in 1% acetic acid for 2 min. The slides were then dehydrated through alcohol by being immersed in; 70% alcohol for 1 minute, 90% alcohol for 1 minute, 100% alcohol for 2 min, two times. The slides were then immersed in Histo-Clear (national-diagnostics, USA) for 5 min, two times. Each slide was mounted in DPX and a coverslip applied. The sections were imaged using the Leica DM500 microscope using light field imaging (Leica, Germany).

#### 5.2.4 Identifying the regions of the AV node

The immunohistochemistry and Masson's trichrome images of each section were reviewed together. They identified connective tissue (blue with Mason's trichrome stain), nodal tissue (high levels of HCN4, low levels of Cx43) and working myocardium (high levels of Cx43, low levels of HCN4). The image sets from each slide were then reviewed sequentially for the whole SA/AV node preparation. This revealed that the nodal tissue was present in the atrium and ran continuously along the tricuspid annulus from the coronary sinus ostium to the apex of the triangle of Koch. At this point the nodal tissue passed through the central fibrous body and into the ventricle where it split into the left and right bundle branches. From these sections six different regions were identified as follows (Figure 5-2):

**Atrial septal myocardium** – myocardial tissue above the level of the central fibrous body showing high levels of Cx43 and low levels of HCN4.

**Ventricular septal myocardium** - myocardial tissue below the level of the central fibrous body showing high levels of Cx43 and low levels of HCN4.

**Penetrating bundle** – myocardial tissue encased within the central fibrous body showing low levels of Cx43 and high levels of HCN4.

**Compact node** – myocardial tissue just before the level of the penetrating bundle which is not encased in the central fibrous body showing low levels of Cx43 and high levels of HCN4. At this level the nodal tissue extended across the entire atrial septum from the right side to the left side.

**Transitional tissue** – in the region between the atrial septal myocardium and the compact node there was an area of intermediate staining for Cx43 and HCN4 with the appearance of intertwining 'strands' of nodal tissue and working myocardium.

**Inferior nodal extension** – as the tissue sections extended inferiorly along the tricuspid valve annulus the nodal tissue no longer ‘straddled’ the atrial septum (as it did for the compact node) and instead the nodal tissue formed a finer band of tissue along the right side of the atrial septum next to the septal tricuspid valve leaflet. The nodal tissue was included as the inferior nodal extension until the inferior part of the coronary sinus was reached to avoid including the AV ring tissue.<sup>180</sup>

### 5.2.5 Hand-assisted micro-dissection of the atrioventricular node

The detailed ‘map’ of the AV node identifying the six regions of the node and surrounding structures was used to guide microdissection from the remaining slides of the SA/AV node preparation. Every fourth slide was used in the map and so there were three slides containing a total of six tissue sections between each element of the map.

During processing of the tissue it was important to protect the mRNA from degradation via the action of ubiquitous ribonucleases (RNAses). In order to achieve this all the stains used were ethanol based as this has been shown to protect from the action of RNAses.<sup>181</sup> A haematoxylin and eosin stain was performed. The slides were immersed in; 100% ethanol for 30 s, haematoxylin for 60 s, 70% ethanol for 30 s, 95% ethanol for 30 s, eosin for 60 s, 70% ethanol for 30 s and 95% ethanol for 30 s. The slides were then immersed in 100% ethanol and were left in the in 100% ethanol until the tissue was microdissected.

The slides were then visualised under a Nikon SMZ800 dissecting microscope (Nikon, Japan) with x63 magnification. The haematoxylin and eosin stained slide was compared to the corresponding images from the AV node ‘map’ in order to correlate the structures seen down the microscope with the regions of the AV node. Each region was then removed from the slide with a sharp surgical needle taking care to ensure that only tissue from the region of interest was removed with no contamination from the surrounding tissues (Figure 5-3). The dissected tissue sections were then placed directly into RNA lysis buffer which was vortexed for approximately 3 s and stored on ice. A separate needle was used for each region of the AV node to avoid contamination of the sample. During the time the slide was being visualised down the microscope, 100% ethanol was pipetted onto the slide to ensure that the section did not dry out.

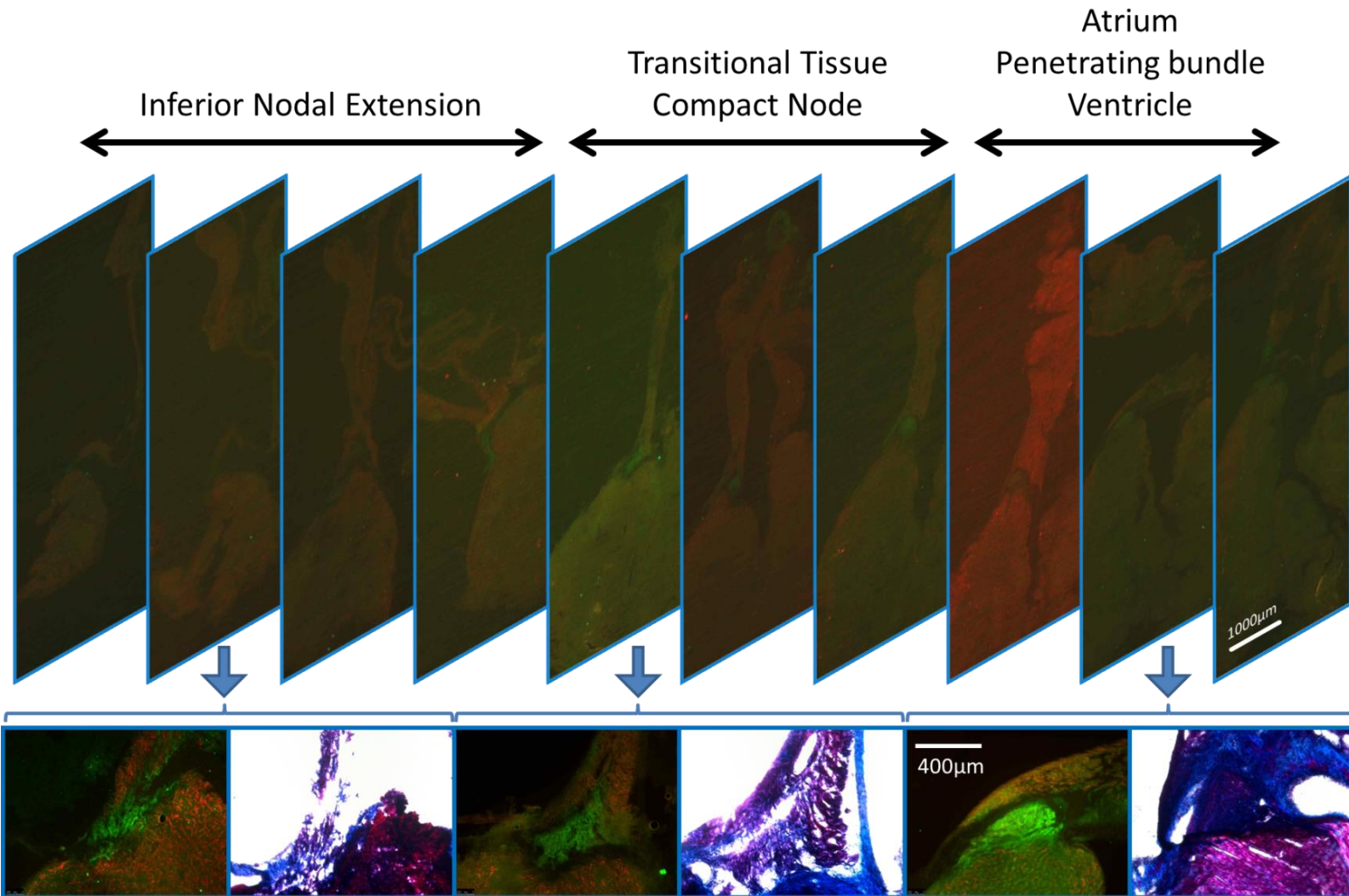


Figure 5-2. Demonstration of the 'AV node map' to determine the locations of the regions within the AV node. Initially the slides were immunolabelled with Cx43 (red) and HCN4 (green). This identified nodal tissue and working myocardium. The slides then underwent Masson's trichrome staining to delineate fibrous tissue (in blue). All the images were then reviewed sequentially to identify six different regions (see section 5.2.4 for details of the criteria for each region)

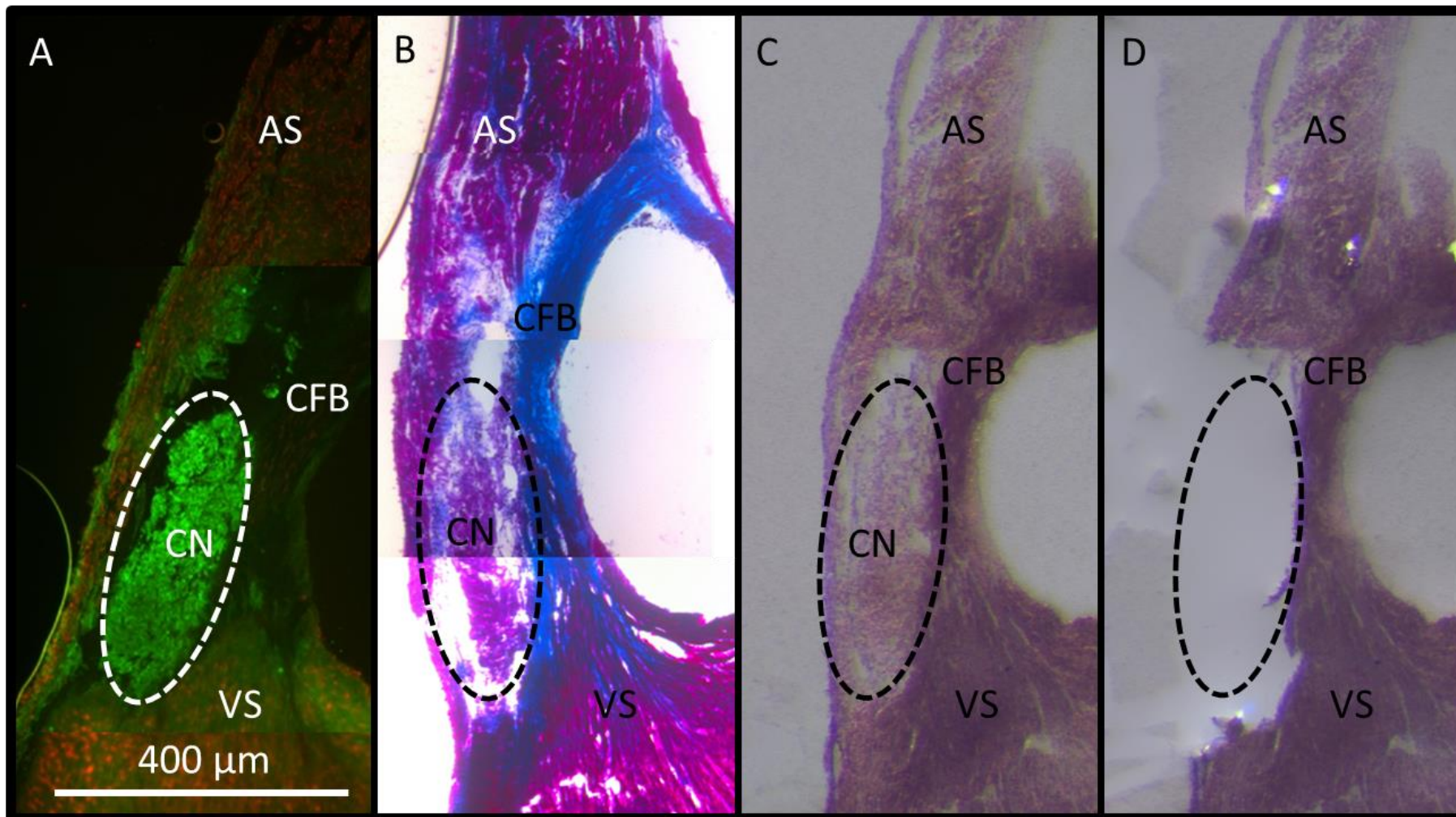


Figure 5-3. Images demonstrating hand assisted microdissection. A) AV node section double labelled for HCN4 (green) and Cx43 (red). The ringed area shows high levels of HCN4 and low levels of Cx43. B) Masson's trichrome staining of a 'sister section'. The area of interest demonstrated in A can be seen to be enclosed within the central fibrous body. The combination of high levels of HCN4, low levels of Cx43 and enclosure within the central fibrous body identifies this area as the penetrating bundle. C) Haematoxylin and Eosin stained section before microdissection. This reveals the area of interest identified from the 'map' created by A and B. D) The same slide as C post microdissection with the area of interest (in this case the penetrating bundle) removed. AS – atrial septum, CFB – central fibrous body, CN – compact node, VS – ventricular septum.

## 5.2.6 RNA extraction

### 5.2.6.1 Optimisation of RNA extraction technique

Two RNA extraction kits were compared: RNeasy micro kit (Quiagen, Netherlands) a silica column based RNA extraction kit and MirVana (Ambion, USA) a phenol-chloroform based RNA extraction kit. A single trial AV node sample was processed according to manufacturers' guidelines with higher RNA yields for the MirVana kit (e.g. for the ventricle there was a total RNA of 93 ng for RNeasy and 930 ng for Mirvana). The MirVana kit was therefore used for all subsequent RNA extraction.

On a trial AV node preparation each tissue region was added to an empty tube and stored until the entire AV node preparation was dissected at which point the lysis buffer from the MirVana kit was added. There was concern regarding RNA degradation due to the action of RNase during the time it took for microdissection of the entire AV nodal preparation. In light of this concern the protocol was altered so that each time a tissue region was microdissected it was added directly to 300  $\mu$ l of the lysis buffer from the MirVana kit.

A strategy of using the tissue homogeniser after the addition of each tissue sample was compared with vortexing the combined tissue sample/lysis buffer after the addition of each new tissue sample. This showed that the final quantity of RNA was similar in both groups (e.g. total RNA was 350ng for the transitional tissue using the homogeniser and 730 ng for the compact node using the vortexer), therefore the vortexing strategy was adopted for all RNA extractions because it was faster and simpler.

The phenol-chloroform extraction technique removes genomic DNA because the genomic DNA is suspended in the organic phase of the phenol-chloroform solution which is separated by centrifugation and removed. There is still the possibility of some genomic DNA contamination and therefore the sample was treated with the TurboDNase system (Life Technology, California, USA) in accordance with the manufacturer's instructions.

RNA concentration were measured using the Nanodrop (Thermoscientific, USA) and the Qubit <sup>®</sup> (Life technologies, USA). Comparison of the reported concentrations revealed good correlation at concentrations above 20 ng/ $\mu$ l but poor correlation below this level with much higher levels reported from the Nanodrop than the Qubit (Figure 5-4). The Nanodrop uses the absorbance of light to determine the concentration of RNA. However, the readings can be inaccurate in the presence of DNA or protein contamination and

therefore the Nanodrop is inaccurate and poorly reproducible at concentrations of less than 5 ng/ $\mu$ l . The Qubit system uses fluorescent dyes that bind specifically to RNA and is therefore more specific than the Nanodrop, particularly at low concentrations. The Qubit system was therefore used for all RNA measurements.<sup>182, 183</sup>

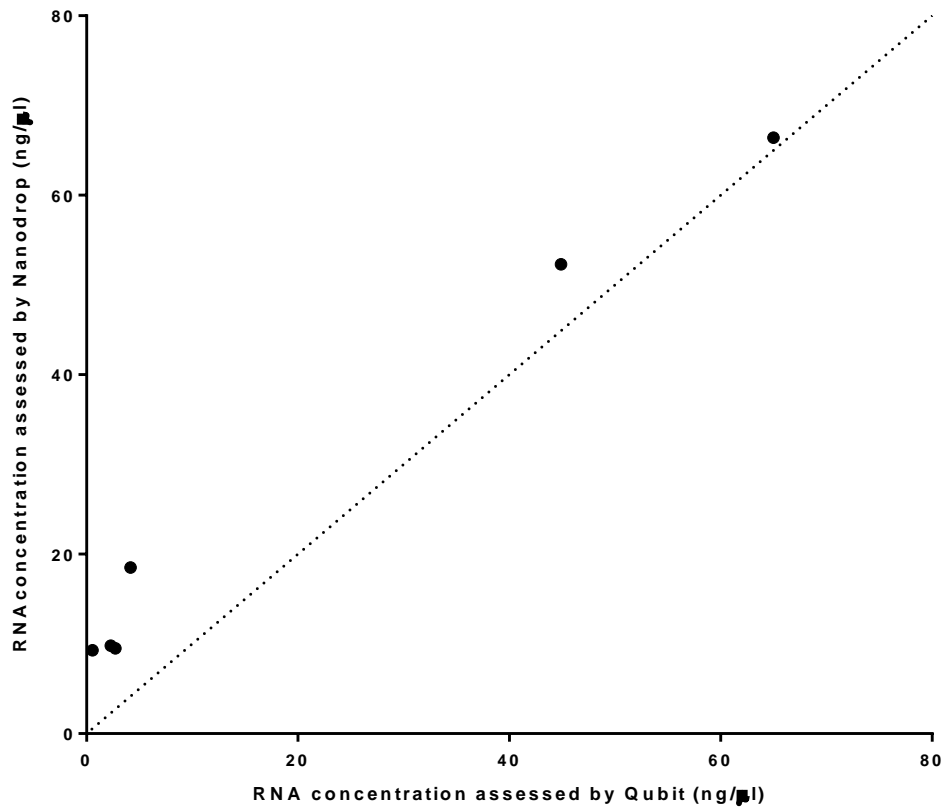


**Figure 5-4. Comparison of Qubit and Nanodrop to measure RNA concentration. The six tissue regions for a single AV node sample were assessed using both the Qubit and Nanodrop. At higher concentrations there is good agreement between the two techniques but at lower concentrations the Nanodrop reports higher concentrations than the Qubit.**

After the experimentation with the different elements of RNA extraction described above the quality of the RNA extracted using the final protocol was compared to the earliest attempts at RNA extraction. This was performed using a gel electrophoresis system (Agilent Bioanalyser, USA) according to the manufacturer's guidelines, using a pico chip, specifically designed to assess small quantities of RNA. This revealed that the final protocol had improved the quality and quantity of RNA extracted (Figure 5-5) and therefore the final protocol described below was used for all RNA extractions.

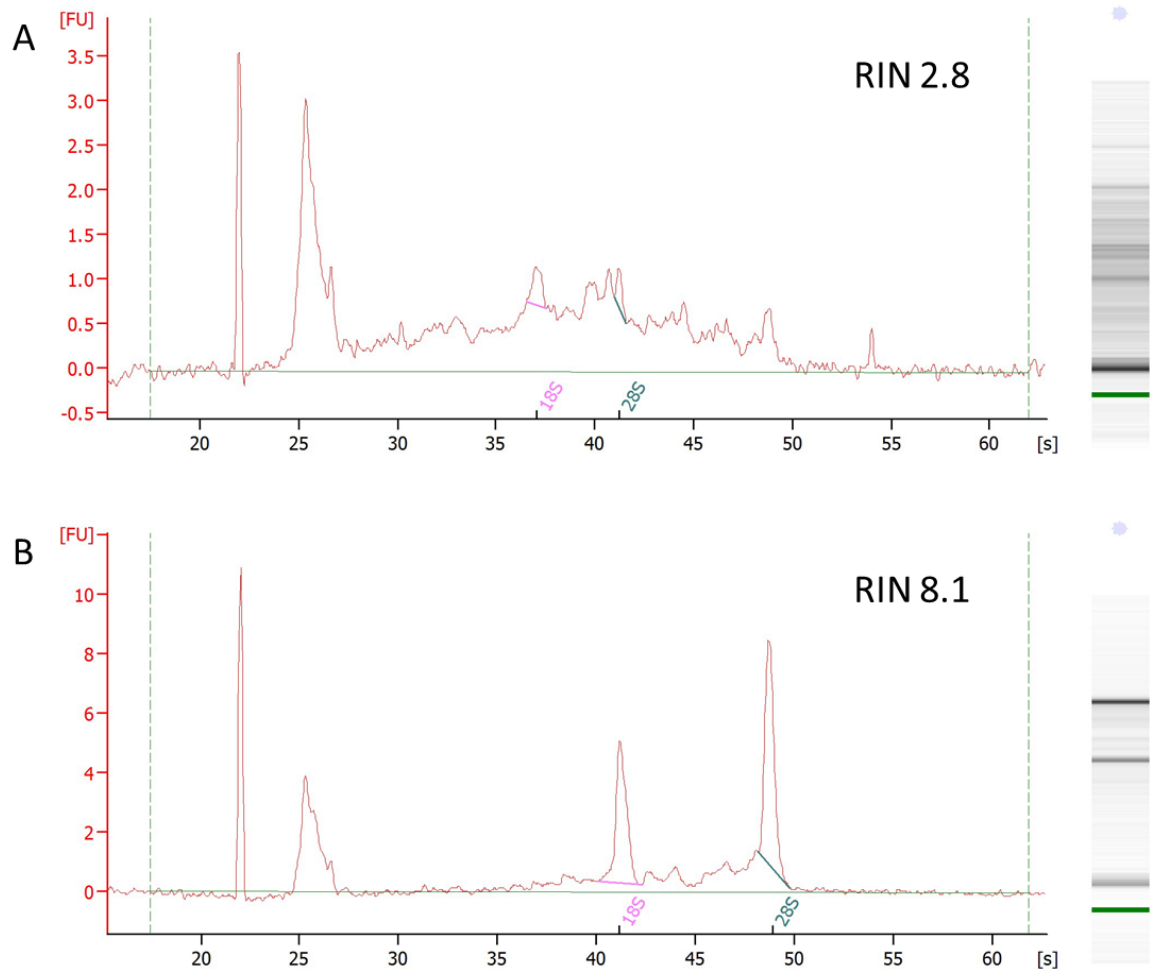


**Figure 5-5. Assessment of mRNA quality from the microdissected compact node samples. A) Sample before microdissection and RNA extraction were optimized. There are no clear peaks of mRNA for 18S and 28S indicating poor mRNA quality. B) Sample after microdissection and extraction were optimized. Clear peaks for 18S and 28S are seen. RIN - RNA integrity number; range 0- 10 with 10 indicating the best RNA quality.**

### **5.2.6.2 Final protocol for AV node dissection and RNA extraction**

The entire AV node was processed within a single day with the process from start to finish taking approximately 8 hours. The slides were stained with a haematoxylin and eosin stain and left submerged in 100% alcohol at room temperature. Each slide was microdissected. Tissue samples from each region were dissected using separate surgical needles and placed directly into 300  $\mu$ l of lysis buffer from the Mirvana kit and stored on ice. When all the regions of the AV node had been dissected, extraction was performed as per manufacturer's guidelines for the Mirvana kit. The sample was treated with TurboDNase as per manufacturer's guidelines. RNA concentration was measured with the Qubit <sup>®</sup> fluorometer. RNA samples were stored in the -80°C freezer for processing at a later date.

### 5.2.7 Reverse transcription

Reverse transcription from RNA to complementary DNA (cDNA) is a crucial step in RT-qPCR and can be a source of technical variability within the experiment. It requires the combination of the enzyme reverse transcriptase, deoxynucleotide triphosphates (dNTPs) and primers. There are three main priming strategies that can be employed for RT:<sup>179, 184</sup>

- Sequence specific primers – primers that are specific for the targets being investigated.
- Oligo-DTs – primers containing repeated deoxy-thymine nucleotides which utilise the poly-A tail at the 3' end of mRNA to synthesize cDNA from the entire mRNA molecule.
- Random hexamers – multiple combinations of nucleotides designed to synthesise cDNA from multiple regions within an mRNA molecule.

A random hexamer priming strategy was chosen as this has the potential to limit the variability in results caused by degraded mRNA. The SuperScript VILO mastermix (Life technologies, USA) kit based on the SuperScript III reverse transcriptase enzyme was chosen.

It is recommended that the same amount of mRNA is reverse transcribed in each reaction to standardise experimental conditions and minimise the variability introduced. For this condition to be met, all samples need to be diluted to the concentration of the least concentrated sample within an experiment. There was concern about the low concentrations of mRNA generated by the microdissection process and therefore we elected to dilute all mRNA to a concentration of 1 ng/ $\mu$ l, but, if samples had a starting concentration of less than 1 ng/ $\mu$ l the undiluted samples were used. The volume of RNA in the reverse transcription reaction is 16  $\mu$ l and therefore a total of 16 ng of RNA was transcribed for the higher concentration samples and a total RNA of 16 x the starting concentration of RNA was used for the lower concentration samples. The starting concentration and dilutions are listed in the Appendix (Table A-2). The atrial and ventricular samples had consistently higher concentrations. This allowed for the creation of another reverse transcription reaction from the same sample with a total mRNA of 160 ng.

Twenty microlitre reaction volumes were used and reverse transcription was performed according to the manufacturer's instructions with the exception that the reaction was

incubated at 42°C for 120 min in accordance with the manufacturer's suggestion that this may increase the yield of cDNA.

### 5.2.8 Quantitative polymerase chain reaction

Quantitative polymerase chain reaction (qPCR) involves the combination of an exponential increase in DNA during thermal cycling and a system for detecting the amplified DNA in real time.

The exponential increase in DNA targets is achieved using a pair of primers that target both ends of a region of interest of DNA. Each primer is complementary to a different strand of the double stranded DNA (dsDNA). During thermal cycling the dsDNA is denatured and cleaved. As the temperature is lowered the primers anneal to the DNA strands and initiate replication using a DNA polymerase enzyme, which synthesises a new complementary strand of DNA from the dNTPs. A new cycle is started when the temperature is raised and the process repeats. The region of interest between the two targets, termed the amplicon, doubles with each cycle until the reagents needed for the reaction are consumed.<sup>185</sup>

Detection of the amplicon can be achieved using two systems, SybrGreen and hydrolysis probes. In the SybrGreen system the fluorescent dye emits a signal when it is interpolated within a dsDNA molecule and therefore the fluorescence is proportional to the quantity of dsDNA present.<sup>179, 184</sup> This system is very sensitive but as the SybrGreen dye will generate a signal with any dsDNA present it is less specific and may give misleading results in the presence of genomic DNA or primer dimers.<sup>179, 184</sup> The hydrolysis probe system uses a target sequence combined with a fluorescent tag/quencher complex. The target sequence binds to a specific region of interest within the amplicon and the probe is then hydrolysed by the action of DNA polymerase cleaving the fluorescent tag from the quencher region and thus enabling the detection of fluorescence from the fluorescent tag. This means that the fluorescence detected is proportional to the quantity of amplicon present. This system is more specific than the SybrGreen based detection system.<sup>179, 184</sup>

### 5.2.9 The TaqMan microfluidic card system

A recent innovation in the performance of RT-qPCR is the TaqMan low density array card (TLDA) (Life Technologies, USA). This card uses a system of microfluidic channels to divide an aliquot of the PCR reaction solution into 48 wells which are preloaded by the

manufacturer with primer sets for gene targets. These targets may be chosen by the experimenter in a custom array and more than one aliquot of the same sample can be used allowing gene targets in multiples of 48 to be rapidly and accurately assessed for a single sample.<sup>186</sup>

### 5.2.10 Endogenous controls

The results of RT-qPCR may be affected by variation due to technical factors including pipetting technique, variable reverse transcription efficiency and variable amplification efficiencies. Normalisation to an internal reference gene is a common method to correct for this variation, but, for this technique to have validity it is important an endogenous control gene is selected that is stably expressed in all the tissues being studied and is not affected by the experimental conditions (i.e. by the development of PH in this study).<sup>179,</sup>

<sup>184</sup> In order to choose a reference gene that met these conditions an experiment was performed using the TaqMan® Rat Endogenous Control Arrays containing 18 commonly used endogenous control genes (Table 5-3).

Gene	Protein
18S rRNA	(Ribosomal RNA)
Actb	B-actin
Arbp	Ribosomal protein, large, P0
B2M	$\beta$ -2 microglobulin
Gapdh	glyceraldehyde-3-phosphate dehydrogenase
Gusb	$\beta$ -glucuronidase
Hmbs	hydroxymethylbilane synthase
Hprt	hypoxanthine guanine phosphoribosyl transferase
Pgk1	Protein PKG-1
Ppia	peptidylprolyl isomerase A (cyclophilin A)
Ppib	peptidylprolyl isomerase B (cyclophilin B)
Rplp2	ribosomal protein, large P2
Tbp	TATA box binding protein
Tfrc	transferrin receptor
Ubc	ubiquitin C
Ywhaz	tyrosine 3-monooxygenase/tryptophan 5-monooxygenase activation protein, zeta

Table 5-3. The gene names and proteins encoded by the 18 targets included on the endogenous control array.

Sixteen additional cDNA samples were created by reverse transcribing a second mRNA samples (total mRNA 16 ng) from mRNA from samples with a relatively high mRNA concentrations as described in section 5.2.7. These samples included all six regions of the AV node with samples from both control and MCT rats (Table 5-4).

	Atrium	Transitional tissue	Inferior nodal extension	Compact node	Penetrating bundle	Ventricle
Control	3	1	0	1	0	2
MCT	2	1	1	1	1	3

**Table 5-4. Sample numbers used in the rat endogenous control array experiments.**

These sixteen samples were used with the Rat Endogenous Control Array cards. The cards were prepared by combining 20 µl of the cDNA reaction with 35 µl nuclease-free water and 55 µl 2x Master Mix (Life Technologies, USA). 100 µl of this reaction mixture was added to each reservoir of the TLDA card. The TLDA cards were centrifuged using a Sorvall centrifuge (Thermoscientific, USA) with a custom bucket and card holder at 1200 rpm for two periods of 1 min. The cards were sealed using the TaqMan Array Micro Fluidic Card Sealer (Life Technologies, USA) and the fill reservoirs were trimmed. The cards were inserted into the ViiA 7 Real-Time PCR system (Life Technologies, USA) and underwent thermal cycling for 40 cycles (Table 5-5).

Step	Hold		Cycle (14 Cycles)	
			Denature	Anneal/Extend
Temperature	50°C	95°C	95°C	60°C
Time	2 min	10 min	15 sec	1 min

**Table 5-5. ViiA 7 Real-Time PCR settings for thermal cycling during PCR.**

The results of this experiment were analysed using the Genorm algorithm contained within the RealTime Statminer (Integromics, S.L., USA) software package. This algorithm uses the principle that if control genes are stably expressed across tissue samples then the ratio between them will remain constant. It then analyses multiple putative control genes using stepwise elimination of the control genes until the most stably expressed combination of control genes is determined.<sup>187</sup> The Genorm algorithm is demonstrated that the most stable combination of endogenous control genes was B2M ( $\beta$ -2 microglobulin) and PKG1. B2M plays a role in the major histocompatibility complex 1, PKG-1 plays a role in the phosphoprotein glycolysis (rat genome database). There are no reports of MCT or PH affecting either of these genes.

### 5.2.11 Gene targets

The TLDA card system allows for the choice of targets using TaqMan (Life Technologies, USA) hydrolysis probes. These are selected from a library of predesigned probes, which

have the advantage of being previously validated via the company but the disadvantage that the primer sequences are not available to the researcher for further investigation.

We selected a strategy of 96 targets, which included markers of fibrosis and inflammation, growth factors and other miscellaneous targets well as the main focus of this study. This study is focussed on expression of the key genes (ion channels and transporters, connexins, intracellular Ca<sup>2+</sup> handling proteins and autonomic receptors) that determine the cardiac action potential and its impulse generation and conduction. A list of all 96 targets is included in the Appendix. This chapter will focus only on the targets of interest to this study, which are shown in Table 5-7.

### 5.2.12 Preamplification of cDNA

The TLDA based system recommends a minimum starting input of 30 ng of RNA, but, the maximum concentration of RNA extracted from the microdissected samples from the AV node regions was 16 ng. Provisional experiments using the cDNA samples were performed using a SYBR-green based detection system looking for targets with known high expression in the working myocardium and nodal tissues including 18S, 28S, Cx43 and HCN4. These experiments showed limited amplification, reinforcing concerns that low starting concentrations of RNA may limit our ability to quantify targets using the TLDA cards. In light of these concerns, a preamplification process was performed.<sup>188, 189</sup>

Preamplification uses the same principles as PCR requiring the combination of specific primer sets for the genes of interest (TaqMan PreAmp pool, Life Technologies, USA), dNTPs and DNA polymerase followed by thermal cycling with an exponential amplification of the amplicon. The benefit of performing preamplification is that the exponential increase in amplicons occurs for all targets before the mRNA is diluted and divided into wells in the TLDA cards. This reduces the stochastic variability associated with low copy numbers of cDNA.<sup>188, 189</sup> The process of preamplification has been shown to increase the sensitivity of the TLDA system in several tissues, but has not previously been used with heart tissue.<sup>188, 189</sup>

Gene name	Protein encoded	Brief description
<b>Inward currents</b>		
Scn1a-Rn00578439_m1	Nav1.1	Alternative Na <sup>+</sup> channel responsible for $I_{Na}^{190}$
Scn5a-Rn00565502_m1	Nav1.5	Na <sup>+</sup> channel responsible for $I_{Na}^{43}$
Scn10a-Rn00568393_m1	Nav1.8	(uncertain)
Scn1b-Rn00441210_m1	Navβ1	β-subunit of Na <sup>+</sup> Channel <sup>43</sup>
Cacna1c-Rn00709287_m1	Ca <sub>v</sub> 1.2	α-subunit of the L type Ca <sup>2+</sup> responsible for $I_{Ca,L}^{43}$
Cacna1d-Rn00568820_m1	Ca <sub>v</sub> 1.3	
Cacna1g-Rn00581051_m1	Ca <sub>v</sub> 3.1	α-subunit of the T type Ca <sup>2+</sup> responsible for $I_{Ca,L}^{43}$
Cacna1h-Rn01460348_m1	Ca <sub>v</sub> 3.2	
Cacna2d1-Rn01442580_m1	Ca <sub>v</sub> α2δ1	(uncertain)
Cacna2d2-Rn00457825_m1	Ca <sub>v</sub> 2δ2	(uncertain)
Cacnb2-Rn00587789_m1	Ca <sub>v</sub> β2	(uncertain)
Hcn1-Rn00670384_m1	HCN1	Hyperpolarisation cation channel responsible for $I_f^{43}$
Hcn2-Rn01408572_mH	HCN2	
Hcn4-Rn00572232_m1	HCN4	
Clcn2-Rn00567553_m1	CLC-2	Stretch activated Cl <sup>-</sup> channels thought to play a role in pacemaking <sup>191, 192</sup>
Clcn3-Rn01535195_m1	CLC-3	
<b>Outward currents</b>		
Kcna2-Rn02769834_s1	Kv1.2	α-subunit responsible for $I_{K,slow}^{52}$
Kcna4-Rn02532059_s1	Kv1.4	α-subunit responsible for $I_{to,f}^{52}$
Kcna5-Rn00564245_s1	Kv1.5	$I_{Kur}^{52}$
Kcnb1-Rn00755102_m1	Kv2.1	α-subunit responsible for $I_{K,slow}^{52}$
Kcnd2-Rn00581941_m1	Kv4.2	$I_{to,f}^{52}$
Kcnd3-Rn00709608_m1	Kv4.3	
Kcnh2-Rn00588515_m1	ERG1	α-subunit responsible for $I_{K,r}^{52}$
Kcnq1-Rn00583376_m1	K <sub>V</sub> LQT1	$I_{K,s}^{52}$
Kcnj2-Rn00568808_s1	K <sub>ir</sub> 2.1	α-subunit responsible for $I_{K1}^{52}$
Kcnj12-Rn02533449_s1	K <sub>ir</sub> 2.2	
Kcnj14-Rn00821873_m1	K <sub>ir</sub> 2.4	Possibly $I_{K1}^{52}$
Kcnj3-Rn00434617_m1	K <sub>ir</sub> 3.1	α-subunit responsible for $I_{K,ACH}^{193}$
Kcnj5-Rn01789221_mH	K <sub>ir</sub> 3.4	
Kcnj8-Rn01492857_m1	K <sub>ir</sub> 6.1	α-subunit responsible for $I_{K,ATP}^{193}$
Kcnj11-Rn01764077_s1	K <sub>ir</sub> 6.2	
Abcc8-Rn00564778_m1	SUR1	Regulatory subunit of $I_{K,ATP}^{193}$
Abcc9-Rn00564842_m1	SUR2	
Kcnip2-Rn01411451_m1	KChIP2	Auxiliary subunit to $I_{to}^{52}$
Kcne1-Rn02094595_s1	minK	Auxiliary subunit to $I_{K,r}$ and $I_{K,s}^{52}$
KCNK1-Hs00158428_m1	TWIK1	Two-pore Domain Potassium Channels <sup>194, 195</sup>
Kcnk3-Rn00583727_m1	TASK1	

Table 5-6. The genes of interest, the proteins they encode for and a brief description of their function.

Gene name	Protein encoded	Brief description
<b>Intracellular Ca<sup>2+</sup> cycling</b>		
Ryr2-Rn01470303_m1	RyR2	Ryanodine receptor <sup>56</sup>
Ryr3-Rn01328415_g1	RyR3	
Slc8a1-Rn00570527_m1	NCX1	Na <sup>+</sup> /Ca <sup>2+</sup> exchanger <sup>56</sup>
Atp2a2-Rn00568762_m1	SERCA2a	Responsible for moving Ca <sup>2+</sup> out of the cytosol into the sarcoplasmic reticulum <sup>56</sup>
Pln-Rn01434045_m1	Phospholamban	Responsible for regulation of SERCA activity <sup>56</sup>
Atp2b1-Rn01502902_m1	PMCA1	Membrane pump responsible for removal of Ca <sup>2+</sup> from the cell <sup>56</sup>
Casq2-Rn00567508_m1	Calsequestrin 2	Ca <sup>2+</sup> binding protein in the sarcoplasmic reticulum <sup>56</sup>
Sln-Rn02769377_s1	Sarcolipin	Responsible for regulation of SERCA activity <sup>196</sup>
<b>Connexins</b>		
Gjd3-Rn01771737_s1	Cx30.2	Ultra-small conductance connexin <sup>61</sup>
Gja1-Rn01433957_m1	Cx43	Medium conductance connexin <sup>61</sup>
Gja5-Rn00570632_m1	Cx40	High conductance connexin <sup>61</sup>
Gja7-Rn01750705_m1	Cx45	Low conductance connexin <sup>61</sup>
<b>Ion channel transporters</b>		
Atp1a1-Rn01533986_m1	Na <sup>+</sup> /K <sup>+</sup> ATPase $\alpha$ 1 subunit	Na <sup>+</sup> /K <sup>+</sup> pump <sup>43</sup>
Atp1a2-Rn00560789_m1	Na <sup>+</sup> /K <sup>+</sup> ATPase $\alpha$ 2 subunit	
Atp1a3-Rn00560813_m1	Na <sup>+</sup> /K <sup>+</sup> ATPase $\alpha$ 3 subunit	
Atp1b1-Rn00565405_m1	Na <sup>+</sup> /K <sup>+</sup> ATPase $\beta$ 1 subunit	$\beta$ subunit of Na <sup>+</sup> /K <sup>+</sup> pump <sup>43</sup>
Slc9a1-Rn00561924_m1	Na <sup>+</sup> /H <sup>+</sup> transporter	Na <sup>+</sup> /H <sup>+</sup> transporter <sup>43</sup>
<b>Autonomic regulators</b>		
Adra1a-Rn00567876_m1	Adrenergic receptor, 1a/1c	$\alpha$ -adrenergic receptor
Adra1b-Rn01471343_m1	Adrenergic receptor, $\alpha$ 1b	$\alpha$ -adrenergic receptor
Adrb1-Rn00824536_s1	Adrenergic receptor, $\beta$ 1	$\beta$ -adrenergic receptor
Adrb2-Rn00560650_s1	Adrenergic receptor, $\beta$ 2	$\beta$ -adrenergic receptor
Chrm2-Rn02532311_s1	M2 muscarinic receptor	Muscarinic receptor
Adora1-Rn00567668_m1	Adenosine A1 receptor	Adenosine receptor

Table 5-7. The genes of interest, the proteins they encode for and a brief description of their function.

Before preamplification can be performed the targets on the TLDA cards must be selected allowing production of a TaqMan PreAmp Pool (Life technologies, USA) which contains primer sets for all of the targets on the TLDA cards (except 18S which is assumed to be of high abundance).

Preamplification was prepared as per manufacturer's guideline. 4 µl of cDNA was combined with 4 µl of custom TaqMan PreAmp Pool and 8 µl of TaqMan PreAmp Master Mix (2X) (Life Technologies, USA). Thermal cycling was performed on the Veriti 96-Well Fast Thermal Cycler (Life Technologies, USA) for 14 cycles (Table 5-8). The resulting preamplification product were stored at -80°C until they were quantified using the TLDA cards.

Step	Hold	Cycle (14 Cycles)		Hold	Hold
		Denature	Anneal/Extend		
Temperature	95°C	95°C	60°C	99.9°C	4°C
Time	10 min	15 sec	4 min	10 min	Until storage at -80°C

Table 5-8. Veriti 96-Well Fast Thermal Cycler settings for preamplification.

### 5.2.13 Preparation of the TaqMan Array Micro Fluidic Card

The preamplified samples were prepared for the TLDA cards by combining 7 µl of the Preamplification product with 103 µl nuclease-free water and 110 µl 2x Master Mix (Life Technologies, USA). 100 µl of the reaction mixture was added to two reservoirs of the TLDA card (allowing assessment of 96 targets).

The atrial and ventricular samples with a total mRNA of 160 ng did not undergo preamplification. These samples were prepared for the TLDA cards by combining 20 µl of the cDNA reverse transcription product with 90 µl nuclease-free water and 110 µl 2x Master Mix (Life Technologies, USA). 100 µl of the reaction mixture was added to two reservoir of the TLDA card.

The TLDA cards were centrifuged using a Sorvall centrifuge with a custom bucket and card holder at 1200 rpm for two periods of 1 min. The cards were sealed using the TaqMan Array Micro Fluidic Card Sealer and the fill reservoirs were trimmed. The cards were inserted into the ViiA 7 Real-Time PCR system and underwent thermal cycling for 40 cycles with the same settings as the endogenous control array cards (Table 5-5). The amplification plots were exported to ExpressionSuite for analysis.

### **5.2.14 Final protocol for RT-qPCR**

Animals were sacrificed and an AV node dissection was prepared. The sample was frozen and sectioned into 50  $\mu\text{m}$  sections. Cx43 and HCN4 immunolabelled sections were created for every 300  $\mu\text{m}$  of tissue. Masson's trichrome sections were created for every 300  $\mu\text{m}$  of tissue. The images from the immunolabelled and Masson's trichrome slides were used to create an AV node 'map'. Haematoxylin and Eosin stains were performed. Samples were microdissected and added immediately into the lysis buffer stored on ice. RNA was extracted using the Mirvana extraction kit. The sample was treated with TurboDNase. RNA concentration was measured using the Qubit fluorometer. RNA was reverse transcribed to cDNA using SS vilo mastermix. cDNA was preamplified using the custom TaqMan pools. cDNA was quantified using the TLDA card system with 96 targets.

### **5.2.15 Control samples**

Control samples were run using a water control and a no-reverse transcriptase enzyme (no-RT) control for mRNA samples both before and after preamplification. The SuperScript VILO mastermix used for the reverse transcription of the experimental samples is 'pre-mixed' with SuperScript III (the reverse transcription enzyme) meaning that it is difficult to use SuperScript VILO mastermix in no-RT experiments. The SuperScript III First-Strand synthesis system (Life technologies, USA) is not 'pre-mixed' meaning the reagents can be prepared as for a standard reverse transcription reaction but without the addition of SuperScript III, therefore the SuperScript III First-Strand synthesis system was used for the no-RT control experiment. Samples were processed as per manufacturer's guidelines using random hexamers but the SuperScript III was replaced with RNA-free water.

### 5.2.16 Data analysis

Data were analysed using a combination of ExpressionSuite and RealTime Statminer software. ExpressionSuite software allows the results of the PCR runs for all the TLDA cards to be loaded simultaneously.<sup>184</sup> The amplification curves were assessed and samples that had failed to amplify for all or most targets were omitted (on the assumption that there was a problem with sample preparation) (Figure 5-6).

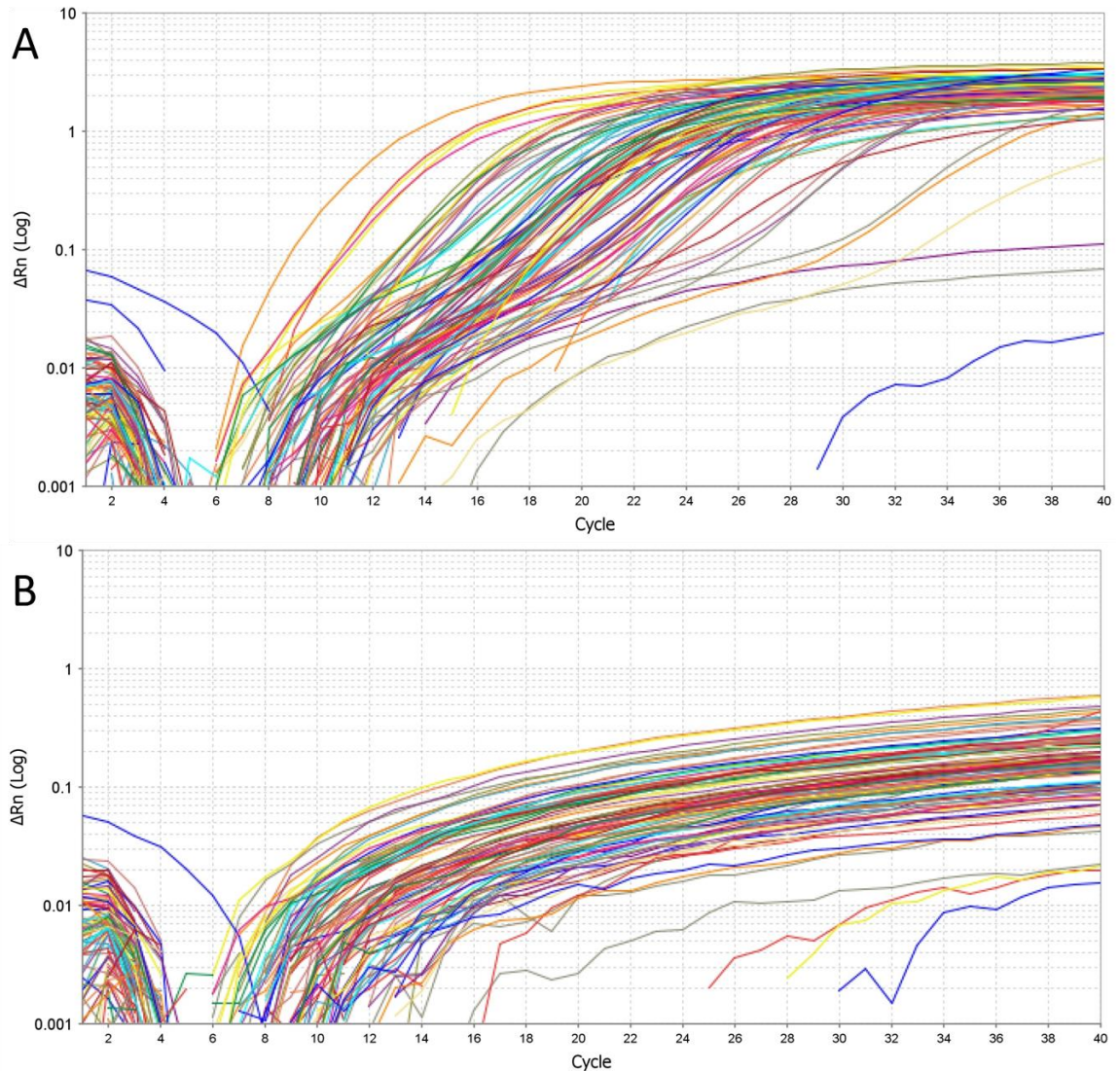


**Figure 5-6.** qPCR amplification plots for all samples.  $\Delta Rn$  is the change in fluorescence due to the PCR reaction (current fluorescence – baseline fluorescence). A) Sample from the compact node showing good amplification with the majority of targets amplifying well. There are three targets which do not amplify which will have an undetermined  $C_q$  value which is replaced with 40. B) Sample from the compact node of a different rat. No targets have amplified indicating a failure of sample preparation; the entire sample was omitted from further analysis.

A threshold of fluorescence can be selected and the fractional cycle at which this fluorescence level is exceeded can be recorded from the x-axis. This is commonly called the threshold cycle ( $C_t$ ), but recent guidance suggests the phrase quantification cycle ( $C_q$ )

be used. It is important to set the threshold above the baseline fluorescence level but within fluorescence levels reached during the exponential phase of the PCR reaction. A graph with cycle number on the x-axis and log (fluorescence) on the y-axis yields a linear increase in log (fluorescence) during the exponential phase of the reaction and aids setting the detection threshold at the correct level (Figure 5-7). It is important that the threshold is kept constant when comparing the same target between different samples.<sup>179, 184</sup>

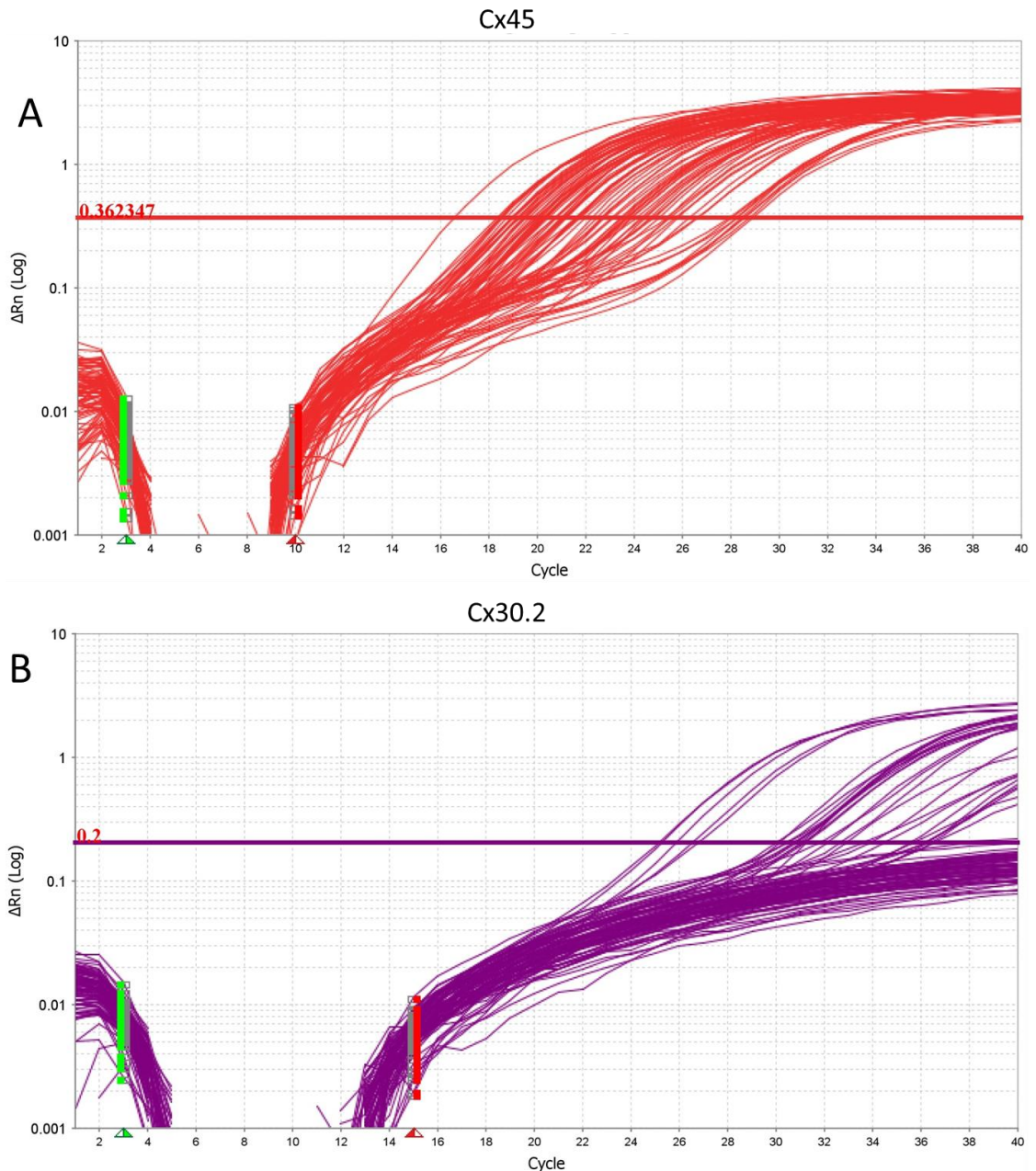


**Figure 5-7. Determining  $C_q$  values for individual targets.** With  $\log(\Delta Rn)$  plotted against cycle number there is a linear amplification phase. The green and red markers represent the beginning and end of the baseline. As long as the detection threshold is placed within this linear phase the difference in  $C_q$  between each sample will be the same (because the linear amplification plots are parallel to each other). A) Amplification curves Cx45. There is a relatively high abundance and therefore all samples cross the detection threshold and will have a relatively low  $C_q$ . B) Amplification curves for Cx30.2. There is a lower abundance and therefore the  $C_q$  values are higher. Some samples do not cross the detection threshold and will therefore not generate a  $C_q$  value, but this has been reported as 40 in this study.

The amplification curves for all samples of a given target were assessed simultaneously and appropriate threshold and  $C_q$  settings applied. After the data had been assessed the  $C_q$  values were calculated for all targets. If a target had not amplified then it did not cross the cycle threshold and therefore the  $C_q$  values were undetermined. Where individual targets had not amplified in a sample where the majority of targets had amplified these undetermined values were replaced with a  $C_q$  value of 40 to represent an assumed very low abundance of the target within that sample (if all or most of the targets had failed to amplify the entire sample had already been omitted as described above) (Figure 5-7).<sup>184</sup>

The  $C_q$  values were analysed with the RealTime Statminer software. This software is specifically designed to handle  $C_q$  data generated from qPCR experiments. The software was informed which of the target genes to use as the endogenous controls and  $\Delta C_q$  was calculated using the formula:<sup>179, 184</sup>

$$\Delta C_q = C_q \text{ endogenous control} - C_q \text{ target}$$

It can be seen from this calculation that a positive  $\Delta C_q$  represents low abundance of the target mRNA and a negative  $\Delta C_q$  represents high abundance of the target mRNA. Assuming an efficiency of 100% (i.e. the amplicon doubles with each PCR cycle) the relative quantification (RQ) can be calculated using the formula:<sup>179</sup>

$$RQ = 2^{-\Delta C_q}$$

With this formula a value of greater than 1 means a greater expression of the target gene than the endogenous control genes and a value of less than 1 means a lower expression of the target gene than the endogenous control genes.

The TLDA microfluidic cards are able to generate large amounts of data with multiple targets and multiple regions of interest. Several specific statistical parameters have been developed for comparing the data generated by gene expression analysis. Limma is a statistical package that allows robust comparison of gene expression even when the sample numbers are small by using data from the variance of all the targets studied to improve the estimates of the variance of each target.<sup>191, 197</sup> The performance of the limma test has been compared with several other statistical methods to analyse gene expression data test and has been found to perform well.<sup>195, 198</sup> The limma package is included in the RealTime Statminer statistical package and has been used for the analysis of all qPCR results.

A potential problem with testing multiple regions with many targets is the possibility of multiple comparisons leading to a number of type I statistical errors (i.e. false positives). Several different approaches to this problem have been suggested; some authors argue that correcting for multiple testing leads to a reduction in the ability to detect real differences between groups (i.e. a type II error) and therefore no corrections should be applied.<sup>193</sup> Other authors use a variety of different algorithms to reduce the chance of a type I error at the expense of increasing the risk of a type II error. The Benjamini-Hochberg correction uses an approach of estimating the false discovery rate (FDR), i.e. the proportion of significant results that are false positives. Using the Benjamini-Hochberg corrected P values a 0.1 and 0.2 correspond to a FDR of 10 and 20% respectively.<sup>122, 194</sup> The value used as the cut off for 'statistical significance' is chosen arbitrarily in a manner analogous to the choice of choice of 0.05 as the P value for 'standard' statistical tests. Using our data it was seen that an FDR corrected P value of less than 0.2 gave broadly similar results to an uncorrected P value of 0.05. For example, in the atrium an FDR corrected P value of 0.2 gives 23 significant results (using the limma test) and the uncorrected P value of less than 0.05 gives of 19 significant results (using the limma test); there were no instances when the uncorrected P value was significant and the FDR was not significant. The corrected P value using the Benjamini-Hochberg calculation was used for all analysis of the mRNA data with two levels of statistical significance, a FDR corrected P value cut-of for significance of 0.05 and 0.2.

The techniques described above were used to compare the same targets across different regions within the control group and for the same regions between the control and MCT groups. Comparisons between two different targets in the same tissue type is made more difficult by the variability in several of the processes key to quantifying mRNA in the qPCR process, for example the efficiency of the reverse transcription step, the efficiency of the primers and the use of different detection thresholds for different targets.

Nevertheless it has been suggested that tentative conclusions about different levels of expression can be made between targets if there is a greater than 10 fold difference in the expression of two targets in the same tissue type.<sup>72</sup>

## 5.3 Results

There was an appropriate lack of amplification for the water, and no-RT control samples.

### 5.3.1 Assessment of preamplification

The samples with a total mRNA of 160 ng that had not undergone preamplification were compared with the samples that had a total mRNA of 16 ng and had been preamplified in order to assess whether preamplification had affected the results of the PCR experiment. In the ideal situation, the  $\Delta C_q$  of target within the sample would be unchanged by preamplification as both the endogenous control amplicon and target amplicon should have increased by the same amount and therefore the  $\Delta C_q$  of the unamplified sample is equal to the  $\Delta C_q$  of the preamplified sample. Figure 5-8 shows the relationship observed. The results were significantly correlated ( $P < 0.0001$ ) with an  $R^2$  value of 0.61 (Figure 5-8). Looking at the relationship it can be seen that the majority of the deviation from a 1:1 relationship occurs when the  $\Delta C_q$  values are greater than 0 in the unamplified samples, i.e. when the starting concentration of the mRNA of interest is low, particularly when looking at the unamplified samples. The absolute values for the  $C_q$  for then non-amplified samples were higher than for the preamplified samples despite their 10 times greater starting concentration. In this context it appears that the very low concentrations of mRNA for the targets in the unamplified samples were at the limits of detection of RTqPCR (despite starting with 160 ng of mRNA) and therefore inaccurate quantification of these targets has caused deviation from the 1:1 relationship. These findings support the need for preamplification with the low concentrations of mRNA in the microdissected tissue samples. The findings also support the validity of the preamplification methodology. Unfortunately because there were no samples with high enough concentrations of mRNA to allow the reverse transcription of 160 ng total mRNA samples in the nodal tissues it was not possible to compare the preamplified and unamplified samples from the nodal tissue.

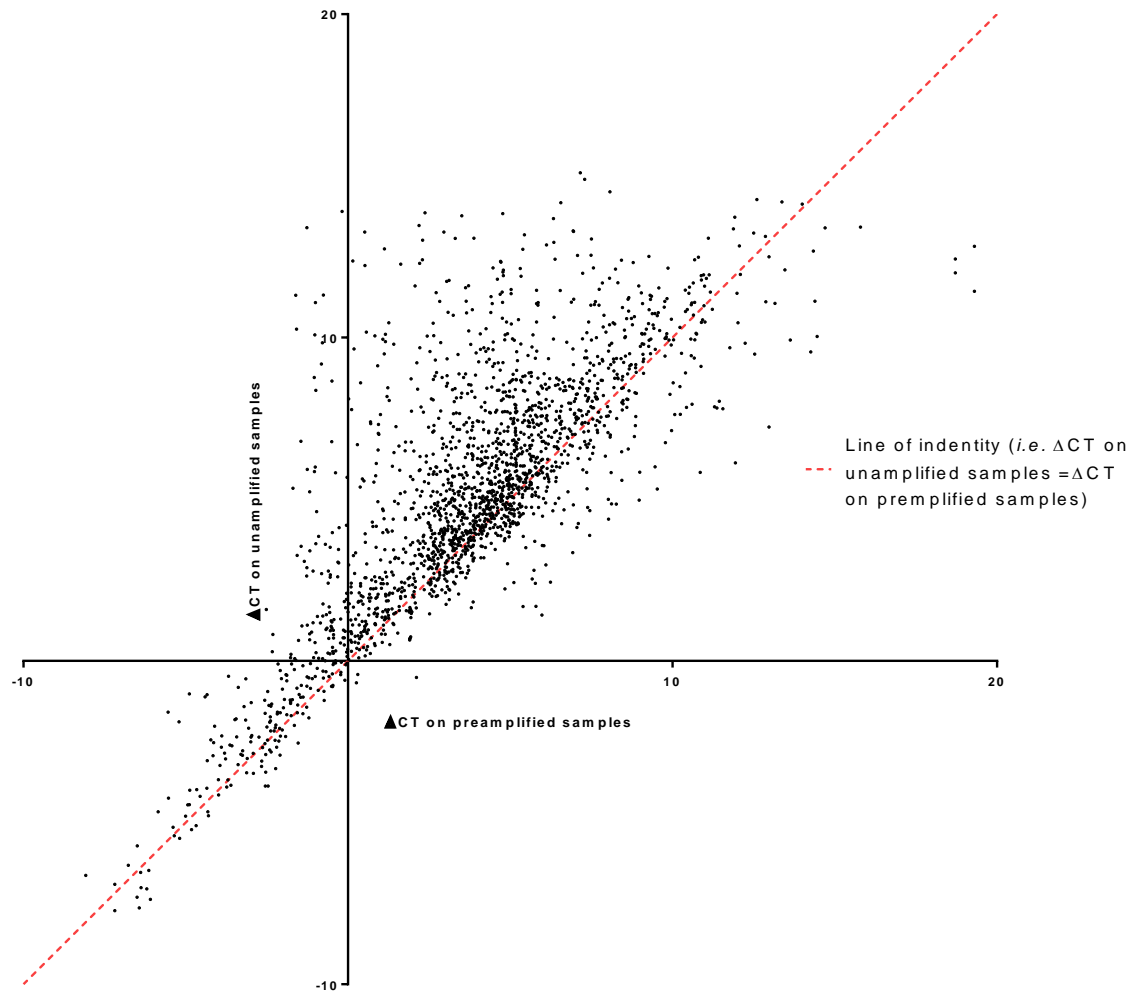


**Figure 5-8.** Correlation of  $\Delta\text{CT}$  from preamplified and unamplified samples from the atrium and ventricle of all rats. Linear regression analysis showed a non-zero gradient of 0.84 ( $P < 0.001$ ),  $R^2 = 0.62$ .

### 5.3.2 Normalisation strategy and interpretation of unamplified samples

The choice of normalisation strategy will affect  $\Delta C_q$  values for all the targets. The endogenous control experiment suggested that B2M and PKG-1 were the most stably expressed across the different tissue regions and not affected by MCT administration. As described above the pooled preamplification primers could only be purchased after the design of the TLDA card had been finalised and therefore the endogenous control genes needed to be selected before preamplification was performed. This led to concern that the preamplification process may distort quantification of either B2M or PKG-1 meaning that they were no longer optimal endogenous controls. To investigate this potential difficulty the Genorm algorithm was run again on the five potential endogenous control genes on the final TLDA card design (18S, B2M, GAPDH, HPRT, PKG-1). This time it suggested that

B2M and HPRT were the optimal endogenous controls, although, this was determined using fewer possible combinations than with the endogenous array experiment.

When a target does not amplify for an individual sample it may be due to mRNA levels being below the limits of detection or due to technical problems with the PCR reaction. As described above if the majority of targets did not amplify in a sample it was assumed to be a technical problem with the sample and this sample was excluded from further analysis. If a target was noted to have consistently high  $C_q$  values and sometimes did not amplify in a sample where other targets had amplified normally it was assumed that this was due to low concentrations of the target within that sample. If all samples that had not amplified due to low concentrations were excluded from analysis this would lead to a systematic exclusion of low concentration samples which could distort the data.

In light of the two concerns outlined above data analysis was compared using normalisation with three strategies, either B2M and HPRT; B2M and PKG-1 or all targets combined as the endogenous control. For each normalisation strategy two methods of dealing with high  $C_q$  values were used; either all  $C_q$  values above 38 were omitted or all samples were included using a  $C_q$  value of 40 for individual targets that did not amplify within a sample. These six different strategies were used to calculate an adjusted P value (using the limma test) comparing the control and MCT rats for each target in each tissue type. The results of these six strategies are shown Figure 5-9. They reveal that all six strategies are qualitatively similar, i.e. where one strategy gave a low P value for a given target in a given tissue region the other five strategies also tended to give a low P value and vice versa for high P values. This finding supports the robustness of the analysis technique and implies that any of the six strategies could be chosen without a major distorting effect on the results.

It was decided to perform all subsequent analyses using a strategy of normalising to the endogenous control targets of B2M and PGK-1 determined in the endogenous control target experiment as these two targets were chosen after analysis of a panel of 18 genes improving the performance of the Genorm analysis. It was also decided that all  $C_q$  values should be included and a  $C_q$  value of 40 was used when an individual target had not amplified despite the overall sample amplifying well to avoid the problem of systematically omitting the data from samples with low concentration of targets.

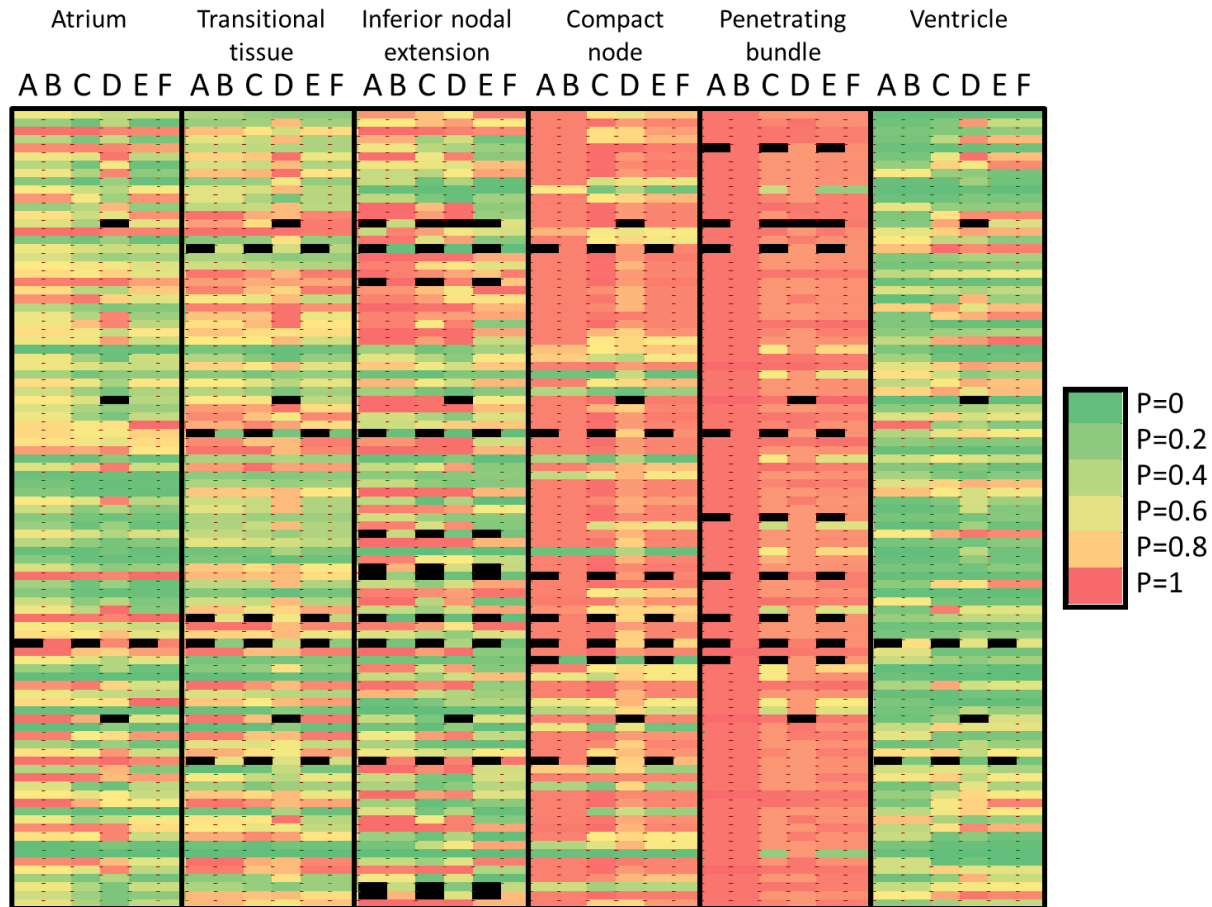


Figure 5-9. Comparison of six different normalisation strategies for all six regions within the AV node. Each target is represented as a horizontal line. The FDR adjusted P value comparing control and MCT rats for significant differences is represented on a colour scale for each target with each normalisation strategy for each tissue region. The black boxes represent missing data due to the exclusion of targets with a CT of greater than 38. Within each tissue region there are qualitatively similar adjusted P values for the different targets demonstrated by a consistent colour bar, but, between tissue regions there are different colour bars. A) P values using B2M and HPRT and excluding  $C_q$  values of  $>38$ , B) P values using B2M and HPRT and including  $C_q$  values. C) P values using normalisation against all targets and excluding  $C_q$  values of  $>38$ , D) P values using normalisation against all targets and including all  $C_q$  values, E) P values using B2M and PKG1 and excluding  $C_q$  values of  $>38$ , F) P values using B2M and PKG-1 and including all  $C_q$  values.

### 5.3.3 Relative expression of mRNA targets

There were a total of nine control and eight MCT treated rats used in the experiment, but all the data from one control rat were omitted as none/very few of the targets amplified for all the regions suggesting a problem with the tissue processing (Figure 5-6). Individual samples from single tissue regions were also omitted due to technical failures in the processing steps or poor amplification across all the targets. The final of experimental rats in each group for each region of the AV node are shown in Table 5-9.

	<b>Control</b>	<b>MCT</b>
Atrium	7	7
Transitional tissue	8	6
Inferior nodal extension	8	8
Compact node	8	7
Penetrating bundle	8	7
Ventricle	8	7

**Table 5-9. n-numbers for all PCR experiments.**

Table 5-10 shows the expression of all the mRNA targets for both control and MCT treated rats in all 6 regions. The data for each target are normalised so that the control atrial sample has an expression of 100%; figures above and below this number represent upregulation and downregulation respectively for the other tissue regions in both the control and MCT treated rats. The figures in the table are normalised to allow comparison of an individual target across regions and between the control and MCT treated rats. Normalisation in this manner prohibits comparison between the different targets and therefore the data are also displayed as relative quantification with normalisation to the most lowly expressed target (Cx30.2) for the control atrium only to give an indication of the differences in expression comparing the targets (Figure 5-10). Using this normalisation strategy, the most highly expressed target (SERCA2a) has a value of 3,807,312 demonstrating the high range of quantification for which RTqPCR can be used. The values are displayed in Figure 5-10 on a logarithmic scale given this wide dynamic range. As described in section 5.2.16, differences of greater than tenfold in expression levels allow tentative conclusions regarding the relative expression levels of the different targets.

	Atrium		Transitional tissue		Inferior nodal extension		Compact node		Penetrating bundle		Ventricle	
	Control	MCT	Control	MCT	Control	MCT	Control	MCT	Control	MCT	Control	MCT
<b>Inward currents</b>												
Nav1.1	100	61	90	40	49	16	67	33	20	23	53	78
Nav1.5	100	169	45	75	11	17	9	21	33	57	167	103
Nav1.8	100	47	16	18	9	88	4	40	687	347	3	7
Navβ1	100	111	70	91	27	44	43	46	22	32	112	121
Ca <sub>v</sub> 1.2	100	46	146	84	93	48	80	36	90	54	62	101
Ca <sub>v</sub> 1.3	100	16	17	0	45	0	36	16	52	3	16	7
Ca <sub>v</sub> 3.1	100	38	41	8	39	9	45	46	30	5	14	10
Ca <sub>v</sub> 3.2	100	45	14	1	22	2	27	12	18	19	43	34
Ca <sub>v</sub> α2δ1	100	77	21	15	18	5	9	8	7	15	71	45
Ca <sub>v</sub> 2δ2	100	83	18	3	31	4	48	79	111	9	58	30
Ca <sub>v</sub> β2	100	113	42	34	15	18	23	36	17	29	87	128
HCN1	100	147	234	213	426	239	426	372	143	235	1	7
HCN2	100	80	32	17	27	16	20	25	18	114	1299	385
HCN4	100	39	487	154	800	143	1162	343	2428	853	78	119
CLC-2	100	71	98	77	58	30	69	69	69	91	86	82
CLC-3	100	79	87	72	182	71	117	106	133	143	55	156
<b>Outward currents</b>												
Kv1.2	100	9	17	1	9	0	3	2	15	2	20	7
Kv1.4	100	36	35	11	8	3	12	10	9	7	25	26
Kv1.5	100	74	158	109	179	51	192	156	136	92	57	48
Kv2.1	100	56	65	38	33	20	35	30	28	30	143	84
Kv4.2	100	14	13	1	10	2	1	1	1	9	97	38
Kv4.3	100	49	61	39	45	22	38	25	31	14	37	15
ERG1	100	39	38	8	13	5	13	13	14	14	54	32
K <sub>v</sub> LQT1	100	83	35	14	16	14	26	17	20	24	109	84
K <sub>i</sub> 2.1	100	48	76	41	20	21	27	24	74	80	149	159
K <sub>i</sub> 2.2	100	33	19	3	19	1	11	4	5	7	43	22
K <sub>i</sub> 2.4	100	117	20	0	24	2	24	2	23	26	357	72
K <sub>i</sub> 3.1	100	26	36	6	8	3	7	3	5	2	18	7
K <sub>i</sub> 3.4	100	58	117	70	59	31	86	51	32	24	10	19
K <sub>i</sub> 6.1	100	72	69	71	83	74	48	65	46	96	96	108
K <sub>i</sub> 6.2	100	36	51	12	25	4	21	19	16	19	208	84
SUR1	100	60	24	9	11	4	10	10	3	15	120	41
SUR2	100	51	72	47	57	39	40	28	71	58	82	72
KChIP2	100	24	59	37	121	11	21	4	39	23	270	170
minK	100	1060	104	96	98	8	240	124	154	77	354	694
TWIK1	100	93	27	3	41	2	13	12	86	32	14	17
TASK1	100	70	37	26	15	7	10	18	9	24	90	54
<b>Intracellular Ca<sup>2+</sup> cycling</b>												
RyR2	100	43	20	3	9	1	20	8	8	14	87	63
RyR3	100	85	49	54	14	16	18	21	9	21	42	48
NCX1	100	73	36	18	30	8	48	34	56	22	65	52
SERCA2a	100	56	69	38	46	19	35	31	12	13	30	81
Phospholamban	100	25	88	29	93	18	92	34	98	61	70	123
PMCA1	100	103	71	69	84	58	77	68	80	82	91	69
Calsequestrin 2	100	87	55	39	29	20	48	38	25	20	83	65
Sarcolipin	100	28	89	31	56	16	38	16	2	1	0	0
<b>Connexins</b>												
Cx30.2	100	47	1743	1	3249	20	3012	1415	1374	65	55	35
Cx43	100	50	17	14	5	2	3	4	2	18	86	56
Cx40	100	170	41	40	43	25	35	36	622	337	188	287
Cx45	100	99	125	113	127	104	158	132	311	247	55	111
<b>Ion channel transporters</b>												
Na <sup>+</sup> /K <sup>+</sup> ATPase α1 subunit	100	71	114	94	66	60	107	85	82	93	34	51
Na <sup>+</sup> /K <sup>+</sup> ATPase α2 subunit	100	40	90	56	103	37	81	54	113	82	174	102
Na <sup>+</sup> /K <sup>+</sup> ATPase α3 subunit	100	129	184	99	896	97	1078	283	405	97	210	34
Na <sup>+</sup> /K <sup>+</sup> ATPase β1 subunit	100	146	30	56	16	25	22	41	21	18	68	44
Na <sup>+</sup> /H <sup>+</sup> transporter	100	88	76	72	45	69	104	81	78	65	53	54
<b>Autonomic regulators</b>												
Adrenergic receptor, 1a/1c	100	58	34	22	29	8	33	27	27	48	121	119
Adrenergic receptor, α-1b	100	34	23	0	24	0	22	14	17	52	370	144
Adrenergic receptor, β 1	100	62	103	82	88	46	85	77	68	42	80	61
Adrenergic receptor, β-2	100	58	121	81	99	75	95	93	63	95	81	85
M2 muscarinic receptor	100	48	23	12	14	4	13	18	5	9	25	30
Adenosine A1 receptor	100	116	21	20	36	12	16	59	8	15	40	34

**Table 5-10. Relative abundance (mean value) of RNA from six tissue regions of the AV node for both control and MCT rats. For each target, the relative quantification was normalised to the atrium of the control animal.**

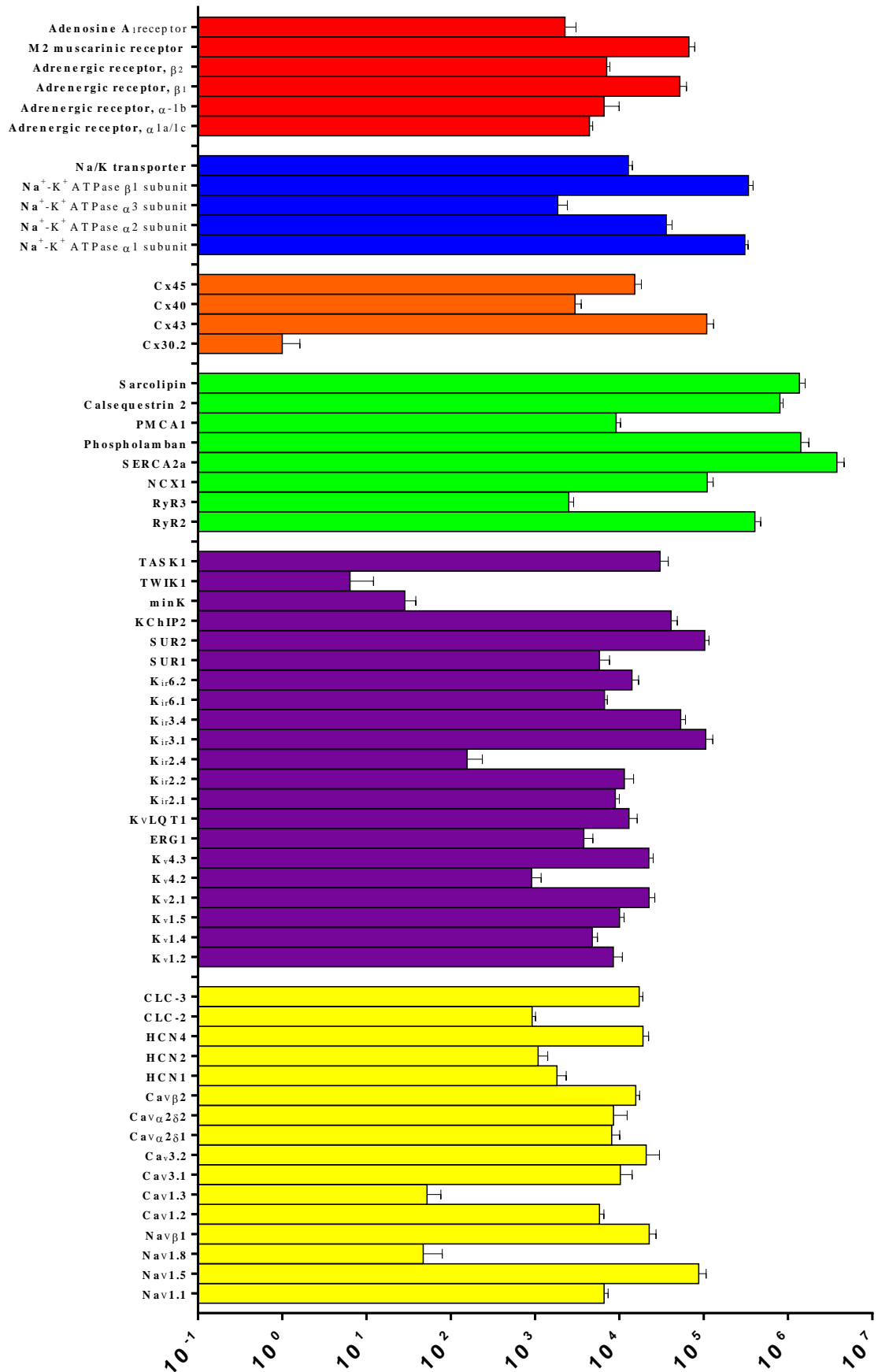


**Figure 5-10.** Relative quantification of targets in the control atrium. All targets are normalised to the lowest expressing target (Cx30.2). The scale is logarithmic and therefore each marked interval is x10 greater than the last. A greater than x10 difference in the expression level allows tentative conclusions to be drawn regarding the expression levels (see section 5.2.16).

### 5.3.4 Regional specific expression of ion channels and connexions in the rat AV node.

As described in section 1.5.2, previous studies describing the ion channel expression of the AV node have used rats, rabbits and humans. Although important species differences exist there is considerable overlap between the species with a characteristic expression profile for ion channels and transporters, connexins, intracellular  $\text{Ca}^{2+}$  handling proteins and autonomic receptors that differentiates the working myocardium from nodal tissue. A comparison of the data from the control rat's AV node with previous studies is important both to validate the results of this study and to develop further understanding of the similarities and differences between the rat AV node and the AV node of other species. Figure 5-11 – Figure 5-16 show how the relative expression for each target across the six regions of the AV node in the control animals.

Figure 5-11 shows the relative expression of the HCN channels in the AV node. One of the most characteristic findings from previous studies of the AV node is an increased expression of HCN4 at both the mRNA and protein level in the nodal tissues, which is in keeping with the pacemaker role of the AV node.<sup>72, 75, 76</sup> The results of this study are entirely in keeping with previous findings showing a significant increase in expression of HCN4 mRNA in the inferior nodal extension, compact node and penetrating bundle compared with both the atrial and ventricular myocardium. In addition to this, HCN1 mRNA levels have previously been shown to be raised in the compact node of rabbits, rats and humans and this is again replicated in this study of the rat.<sup>72, 75, 76</sup> A study of the human AV node showed no significant differences in the expression of HCN2 across the atrium, ventricle or nodal tissues although both mouse and rat studies have shown that HCN2 is up-regulated in the ventricle compared with both the nodal tissues and atrium.<sup>72, 83, 87</sup> The results of this study are in keeping with the expectation of high levels of HCN2 in the working myocardium with significantly greater quantities in the ventricle and atrium compared to the nodal tissue. This supports the idea that there may be species specific differences in ion channel expression although it is important to note that all the patients in the human study had cardiomyopathy which may also account for the differences.<sup>72</sup> The relative contributions of the different HCN channels to the pacemaker potential is uncertain, although the ratio of expression for HCN1:HCN2:HCN4 is 127:1:447 within the compact node strongly suggesting that HCN4 is to be the most significant ion channel contributing to the funny current in the AV node.

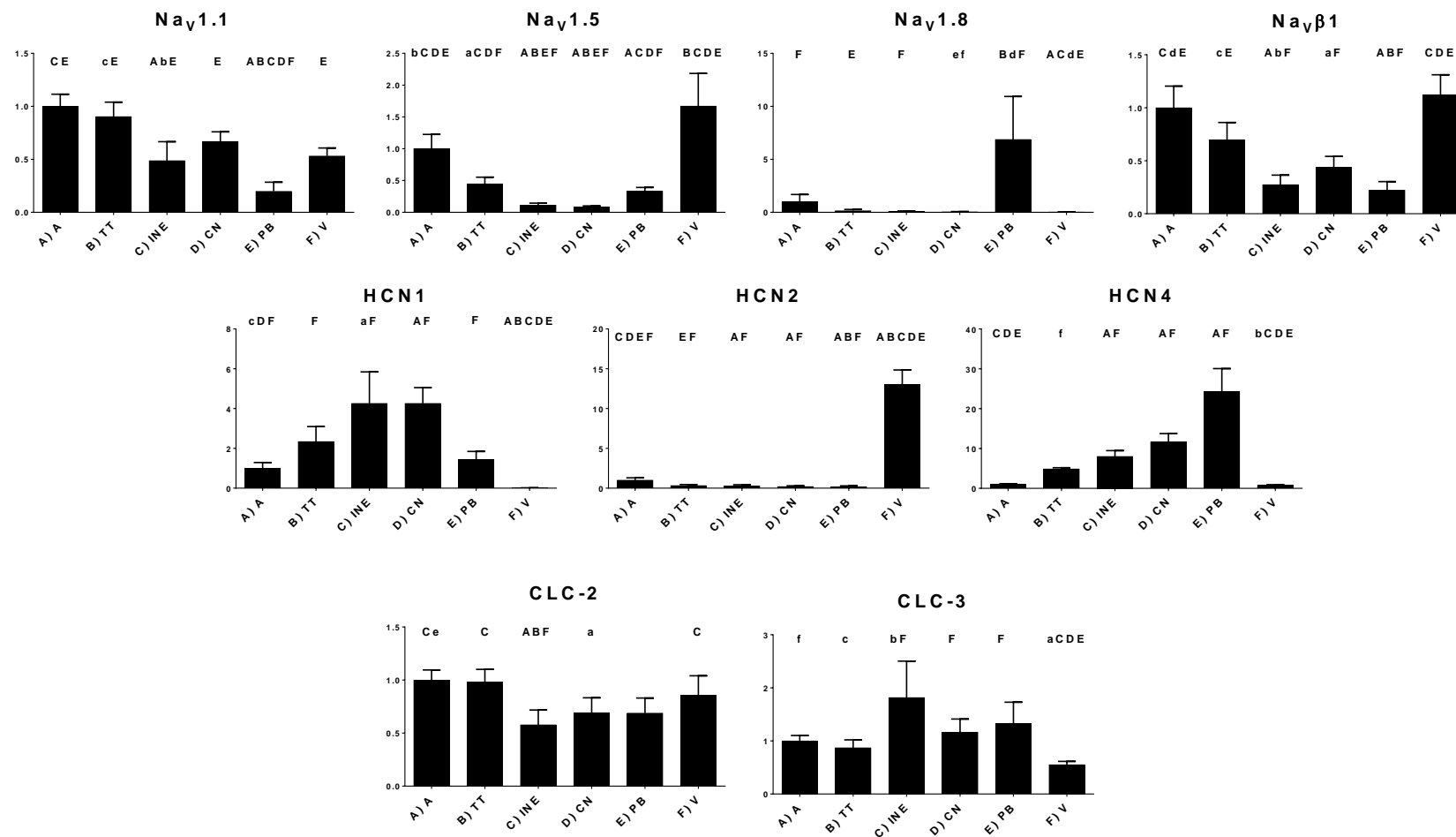


**Figure 5-11. Relative quantification of mRNA for the six different regions of the AV node in control rats. Letters above the bar graphs denote a significant difference between that region and the region with the corresponding letter. Capital letters indicate significance with a corrected P value of <0.05 and lower case letters indicate significance with a corrected P value of <0.20 (using the limma test). Expression of  $\alpha$  and  $\beta$  subunits of inward current carrying ion channels. A - Atrium, TT - Transitional tissue, INE - Inferior nodal extension, CN - Compact node, PB - Penetrating bundle, V - Ventricle.**

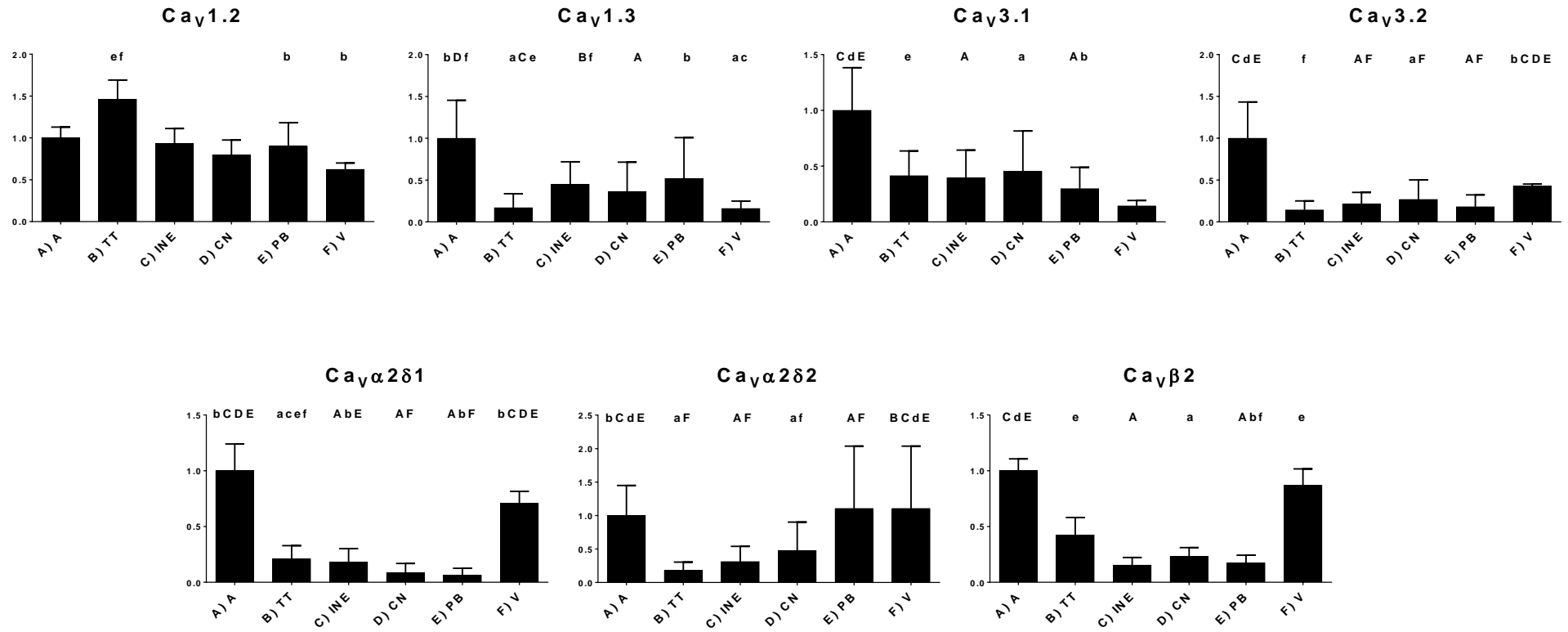


**Figure 5-12. Relative quantification of mRNA for the six different regions of the AV node in control rats. Letters above the bar graphs denote a significant difference between that region and the region with the corresponding letter. Capital letters indicate significance with a corrected P value of <0.05 and lower case letters indicate significance with a corrected P value of <0.20 (using the limma test). Expression of  $\alpha$  and  $\beta$  subunits of further inward current carrying ion channels. A - Atrium, TT - Transitional tissue, INE - Inferior nodal extension, CN - Compact node, PB - Penetrating bundle, V - Ventricle.**

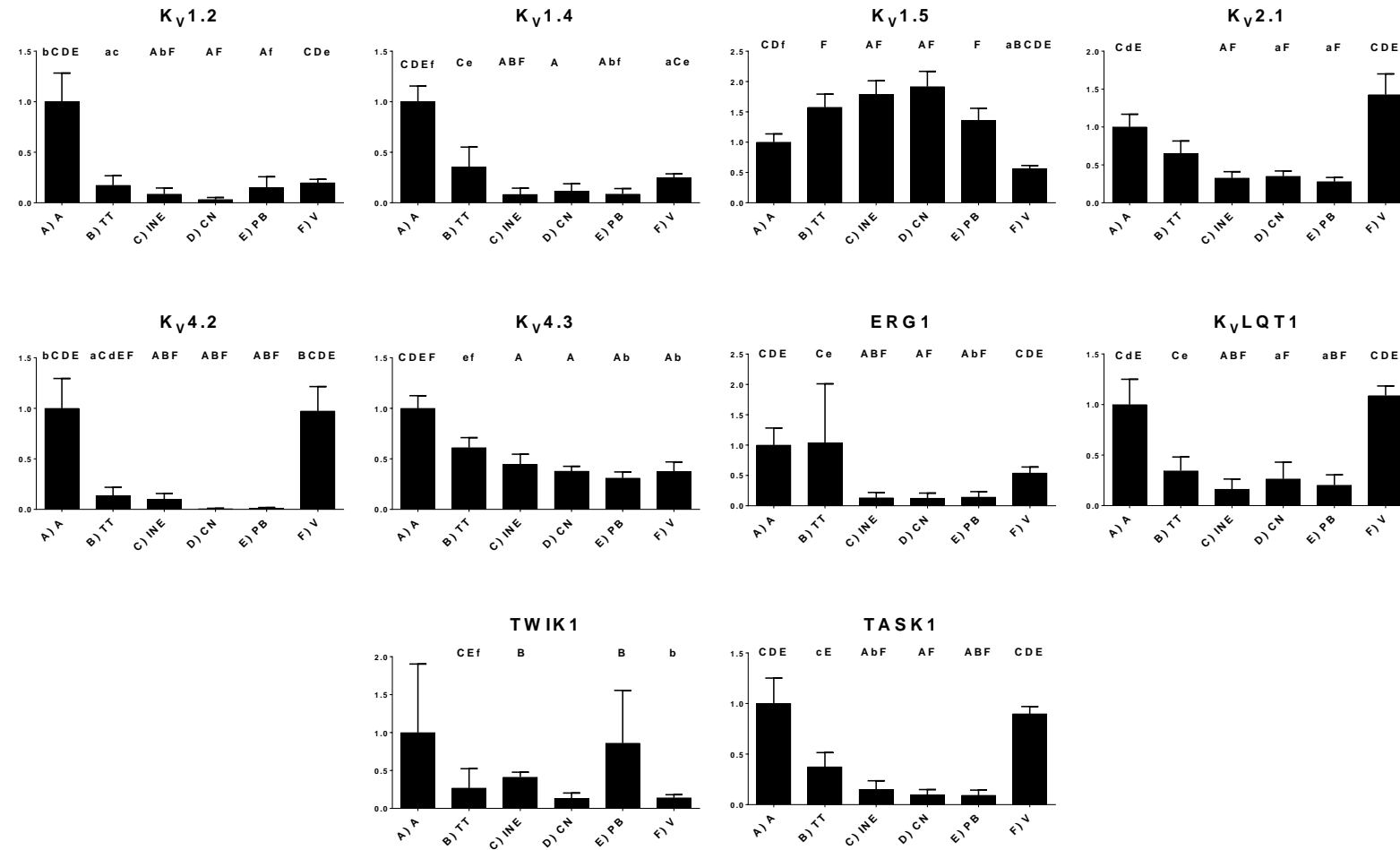


**Figure 5-13. Relative quantification of mRNA for the six different regions of the AV node in control rats. Letters above the bar graphs denote a significant difference between that region and the region with the corresponding letter. Capital letters indicate significance with a corrected P value of <0.05 and lower case letters indicate significance with a corrected P value of <0.20 (using the limma test). Expression of  $\alpha$  and  $\beta$  subunits of K<sup>+</sup> channels. A - Atrium, TT - Transitional tissue, INE - Inferior nodal extension, CN - Compact node, PB - Penetrating bundle, V - Ventricle.**

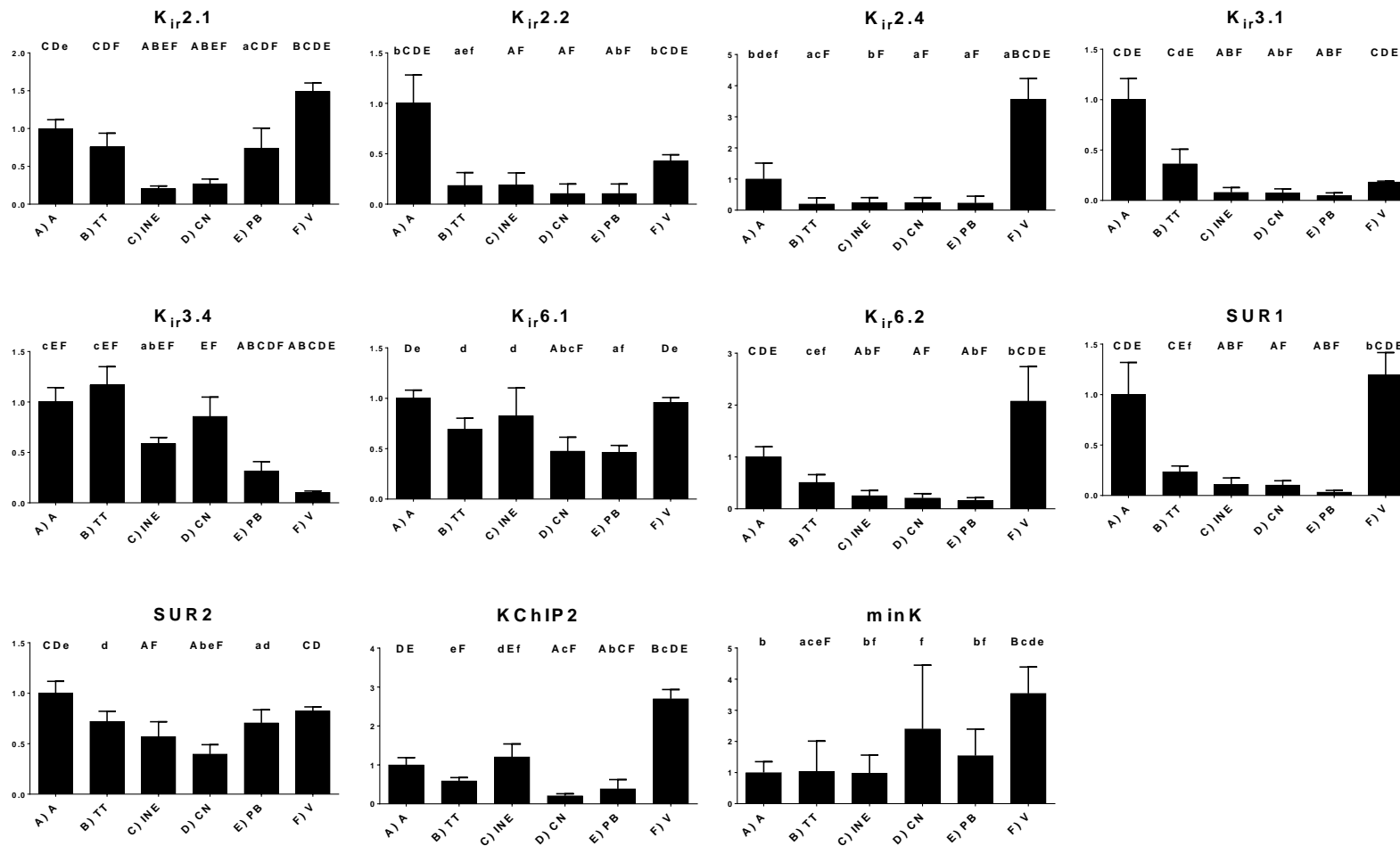


**Figure 5-14. Relative quantification of mRNA for the six different regions of the AV node in control rats. Letters above the bar graphs denote a significant difference between that region and the region with the corresponding letter. Capital letters indicate significance with a corrected P value of <0.05 and lower case letters indicate significance with a corrected P value of <0.20 (using the limma test). Expression of  $\alpha$  and  $\beta$  subunits of further  $K^+$  channels. A - Atrium, TT - Transitional tissue, INE - Inferior nodal extension, CN - Compact node, PB - Penetrating bundle, V - Ventricle.**

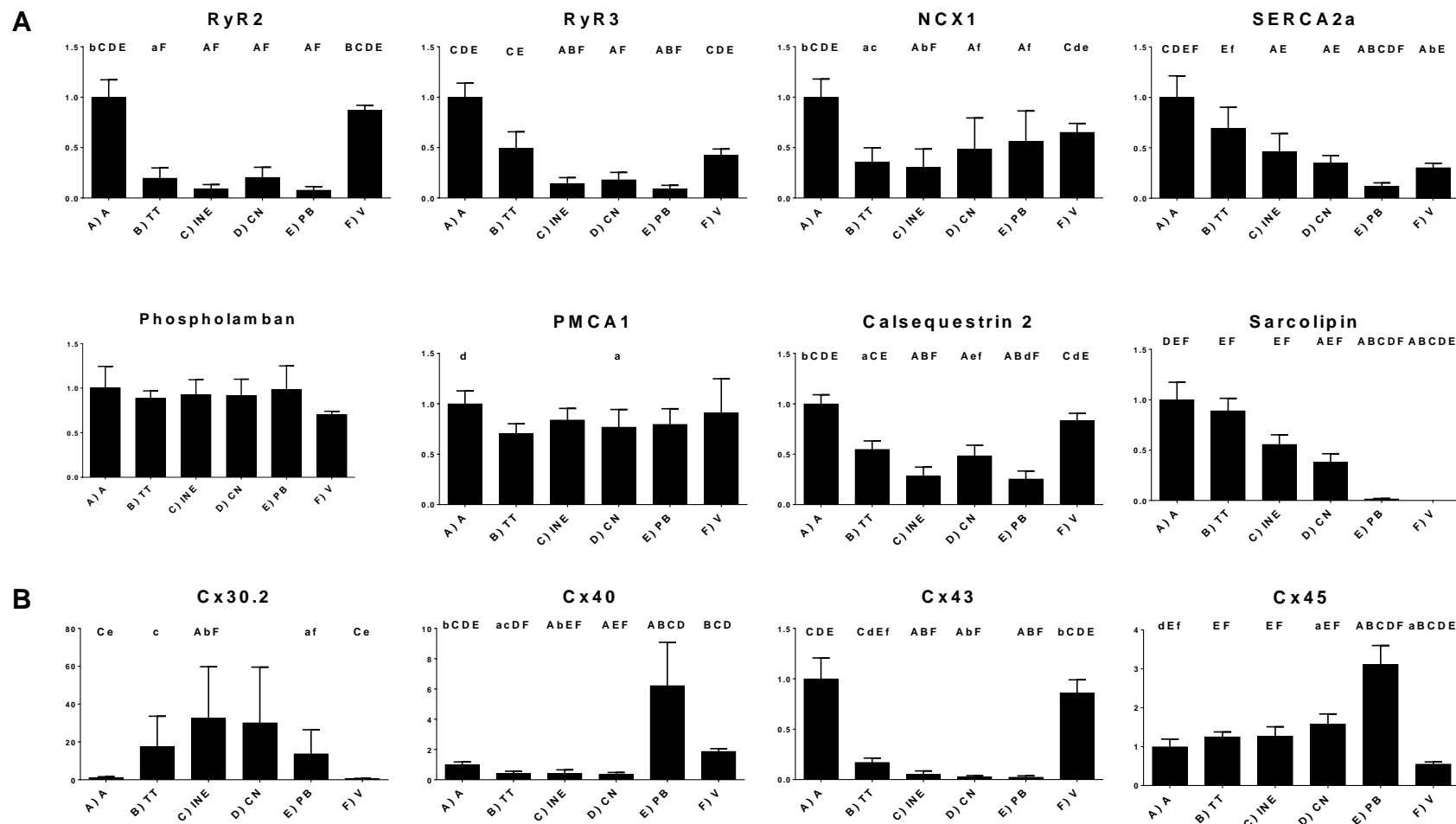


**Figure 5-15. Relative quantification of mRNA for the six different regions of the AV node in control rats. Letters above the bar graphs denote a significant difference between that region and the region with the corresponding letter. Capital letters indicate significance with a corrected P value of <0.05 and lower case letters indicate significance with a corrected P value of <0.20 (using the limma test). A and B). Expression of Ca<sup>2+</sup> handling proteins (A) and connexins (B). A - Atrium, TT - Transitional tissue, INE - Inferior nodal extension, CN - Compact node, PB - Penetrating bundle, V - Ventricle.**

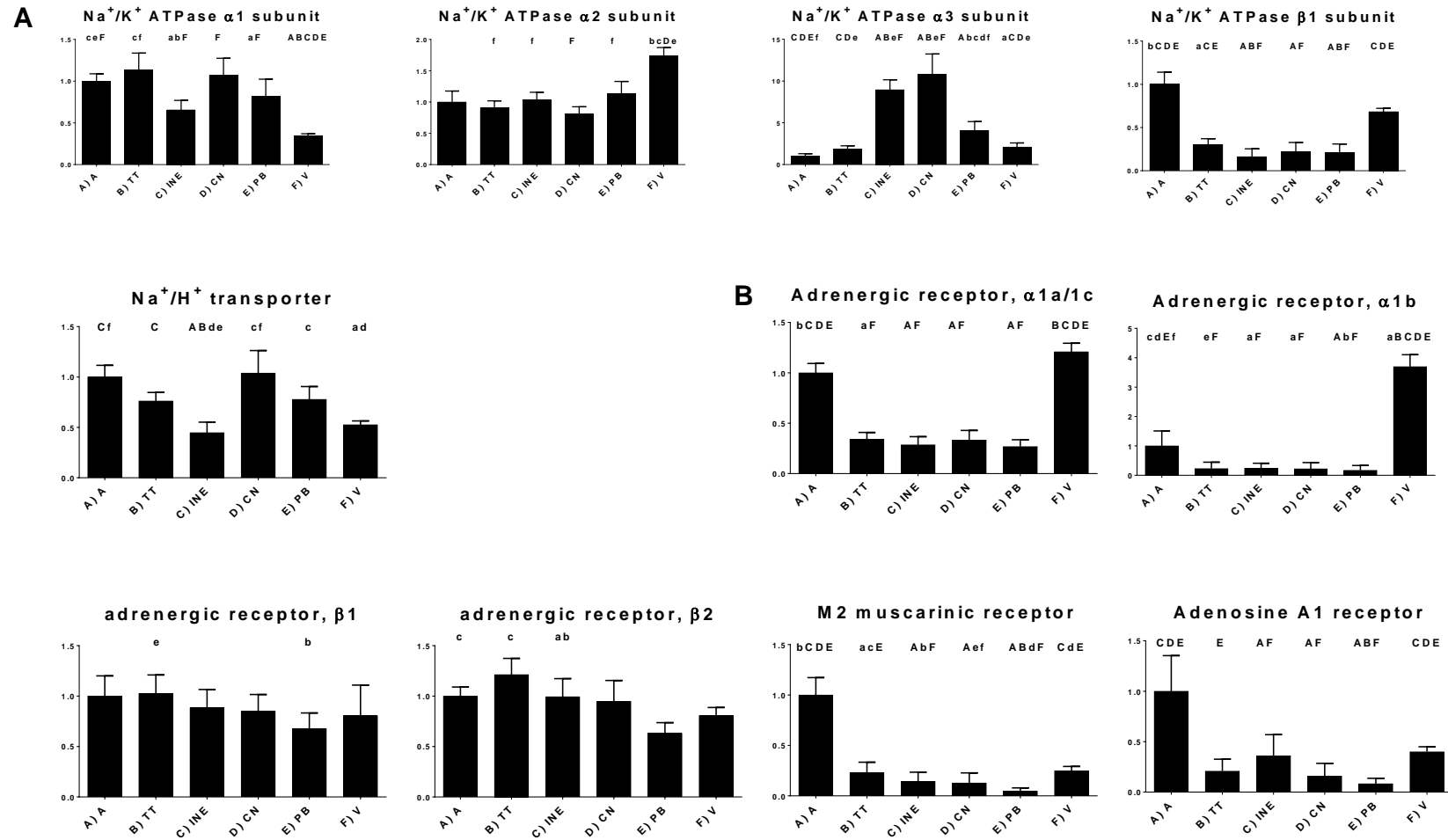


**Figure 5-16. Relative quantification of mRNA for the six different regions of the AV node in control rats. Letters above the bar graphs denote a significant difference between that region and the region with the corresponding letter. Capital letters indicate significance with a corrected P value of <0.05 and lower case letters indicate significance with a corrected P value of <0.20 (using the limma test). A and B). Expression of ion exchangers (A) and autonomic receptors (B). A - Atrium, TT - Transitional tissue, INE - Inferior nodal extension, CN - Compact node, PB - Penetrating**

Another characteristic finding within the AV node is the down regulation of Na<sub>v</sub>1.5 which has been demonstrated in the rat and human although this was not demonstrated (to statistical significance) within the rabbit.<sup>72, 75, 76</sup> This study again replicates previous findings with a significant decrease in mRNA for Na<sub>v</sub>1.5 in the transitional tissue, inferior nodal extension, compact node and penetrating bundle (Figure 5-11 Ai). This study also demonstrates a reduction in the mRNA for Na<sub>v</sub>β1, the main β subunit of Na<sub>v</sub>1.5, in the inferior nodal extension, compact node and penetrating bundle, which was not demonstrated in the human study and not studied in other species.<sup>72</sup> A decrease in Na<sub>v</sub>1.1 and an increase in Na<sub>v</sub>1.8 were also noted although the expression levels of these channels were much lower than for both Na<sub>v</sub>1.5 and Na<sub>v</sub>β1 and therefore the functional relevance of these changes is uncertain.

Studies looking at the expression of the proteins underlying the Ca<sup>2+</sup> channels within the AV node have been undertaken using rat, rabbit and human hearts.<sup>72, 76, 83</sup> These studies demonstrated an increase in Ca<sub>v</sub>1.3 and Ca<sub>v</sub>3.1 in the compact node but no change in Ca<sub>v</sub>1.2 in rabbits and humans.<sup>72, 76</sup> In rats higher levels of Ca<sub>v</sub>1.3, Ca<sub>v</sub>3.1 and Ca<sub>v</sub>3.2 have been shown in the nodal tissue compared with the working myocardium, but low levels of Ca<sub>v</sub>1.2 in the nodal tissues compared with the myocardium.<sup>83</sup> There is low expression of Ca<sub>v</sub>1.3 compared with the other Ca<sup>2+</sup> channels.<sup>83</sup> Ca<sub>v</sub>1.3 activates at more hyperpolarised potentials than Ca<sub>v</sub>1.2 and therefore may play an important role in AV node conduction,<sup>80</sup> supporting this AV block is evident in Ca<sub>v</sub>1.3 deficient mice.<sup>199</sup> This study shows no consistent pattern of change in Ca<sub>v</sub>1.2 and Ca<sub>v</sub>1.3 (Figure 5-12). Perhaps even more strikingly the expression level of Ca<sub>v</sub>1.3 mRNA was lower than the other three Ca<sub>v</sub> channels by a factor of approximately 300; this is similar to the previous rat study<sup>83</sup> and suggests that there may be important species differences in the Ca<sup>2+</sup> currents with Ca<sub>v</sub>1.3 playing a much less significant role in rats than mice.<sup>79, 83</sup> In contrast to the previous study in rats which demonstrated increased Ca<sub>v</sub>1.3, Ca<sub>v</sub>3.1 and Ca<sub>v</sub>3.2 in the nodal tissues compared to the working myocardium, this study demonstrated a reduction in the levels of Ca<sub>v</sub>3.1 in the nodal tissues compared with the atrium (but not the ventricle) and a reduction in Ca<sub>v</sub>3.2 in the nodal tissues compared with the both the atrium and the ventricle.<sup>83</sup> A similar pattern was seen with the mRNAs encoding for accessory subunits of the Ca<sup>2+</sup> channels (Ca<sub>v</sub>α2δ1, Ca<sub>v</sub>α2δ2 and Ca<sub>v</sub>β2) with reductions seen in the nodal tissue compared with the working myocardium.

There are no data regarding the distribution of the Cl<sup>-</sup> channels within the AV node, although CLC-2 has been shown to be present in the SA node consistent with its role in

pacemaking.<sup>192</sup> In our study there was a reduction of CLC-2 in the inferior nodal extension compared to the working myocardium, but an increase in CLC-3 (Figure 5-11). The functional consequences of these findings are undetermined.

As described in section 1.4.1 there is considerable diversity in  $K^+$  channels and also considerable variation in the expression of the different  $K^+$  channels between species. The most characteristic finding within the nodal tissues (both SA node and AV node) is low expression of  $K_{ir}2.1$  in both rabbits and humans.<sup>72, 76</sup>  $K_{ir}2.1$  is responsible for the inwardly rectifying  $I_{K1}$ , which is a significant determinant of the negative resting potential of the working cardiac myocytes. Low levels of  $K_{ir}2.1$  results in a less negative resting potential in the nodal cells and facilitates pacemaker function (see section 1.4.2). The results of this study are again in keeping with previous findings with significant reductions of  $K_{ir}2.1$  in both the inferior nodal extension and compact node (Figure 5-15). There is a more mixed picture with the other  $K_{ir}$  channels. In humans there is an increase in  $K_{ir}2.2$  in the compact node, in rabbits  $K_{ir}2.2$  was expressed in low quantities in all tissues other than the ventricle.<sup>72, 76</sup> In my study the ratio of expression for  $K_{ir}2.1:K_{ir}2.2:K_{ir}2.4$  in the compact node was 3117:22:1 suggesting that  $K_{ir}2.1$  is the main determinant of  $I_{K1}$  in rats; despite this the pattern was similar in all the  $K_{ir}2.x$  channels with a marked reduction in the nodal tissues.

There is a more mixed picture with regards to the other voltage-gated  $K^+$  channels. The previous literature describes a reduced expression of all the  $\alpha$  and  $\beta$  subunits for the  $K^+$  channels in the AV node compared with the working myocardium ( $K_v1.4$ ,  $K_v4.2$ ,  $KChIP2$ ,  $ERG$ ,  $K_{ir}6.2$  and  $SUR2A$ ) in the rabbit.<sup>76</sup> In contrast the human study demonstrated increases in  $K_v1.4$ ,  $K_v4.2$ ,  $K_{ir}3.1$   $K_{ir}3.4$  and  $minK$  in the compact node compared to the working myocardium and no change in  $K_v4.3$ ,  $K_v1.5$ ,  $ERG$ ,  $K_vLQT$  and  $KChAP$ .<sup>72</sup> Apart from the reduction in  $K_{ir}2.1$  described above there were no  $K^+$  channels which showed a reduced expression in the human AV node.<sup>72</sup> The results of this study are much more in keeping with the findings from the rabbit study with a widespread reduction in mRNA expression of the proteins that form both the  $\alpha$  and  $\beta$  subunits of the  $K^+$  channels (Figure 5-13 and Figure 5-14). This includes a reduction in the expression of  $K_v1.4$ ,  $K_v4.2$ ,  $K_v4.3$  and  $KChIP2$  in the inferior nodal extension and compact node; these mRNAs encode the proteins that underlie the channels that give rise to  $I_{to,f}$  which is the dominant repolarising current seen in the working myocardium of the rat. A strikingly similar pattern is also seen in the levels of the mRNAs which are responsible for other  $K^+$  channels including  $I_{to,s}$  ( $K_v1.2$  and  $K_v2.1$ ),  $I_{K,ATP}$  ( $K_{ir}6.$ ,  $K_{ir}6.2$ ,  $SUR1$  and  $SUR2$ ),  $I_{K,r}$  ( $ERG1$ ,  $MinK$ ) and  $I_{K,s}$

(K<sub>v</sub>LQT1). The two pore K<sup>+</sup> channel, TASK1, also showed a pattern of reduced expression within the node with downregulation seen in the inferior nodal extension, compact node and penetrating bundle compared with the working myocardium. The other two pore K<sup>+</sup> channel, TWIK1, was expressed in very low levels in all tissue with no consistent pattern of expression. K<sub>ir</sub>3.1 and K<sub>ir</sub>3.4 which form the ion channel responsible for I<sub>K,ACh</sub> are highly expressed in the atrium with low expression levels in both the nodal tissues and the ventricles. This is surprising given the importance of I<sub>K,ACh</sub> in slowing AV node conduction.<sup>200</sup> There are no previous reports of the relative quantification of K<sub>ir</sub>3.1 and K<sub>ir</sub>3.4 in the nodal tissues and working myocardium but a lower relative quantity does not necessarily mean that the currents are not important (for example the low expression of the mRNAs for the proteins of the calcium clock described below). Only the mRNA encoding for K<sub>v</sub>1.5 showed up-regulation in both the compact node and inferior nodal extension; this protein is responsible for the current, I<sub>K,ur</sub> and has been shown to play a role in repolarisation in the rat.<sup>52</sup> The finding of upregulation in the node is consistent with the study of the human AV node and also the rat SA node.<sup>72, 121</sup>

As described in section 2.1.2.1, there is debate as to which currents are relevant to the action potential in rats, but, it is interesting to note that mRNA expression levels for proteins known to have an important role, e.g. K<sub>ir</sub>2.1, were similar to the expression levels of K<sup>+</sup> channels that have not previously been shown to be important in rats, e.g. K<sub>v</sub>LQT1 (in the compact node the relative quantification was 1:1.5 for K<sub>ir</sub>2.1: K<sub>v</sub>LQT1). Despite the difficulty in knowing the relevance of each individual K<sup>+</sup> channel responsible for the K<sup>+</sup> currents, the widespread reduction of the K<sup>+</sup> channels with a similar pattern across the different mRNAs suggests that the repolarising K<sup>+</sup> currents in the AV node are generally significantly reduced.

No consistent pattern of expression has been demonstrated with regards to the expression of the proteins controlling intracellular Ca<sup>2+</sup> handling within the AV node. In the rabbit AV node there is a reduction of SERCA2a, RyR2 and RyR3 but in the human no change is seen in NCX, SERCA2a or RyR2 but there is an increase in RyR3 compared with the ventricle.<sup>72, 76, 105</sup> The results of this study are shown in Figure 5-15A. There is a consistent pattern with reduction in the expression of RyR2, RyR3, calsequestrin 2, NCX1 and SERCA2a in the nodal tissues compared with the working myocardium. As expected there is high expression of sarcolipin in the atrium but very low expression in the ventricle.<sup>196</sup> Interestingly there was a gradually decreasing expression of sarcolipin throughout the tissues of the AV node. No consistent pattern of change was seen with PMCA1,

phospholamban or calsequestrin 2. These findings are consistent with the previous studies although they are surprising given the importance of these proteins in pacemaker function in the 'calcium clock' hypothesis. However, a reduced expression of RyR2 and SERCA2a has previously been shown in the rat sinus node compared with the atrial myocardium<sup>121</sup> indicating that the findings in this study are not incompatible with the pacemaking function of the AV node.

The distribution of the connexin isoforms in the mouse, rat, rabbit and human have previously been described with a characteristic finding of reduced expression of the medium conductance Cx43 in the nodal tissues and high levels of the high conductance Cx40 in the His-Purkinje system.<sup>72, 75, 76</sup> There are some important species differences seen with high levels of Cx40 seen in the atrium in humans, but low levels in the atrium of rats.<sup>72, 75</sup> The findings of this study are in keeping with previous results showing the expected pattern of a reduction in Cx43 in the transitional tissue, inferior nodal extension, compact node and penetrating bundle compared with the working myocardium (Figure 5-15B). Cx40 is expressed in low levels in all tissues apart from the penetrating bundle. Previous studies in the rabbit and human have shown no changes in the distribution of the low conductance Cx45 across the working myocardium and nodal tissues, but in this study the levels of Cx45 were greater in the penetrating bundle than the other tissues with higher levels in both the atrial and nodal tissues than the ventricle.<sup>72, 76</sup> In mice, the ultra-low conductance Cx30.2 is functionally important with increased levels of Cx30.2 leading to a paradoxical slowing of conduction in the AV node.<sup>105</sup> In this study, greater expression levels of Cx30.2 were seen in the inferior nodal expression although the relative expression of Cx30.2 was much lower than the other three connexin mRNAs (in the inferior node, the ratio of expression for Cx30.2:Cx40:Cx43:Cx45 is 1:40:182:595) suggesting that Cx30.2 may only play a limited role in rats.

The distribution of the Na<sup>+</sup>/K<sup>+</sup> ATPase in the AV node has not previously been investigated. There is no consistent pattern seen across the different subunits with a lower expression of the  $\alpha$ 1 subunit in the ventricle and a greater expression of the  $\alpha$ 2 subunit in the ventricle compared with both the atrium and the nodal tissues (Figure 5-16 A). Interestingly, there was an increase in the expression of the  $\alpha$ 3 subunit in both the inferior nodal extension and the compact node. This has not previously been demonstrated in the AV node, although a greater expression of the  $\alpha$ 3 subunit has been shown in the SA node compared with the atrium, suggesting that the expression of the  $\alpha$ 3 subunit may be related to a 'nodal phenotype'.<sup>121</sup> Despite these regional differences, the relative expression of the

$\alpha_1$  phenotype was much greater than that of both the  $\alpha_2$  and  $\alpha_3$  subunits (in the compact node the ratio for  $\alpha_1:\alpha_2:\alpha_3$  is 16:1:1). The  $\beta$  subunit of the  $\text{Na}^+/\text{K}^+$  ATPase showed a reduced expression in the nodal tissues. There is no consistent pattern in the expression of the  $\text{Na}^+/\text{H}^+$  transporter with low levels in the inferior nodal extension and ventricle but higher levels in the atrium and compact node.

The distribution of the  $\alpha$  and  $\beta$  adrenoceptors and the muscarinic receptors within the AV node have not previously been investigated. The  $\beta_1$  adrenoceptor was the most highly expressed of the adrenoceptors that were measured. There was no consistent pattern in the expression of the  $\beta_1$  and  $\beta_2$  adrenoceptor across the different regions of the AV node but there was a significant reduction in both the  $\alpha_1$  and  $\alpha_2$  adrenoceptors in the nodal tissues (Figure 5-16 B). There was also a reduction in the  $M_2$  muscarinic receptor and the adenosine A1 receptor seen in the nodal tissues. The reduction of the  $M_2$  muscarinic receptor in the nodal tissues mirrors the changes seen in  $\text{K}_{ir}3.1$  and  $\text{K}_{ir}3.4$  which are activated in response to activation of the  $M_2$  muscarinic receptor and adenosine A1 receptor by acetylcholine and adenosine respectively and give rise to the current,  $I_{\text{K,ACh}}$ .<sup>200</sup>

### 5.3.5 Remodelling of ion channels in the monocrotaline model

The qPCR experiment to measure the relative quantification of the ion channels, connexins, intracellular  $\text{Ca}^{2+}$  handling proteins, ion exchangers and autonomic receptors within the control rat's AV node has largely confirmed the previous data available but has also highlighted some important species differences. The agreement between the control group and previously published data supports the validity of the methodology employed and suggests that the comparison of the control and MCT animals for each region of the AV node will give meaningful insights into remodelling due to PH.

There are currently no other studies that demonstrate ion channel remodelling in the AV node in animal models that mimic disease process (in contrast to specific 'knock-out' studies) and therefore there are limited data with which to compare the changes seen in this study. There are however data looking at remodelling within the working myocardium in the MCT model with the majority of studies looking at the ventricle<sup>128-131, 136, 137, 140, 142</sup> and more limited studies and unpublished results from our laboratory looking at ion channel remodelling within the atrium<sup>124</sup> and sinus node (unpublished observations).

Figure 5-17 to Figure 5-22 demonstrate the changes seen for each target in the MCT rats for each region of the AV node with respect to the control rats. The values are normalised

to the control region such that a value of less than 1 represents downregulation and a value of greater than 1 indicates upregulation. Two levels of significance are denoted as described in section 5.2.16.

### 5.3.5.1 Ventricular tissue

Previous studies measuring mRNA expression for the ion channels of the ventricle looked separately at the LV and RV free walls<sup>130, 137</sup> or used the whole heart<sup>128</sup>, in contrast my study has investigated the septum of the ventricle which may limit the agreement between my results and previous studies. When the LV and RV have been compared, the most dramatic changes are in the RV with more limited changes in the LV.<sup>137</sup> There is a down-regulation of a wide range of K<sup>+</sup> channels in the RV in the MCT treated rats. There is substantial although not complete overlap between our study and the study of Benoist *et al.*;<sup>137</sup> in the study of Benoist *et al.* there was a reduction in K<sub>v</sub>1.4, K<sub>v</sub>1.5, K<sub>v</sub>4.2, K<sub>v</sub>4.3, K<sub>v</sub>LQT1, HERG, K<sub>ir</sub>2.1, K<sub>ir</sub>3.1 and KChIP2 with no K<sup>+</sup> channels showing upregulation. In this study there was a down-regulation of K<sub>v</sub>2.1, K<sub>v</sub>4.2, K<sub>v</sub>4.3, K<sub>v</sub>LQT1, KChIP2, K<sub>ir</sub>2.2, K<sub>ir</sub>2.4, K<sub>ir</sub>3.1, K<sub>ir</sub>6.2, SUR2 and TASK1 (Figure 5-22). There was a borderline increase in K<sub>ir</sub>3.4 (adjusted P value=0.08; limma test). Both studies support the idea that there is a widespread reduction in both the resting K<sup>+</sup> currents and the voltage-activated K<sup>+</sup> currents which may account for the prolongation of the QT interval in the MCT treated rats.

There are some differences between the two studies in terms of the Ca<sup>2+</sup> channels with Benoist *et al.*<sup>137</sup> demonstrating a reduction in Ca<sub>v</sub>1.2 but an increase in Ca<sub>v</sub>3.1 whereas this study demonstrated a borderline increase in Ca<sub>v</sub>1.2 (adjusted P value=0.19; limma test) and no change in Ca<sub>v</sub>3.1 (Figure 5-22). This study also demonstrated a reduction in Ca<sub>v</sub>3.2 and Ca<sub>v</sub>α2δ2 which have not previously been investigated (Figure 5-22). The expression of HCN1 and HCN4 have previously been shown to be unchanged (unpublished observations), which is in keeping with this study (Figure 5-22); HCN2 channels have not previously been measured but in my study they show a downregulation. This may be of relevance given the increased expression of HCN2 in the ventricle compared with the other HCN isoforms in the control rats in this study and in previous studies of HCN expression in rats.<sup>87</sup> There are no previous studies describing changes in Cl<sup>-</sup> channels in response to PH. In my study there was an upregulation of CLC-3 but no change in CLC2 (Figure 5-22). Up-regulation in CLC-3 would be expected to shorten the action potential which may protect against EADs and DADs.<sup>191</sup>

Studies looking at connexins in the MCT model have focused on Cx43. No difference has been demonstrated in the total protein expression of Cx43 although there is increased lateralisation which accounts for a reduction in function.<sup>140</sup> The results of this study are in keeping with these findings with no differences in the total expression levels of mRNA for Cx43 (Figure 5-22); qPCR is not able to address the question of lateralisation. There are no previous data on expression of the other connexin isoforms in the ventricle. In this study there was an increase in the expression of Cx45 (Figure 5-22) which is a novel finding, although given that this is a low conductance connexin the relative contribution of this to conduction in the ventricle is uncertain.

There are limited data regarding intracellular  $\text{Ca}^{2+}$ -handling proteins and ion exchangers although a reduction in SERCA2a, an increase in RyR3 and preserved phospholamban has been demonstrated previously (unpublished observations). In this study no changes were seen in any of the intracellular  $\text{Ca}^{2+}$  handling proteins (Figure 5-22).

A decrease in  $\beta_1$  adrenergic receptors in the ventricle of MCT animals has previously been described and is thought to underlie the poor inotropic response to adrenergic stimulation in PAH.<sup>201</sup> In this study, no significant changes were seen in the  $\beta$  adrenergic receptors although there was a reduction in the  $\alpha 1b$  adrenergic receptor (Figure 5-22). There are no studies demonstrating the effects of MCT on the  $\text{Na}^+$ - $\text{K}^+$  ATPase; in this study there was an increase in the  $\alpha 1$  subunit but a decrease in the  $\alpha 2$ ,  $\alpha 3$  and  $\beta$  subunits (Figure 5-22).

### 5.3.5.2 Atrial tissue

Within the atrium previous studies have again demonstrated a dramatic reduction in the expression of many  $\text{K}^+$  channel isoforms including  $\text{K}_v1.4$ ,  $\text{K}_v4.2$ , ERG,  $\text{K}_{ir}2.2$   $\text{K}_{ir}6.2$  and SUR1 but also an up-regulation of  $\text{K}_{ir}2.1$  (unpublished observations). In this study a reduction were seen in  $\text{K}_v1.2$ ,  $\text{K}_v1.4$ ,  $\text{K}_v2.1$ ,  $\text{K}_v4.2$ ,  $\text{K}_v4.1$ , ERG, KChIP2,  $\text{K}_{ir}2.1$ ,  $\text{K}_{ir}3.1$ ,  $\text{K}_{ir}3.4$   $\text{K}_{ir}6.1$ ,  $\text{K}_{ir}6.2$  and SUR2 with no  $\text{K}^+$  channels being upregulated (Figure 5-17). Despite the quantitative differences seen these results suggest a reduction in the overall outward  $\text{K}^+$  currents and therefore prolonged atrial repolarisation which would be expected to lead to an increase in the atrial refractory period. There is again some discrepancy in the changes in the  $\text{Ca}^{2+}$  channels with either no change or a decrease in  $\text{Ca}_v1.2$  reported but no change seen in  $\text{Ca}_v1.3$ ,  $\text{Ca}_v3.1$  and  $\text{Ca}_v3.2$ .<sup>124</sup> In this study there was a decrease in  $\text{Ca}_v1.2$  but no other changes in  $\text{Ca}^{2+}$  channel mRNA expression (Figure 5-17). Previously no

change was seen in HCN4 levels (unpublished observations) although in this study there was a significant downregulation (Figure 5-17).

An upregulation of Cx43 and Cx45 has previously been shown (unpublished observations), but no differences were seen in any of the connexin isoforms in this study (Figure 5-17). In one previous study a reduction in right atrial sarcolipin, phospholamban and SERCA2a was shown<sup>196</sup>, in another study no changes were seen in SERCA2a, RyR2 and RyR3, and there was an upregulation in NCX (unpublished observations). In this study SERCA2a was unchanged but there was a reduction in sarcolipin, phospholamban and RyR2. A reduction in the  $\alpha 2$  subunit of the  $\text{N}^+/\text{K}^+$  ATPase, the  $\alpha 1$  adrenergic receptor,  $\beta 1$  adrenergic receptor and the M2 muscarinic receptor was also seen (Figure 5-17). There are no previous data with which to compare these results.

### *5.3.5.3 Remodelling within the atrioventricular node*

There are no studies demonstrating remodelling of ion channels, connexins and  $\text{Ca}^{2+}$ -handling proteins within the AV node in response to disease; however, there are several studies that have demonstrated remodelling in the SA node in the MCT model, a heart failure model and ageing (unpublished observations).<sup>121, 122</sup> These studies have demonstrated different patterns of remodelling for the different disease processes. For example, HCN4 is upregulated in the sinus node in response to myocardial infarction, unchanged in ageing and downregulated in the MCT model (unpublished observations).<sup>121, 122</sup>

In the present study the most consistent finding was that of downregulation of HCN4 across the transitional tissue, inferior nodal extension and compact node (Figure 5-18, Figure 5-19 and Figure 5-20). There were no significant changes seen in the penetrating bundle (Figure 5-21). Another consistent finding was downregulation of the  $\text{K}^+$  channels which was seen in the transitional tissue, inferior nodal extension and compact node although there are different  $\alpha$  and  $\beta$  subunits affected in the different regions. The largest number of changes were seen in the inferior nodal extension with a reduction in  $\text{K}_v2.1$ ,  $\text{K}_v4.2$ ,  $\text{K}_v4.3$ , minK, KChIP2,  $\text{K}_{ir}2.4$   $\text{K}_{ir}3.4$  and TWIK1 (Figure 5-19); there was a reduction in KChIP2,  $\text{K}_{ir}3.1$  and  $\text{K}_{ir}6.2$  in the transitional tissue (Figure 5-18) and a reduction KChIP2 in the compact node (Figure 5-20). No changes were seen in the  $\text{Na}^+$  channels and the only the voltage-dependent  $\text{Ca}^{2+}$  channels to change were  $\text{Ca}_v1.2$  and  $\text{Ca}_v1.3$  in the inferior nodal extension, where they were downregulated (Figure 5-18,

Figure 5-19 and Figure 5-20). Cx30.2 showed reduced expression in both the inferior nodal extension and transitional tissue (Figure 5-18 and Figure 5-19). No changes were seen in the other connexin isoforms in any of the nodal tissues (Figure 5-18, Figure 5-19, and Figure 5-20). A reduction in CLC-3 was seen in the inferior nodal extension, but there were no other changes seen in the expression of the Cl<sup>-</sup> channels (Figure 5-18, Figure 5-19 and Figure 5-20).

With regards to the intracellular Ca<sup>2+</sup>-handling proteins, a reduction in both phospholamban and sacrolopin was seen in both the transitional tissue and inferior nodal extension (Figure 5-18 and Figure 5-19). There was also a reduction in RyR2 in the inferior nodal extension and PMCA1 in the compact node (Figure 5-19 and Figure 5-20). Regarding the Na<sup>+</sup>/K<sup>+</sup> ATPase, there was reduced expression of the  $\alpha$ 2 subunit in the inferior nodal extension and the  $\alpha$ 3 subunit in both the inferior nodal extension and the compact node (Figure 5-19 and Figure 5-20). The Na<sup>+</sup>/H<sup>+</sup> antiporter was upregulated in the inferior nodal extension and indeed this was the only transcript to show upregulation in the nodal tissue (Figure 5-19). Both the  $\alpha$ 1 and  $\beta$ 1 adrenergic receptors were decreased in the inferior nodal extension but unchanged in the other regions of the nodal tissue (Figure 5-19).

It is notable that the penetrating bundle was the only region investigated in which no significant changes were seen in any of the mRNA transcripts measured (Figure 5-21). It is tempting to speculate that this may be because the penetrating bundle is enclosed within the central fibrous body giving it a degree of protection from the raised pressures within both the RV and RA. Similarly it is possible that the thin walled RA may be more susceptible to the raised pressures than the relatively thick walled ventricular septum. Supporting this hypothesis is the fact that there was downregulation of a total of 23 transcripts in the RA versus 17 in the ventricle (Figure 5-17 and Figure 5-22). This observation may provide a clue to suggest that remodelling seen is a direct effect of the raised pressure within the RV although this question cannot be assessed further within the current study.





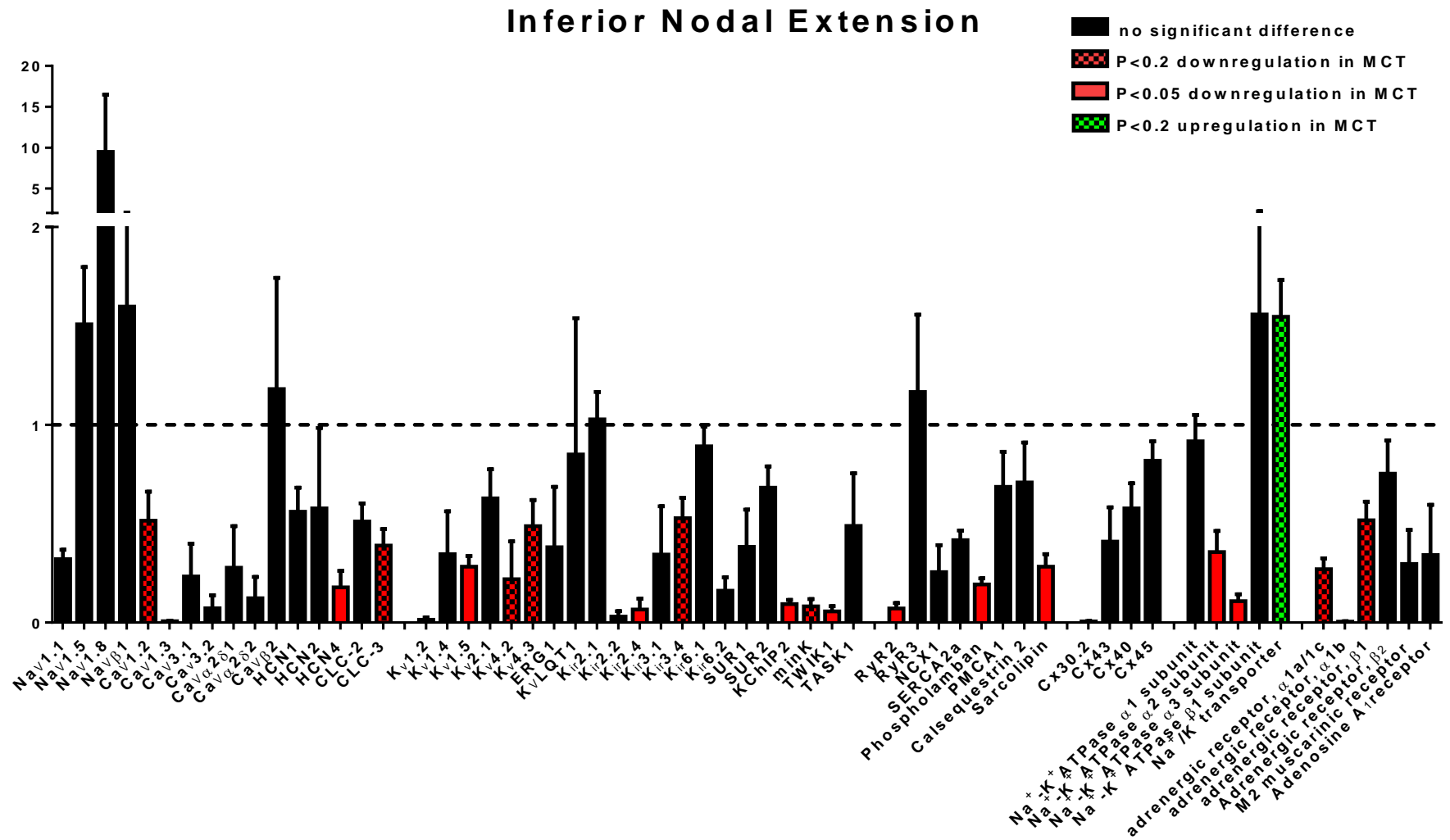


Figure 5-19. Remodelling of ion channel expression in the inferior nodal extension of the MCT treated rats. All the values are normalised to the corresponding control value for the target and tissue region. Therefore a value greater than 1 represents upregulation and a value less than 1 represents downregulation.

## Compact node

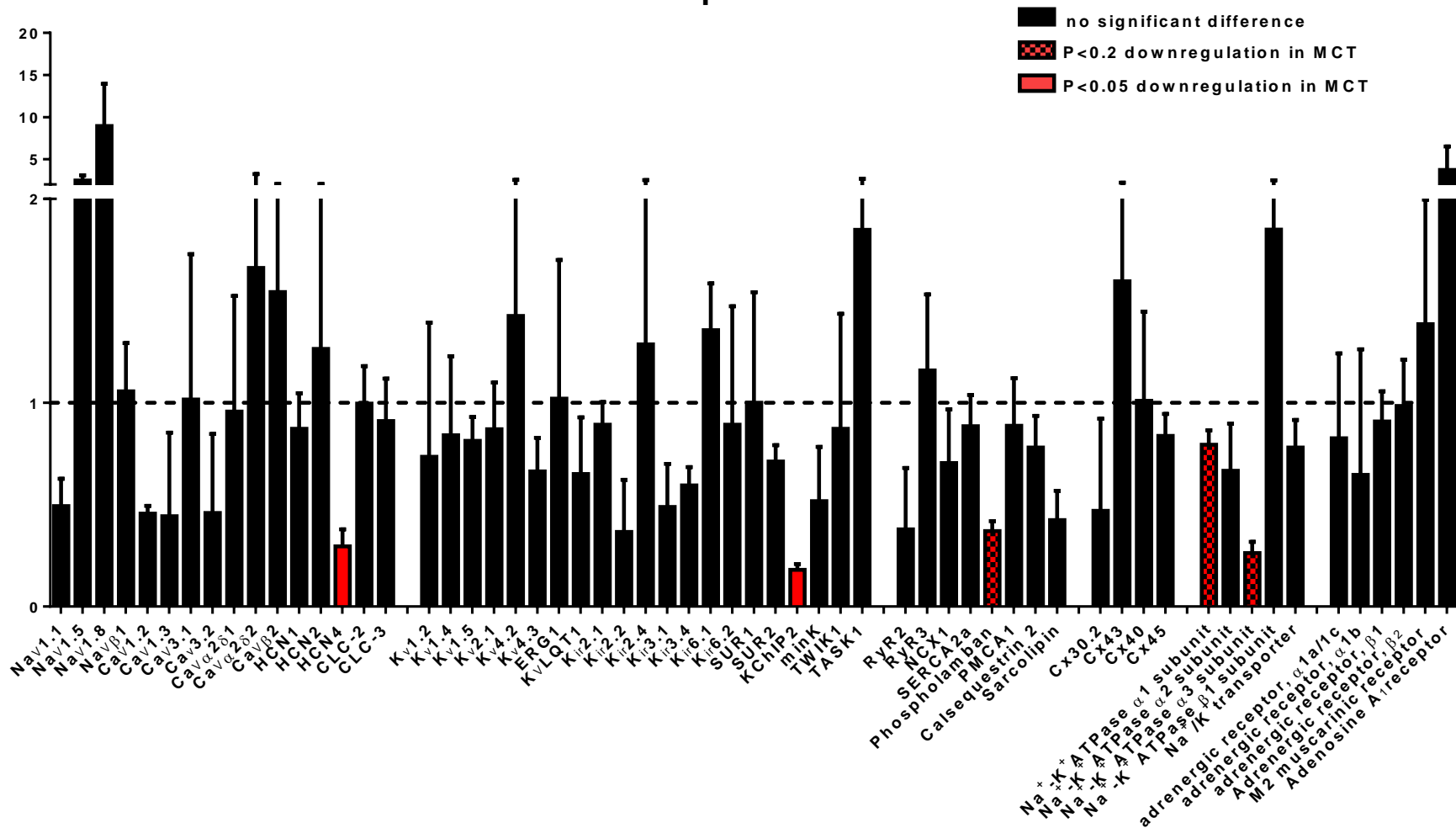


Figure 5-20. Remodelling of ion channel expression in the compact node of the MCT treated rats. All the values are normalised to the corresponding control value for the target and tissue region. Therefore a value greater than 1 represents upregulation and a value less than 1 represents downregulation.

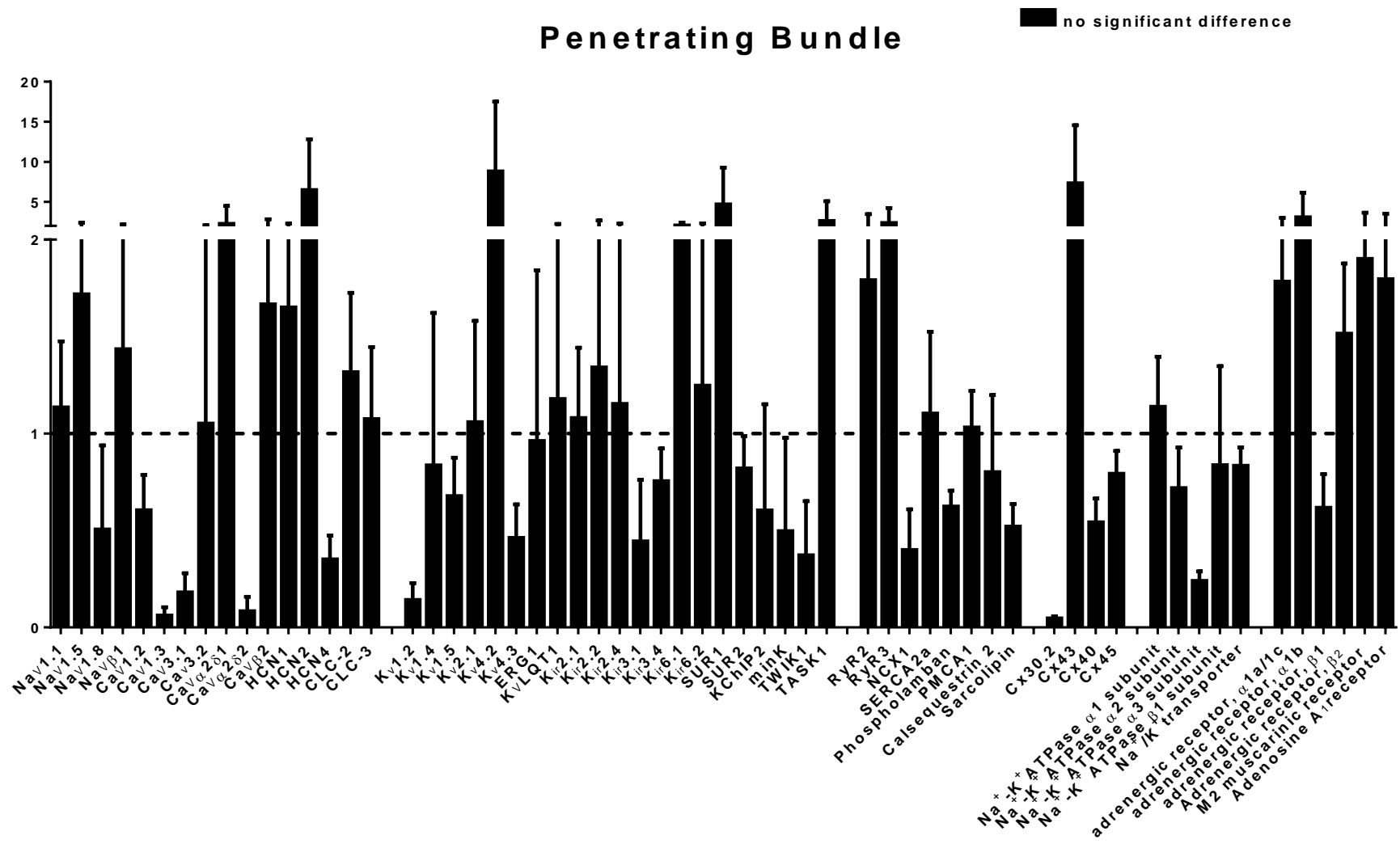


Figure 5-21. Remodelling of ion channel expression in the penetrating bundle of the MCT treated rats. All the values are normalised to the corresponding control value for the target and tissue region. Therefore a value greater than 1 represents upregulation and a value less than 1 represents downregulation.

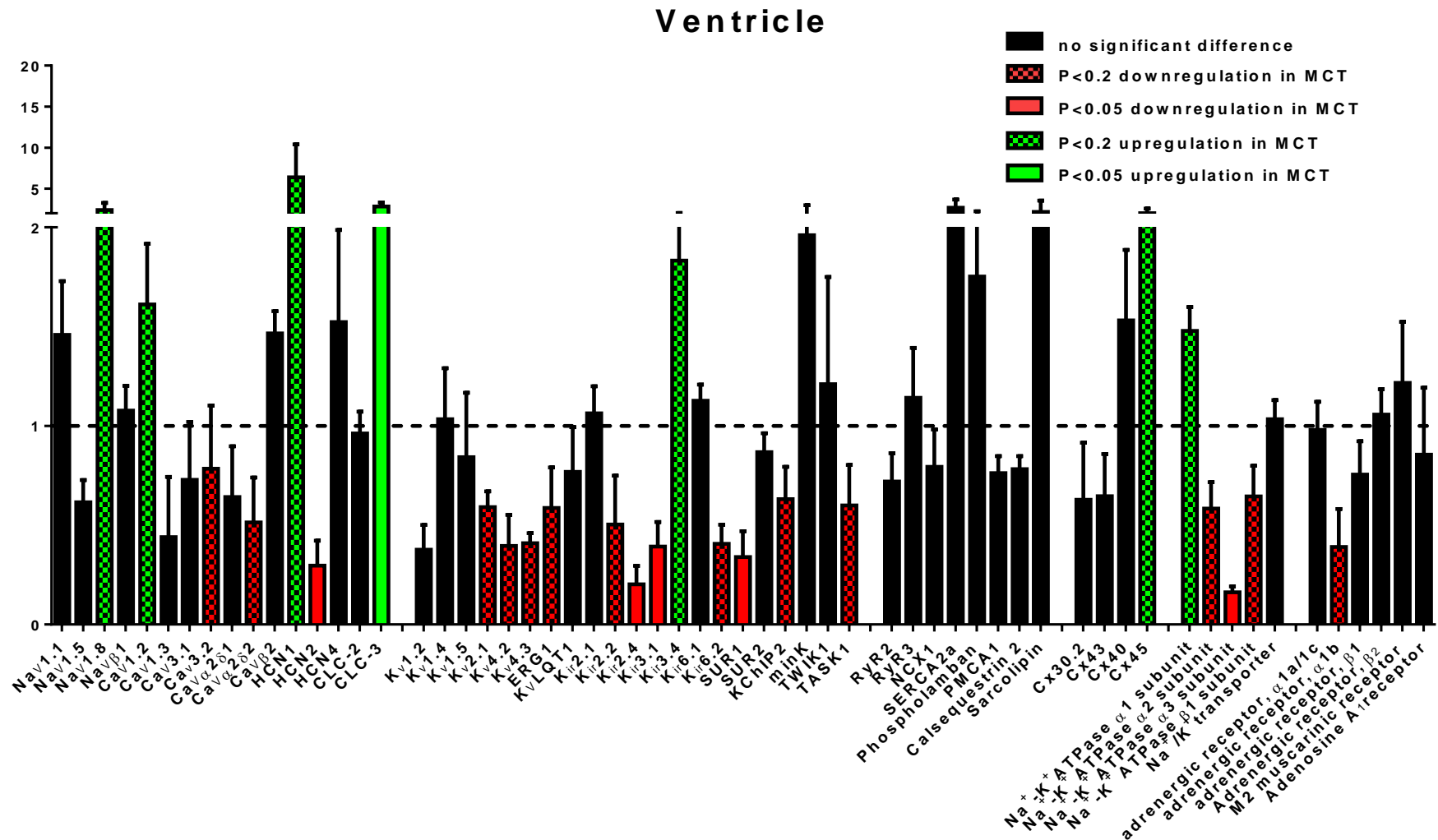


Figure 5-22. Remodelling of ion channel expression in the ventricle of the MCT treated rats. All the values are normalised to the corresponding control value for the target and tissue region. Therefore a value greater than 1 represents upregulation and a value less than 1 represents downregulation.

## 5.4 Discussion

As described in the Introduction (see section 1.4.1) there is a complex set of interactions including the assembly of the  $\alpha$  and  $\beta$  subunits of the ion channels, the voltage and time dependent properties of the individual transmembrane ionic currents, cell:cell coupling and the complex anatomy of the heart that determines impulse generation and propagation. This makes it difficult to anticipate the effects that the upregulation and downregulation of individual mRNA transcripts may have.

The functional experiments in Chapters 3 and 4 demonstrated a relative failure of conduction within the AV node in response to MCT with the suggestion that both the fast and slow pathways were affected proximal to the penetrating bundle. Given their critical role in conduction it may have been anticipated that there would be an alteration in the connexins. However, the only connexin that was significantly affected within the nodal tissue was Cx30.2 which was downregulated (Figure 5-18 and Figure 5-19). This is somewhat surprising given that studies have demonstrated that ‘knocking-out’ the very low conductance Cx30.2 leads to an increased conduction velocity across the AV node.<sup>105</sup> However, there is not a simple relationship between conduction velocity and the safety of conduction. Modelling studies have suggested that intermediate reductions in cell:cell coupling leads to a reduced conduction velocity but an increase in the safety of conduction (section 1.4.5).<sup>64</sup> Within this framework a reduction in the very low conductance Cx30.2 could lead to an increase in cell to cell coupling which maintains conduction velocity but reduces the safety of conduction. It is also notable that the relative expression of Cx30.2 was much lower than all the other connexins and it may be that any changes in Cx30.2 are only having very limited effects (Figure 5-10).

There was a consistent downregulation of HCN4 (the main protein underlying  $I_f$ ) across the atrium, transitional tissue and inferior nodal extension (Figure 5-17, Figure 5-18 and Figure 5-19) and this raises the question as to whether  $I_f$  may also have a role in conduction across the AV node.  $I_f$  has mainly been considered in relation to pacemaking function, generating an inward current during diastole that is responsible for phase 4 depolarisation and subsequent activation of voltage dependent  $Ca^{2+}$  and  $Na^+$  channels. Indeed an  $I_f$  blocking drug ivabradine is used clinically to reduce sinus rate. Initial studies on a small number of patients demonstrated no effects on the AV node and therefore subsequent larger studies have not investigated the effects of ivabradine on the AV

node.<sup>202-204</sup> There are several recent studies that suggest that  $I_f$  may play a more significant role in AV node conduction than previously recognised. Both this study and previous studies have demonstrated high levels of HCN4 in the AV node (Figure 5-11).<sup>72, 75, 76</sup> Indeed, in this study and previous studies HCN4 has been used as a marker of AV nodal tissue.<sup>72, 75, 76</sup> There is also functional evidence that  $I_f$  plays a role in AV nodal conduction; although ivabradine was not shown to have an effect on the human AV node another  $I_f$  blocking agent, zatebradine, has been shown to increase in AH interval, AVERP and Wenckebach cycle length in humans.<sup>192</sup> Ivabradine has also been shown to slow the ventricular response to AF in dogs with the mechanism thought to be specific to  $I_f$  blockade within the AV node slowing conduction and not a direct effect of  $I_f$  blockade on the atrium.<sup>205</sup> Finally as discussed in section 1.5.2.2 cardiac specific knockout of HCN4 in mice is lethal at around day 5 due to the development of CHB.<sup>84</sup>

The mechanism by which a reduction in  $I_f$  could lead to a reduction in AV node conduction has not been elucidated. As described in section 1.4.4, conduction relies on the electrotonic flow of ions between cells from an upstream ‘source’ to a downstream ‘sink’ with conduction failing if the current consumed by the ‘sink’ is greater than current generated by the ‘source’.<sup>64</sup> Within this framework it is possible that  $I_f$  may make the resting potential during diastole more positive and therefore reduce the current consumed by the nodal cells in order to trigger an action potential. This reduction in the ‘sink’ could improve both the velocity and safety of conduction. The downregulation of HCN4 seen would be expected to lead to a reduced  $I_f$  and therefore a reduction in diastolic depolarisation which could lead to the nodal cells acting as a larger ‘sink’ and hence reducing the velocity of impulse propagation and the safety of conduction. Further experimental evidence is needed to test this hypothesis this but it may provide a link between the reduced HCN4 expression seen in this chapter and the reduced velocity and safety of conduction seen in the functional experiments.

As well as  $I_f$  the ‘calcium clock’ is thought to play an important role in phase 4 diastolic depolarisation therefore pacemaking (section 1.4.4). As described above, reductions were seen in phospholamban, sacrolopin and RyR2 levels in the nodal tissues. SERCA2a and NCX were not statistically significantly reduced although the mean value for mRNA expression was lower in both cases for the MCT treated rats compared with the control rats (Figure 5-18, Figure 5-19 and Figure 5-20). There is no current evidence regarding how downregulation of these calcium clock genes may affect AV node conduction, although it could be a similar mechanism to that discussed for HCN4, i.e. a reduction in

phase 4 depolarisation and therefore a more negative resting potential leading to a greater current 'sink' during conduction with subsequent reduction in conduction velocity and the safety of conduction.

Another striking change seen in all the areas investigated was the reduction in the transcripts encoding for the  $K^+$  channels (Figure 5-17, Figure 5-18, Figure 5-19, Figure 5-20 and Figure 5-22). Reduction of the  $K^+$  currents in the ventricle has been shown in a number of different disease models including heart failure, myocardial infarction and PH.<sup>120, 137</sup> In these disease models the reduction in the both the voltage dependent repolarising  $K^+$  currents and the inward rectifying  $K^+$  currents leads to a prolongation of the action potential duration which predisposes to both EADs and DADs. Within our study the functional experiments demonstrated an increased VERP and suggested an increased AERP which are consistent with previous functional experiments and are in keeping with a prolonged action potential duration. There was also a suggestion of an increased incidence of ectopic beats coming from the AV node tissue. The mechanism of these ectopics cannot be elucidated from the current methodology, however, it is possible that they may be due to either EADs or DADs in the context of the prolonged action potential.

Several different action potentials have been described within the AV node with different morphologies and responses to early stimuli defining which population they belong to. Despite these differences in morphology the action potential of the nodal cells is broadly similar within the AN and N cells (APD<sub>80</sub>, 75-80 ms) but longer within the NH cells (APD<sub>80</sub>, 92 ms) (see section 1.5.2.2).<sup>69, 74</sup> The action potential duration within the nodal cells is longer than that of the atrial myocardium but shorter than that of the His bundle cells.<sup>69, 74</sup> It is tempting to think that a reduction in the voltage dependent  $K^+$  currents and action potential duration prolongation in the nodal tissues would lead to a reduction of excitability for subsequent beats and therefore could explain a reduction in AV node conduction and increase in Wenckebach cycle length. Supporting this interpretation  $K^+$  current blocking agents specific for  $I_{K,r}$  (E4031 and (R)-2-(2,4-bis-trifluoromethyl-phenyl)-N-[2-oxo-5-phenyl-1-(2,2,2-trifluoro-ethyl)-2,3-dihydro-1H-benzo[e]1,4-diazepin-3-yl]-acetamide) cause a prolonged AH interval and AVERP in rats.<sup>92</sup> As described in section 1.5.2.5 single cell studies in both guinea-pig ventricular cells and rabbit AV nodal cells have suggested that the Wenckebach phenomenon may be due to slow inactivation of the voltage-dependent  $K^+$  currents leading to 'post-repolarisation refractoriness'.<sup>112, 113</sup> This demonstrates that although the voltage-dependent  $K^+$  currents are required for nodal cell repolarisation and recovery of excitability their ongoing

activation also contributes to a reduction in excitability.<sup>112, 113</sup> Within this context the effects of a reduction in the voltage-dependent  $K^+$  currents could either promote or inhibit AV nodal conduction. The pharmacological studies suggest that reductions in  $K^+$  currents may reduce AV node conduction and therefore that the reductions seen in  $K_v2.1$ ,  $K_v4.2$ ,  $K_v4.3$ , minK and KChIP2 in the inferior nodal extension may play some role in the relative failure of conduction in the MCT treated rats (Figure 5-19).<sup>92</sup>

In working myocardium conduction is dependent on the upstroke of the action potential which is largely determined by  $I_{Na}$  which for which the principle  $\alpha$  subunit is  $Na_v1.5$ . Levels of  $Na_v1.5$  were unchanged in all the tissue types studied suggesting that alterations in  $I_{Na}$  may not be the cause of either the slowed conduction in the atrium or the failure of conduction in the AV node (Figure 5-17, Figure 5-18, Figure 5-19, Figure 5-20, Figure 5-21 and Figure 5-22). Despite this both experimental and modelling studies have shown that in regions of reduced cell:cell coupling, such as the AV node, conduction becomes more dependent on the more slowly activating and inactivating  $Ca^{2+}$  currents.<sup>77</sup> A reduction in  $Ca_v1.2$  and  $Ca_v1.3$  was demonstrated in the inferior nodal extension (Figure 5-19), an area of particularly low cell:cell coupling. Although the reduction was only statistically significant in the atrium and inferior nodal extension a similar qualitative reduction was seen in all the nodal regions investigated (Figure 5-17, Figure 5-18, Figure 5-19, Figure 5-20 and Figure 5-21). Surgical disruption of the inferior nodal extension has been shown to increase the Wenckebach cycle length and it seems possible that the down-regulation of  $Ca_v1.2$  may also provide part of the explanation for the relative failure of conduction in the AV node of the MCT treated animals.<sup>114</sup>

# 6 Remodelling in response to pulmonary hypertension at the protein level

---

## 6.1 Introduction

The results of the previous chapter demonstrate marked changes in mRNA expression of key ion channels, intracellular  $\text{Ca}^{2+}$  handling proteins and connexins across the different regions of the AV node and between the control and MCT treated rats. The functional consequences of these changes were discussed using the assumption that a downregulation of mRNA levels led to a reduction in functional current. This is an approach that has been used in several studies and offered valuable insights into arrhythmogenic remodelling in various disease conditions.<sup>47, 49, 121, 122</sup> However, there are many important processes that occur between mRNA expression and functional effects within the cell including translation of the mRNA into a protein, the folding, transport and assembly into a functional channel, the phosphorylation state of the proteins and the degradation of the proteins. In addition to these processes microRNAs may lead to degradation of mRNA (which will lead to a reduction in the measured quantities of mRNA), or repression of translation into protein (which will lead to maintained mRNA measurements but will reduce the protein production and therefore function).<sup>49</sup>

In light of these potential confounding factors it is useful to measure expression of the protein levels as well as the mRNA levels of the molecules of interest. Protein measurement can be undertaken with both immunofluorescence and Western blotting. Experience in our laboratory has suggested that the quantities of tissue available from the rat AV node are insufficient to allow for accurate detection by Western blotting and therefore immunohistochemistry was the technique that was chosen for this study. Both immunohistochemistry and Western blotting require antibodies with a high specificity for the proteins of interest. Within our laboratory we have validated antibodies for HCN4, RyR2, Cx40 and Cx43 on rat tissue. In light of this, immunohistochemistry experiments were restricted to these targets with the aim of validating the assumption that mRNA

levels measured in the RT-qPCR experiment will give information about protein expression in the cells.

## 6.2 Methods

The animals were generated as described in section 2.2.2. Prior to termination *in vivo* ECG was performed and PH was confirmed in all the MCT animals as described in section 2.4. Tyrode's solution ( NaCl – 120 mM, CaCl – 1.2 mM, KCl – 4mM, MgSO<sub>4</sub>.7H<sub>2</sub>O – 1.3 mM, NaH<sub>2</sub>PO<sub>4</sub>.2H<sub>2</sub>O 1.2 mM, NaHCO<sub>3</sub> – 25.2 mM, glucose – 5.8 mM) was generated on the day of the termination and bubbled with 95% O<sub>2</sub>/5% CO<sub>2</sub>. Heparin 1000 U was injected. 30 min later the rats were sacrificed and the heart excised. Hearts were immersed with oxygenated Tyrode's solution and the aorta was retrogradely perfused to flush the heart. The hearts were snap frozen with isopentane that had been chilled by immersion in liquid nitrogen and the hearts were stored at -80°C.<sup>179</sup>

The whole hearts were sectioned at 10 µm in a LM cryostat (Leica, Germany) at a temperature of -18 °C. Three sections were created per slide. The slides were stored at -80 °C for processing at a later date.

For each animal every 15<sup>th</sup> slide was selected and underwent Masson's trichrome staining as per the protocol described in section 5.2.3. The slides were imaged with the panoramic 250 Flash II (3DHistech, Hungary) and viewed using the panoramic viewer software (3DHistech, Hungary). The images were reviewed and for every slide demonstrating AV nodal tissue a corresponding slide underwent immunostaining as per protocol in section 5.2.2. Each slide contained three sections allowing for a dual labelling of Cx43 and HCN4 on one section, Cx40 and RyR2 on another and a control sample on the final section. The specificity of the antibodies, optimum dilutions and appropriate secondary antibodies has previously been empirically determined within our laboratory and are shown in Table 6-1 and Table 6-2. The immunolabelled slides were imaged with the panoramic 250 Flash II using epifluorescence and viewed using the panoramic viewer software.

A combination of the Masson's trichrome stained slides and the immunostained slides imaged using the panoramic viewer software was used to define the different regions of the AV node. These regions were then imaged using a LSM5 PASCAL confocal laser scanning microscope (Zeiss, Germany). The specificity of the staining was assessed by comparing the patterns of staining with each antibody with previously demonstrated

staining patterns in cardiac myocytes. The confocal images were quantified by assessing the intensity of the signals within the region of interest using the Volocity (Improvision, Waltham, MA, USA) software package.

<b>Antibody</b>	<b>Manufacturer</b>	<b>Species antibody raised in</b>	<b>Monoclonal/ Polyclonal</b>	<b>Concentration used</b>
HCN4	Alomone, Israel (ACC-052)	Rabbit	Polyclonal	1:100
RyR2	Thermo-Scientific, USA (MA3-926)	Mouse	Monoclonal	1:1000
Cx40	Santa Cruz, USA (sc-20466)	Goat	Polyclonal	1:100
Cx43	Millipore, Germany (MAB3068)	Mouse	Monoclonal	1:1000

**Table 6-1. Primary antibodies used for immunohistochemistry experiments.**

<b>Primary antibodies bound</b>	<b>Manufacturer</b>	<b>Species antibody raised in</b>	<b>Specificity</b>	<b>Fluorescent tag</b>	<b>Concentration used</b>
RyR2 and Cx43	Millipore, Germany (AP192 C)	Donkey	Mouse IgG	Cy3	1:400
HCN4	Millipore, Germany (AP 182F)	Donkey	Rabbit IgG	FitC	1:100
Cx40	Life Technologies, USA (A-11055)	Donkey	Goat IgG	Alexa Fluro 488	1:100

**Table 6-2. Secondary antibodies used for immunohistochemistry experiments.**

The differences between control and MCT treated rats for each region were compared using a Student's *t*-test. The differences between the control regions were compared using a 2-way ANNOVA with multiple comparisons.

## 6.3 Results

The histology and immunofluorescence images were used to look for morphological differences in the AV node of the control and MCT rats. Examples are shown in Figure 6-1 and Figure 6-2. No gross changes in morphology of the AV node were seen between the control and MCT rats and therefore further analysis was not performed with the Masson's trichrome or epifluorescent images. The images were analysed for all the rats

and used to determine the position of the six regions of the AV node as described in section 5.2.4 (Figure 6-1 and Figure 6-2).

The staining patterns for HCN4, RyR2, Cx40 and Cx43 are shown in Figure 6-3 to Figure 6-8. RyR2 showed mainly striated intracellular staining in the working myocardium which is in keeping with previous studies demonstrating alignment along the T-tubules (Figure 6-3 and Figure 6-8). In the nodal tissues there was a less clear staining pattern with mainly membranous staining and limited intracellular staining with striations (Figure 6-4, Figure 6-5 and Figure 6-6). There are limited data regarding RyR2 distribution patterns in the nodal tissues, but a similar pattern has previously been demonstrated in the rabbit in both the neonatal AV node and the adult SA node.<sup>75, 199</sup>

HCN4 was present in the inferior nodal extension, compact node and penetrating bundle where there was patchy staining in both the cell membrane and intracellular space (Figure 6-4, Figure 6-5 and Figure 6-6). Within the transitional tissue there were regions of positive and negative staining for HCN4 suggesting strands of nodal like tissue extending from the compact node into the atrium (Figure 6-4). There was only background staining seen in the working myocardium (Figure 6-3 and Figure 6-8).<sup>75</sup>

In the tissues studied Cx40 was expressed in the penetrating bundle where it showed a punctate membranous staining pattern (Figure 6-7). Only background staining was seen in all other tissue regions (Figure 6-3, Figure 6-4, Figure 6-5, Figure 6-6 and Figure 6-8). Cx43 was present in the working myocardium but absent from the nodal tissues (Figure 6-3, Figure 6-4, Figure 6-5, Figure 6-6, Figure 6-7 and Figure 6-8). The distribution was strongly localised to the gap junctions connecting the working myocardial cells longitudinally.<sup>75</sup>

The results of the protein quantification are shown in Table 6-3. Within the control group HCN4 protein expression was significantly greater in the compact node than the atrium, transitional tissue and the ventricle. Cx40 was highly expressed in the penetrating bundle with a low level in all other regions of the myocardium. Cx43 expression was significantly greater in the ventricle than the inferior nodal extension, compact node and penetrating bundle. No regional differences in expression were shown for RyR. Comparisons between the control and MCT groups revealed no significant differences in any of the regions.

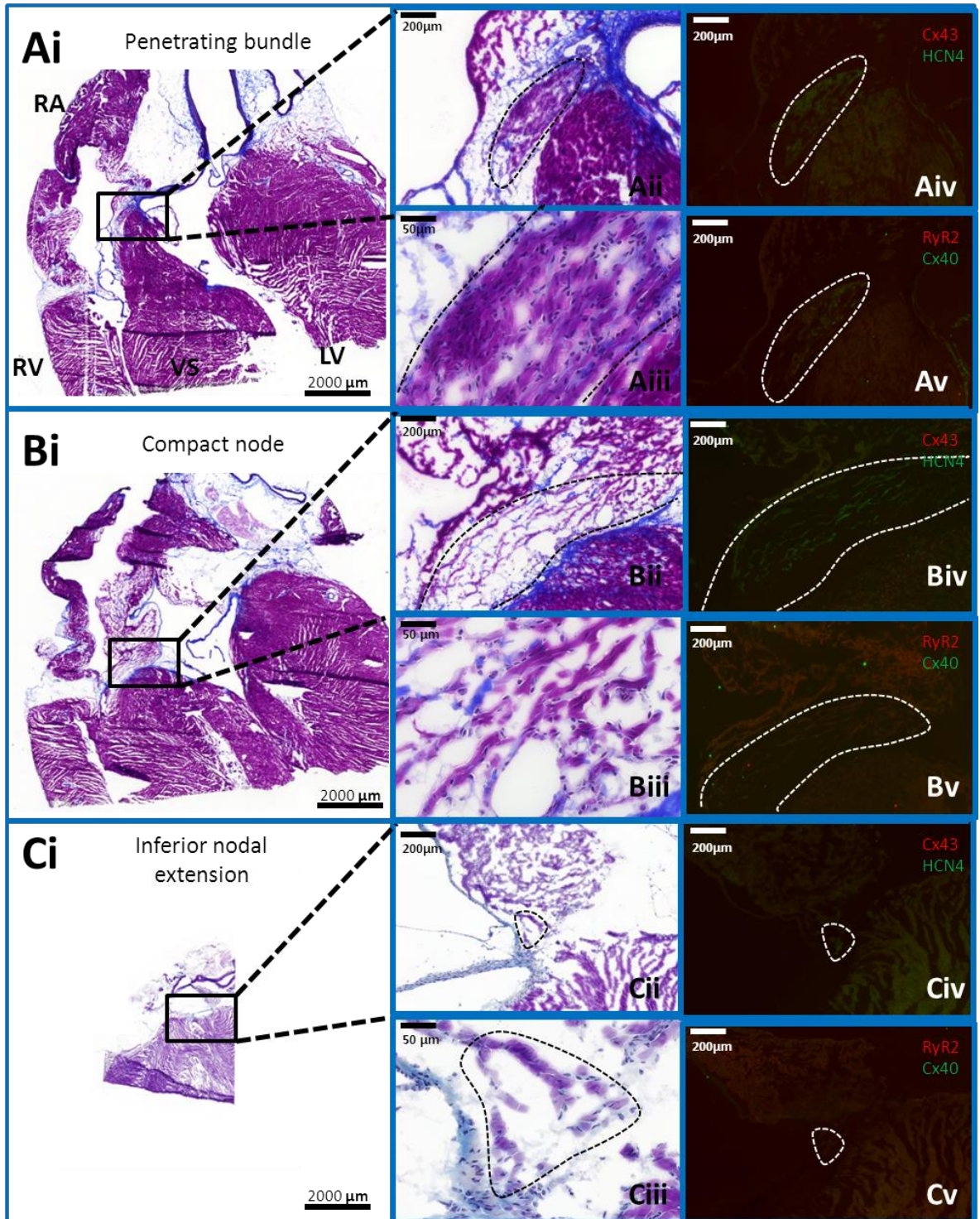


**Figure 6-1.** Images from the slidescanner for Masson's trichrome staining and immunohistochemistry in the control rat. **A)** Penetrating bundle. Ai-iii show identification of the penetrating bundle which is encased in the central fibrous body. Aiv) Immunostaining for Cx43 (red) and HCN4 (green) The penetrating bundle stains strongly for HCN4 but Cx43 is absent. The atrium and ventricle stain strongly for Cx43 but HCN4 is absent. Av) Immunostaining for RyR2 (red) and Cx 40 (green). RyR2 is expressed throughout all the myocardial tissues but Cx40 is only present in the penetrating bundle. **B)** Images as per section A demonstrating the compact node and transitional tissue. The compact node is bounded by the tricuspid valve annulus inferiorly and extends into the transitional tissue. The compact node stains strongly for HCN4; Cx43 is absent. The transitional tissue shows an intermediate staining pattern. RyR2 is expressed throughout the myocardial tissues; Cx40 is absent. **C)** Images as per section A demonstrating the inferior nodal extension. The inferior nodal extension is a small area of tissue on the tricuspid annulus along the right atrial side of the atrial septum. It stains for HCN4 but Cx43 is absent. RyR2 is present throughout the myocardial tissues; Cx40 is absent. See section 5.2.4 for further details. LV – left ventricle, RA – right atrium, RV, right ventricle, VS – ventricular septum.

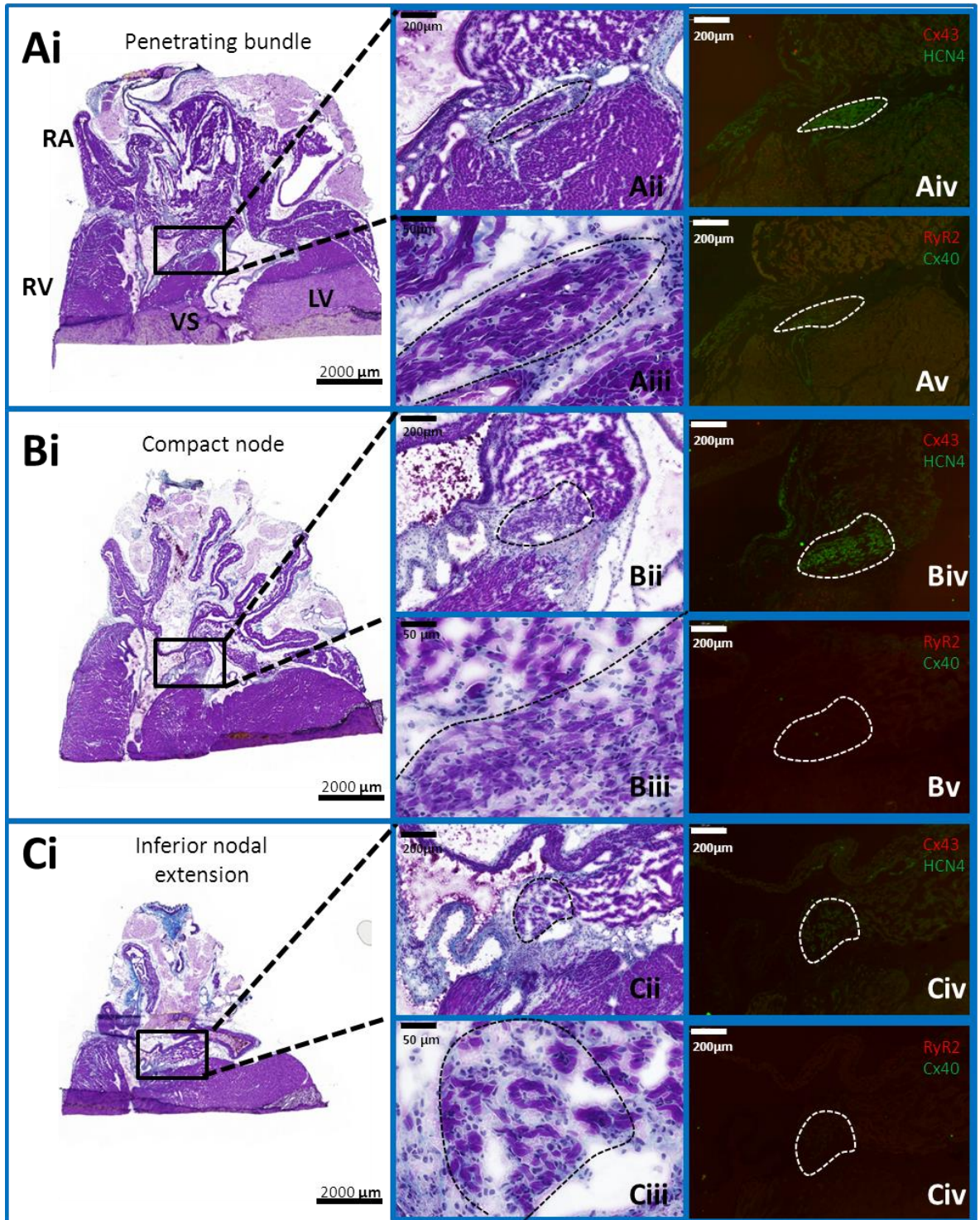


Figure 6-2. Images from the slidescanner for Masson's trichrome staining and immunohistochemistry in the MCT treated rat. All labels as per Figure 6-1.

# Atrium

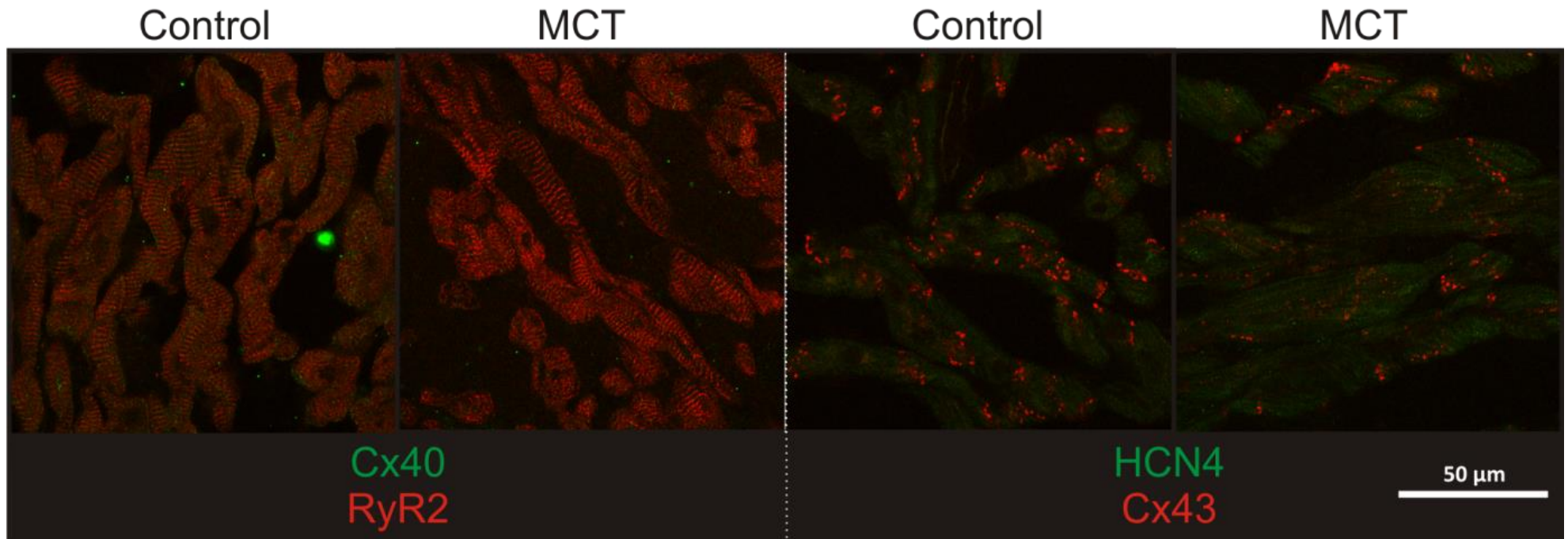


Figure 6-3. Immunohistochemistry staining patterns for the atrium in control and MCT rats. In the left panel Cx40 is stained green and RyR2 is stained red, in the right panel HCN4 is stained green and Cx43 is stained red.

# Transitional tissue

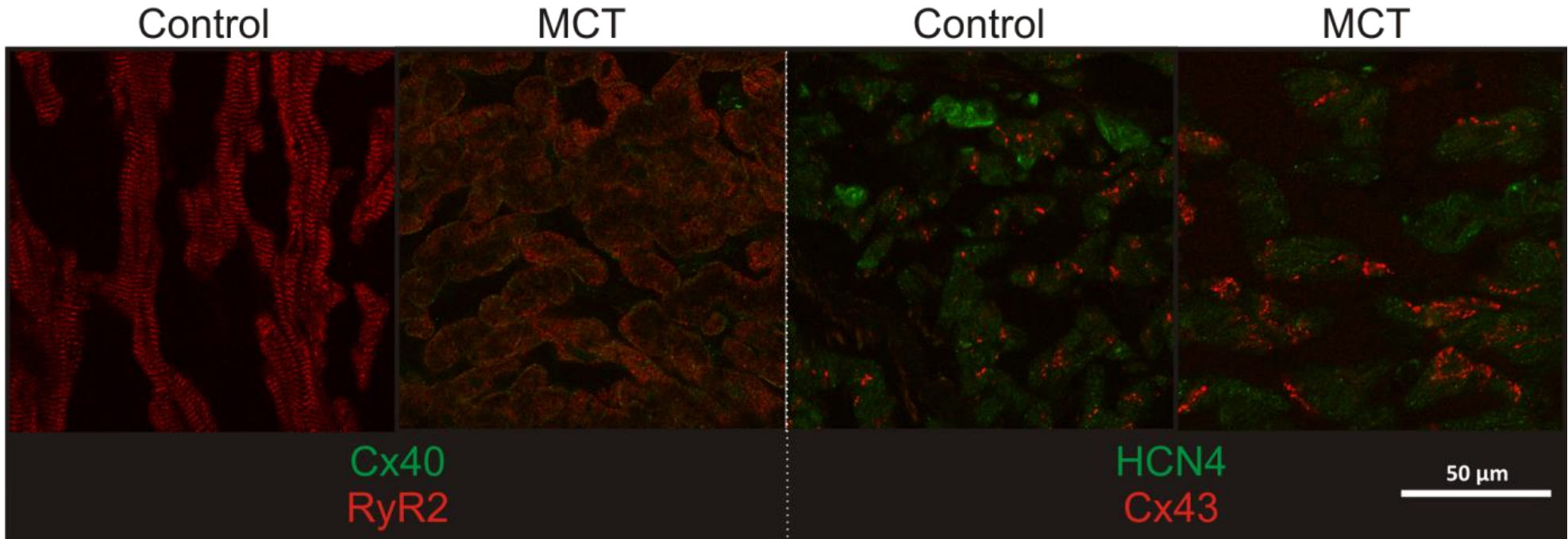


Figure 6-4. Immunohistochemistry staining patterns for the transitional tissue in control and MCT rats. In the left panel Cx40 is stained green and RyR2 is stained red, in the right panel HCN4 is stained green and Cx43 is stained red.

## Inferior nodal extension

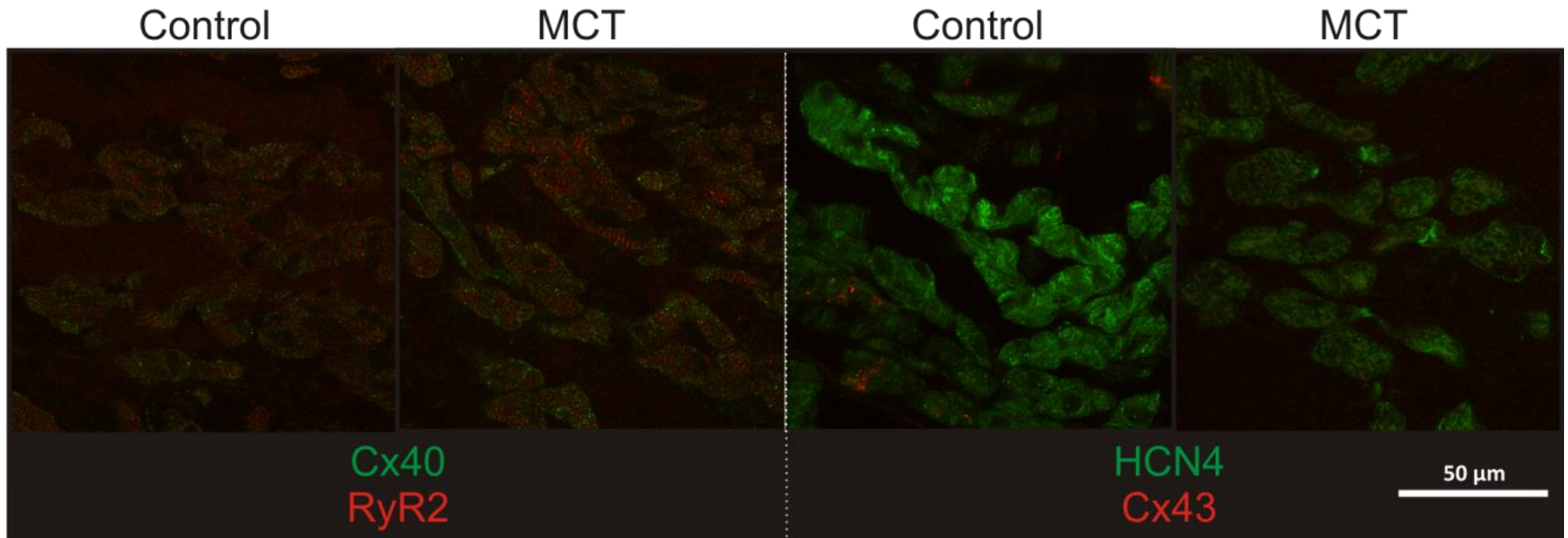


Figure 6-5. Immunohistochemistry staining patterns for the inferior nodal extension in control and MCT rats. In the left panel Cx40 is stained green and RyR2 is stained red, in the right panel HCN4 is stained green and Cx43 is stained red.

## Compact node

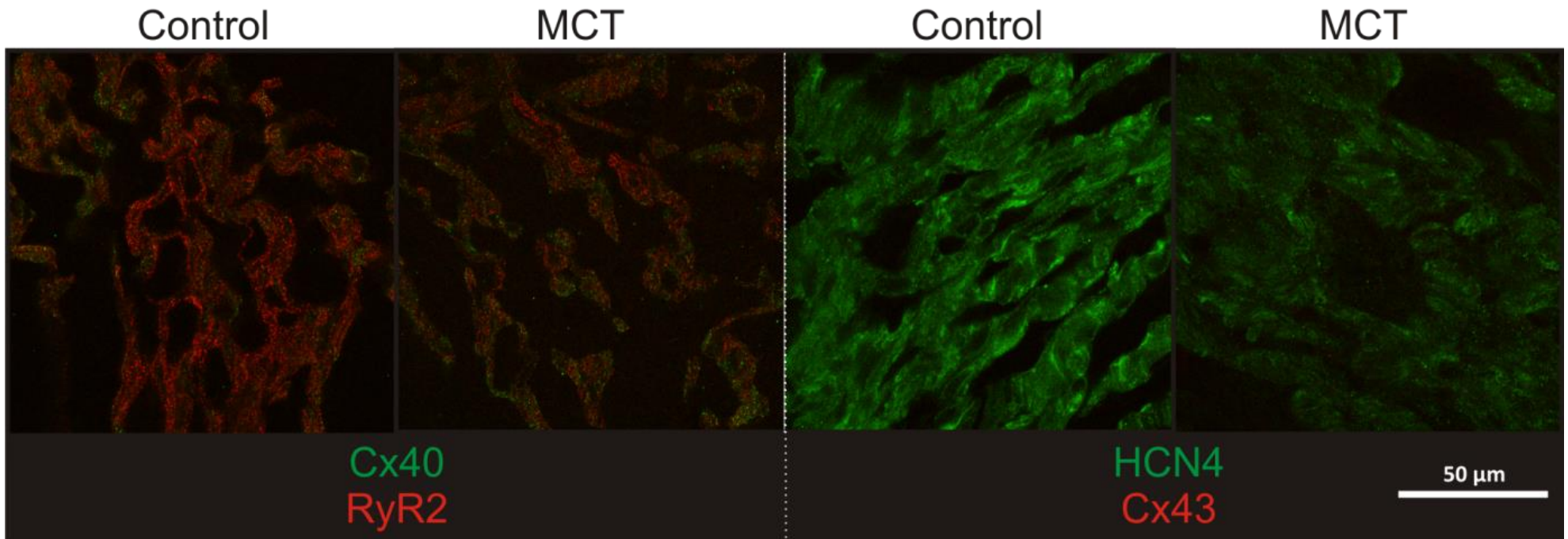


Figure 6-6. Immunohistochemistry staining patterns for the compact node in control and MCT rats. In the left panel Cx40 is stained green and RyR2 is stained red, in the right panel HCN4 is stained green and Cx43 is stained red.

## Penetrating bundle

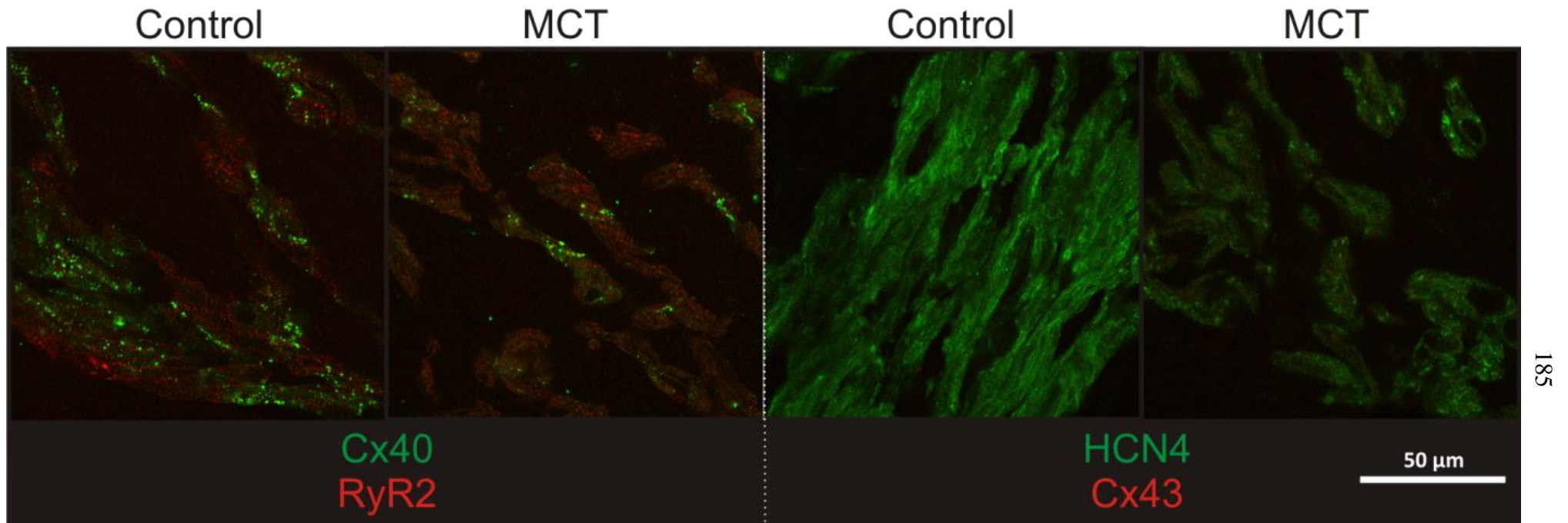


Figure 6-7. Immunohistochemistry staining patterns for the penetrating bundle in control and MCT rats. In the left panel Cx40 is stained green and RyR2 is stained red, in the right panel HCN4 is stained green and Cx43 is stained red.

# Ventricle

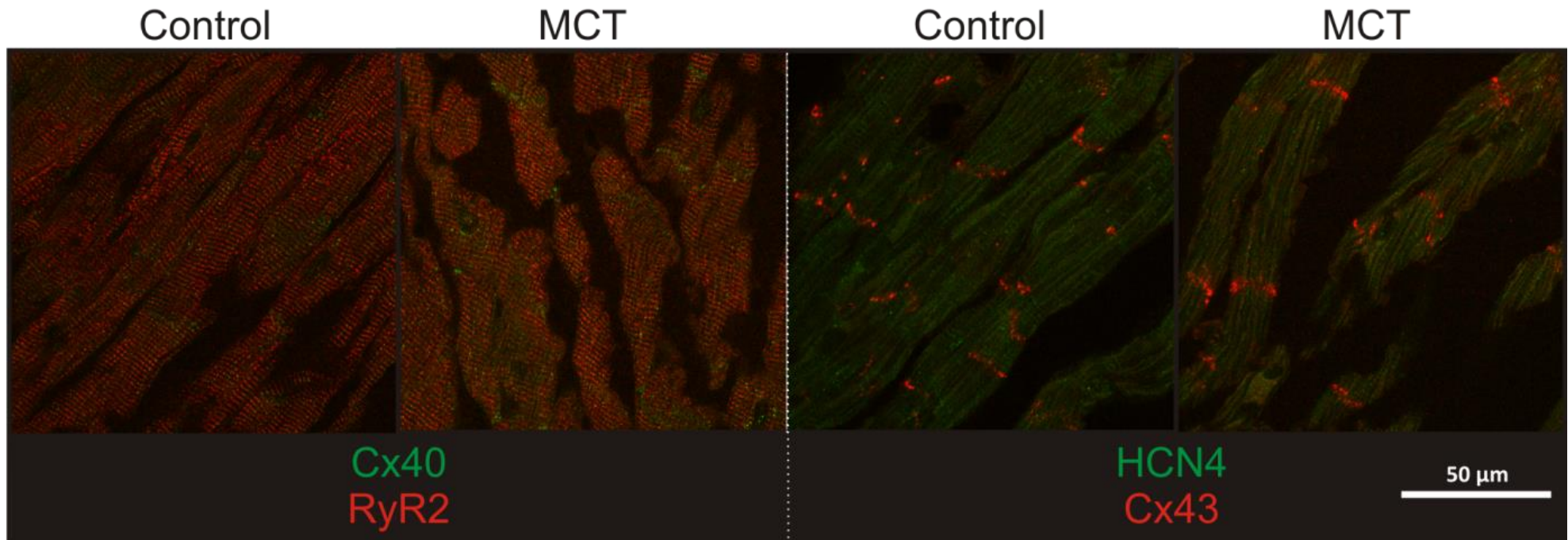


Figure 6-8. Immunohistochemistry staining patterns for the ventricle in control and MCT rats. In the left panel Cx40 is stained green and RyR2 is stained red, in the right panel HCN4 is stained green and Cx43 is stained red.

	Atrium		Transitional tissue		Inferior nodal extension		Compact node		Penetrating bundle		Ventricle	
	Control (n=4)	MCT (n=4)	Control (n=4)	MCT (n=4)	Control (n=4)	MCT (n=3)	Control (n=4)	MCT (n=4)	Control (n=4)	MCT (n=4)	Control (n=4)	MCT (n=4)
HCN4	22.70 ± 0.67	22.60 ± 0.937	22.89 ± 0.94	24.06 ± 2.38	38.38 ± 5.28	35.48 ± 4.63	46.64 ± 2.03	44.47 ± 7.99	39.54 ± 3.46	36.99 ± 5.50	25.63 ± 2.32	25.77 ± 0.89
RyR2	47.04 ± 2.44	48.89 ± 4.47	51.20 ± 5.85	35.53 ± 7.21	35.77 ± 5.72	29.69 ± 2.91	46.53 ± 4.06	35.17 ± 6.25	29.15 ± 1.04	33.30 ± 4.91	47.04 ± 2.45	59.17 ± 8.89
Cx40	20.64 ± 0.93	21.49 ± 1.16	19.10 ± 0.4528	19.27 ± 0.39	22.29 ± 1.34	20.02 ± 1.35	21.71 ± 1.09	22.57 ± 1.29	30.41 ± 3.40	24.48 ± 1.78	19.89 ± 0.36	20.83 ± 0.62
Cx43	24.07 ± 2.33	24.25 ± 0.80	24.19 ± 3.89	23.71 ± 2.10	16.95 ± 0.77	17.74 ± 1.41	14.32 ± 1.07	15.77 ± 1.20	16.77 ± 2.76	15.61 ± 1.01	32.19 ± 5.60	35.33 ± 3.23

**Table 6-3. Results of protein quantification with epifluorescence. All values are means ± SEM and are in arbitrary fluorescence units.**

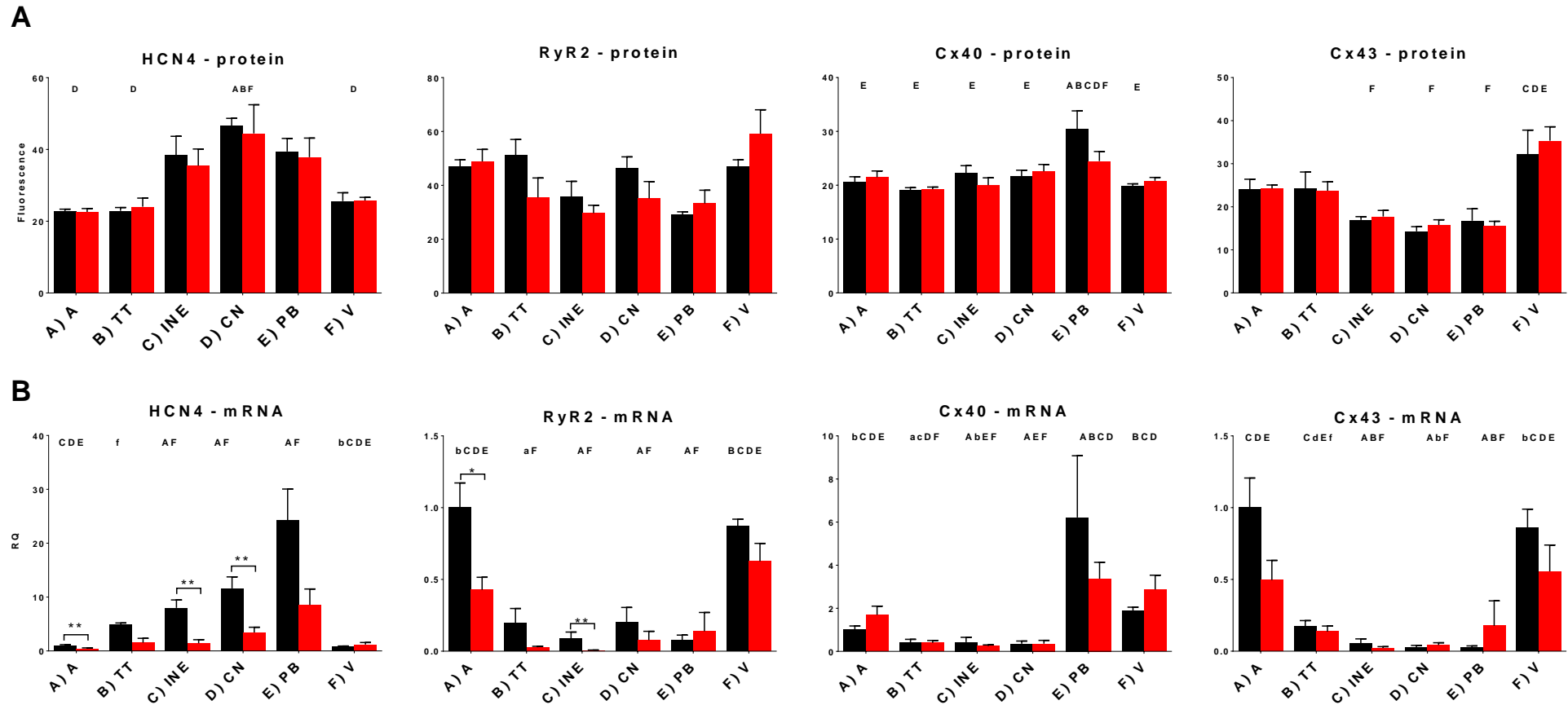


Figure 6-9. A) Protein expression level assessed by fluorescence for each region in control and MCT treated rats. The significant differences ( $P < 0.05$  using ANNOVA with multiple comparisons) are marked with letters above each region. There were no significant differences between control and MCT treated animals assessed by Student's *t*-Test. B) Corresponding data from the RT-qPCR experiment (see Chapter 5). Letters correspond to significant differences between the control regions (lower case letters,  $P < 0.2$ , upper case letters,  $P < 0.05$ ; see section 5.2.16). The bars indicate significant differences between the control and MCT rats assessed by limma test (\*  $P < 0.2$ ; \*\*  $P < 0.05$  see section 5.2.16). A) Atrium; B) Transitional tissue; C) Inferior nodal extension; D) Compact node; E) Penetrating bundle F) Ventricle.

## 6.4 Discussion

Quantification of protein using the confocal images reveals qualitatively similar results to those demonstrated by PCR for the control rats. For HCN4 the highest levels of protein were detected in the compact node whereas the mRNA experiments demonstrated the greatest quantity of HCN4 within the penetrating bundle but in both experiments the nodal tissue showed greater quantities of HCN4 than the working myocardium (Figure 6-9). Similarly Cx43 protein expression was high in the atrium and ventricle with low levels in the compact node and inferior nodal extension which is in concordance with the mRNA data in which Cx43 expression was high in the atrium and ventricle but low in the inferior nodal extension, compact node and penetrating bundle (Figure 6-9). The pattern of Cx40 expression was similar between the protein and mRNA experiments with high levels seen in the penetrating bundle and relatively low levels seen in all other areas (Figure 6-9). Some differences were seen with RyR2: in the protein experiments there were no significant differences detected between any of the regions and although the atrium and ventricle showed high levels of RyR2 as in the mRNA experiments there was also surprisingly high expression of RyR2 in both the transitional tissue and compact node.

Comparing the signal intensity of the staining pattern for the four targets (RyR2, HCN4, Cx40 and Cx43) in each region between the control and MCT treated rats revealed no significant differences in the means. This is in contrast to the findings from the mRNA experiments where significant reductions were demonstrated for HCN4 and RyR2 in the nodal tissues. This discrepancy raises questions regarding the importance of the mRNA remodelling in determining functional changes in electrophysiology of the MCT animals.

It is possible that the failure of the protein data to follow the mRNA data is due to technical factors. The most obvious of these is the smaller sample size in the immunofluorescence experiments. There are other issues regarding the use of immunofluorescence to quantify protein expression. Immunofluorescence involves the binding of antibodies as an intrinsic part of the methodology but this is an inherently variable process that is affected by the preservation and thickness of the tissue preparations, the time of the antibody application, the concentration of the antibody and temperature. These factors were standardised by performing the staining for all rats on the same day and imaging all the slides on the same day. Despite this the results show a relatively large standard error which makes determining differences between the control and MCT treated animals difficult. The compact node for all control and MCT treated

animals are shown in Figure 6-10. It can be seen that there are differences in staining intensity within both the control and MCT groups although the differences are much greater in the MCT group. Although the mean value of the signal intensity was lower in the MCT treated rats the compact node from a single MCT treated rat showed a high signal intensity which was greater than that from any of the control rats. There was no significant difference in the mean value but there was a significant difference in the variance of the control and MCT animals assessed by the F-test ( $P=0.05$ ).

Background fluorescence and non-specific staining reduce the specificity of the fluorescent signal for the protein of interest. This results in a large 'signal to noise ratio' when using immunofluorescence to quantify protein; for example the ratio between the highest and lowest signal for HCN4 is 2:1 (compact node:atrium) in the immunofluorescence experiments and 31:1 (penetrating bundle:ventricle) in the RTqPCR experiments. In order to correct for the problems of non-specific staining and background fluorescence I have attempted to 'correct' the values for each region by subtracting the fluorescence of a region with no specific labelling for the protein of interest from all other regions for that animal. For this technique to be used, a region with no specific staining is required. For HCN4 and Cx40 the fluorescence from the atrium has been subtracted from all other regions and for Cx43 the fluorescence from the compact node has been subtracted from all other regions. There were no regions which showed an absence of labelling for RyR2 and therefore 'correction' has not been applied to the RyR data. Although the corrected data are more similar to the mRNA data there are still no differences between the control and MCT treated rats for the protein levels (Figure 6-11).

In a further attempt to clarify the situation an analysis has been performed pooling the values for the nodal tissues (i.e. inferior nodal extension, compact node and penetrating bundle) and omitting the values for the MCT treated animal that had abnormally high fluorescence (Figure 6-10). Using a *t*-test to compare the difference between the control and MCT treated rats gave a P value for of 0.06 with a trend towards reduced HCN4 expression in the MCT treated rats.

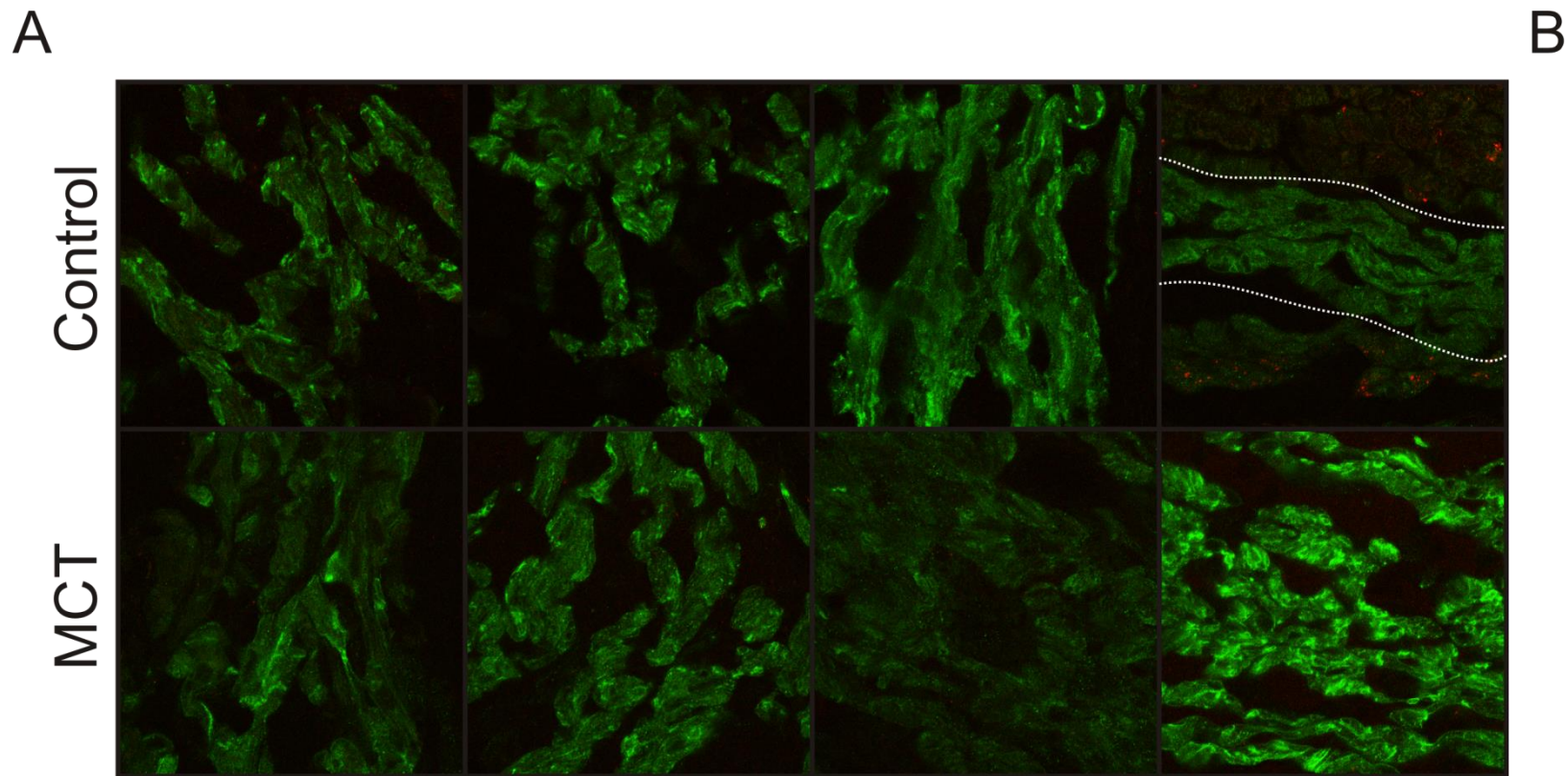


**Figure 6-10. HCN4 labelling in the compact node (green signal). A)** The samples used for assessment of the quantity of HCN4 in the compact node are shown for all the control and MCT treated rats. One MCT treated rat showed very high levels of HCN4 staining (bottom right panel). **B)** Scatter plot of HCN4 protein expression in the compact node. Mean and standard error bars shown demonstrating the greater variability in the MCT rats.

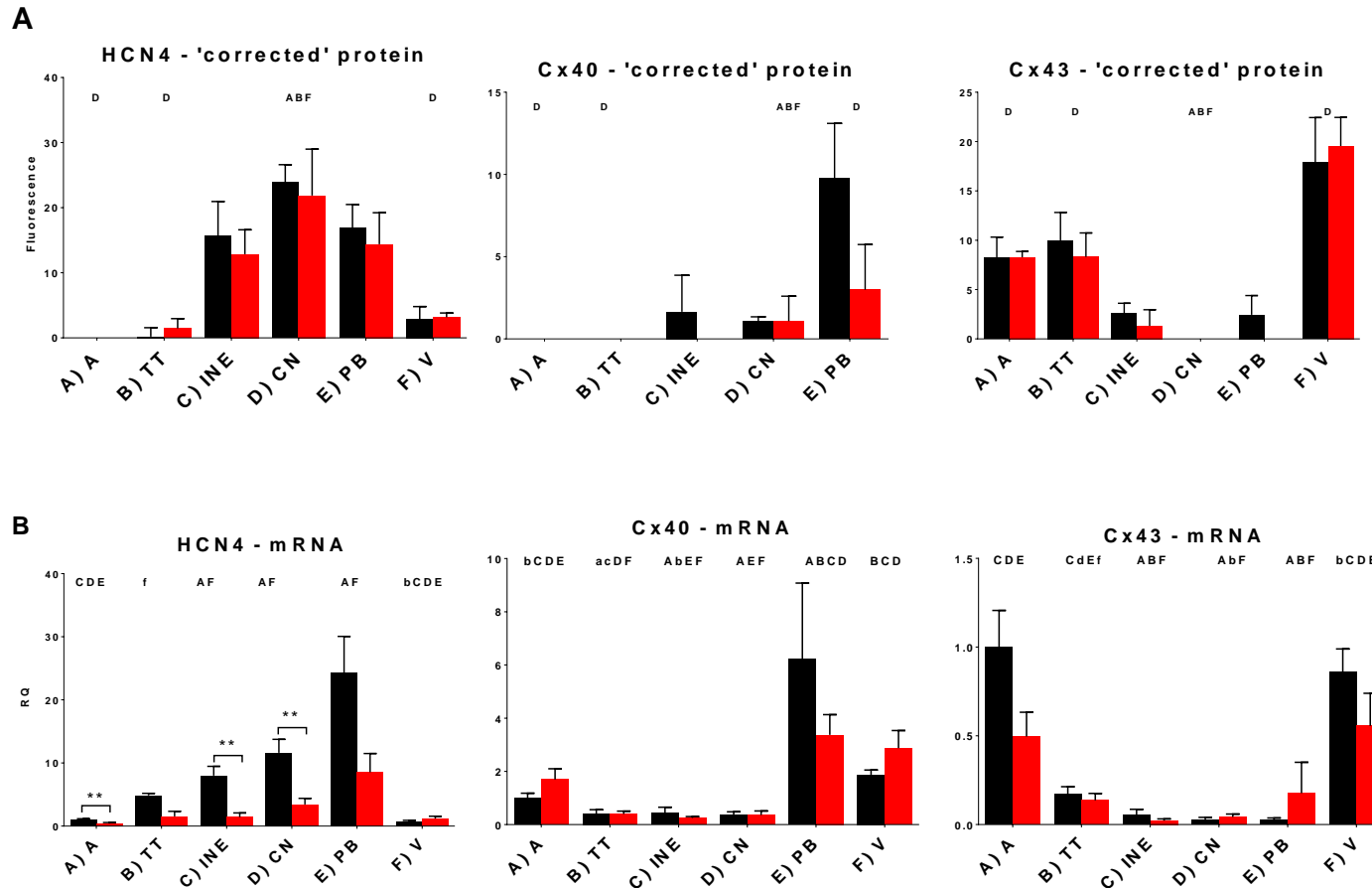


Figure 6-11 A) Protein expression level assessed by fluorescence for each region corrected by removing the value for regions with no specific staining (see text for details). The significant differences between regions ( $P < 0.05$  using ANNOVA with multiple comparisons) are marked with letters above each region. There were no significant differences between control and MCT treated animals assessed by Student's *t*-test. B) Corresponding data from the RT-qPCR experiment (see Chapter 5). Letters correspond to significant differences between the control regions (lower case letters,  $P < 0.2$ ; upper case letters,  $P < 0.05$ ; see section 5.2.16). The bars indicate significant differences between the control and MCT treated rats assessed by the limma test; \*  $P < 0.2$ , \*\*  $P < 0.05$  (see section 5.2.16). A) Atrium; B) Transitional tissue; C) Inferior nodal extension; D) Compact node; E) Penetrating bundle F) Ventricle.

The difficulties with immunofluorescence outlined above mean that it is difficult to know if there is no change in protein expression in the MCT treated rats or simply an inadequate methodology with insufficient n-numbers to demonstrate a change. If there is no change in the expression of proteins in the MCT treated rats it is possible that this is due to the acuteness of the MCT model meaning that there is insufficient time between the development of pulmonary hypertension and animal sacrifice for the transcriptional changes at the mRNA level to be reflected in the protein levels; however, if this is the case it raises questions regarding the relevance of the mRNA changes seen in Chapter 5 for the functional changes seen in the AV node (Chapters 3 and 4).

Despite the limitations described above the protein expression experiments have delivered findings consistent with the qPCR data for the control rats. Further work with larger n-numbers is required to characterise the change in protein levels seen in the AV node in the MCT model.

# 7 Effects of macitentan administration in the monocrotaline model

---

## 7.1 Introduction

Studies using the MCT model have given positive results from drug therapy including ERAs, sildenafil and prostanoids which are now widely used in clinical practice as well as several experimental compounds which are under investigation for the treatment of PAH in the future.<sup>149, 206-209</sup> There are no data on the effects of treatment for PAH on arrhythmias in patients with PAH and there are limited data documenting the effects of experimental compounds on arrhythmias in models of PH, although as described in section 1.6.4 a reduction of lateralisation of Cx43 has been shown with ERAs and sildenafil and a reduction of dysregulation of the Ca<sup>2+</sup> handling proteins with sildenafil in the MCT model.<sup>140, 141</sup>

Endothelin is a 21-amino acid peptide which is produced mainly by the vascular system and acts in a paracrine manner to regulate vasoconstriction, cell proliferation, cell migration and fibrosis.<sup>210</sup> Activation of the endothelin system plays a central role in the pathogenesis of PAH.<sup>210</sup> ERAs are widely used in clinical practice for patients with World Health Organisation (WHO) class II to IV symptoms, either as monotherapy or in combination with other agents.<sup>1, 211-213</sup> They have beneficial effects on haemodynamic parameters, objective measurements of exercise capacity and subjective symptom scores.<sup>1, 211, 212</sup> Data regarding ERAs and mortality are limited, although registry data suggest a survival benefit with the ERA bosentan.<sup>1, 211, 212</sup> Macitentan is a new ERA which has been shown in animal studies to have improved tissue penetration, longer receptor binding and affinity for both the endothelin A and B receptor compared with the older ERA bosentan.<sup>207</sup> The use of macitentan to treat PAH has been investigated in a phase III clinical trial enrolling WHO class II to IV patients showing a significant improvement in exercise capacity and haemodynamic parameters at 6 months and a significant reduction in morbidity over a follow up period of up to 36 months.<sup>214</sup>

The experimental design of the animal studies in the MCT model has varied such that some studies have started therapy on the same day as the MCT injection, i.e. a 'prevention' strategy, whereas others have waited until there is evidence of the animals displaying PH

before commencing therapy, i.e. a ‘treatment’ strategy. In cases where ‘prevention’ and ‘treatment’ have been compared there has been a greater effect with ‘prevention’ than with ‘treatment’ in terms of survival, parameters of heart failure and arrhythmogenic remodelling of the  $\text{Ca}^{2+}$ -handling proteins.<sup>142, 206, 208, 215</sup> These findings raise questions about the extent to which ‘prevention’ studies are applicable to clinical practice, particularly given that the dramatic successes seen in ‘prevention’ studies have not been borne out in clinical practice.

The effect of macitentan on the echo and ECG parameters of PH demonstrated in chapters 2 and 3, and also the possibility of macitentan administration leading to survival benefits were investigated.

## 7.2 Methods

The MCT model was created in a similar manner to chapter 0; however, some minor alterations to the protocol were made to allow the administration of macitentan. Male Wistar rats (n=36; weight 200 g; Charles River, UK) were arbitrarily assigned to three equal groups (n=12). All animals received pulverised chow only from day 0 to day 11. The control group (CON) received saline injection (3 ml/kg) by ip injection on day 0 and macitentan (Actelion Pharmaceuticals Ltd, Allschwil, Switzerland) 30 mg/kg/day admix to pulverized chow from day 11 to the day of termination. The MCT only group received MCT 60 mg/kg by ip injection on day 0 and pulverized chow only from day 11 to the day of termination. The macitentan treated group (MACI) received MCT injection 60 mg/kg by ip injection on day 0 and macitentan 30 mg/kg/day admix to pulverized chow day 11 to the day of termination.<sup>207</sup> Monocrotaline was prepared as described in section 2.2.2.

ECG and echo recordings were performed as described in section 2.2.4 and 2.2.5. ECG and echo were recorded on day 0 immediately prior to injection, and on day 7, day 14 and day 21.

The animals were weighed and their clinical condition was assessed twice weekly in the first 18 days and daily thereafter. Animals were sacrificed on the day that the following pre-specified symptomatic endpoints were met as described in section 2.2.3 i.e. tachypnoea, reduced movement, piloerection and distress or weight loss greater than 10g over a 48 hour period. Unlike the protocol described in section 2.2.3 the control animals were not sacrificed within 24 hours of the monocrotaline animals. Each animal was

monitored with those that did not meet the symptomatic criteria electively sacrificed on day 28. This change was made to allow assessment of mortality differences between the groups.

Analysis of the echo and ECG parameters was performed using two-way repeated measures ANNOVA with the two factors being time and treatment group; time was the repeated measure. Multiple comparisons were made to compare the means of each measured parameter between the three treatment groups at each timepoint. Corrections for multiple testing were not made due to the small sample size.<sup>193</sup> Survival analysis was performed using the log-rank (Mantel-Cox) test.

## 7.3 Results

Table 7-1 shows that both the MCT group and the MACI group had increased heart weight and decreased body weight compared with the CON group. The differences between the MCT group and MACI group were not significant. There was no difference in lung weight between the MACI group and the CON group. Although the MCT group did show an increase in lung weight compared with the CON group, there was no significant difference when the MCT group and MACI group were compared directly.

	CON (n=12)	MCT (n=11-12)	MACI (n=12)
Body weight at day 21 (g)	359 ± 11	331 ± 6 *	328 ± 6 *
Heart Weight (g)	1.24 ± 0.12	1.541 ± 0.21 **	1.46 ± 0.14 **
Lung weight (g)	2.36 ± 1.08	3.206 ± 0.71 *	2.85 ± 0.35

**Table 7-1. Body weights on day 21 and heart and lung weights on termination of the CON, MCT and MACI groups. Mean ± SEM. \* P<0.05 MCT or MACI vs. CON assessed by unpaired Student's *t*-test; \*\*P<0.005 MCT or MACI vs. CON assessed by unpaired Student's *t*-test.**

Figure 7-1 shows that both the MCT and MACI group developed echo evidence of PH with a change from a 'rounded' pulmonary velocity profile to a 'spike and dome' morphology. The timings of these changes are summarised in Figure 7-2. The earliest changes in echo parameters were seen at day 7 with a reduction in PVmax of 10% in the MCT group and 13% in the MACI group compared with the CON group (Table 7-2 and Figure 7-2A). The reduction of PVmax in both MCT and MACI groups when compared with the CON group suggests that PH had begun to develop by day 7. The only other parameter to show a significant difference was a reduction of LV internal diameter by 17% in the MACI group compared with the control group.

At day 14 there was evidence of PH in both the MCT and MACI groups, with reductions in PVmax of 20% in the MCT group and 14% in the MACI group compared to the CON group. The PAAT was reduced by 25% in the MCT group compared with the CON group and 20% compared with the MACI group. There was no significant change in PAAT in the MACI group compared with the CON group. No other significant changes were seen between the MACI and MCT groups. (Figure 7-2 and Table 7-3)

At day 21, both the MCT and MACI groups continued to show evidence of PH with a reduction in PAAT of 39% in the MCT group and 21% in the MACI group compared with the CON group. The rise in RV pressure caused compression of the LV which resulted in a decrease in LV internal diameter in both diastole and systole in both the MCT and MACI groups (Table 7-4). Although the MACI group continued to show evidence of PH, this was less severe than in the MCT group. The MACI group had a 28% greater PAAT and a 50% lower PAD than the MCT group. Further demonstration that pulmonary hypertension was less severe in the MACI group than the MCT group was the finding that the RV wall thickness in systole was 23% smaller in the MACI group. There was also a borderline 28% reduction in RV internal dimension in systole ( $p=0.052$ ) (Table 7-4; Figure 7-2 B-D).

	CON (n=11/12)	MCT (n=11/12)	MACI (n=11/12)
PAAT ms	29.9 ± 1.5	30.5 ± 1.4	30.4 ± 1.6
PAD m/s <sup>2</sup>	13.9 ± 0.9	15.1 ± 1.9	13.1 ± 0.7
PVmax m/s	1.15 ± 0.04	1.05 ± 0.03 *	0.99 ± 0.02 **
RV internal diameter (diastole) (cm)	0.12 ± 0.03	0.19 ± 0.03	0.16 ± 0.02
RV internal diameter (systole) (cm)	0.07 ± 0.01	0.06 ± 0.01	0.06 ± 0.01
RV wall thickness (diastole) (cm)	0.05 ± 0.01	0.06 ± 0.01	0.05 ± 0.00
RV wall thickness (systole) (cm)	0.07 ± 0.01	0.07 ± 0.00	0.08 ± 0.01
LV internal diameter (diastole) (cm)	0.71 ± 0.01	0.72 ± 0.02	0.69 ± 0.01
LV internal diameter (systole) (cm)	0.35 ± 0.01	0.33 ± 0.03	0.29 ± 0.01 *
LV anterior wall thickness (diastole) (cm)	0.18 ± 0.01	0.18 ± 0.01	0.17 ± 0.01
LV anterior wall thickness (systole) (cm)	0.30 ± 0.01	0.31 ± 0.01	0.30 ± 0.01

**Table 7-2. Echo parameters of PH at day 7 post injection. Mean ± SEM. \*  $P<0.05$  MCT or MACI vs. CON assessed by two-way repeated measures ANNOVA with multiple comparisons; \*\*  $P<0.005$  MCT or MACI vs. CON assessed by unpaired two-way repeated measures ANNOVA with multiple comparisons.**

	CON (n=11/12)	MCT (n=11/12)	MACI (n=11/12)
PAAT ms	30.2 ± 1.0	22.8 ± 1.7 **	29.1 ± 1.0 ††
PAD m/s <sup>2</sup>	14.9 ± 1.4	18.8 ± 1.5	16.3 ± 1.2
PVmax m/s	1.20 ± 0.04	0.96 ± 0.02 **	1.03 ± 0.03 **
RV internal diameter (diastole) (cm)	0.16 ± 0.03	0.17 ± 0.02	0.22 ± 0.02
RV internal diameter (systole) (cm)	0.07 ± 0.01	0.08 ± 0.02	0.10 ± 0.01
RV wall thickness (diastole) (cm)	0.05 ± 0.00	0.06 ± 0.01	0.06 ± 0.00
RV wall thickness (systole) (cm)	0.07 ± 0.01	0.09 ± 0.01	0.08 ± 0.00
LV internal diameter (diastole) (cm)	0.75 ± 0.01	0.70 ± 0.02	0.70 ± 0.01*
LV internal diameter (systole) (cm)	0.34 ± 0.01	0.32 ± 0.02	0.31 ± 0.02
LV anterior wall thickness (diastole) (cm)	0.17 ± 0.00	0.18 ± 0.01	0.18 ± 0.01
LV anterior wall thickness (systole) (cm)	0.29 ± 0.01	0.31 ± 0.01	0.34 ± 0.02

**Table 7-3. Echo parameters of PH at day 14 post injection. Mean ± SEM. \* P<0.05 MCT or MACI vs. CON assessed by two-way repeated measures ANNOVA with multiple comparisons; \*\* P<0.005 MCT or MACI vs. CON assessed by two-way repeated measures ANNOVA with multiple comparisons; †† P<0.005 MCT vs. MACI assessed by two-way repeated measures ANNOVA with multiple comparisons.**

	CON (n=11/12)	MCT (n=11)	MACI (n=11/12)
PAAT ms	28.7 ± 0.9	17.5 ± 1.6 **	22.5 ± 1.0 ** †
PAD m/s <sup>2</sup>	15.8 ± 2.2	34.7 ± 3.7 **	17.3 ± 1.9 ††
PVmax m/s	1.18 ± 0.04	0.97 ± 0.03 **	1.00 ± 0.05 **
RV internal diameter (diastole) (cm)	0.16 ± 0.02	0.27 ± 0.03 **	0.21 ± 0.02 (p=0.052)
RV internal diameter (systole) (cm)	0.08 ± 0.02	0.14 ± 0.03 *	0.12 ± 0.03
RV wall thickness (diastole) (cm)	0.05 ± 0.01	0.09 ± 0.01 **	0.07 ± 0.01 *
RV wall thickness (systole) (cm)	0.07 ± 0.01	0.13 ± 0.01 **	0.10 ± 0.01 ** †
LV internal diameter (diastole) (cm)	0.78 ± 0.01	0.66 ± 0.04 **	0.68 ± 0.02 **
LV internal diameter (systole) (cm)	0.39 ± 0.02	0.26 ± 0.03 **	0.27 ± 0.02 **
LV anterior wall thickness (diastole) (cm)	0.17 ± 0.01	0.21 ± 0.02 *	0.21 ± 0.01 *
LV anterior wall thickness (systole) (cm)	0.29 ± 0.01	0.37 ± 0.03 **	0.34 ± 0.02 *

**Table 7-4. Echo parameters of PH at day 21 post injection. Mean ± SEM. \* P<0.05 MCT or MACI vs. CON assessed by two-way repeated measures ANNOVA with multiple comparisons; \*\* P<0.005 MCT or MACI vs. CON assessed by two-way repeated measures ANNOVA with multiple comparisons; † P<0.05 MCT vs. MACI assessed by two-way repeated measures ANNOVA with multiple comparisons; †† P<0.005 MCT vs. MACI assessed by two-way repeated measures ANNOVA with multiple comparisons.**

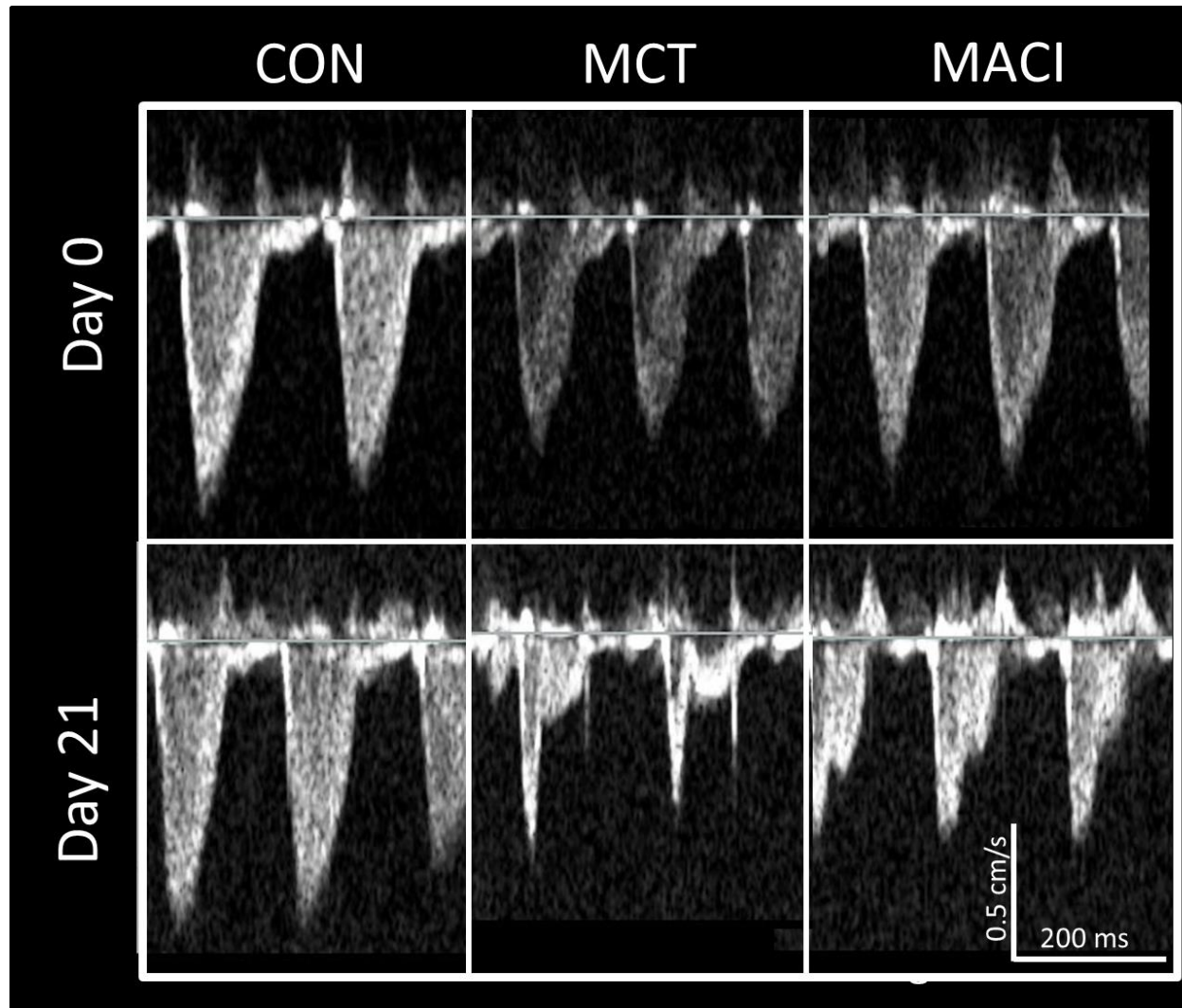
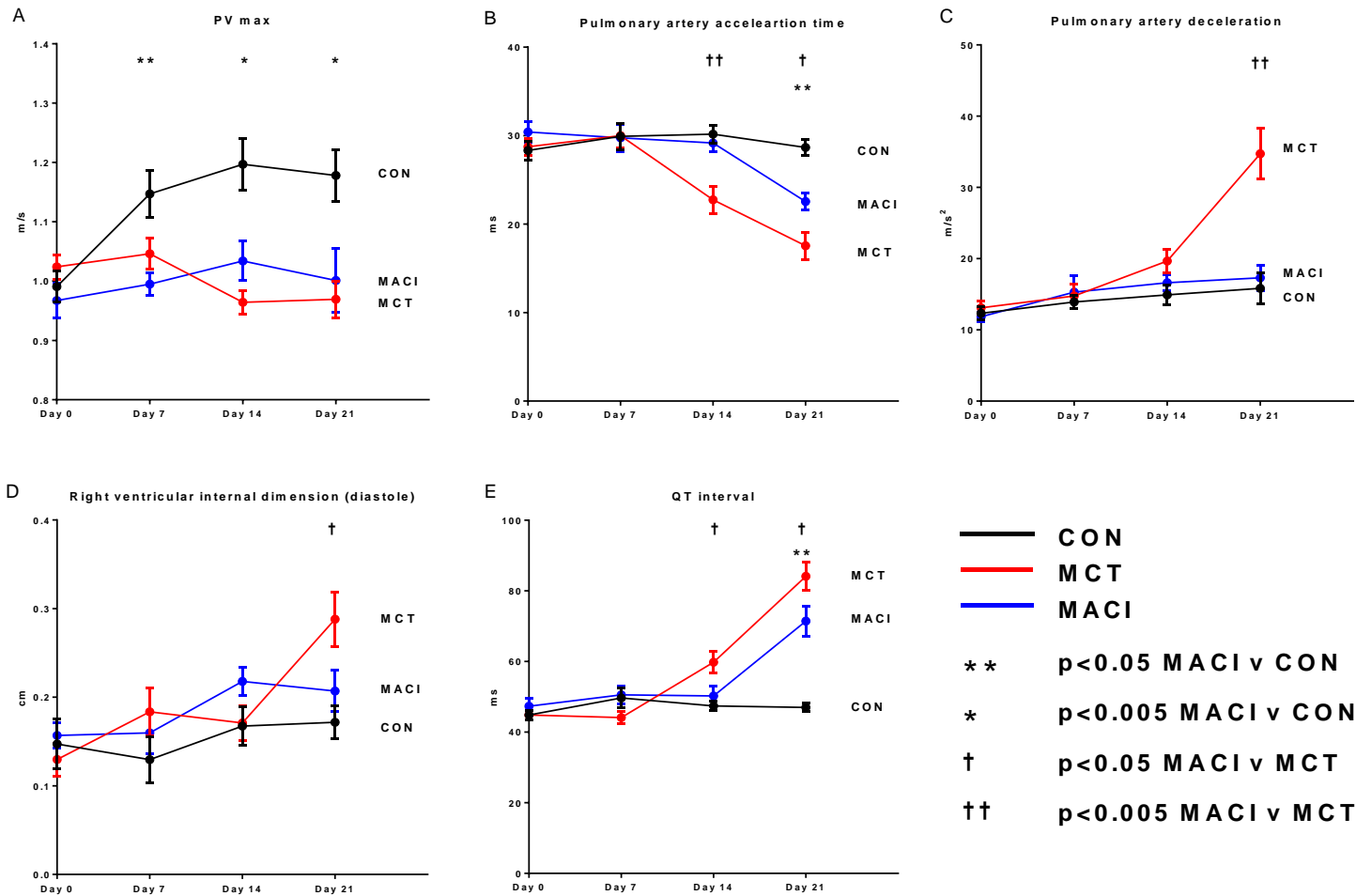


Figure 7-1. Echo images showing the development of PH assessed by the pulmonary velocity profile. The profile has a typical 'rounded' shape prior to injection. At day 21 no change is seen in the CON animal but the MCT animal shows a change to a typical 'spike and dome' morphology with a reduced PAAT and increased PAD. The MACI animal has an intermediate profile between the two groups.

The results of the *In vivo* ECG recordings are shown in Table 7-5 and Figure 7-2. There were no significant changes in any parameters at day 7. At day 14, the QT interval was prolonged in the MCT group by 25% compared with the CON group and 20% compared with the MACI group. There was no change in the QT interval in the MACI group compared with the CON group. At day 21, QT interval was increased by 98% in the MCT group and by 61% in the MACI group compared with the CON group. QT interval was shorter by 18% in the MACI group than in the MCT group. The only other ECG parameter to show any significant changes was an increase in heart rate of 7% in the MACI group compared to the MCT group at day 14 but no changes were seen at day 21.

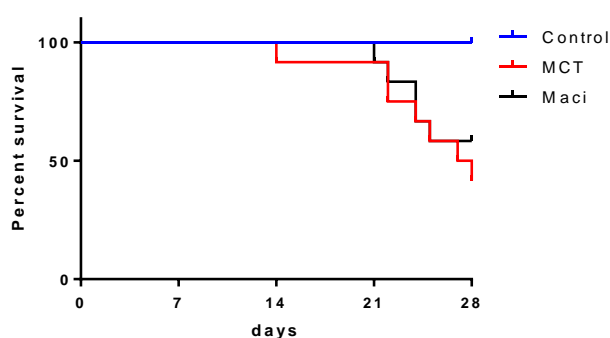
	CON (n=12)	MCT (n=11)	MACI (n=12)
<b>Day 7</b>			
Heart rate (bpm)	395.1 ± 11.0	405.0 ± 9.5	395.8 ± 11.5
PR interval (ms)	49.53 ± 1.52	49.11 ± 1.08	46.53 ± 1.08
QRS duration (ms)	13.9 ± 0.31	13.4 ± 0.59	13.84 ± 0.48
QT interval (ms)	49.67 ± 2.72	43.85 ± 1.76	50.55 ± 2.53
<b>Day 14</b>			
Heart rate (bpm)	401.6 ± 6.7	383.6 ± 8.5	412.2 ± 7.6 †
PR interval (ms)	48.07 ± 1.19	49.01 ± 1.16	47.79 ± 3.37
QRS duration (ms)	14.40 ± 0.33	14.84 ± 0.46	13.65 ± 0.52
QT interval (ms)	47.41 ± 1.34	59.73 ± 3.27 **	50.26 ± 2.87 †
<b>Day 21</b>			
Heart rate (bpm)	393.5 ± 7.8	372.1 ± 8.1	380.5 ± 12.2
PR interval (ms)	48.54 ± 0.94	47.87 ± 1.41	48.21 ± 1.55
QRS duration (ms)	14.33 ± 0.34	15.29 ± 0.78	14.07 ± 0.40
QT interval (ms)	47.00 ± 1.15	84.13 ± 3.96 **	71.41 ± 4.30 ** ††

Table 7-5. ECG measurements at day 7, day 14 and 21 post injection. Mean ± SEM. \*\* P<0.005 MCT or MACI vs. CON, † P<0.05 MCT vs. MACI.



**Figure 7-2.** Development of PH. Mean and SEM plotted at each time point. The MACI group was compared with the MCT group and the CON group assessed by two-way repeated measures ANNOVA with multiple comparisons. Pulmonary hypertension developed in the MACI group by day 7 (i.e. before the initiation of macitentan) with a reduced PVmax. There is a significant improvement in the MACI group compared to the MCT group at day 14 and day 21 with a reduced PAD, right ventricular internal dimension and QT interval and an increased pulmonary artery acceleration time.

The mean  $\pm$  SEM day of termination was  $28 \pm 0$  in the CON group,  $25 \pm 1$  in the MCT group and  $26 \pm 1$  in the MACI group. The median (interquartile range) day of survival was 28 (28-28) in the CON group, 28 (23-28) in the MCT group and 28 (24-28) in the MACI group. Freedom from symptomatic endpoints at day 28 was 100% in the CON group, 42% in the MCT group and 58% in the MACI group. There was a significantly worse survival in both the MCT and MACI groups when compared with the CON group (MCT  $P=0.002$ , MACI  $P=0.014$ ). The difference in freedom from symptomatic endpoints between the MCT and MACI groups was not statistically significant ( $P=0.50$ ) (Figure 7-3)..



**Figure 7-3. Kaplan-Meier curves showing the freedom from symptomatic endpoints. The animals were sacrificed on the day they met their symptomatic endpoints. There is a significant difference between the CON and MACI treated groups ( $p=0.01$ ) but no difference between the MACI treated and MCT groups ( $p=0.50$ ).**

## 7.4 Discussion

This study shows that treatment with the ERA macitentan delays the progression of established PH in the rat MCT model. PH is developing by day 7 in the MCT and MACI groups. Macitentan treatment was initiated at day 11, and the data show significant slowing of progression of the echo and ECG parameters of PH by as early as day 14 (Figure 7-2 B). The MACI group showed less severe parameters of PH than the MCT group at both day 14 and day 21 as evidenced by the higher PAAT and lower PAD (Figure 7-2. 3B-C). Delaying the progression of PH resulted in reduced structural and electrical remodelling with improvements in right ventricular internal diameter and QT interval at day 21 (Table 7-5; Figure 7-2 E). These findings suggest that treatment with macitentan is able to improve haemodynamic parameters in animals with established PH in earlier stages of the disease. Despite the early beneficial effects of macitentan on pulmonary pressures the data shows that the pulmonary pressures do increase in the MACI group, albeit later than in the untreated MCT group with a significant decrease in PAAT and increase in  $QT_c$  in the MACI group compared with the CON group (Figure 7-2).

In spite of increasing interest in treating patients with PAH earlier in their disease course, advanced therapies for PAH are considered only in patients who have proven raised pulmonary vascular resistance and symptoms.<sup>1, 216</sup> Invasive pulmonary pressure monitoring in MCT injected rats has demonstrated that pulmonary pressures are significantly raised by day 10 and increase progressively, leading to RV failure and death.<sup>170, 217</sup> In the light of such previous studies we elected to initiate therapy at day 11, in order to mirror the clinical situation with respect to initiation of treatment. In my study, the earliest indication of PH was seen at day 7 with a reduced PVmax, and there was clear evidence of PH in the untreated MCT group at day 14. This suggests that our experimental protocol is comparable to the clinical situation.

The characteristic finding from the previous chapters in both *in vivo* and *ex vivo* experiments was QT prolongation which is thought to be due to a combination of an increase in Ca<sup>2+</sup> currents and a decrease in K<sup>+</sup> currents and promotes the formation of EADs and DADs (section 1.6.4). In patients with PAH the QT<sub>C</sub> is raised and a QT<sub>C</sub> of greater than 480 ms is an independent predictor of mortality.<sup>20</sup> In addition to this the QT<sub>C</sub> is correlated to pulmonary pressures and RV dilation and inversely correlated to RV function.<sup>20</sup> The lesser degree of prolongation of the QT interval in the MACI group suggests that macitentan may act to reduce the risk of ventricular arrhythmias as well as improving haemodynamic parameters.

In this macitentan study no change was seen in heart rate in the *in vivo* ECG at day 21 which is in contrast to the results in chapter 3, but it should be noted that the termination day ECG data described in chapter 3 is not comparable with the day 21 data described in this chapter. In the current study there is a non-significant 5% reduction in heart rate at day 21 which can be compared with the non-significant reduction of 2% seen in chapter 3 at day 21. The heart rate of the MACI group is in between the MCT and CON, but no significant differences were seen in comparison with either group. Consistent with previous findings no change in the PR interval and QRS duration was documented in any of the three groups. In order to investigate whether treatment with macitentan in the MACI groups has reversed the arrhythmic remodelling seen in previous chapters with the MCT injected rats a more detailed experimental protocol including both functional and molecular biology experiments would be required. However, it should be noted that both the MCT and MACI group developed PH and the experiment was allowed to progress until the symptomatic endpoints were developed, which is likely to minimise any differences between the two groups.

It is interesting to note that despite the using the same dose regime of MCT to that of Iglarz *et al.* we have seen a considerably more severe phenotype in the MCT group than previously demonstrated. In my study, 28-day freedom from symptomatic endpoints was 42% compared with a survival at day 28 of approximately 90% in their experiments.<sup>207</sup> Although these outcomes are not directly comparable, the severe phenotype seen in our experiments may be attributable to the relatively low body weight of the rats at the time of MCT injection. Therefore the benefits of macitentan therapy may to some extent have been masked by the severity of the MCT model phenotype, due to more rapid progression of the underlying lung pathology, together with a shorter treatment duration before symptomatic endpoints were reached.

The mechanism by which MCT treatment leads to PH is still debated.<sup>210</sup> The initial insult is thought to occur in the pulmonary endothelial cells provoking an inflammatory response.<sup>148</sup> Progressive smooth muscle medial hypertrophy takes place from around day 4, and increases progressively until day 15.<sup>148, 218</sup> Circulating levels of endothelin are raised in the MCT model and these raised levels are not affected by ERAs, even if these drugs are given at the same time as the MCT injection.<sup>219</sup> The beneficial effects of ERAs are thought to be attributable to a combination of improved endothelial function, vasodilating properties, and a reduction of smooth muscle hypertrophy within the media of the pulmonary vessels.<sup>210, 219-222</sup> Given the importance of inflammation and medial hypertrophy in the early stages of the MCT model it is tempting to suggest that macitentan treatment may limit the pro-inflammatory and proliferative effects of endothelin if it is given early in the model development, before PH has developed. The relatively rapid improvement in haemodynamic parameters seen in my study suggests that the vasodilating effects of endothelin blockade may be more relevant in established PH, as was present in my study.

The results from my study are in keeping with clinical trials of PAH, in which despite early functional improvements, clear mortality benefit has not been shown.<sup>1</sup> In clinical practice PAH has an insidious presentation and diagnosis is typically late. Therefore the direct relevance of animal studies in which treatment is commenced before the development of PH to clinical practice is debatable. The results of my study suggest that treatment with macitentan may offer benefits in terms of haemodynamic parameters, RV function and QT prolongation, although we have not demonstrated a survival benefit. The relative contribution of anti-inflammatory, anti-proliferative and vasodilating actions of

ERAs to treatment of PAH at different timepoints in the disease process are yet to be determined.

In this set of experiments the CON group received saline injections at day 0 and macitentan from day 11 to assess whether macitentan treatment had any effect on rats without PH. There were no adverse events seen in the CON group confirming the safety of macitentan. Given the experience of the control and MCT groups described in previous chapters a decision was made not to create a new control group that received saline injection and pulverized chow from day 11 for these experiments. Comparison of the control group previously described in chapter 0 with the CON group in this set of experiments does reveal some significant baseline differences at day 0 with a borderline greater weight in the controls in the current study (223.7 g *vs.* 208.0 g,  $P=0.07$ ) suggesting that the CON group were older than the control group in chapter 2. In keeping with this suggestion there was a significantly lower heart rate in CON compared with the control group from chapter 0 heart rate (402 bpm *vs.* 450 bpm,  $P<0.0005$ ). Although the echo images are similar between the CON group and the control group from chapter 2 these baseline differences and small differences in methodology have precluded a direct comparison between the CON group and control group from chapter 2. Nevertheless the main aim of the macitentan study was to compare the differences between the untreated PH in the MCT group and the treated PH in the MACI group.

Macitentan was administered *via* food admix to animal cages housing four rats. The dose was adjusted to animal weight and food intake was monitored to ensure that the correct dose of macitentan was being consumed on average between the four rats. However, it was not possible to ensure that each individual rat received exactly the specified dose. In addition to this when the animal's health deteriorated their food intake may have diminished. Despite this, the earliest deterioration in the MACI group was seen on day 21, meaning that the animal would have received macitentan treatment for a minimum of 10 days.

The macitentan treatment study shows that while macitentan treatment does not reverse the progression of established PH, nevertheless worthwhile haemodynamic benefit takes place. The beneficial effect on QT prolongation suggests that the haemodynamic benefits of macitentan treatment may reduce the arrhythmogenic remodelling that takes place, in the ventricle at least. This study did not investigate the effects of macitentan treatment on

the AV node dysfunction and arrhythmogenic remodelling that has been demonstrated in previous chapters.

## 8 Summary and future directions

---

This study is the first to demonstrate down-regulation of the key ion channels and  $\text{Ca}^{2+}$  handling proteins in the AV node in response to a disease process. These findings are consistent with the literature regarding the importance of ion channels in normal AV node physiology and offer new insights into mechanisms underlying AV node dysfunction in response to abnormal cardiac physiology.

AV node block is a common clinical condition and is the indication for over half of all implanted pacemakers.<sup>223</sup> Despite the high frequency and severity of AV block there is limited data regarding the pathological basis and location of dysfunction within the cardiac conduction system. A prolonged conduction time from the His bundle to the Ventricle implies disease in the His-Purkinje system and is predictive of AV block.<sup>224</sup> However, the conduction time from the His bundle to the ventricle may be normal in patients who go on to require pacemaker implantation for AV block.<sup>224</sup> Wenckebach conduction normally occurs within the AV node itself and although this phenomenon used to be thought to be a benign finding there is increasing data that it predicts AV block and poor outcomes, particularly in older, non-athletic populations.<sup>225-227</sup> These findings point to the importance of pathology within the AV itself as the cause of AV block, but there are limited data regarding the cellular mechanisms underlying this AV node dysfunction.

There is recent data pointing to the importance of ion channels in normal AV conduction. A genome wide association study has demonstrated several loci are associated with a prolonged PR interval.<sup>228</sup> These loci includes genes for ion channels and several cardiac developmental genes known to be important for the patterning of ion channels during embryogenesis.<sup>228</sup> There is also a recognition that several disease causing ion channel mutations that have been characterised as causing Brugada syndrome and long-QT syndrome are also associated with conduction system disturbances and AV block.<sup>65</sup> In addition to these findings in patients gene knockout studies have pointed to the importance of several ion channels including HCN4<sup>84</sup> and the voltage sensitive  $\text{Ca}^{2+}$  channels<sup>79, 199</sup> in maintaining normal AV conduction.

The changes seen in this study have offered new insights into the normal function of the AV node. The findings of down-regulation in HCN4 and the intracellular  $\text{Ca}^{2+}$ -handling proteins are particularly intriguing and point to the possibility that both the membrane

clock and  $\text{Ca}^{2+}$  clock could play a role conduction in the normal AV node (as described in the discussion for Chapter 5, section 5.4). This hypothesis is in line with the findings from recent studies that point to the importance of  $I_f$  in AV nodal conduction. The importance of  $I_f$  and the  $\text{Ca}^{2+}$  clock in AV nodal conduction could be examined in whole heart and AV node tissue preparations similar to those described in Chapters 3 and 4. Several techniques including pharmacological blockade of  $I_f$  and the  $\text{Ca}^{2+}$  clock, and genetic ‘knock-out’ of the key components of both the membrane and  $\text{Ca}^{2+}$  clocks could be used to identify which factors are most important.

Computer modelling is used to integrate experimental data regarding the structure and function of the heart and can be used to generate predictions about the effects that a change seen at the molecular level will have on both individual cardiac cells and the heart as a whole organ. Provisional work has been performed investigating possible effects caused by the alterations in mRNA level seen in Chapter 5. This work has been performed in collaboration with Simon Castro and Dr Michael Coleman from Professor Zhang’s group (School of Physics and Astronomy, Manchester University). A Pre-existing model of the rabbit AV node has been used.<sup>74</sup> Within each tissue region the cell models have been modified by changing the current density for the each of the currents in proportion to the changes in mRNA expression for the proteins that underlie the currents. In this provisional experiment all currents densities have been modified according to the ratio of relative quantification of mRNA for control:MCT regardless of whether the difference in mRNA expression between the control and MCT group were significant, this has been done to avoid loss of data at this provisional stage. Where there are several proteins underlying a single current the ratio of relative quantification for control:MCT has been calculated and this has then been scaled in accordance with the conductance of the individual proteins to provide a final figure for the modification of the current density. This approach has previously been used to model the action potential of rabbit Purkinje fibres in a heart failure model using the formula:

$$\text{Scaling factor for ionic current density in the MCT animals} = \frac{(\sum_{i=1}^n \gamma_{ion}^i d_{ion}^i)_{\text{MCT}}}{(\sum_{i=1}^n \gamma_{ion}^i d_{ion}^i)_{\text{control}}} \times 100\% \quad 229$$

Where  $d_{ion}$  is ion channel expression (or density) for each channel included in the model and  $\gamma_{ion}$  is the channel conductance for that ion channel.  $n$  is the total number of different

ion channel types which contribute to an ionic current.<sup>229</sup> Modelling of cell:cell coupling has used a similar approach in which the ratio of mRNA in the control:MCT group has been calculated for each connexin and then a final figure for modification of cell:cell coupling has been calculated for each region based on both the relative expression of the mRNA for each connexin isoform and the relative conductance of each connexin isoform. The ion channels and connexins used in the cell models, expression of these ion channels and subsequent calculations used for modification of the ionic currents in each region of the AV node are shown in the appendix (Table A-2 to Table A-7).

The new MCT cell models are then incorporated into the model for the whole AV node. In this provisional experiment the data for the atrium and ventricle mRNA expression has been used to model the atrial and ventricular cells respectively. The data for the inferior nodal extension mRNA expression has been used to model the AN cells, the data for the compact node mRNA expression has been used to model the N cells and the data for the penetrating bundle mRNA expression has been used to modify the NH cells. There is no data for the Purkinje fibre cells and therefore this region has not been altered. Although this approach makes many assumptions it has been used to model currents in the sinus node.<sup>47</sup> The model of the AV node derived from the MCT treated rats exhibits AV node block within the compact node (Figure 8-1). This is similar to the findings of Chapter 4 in which block was demonstrated in the AV node proximal to the His bundle. Further work is planned to refine this model to more accurately reflect the rat AV node and to look at the effects of changing individual currents in order to generate a hypothesis regarding which changes in mRNA expression are likely to be significant with regards to AV node dysfunction and to see if these differences were statistically significant in the mRNA experiment.

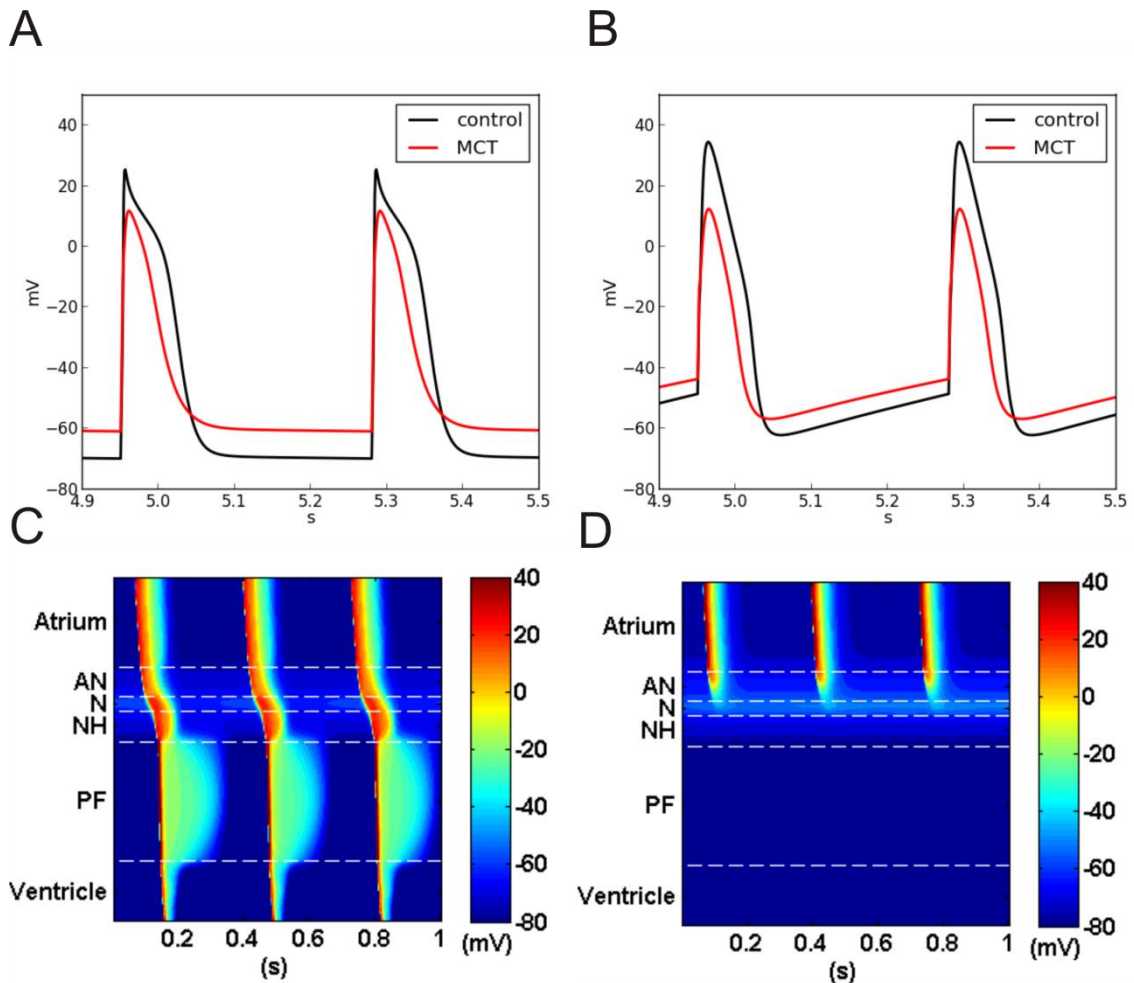


**Figure 8-1.** Results of the computer simulation with incorporating the mRNA data. **A** Control and MCT action potential from AN cells. **B** Control and MCT action potential from N cells. **C.** 1D simulation for control AV node. The model is paced from the atrium at a cycle length of 330ms, there is 1:1 conduction through the from the atrium, through the AV node and into the ventricle. **D.** 1D simulation for MCT AV node. The model is paced from the atrium at a cycle length of 330ms. Block occurs in the region of the AN to N cells, corresponding to the anatomical compact node.

Some of the findings of this thesis require further investigation. In the first instance, it would be valuable to do further work with the MCT model to understand the significance of the changes in mRNA expression demonstrated in Chapter 6. This could involve expanding the study by measuring changes in protein expression for the targets identified as changing at the mRNA level. This would ideally involve an increase in the sample numbers for the experiments in Chapter 6 and expanding these experiments to look at other proteins, for example the  $K^+$  channels that were shown to be down-regulated in both the working myocardium and the nodal tissues. I have used immunohistochemistry to quantify protein because immunohistochemistry can be used with small tissue samples - it gives information about the distribution of protein, and it can be used to quantify protein. The ability to study small samples and gain information regarding protein distribution is

important because of the structural complexity of the AV node. The main drawback to the use of immunohistochemistry is that it is only semi-quantitative, which may limit the ability of immunohistochemistry to show differences between the control and MCT treated rats. It may be that other techniques to quantify protein such as Western-blotting or proteomics could quantify protein more accurately. However, there are considerable technical challenges with either technique to quantify protein from the small tissue regions of the AV node in rats. Another aspect to validating the functional significance of the changes in ion channels and  $\text{Ca}^{2+}$  - handling proteins is to look at the characteristics of the ionic currents in the myocardial cells. For example the mRNA data shows a reduction in both HCN4 and the proteins underlying the repolarising  $\text{K}^+$  currents. These currents could be quantified using the patch-clamp technique on both working myocardial cells and AV nodal cells to see if there was a down-regulation in current corresponding to the down-regulation of mRNA expression.

Chapter 7 outlined treatment of PH in the MCT model, but it was limited to *in vivo* echo and ECG to assess these changes and was therefore not able to offer any further insight into the potential benefits for AV node dysfunction. Further studies could be performed using the techniques described in Chapters 3 - 6 to assess if treatment of PH has protected the AV node. These studies are complicated by the fact that the macitentan treatment group did go on to develop PH, albeit later than the MCT only group. On this basis it seems likely that the AV node would show less dysfunction in the macitentan treated group than the MCT only group, but still have some evidence of dysfunction compared with the control group. Possible solutions to this problem would include electively sacrificing all rats at day 21 post injection, at which timepoint there were maximal differences between the macitentan and MCT only treated rats. It would also be possible to vary the timing of the initiation of macitentan. A 'prevention' strategy with macitentan treatment commencing on the day of injection could be used, although the clinical relevance of this strategy is debatable. Alternatively macitentan could be initiated after injection but earlier than day 11, for example at day 7 by which time the PVmax was already reduced. Supporting this, clinical studies have demonstrated that earlier treatment in PAH leads to maximal clinical benefit.<sup>216</sup> Finally, if a therapeutic agents that was able to reverse established PH was used it would be possible to investigate whether this also reversed the AV node dysfunction caused by PH.

AV node dysfunction is seen in many different pathological conditions. This study has been limited to investigating PH in the MCT model. It would be interesting to study other

pathological conditions that lead to AV node dysfunction to see if similar dysregulation of ion channels and  $\text{Ca}^{2+}$  handling proteins are seen in other settings.

This study has offered new insights into AV node function in both the physiological and pathological state that enhance the understanding of normal AV node function and dysregulation in disease. The insights offered by this study require further investigation, but may provide a better understanding of AV node function and dysfunction which could in turn lead to the development of new therapies.

## References

---

1. Galie N, Hoeper MM, Humbert M, Torbicki A, Vachiery JL, Barbera JA, et al. Guidelines for the diagnosis and treatment of pulmonary hypertension: the Task Force for the Diagnosis and Treatment of Pulmonary Hypertension of the European Society of Cardiology (ESC) and the European Respiratory Society (ERS), endorsed by the International Society of Heart and Lung Transplantation (ISHLT). *Eur Heart J*. 2009 Oct;30(20):2493-537.
2. Peacock AJ, Murphy NF, McMurray JJ, Caballero L, Stewart S. An epidemiological study of pulmonary arterial hypertension. *Eur Respir J*. 2007 Jul;30(1):104-9.
3. Coghlan G, Corris PA, Gaine S, Gatzoulis MA, Gibbs JSR, G. HS, et al. Consensus statement on the management of pulmonary hypertension in clinical practice in the UK and Ireland. *Thorax*. 2008 Mar;63 Suppl 2:ii1-ii41.
4. Stenmark KR, Meyrick B, Galie N, Mooi WJ, McMurtry IF. Animal models of pulmonary arterial hypertension: the hope for etiological discovery and pharmacological cure. *Am J Physiol Lung Cell Mol Physiol*. 2009 Dec;297(6):L1013-32.
5. Sommer N, Dietrich A, Schermuly RT, Ghofrani HA, Gudermann T, Schulz R, et al. Regulation of hypoxic pulmonary vasoconstriction: basic mechanisms. *Eur Respir J*. 2008 Dec;32(6):1639-51.
6. Tapson VF, Humbert M. Incidence and prevalence of chronic thromboembolic pulmonary hypertension: from acute to chronic pulmonary embolism. *Proc Am Thorac Soc*. 2006 Sep;3(7):564-7.
7. Schermuly RT, Ghofrani HA, Wilkins MR, Grimminger F. Mechanisms of disease: pulmonary arterial hypertension. *Nat Rev Cardiol*. 2011 Aug;8(8):443-55.
8. Tuder RM, Marecki JC, Richter A, Fijalkowska I, Flores S. Pathology of pulmonary hypertension. *Clin Chest Med*. 2007 Mar;28(1):23-42, vii.
9. McLure LE, Peacock AJ. Cardiac magnetic resonance imaging for the assessment of the heart and pulmonary circulation in pulmonary hypertension. *Eur Respir J*. 2009 Jun;33(6):1454-66.
10. van Wolferen SA, Marcus JT, Boonstra A, Marques KM, Bronzwaer JG, Spreuwenberg MD, et al. Prognostic value of right ventricular mass, volume, and function in idiopathic pulmonary arterial hypertension. *Eur Heart J*. 2007 May;28(10):1250-7.
11. Saba TS, Foster J, Cockburn M, Cowan M, Peacock AJ. Ventricular mass index using magnetic resonance imaging accurately estimates pulmonary artery pressure. *Eur Respir J*. 2002 Dec;20(6):1519-24.
12. Saito H, Dambara T, Aiba M, Suzuki T, Kira S. Evaluation of cor pulmonale on a modified short-axis section of the heart by magnetic resonance imaging. *Am Rev Respir Dis*. 1992 Dec;146(6):1576-81.

13. Vonk Noordegraaf A, Marcus JT, Roseboom B, Postmus PE, Faes TJ, de Vries PM. The effect of right ventricular hypertrophy on left ventricular ejection fraction in pulmonary emphysema. *Chest*. 1997 Sep;112(3):640-5.
14. Bogaard HJ, Natarajan R, Henderson SC, Long CS, Kraskauskas D, Smithson L, et al. Chronic pulmonary artery pressure elevation is insufficient to explain right heart failure. *Circulation*. 2009 Nov 17;120(20):1951-60.
15. Lehtonen J, Sutinen S, Ikaheimo M, Paakko P. Electrocardiographic criteria for the diagnosis of right ventricular hypertrophy verified at autopsy. *Chest*. 1988 Apr;93(4):839-42.
16. Myers GB, Klein HA, Stofer BE. The electrocardiographic diagnosis of right ventricular hypertrophy. *Am Heart J*. 1948 Jan;35(1):1-40.
17. Sokolow M, Lyon TP. Criteria for the diagnosis of right ventricular hypertrophy using unipolar limb and precordial leads. *Am J Med*. 1947 Jul;3(1):125.
18. Hancock EW, Deal BJ, Mirvis DM, Okin P, Kligfield P, Gettes LS, et al. AHA/ACCF/HRS recommendations for the standardization and interpretation of the electrocardiogram: part V: electrocardiogram changes associated with cardiac chamber hypertrophy: a scientific statement from the American Heart Association Electrocardiography and Arrhythmias Committee, Council on Clinical Cardiology; the American College of Cardiology Foundation; and the Heart Rhythm Society. Endorsed by the International Society for Computerized Electrocardiology. *J Am Coll Cardiol*. 2009 Mar 17;53(11):992-1002.
19. Rowlands DJ. Left and right bundle branch block, left anterior and left posterior hemiblock. *Eur Heart J*. 1984 Mar;5 Suppl A:99-105.
20. Rich JD, Thenappan T, Freed B, Patel AR, Thisted RA, Childers R, et al. QTc prolongation is associated with impaired right ventricular function and predicts mortality in pulmonary hypertension. *Int J Cardiol*. 2013 Aug 10;167(3):669-76.
21. Tuncer M, Gunes Y, Guntekin U, Aslan S, Gumrukcuoglu HA, Eryonucu B, et al. Association of increased QTc dispersion and right ventricular hypertrophy. *Med Sci Monit*. 2008 Feb;14(2):CR102-5.
22. Zhang HL, Luo Q, Liu ZH, Zhao ZH, Xiong CM, Ni XH, et al. Heart rate-corrected QT interval and QT dispersion in patients with pulmonary hypertension. *Wien Klin Wochenschr*. 2009 Jun;121(9-10):330-3.
23. Chen PS, Moser KM, Dembitsky WP, Auger WR, Daily PO, Calisi CM, et al. Epicardial activation and repolarization patterns in patients with right ventricular hypertrophy. *Circulation*. 1991 Jan;83(1):104-18.
24. Bossone E, Paciocco G, Iarussi D, Agretto A, Iacono A, Gillespie BW, et al. The prognostic role of the ECG in primary pulmonary hypertension. *Chest*. 2002 Feb;121(2):513-8.
25. Kanemoto N, Sasamoto H. Arrhythmias in primary pulmonary hypertension. *Jpn Heart J*. 1979 Nov;20(6):765-75.

26. Tongers J, Schwerdtfeger B, Klein G, Kempf T, Schaefer A, Knapp JM, et al. Incidence and clinical relevance of supraventricular tachyarrhythmias in pulmonary hypertension. *Am Heart J*. 2007 Jan;153(1):127-32.
27. Ruiz-Cano MJ, Gonzalez-Mansilla A, Escribano P, Delgado J, Arribas F, Torres J, et al. Clinical implications of supraventricular arrhythmias in patients with severe pulmonary arterial hypertension. *Int J Cardiol*. 2011 Jan 7;146(1):105-6.
28. Medi C, Kalman JM, Ling LH, Teh AW, Lee G, Spence SJ, et al. Atrial electrical and structural remodeling associated with longstanding pulmonary hypertension and right ventricular hypertrophy in humans. *J Cardiovasc Electrophysiol*. 2012 Jun;23(6):614-20.
29. Showkathali R, Tayebjee MH, Grapsa J, Alzetani M, Nihoyannopoulos P, Howard LS, et al. Right atrial flutter isthmus ablation is feasible and results in acute clinical improvement in patients with persistent atrial flutter and severe pulmonary arterial hypertension. *Int J Cardiol*. 2011 Jun 2;149(2):279-80.
30. Folino AF, Bobbo F, Schiraldi C, Tona F, Romano S, Buja G, et al. Ventricular arrhythmias and autonomic profile in patients with primary pulmonary hypertension. *Lung*. 2003 Nov-Dec;181(6):321-8.
31. Hoepfer MM, Galie N, Murali S, Olschewski H, Rubenfire M, Robbins IM, et al. Outcome after cardiopulmonary resuscitation in patients with pulmonary arterial hypertension. *Am J Respir Crit Care Med*. 2002 Feb 1;165(3):341-4.
32. Orejarena LA, Vidaillet H, Jr., DeStefano F, Nordstrom DL, Vierkant RA, Smith PN, et al. Paroxysmal supraventricular tachycardia in the general population. *J Am Coll Cardiol*. 1998 Jan;31(1):150-7.
33. Vidaillet H, Granada JF, Chyou P, Maassen K, Ortiz M, Pulido JN, et al. A population-based study of mortality among patients with atrial fibrillation or flutter. *Am J Med*. 2002 Oct 1;113(5):365-70.
34. Aro AL, Anttonen O, Kerola T, Junttila MJ, Tikkanen JT, Rissanen HA, et al. Prognostic significance of prolonged PR interval in the general population. *Eur Heart J*. 2013 May 14.
35. Markowitz S, Stein K, Mittal S, Lerman B. Dual atrionodal physiology in the human heart. In: Mazgalev T, Tchou, MD, editor. *Atrial-AV nodal electrophysiology: a view from the millennium* .: Armonk, New York: Futura Publishing Company; 2000. p. 353-70.
36. Peacock AJ. Treatment of pulmonary hypertension. *BMJ*. 2003 Apr 19;326(7394):835-6.
37. Gabbay E, Fraser J, McNeil K. Review of bosentan in the management of pulmonary arterial hypertension. *Vasc Health Risk Manag*. 2007;3(6):887-900.
38. Ramani GV, Park MH. Update on the clinical utility of sildenafil in the treatment of pulmonary arterial hypertension. *Drug Des Devel Ther*. 2010;4:61-70.
39. Rich S, Brundage BH. High-dose calcium channel-blocking therapy for primary pulmonary hypertension: evidence for long-term reduction in pulmonary arterial pressure and regression of right ventricular hypertrophy. *Circulation*. 1987 Jul;76(1):135-41.

40. McLaughlin VV, Genthner DE, Panella MM, Rich S. Reduction in pulmonary vascular resistance with long-term epoprostenol (prostacyclin) therapy in primary pulmonary hypertension. *N Engl J Med.* 1998 Jan 29;338(5):273-7.
41. Miyauchi T, Yorikane R, Sakai S, Sakurai T, Okada M, Nishikibe M, et al. Contribution of endogenous endothelin-1 to the progression of cardiopulmonary alterations in rats with monocrotaline-induced pulmonary hypertension. *Circ Res.* 1993 Nov;73(5):887-97.
42. Shah M, Akar FG, Tomaselli GF. Molecular basis of arrhythmias. *Circulation.* 2005 Oct 18;112(16):2517-29.
43. Katz AM. *Physiology of the Heart: Lippincott Williams & Wilkins; 2010.*
44. Rees SA, Curtis MJ. Selective  $I_K$  blockade as an antiarrhythmic mechanism: effects of UK66,914 on ischaemia and reperfusion arrhythmias in rat and rabbit hearts. *Br J Pharmacol.* 1993 Jan;108(1):139-45.
45. Benardeau A, Hatem SN, Rucker-Martin C, Le Grand B, Mace L, Dervanian P, et al. Contribution of  $\text{Na}^+/\text{Ca}^{2+}$  exchange to action potential of human atrial myocytes. *Am J Physiol.* 1996 Sep;271(3 Pt 2):H1151-61.
46. Courtemanche M, Ramirez RJ, Nattel S. Ionic mechanisms underlying human atrial action potential properties: insights from a mathematical model. *Am J Physiol.* 1998 Jul;275(1 Pt 2):H301-21.
47. Chandler NJ, Greener ID, Tellez JO, Inada S, Musa H, Molenaar P, et al. Molecular architecture of the human sinus node: insights into the function of the cardiac pacemaker. *Circulation.* 2009 Mar 31;119(12):1562-75.
48. Boyett MR. 'And the beat goes on.' The cardiac conduction system: the wiring system of the heart. *Exp Physiol.* 2009 Oct;94(10):1035-49.
49. Nattel S, Frelin Y, Gaborit N, Louault C, Demolombe S. Ion-channel mRNA-expression profiling: Insights into cardiac remodeling and arrhythmic substrates. *J Mol Cell Cardiol.* 2010 Jan;48(1):96-105.
50. Baruscotti M, Bucchi A, DiFrancesco D. Physiology and pharmacology of the cardiac pacemaker ("funny") current. *Pharmacol Ther.* 2005 Jul;107(1):59-79.
51. DiFrancesco D. A study of the ionic nature of the pace-maker current in calf Purkinje fibres. *J Physiol.* 1981 May;314:377-93.
52. Nerbonne JM. Molecular basis of functional voltage-gated  $\text{K}^+$  channel diversity in the mammalian myocardium. *J Physiol.* 2000 Jun 1;525 Pt 2:285-98.
53. Glitsch HG. Electrophysiology of the sodium-potassium-ATPase in cardiac cells. *Physiol Rev.* 2001 Oct;81(4):1791-826.
54. Baartscheer A, Schumacher CA, Coronel R, Fiolet JW. The Driving Force of the  $\text{Na}^+/\text{Ca}^{2+}$ -Exchanger during Metabolic Inhibition. *Front Physiol.* 2011;2:10.

55. Nass RD, Aiba T, Tomaselli GF, Akar FG. Mechanisms of disease: ion channel remodeling in the failing ventricle. *Nat Clin Pract Cardiovasc Med*. 2008 Apr;5(4):196-207.
56. Lakatta EG, DiFrancesco D. What keeps us ticking: a funny current, a calcium clock, or both? *J Mol Cell Cardiol*. 2009 Aug;47(2):157-70.
57. Tardif JC, Ford I, Tendera M, Bourassa MG, Fox K. Efficacy of ivabradine, a new selective  $I_f$  inhibitor, compared with atenolol in patients with chronic stable angina. *Eur Heart J*. 2005 Dec;26(23):2529-36.
58. Spray DC, Burt JM. Structure-activity relations of the cardiac gap junction channel. *Am J Physiol*. 1990 Feb;258(2 Pt 1):C195-205.
59. Severs NJ, Dupont E, Coppin SR, Halliday D, Inett E, Baylis D, et al. Remodelling of gap junctions and connexin expression in heart disease. *Biochim Biophys Acta*. 2004 Mar 23;1662(1-2):138-48.
60. Delmar M, Liang FX. Connexin43 and the regulation of intercalated disc function. *Heart Rhythm*. 2012 May;9(5):835-8.
61. Temple IP, Inada S, Dobrzynski H, Boyett MR. Connexins and the atrioventricular node. *Heart Rhythm*. 2013 Feb;10(2):297-304.
62. Smyth JW, Shaw RM. The gap junction life cycle. *Heart Rhythm*. 2012 Jan;9(1):151-3.
63. Boyett MR, Inada S, Yoo S, Li J, Liu J, Tellez J, et al. Connexins in the sinoatrial and atrioventricular nodes. *Adv Cardiol*. 2006;42:175-97.
64. Kleber AG, Rudy Y. Basic mechanisms of cardiac impulse propagation and associated arrhythmias. *Physiol Rev*. 2004 Apr;84(2):431-88.
65. Dobrzynski H, Anderson RH, Atkinson A, Borbas Z, D'Souza A, Fraser JF, et al. Structure, function and clinical relevance of the cardiac conduction system, including the atrioventricular ring and outflow tract tissues. *Pharmacol Ther*. 2013 Aug;139(2):260-88.
66. Cosio FG, Anderson RH, Kuck KH, Becker A, Borggrefe M, Campbell RW, et al. Living anatomy of the atrioventricular junctions. A guide to electrophysiologic mapping. A Consensus Statement from the Cardiac Nomenclature Study Group, Working Group of Arrhythmias, European Society of Cardiology, and the Task Force on Cardiac Nomenclature from NASPE. *Circulation*. 1999 Aug 3;100(5):e31-7.
67. Munk AA. Electrophysiological properties of two distinct populations of myocytes isolated from the rabbit atrioventricular node. *J Electrocardiol*. 1995 Oct;28(4):352-3.
68. Munk AA, Adjemian RA, Zhao J, Ogbaghebriel A, Shrier A. Electrophysiological properties of morphologically distinct cells isolated from the rabbit atrioventricular node. *J Physiol*. 1996 Jun 15;493 ( Pt 3):801-18.
69. Billette J. Atrioventricular nodal activation during periodic premature stimulation of the atrium. *Am J Physiol*. 1987 Jan;252(1 Pt 2):H163-77.

70. Anderson RH, Janse MJ, van Capelle FJ, Billette J, Becker AE, Durrer D. A combined morphological and electrophysiological study of the atrioventricular node of the rabbit heart. *Circ Res.* 1974 Dec;35(6):909-22.
71. Efimov IR, Nikolski VP, Rothenberg F, Greener ID, Li J, Dobrzynski H, et al. Structure-function relationship in the AV junction. *Anat Rec A Discov Mol Cell Evol Biol.* 2004 Oct;280(2):952-65.
72. Greener ID, Monfredi O, Inada S, Chandler NJ, Tellez JO, Atkinson A, et al. Molecular architecture of the human specialised atrioventricular conduction axis. *J Mol Cell Cardiol.* 2011 Apr;50(4):642-51.
73. Ren FX, Niu XL, Ou Y, Han ZH, Ling FD, Zhou SS, et al. Morphological and electrophysiological properties of single myocardial cells from Koch triangle of rabbit heart. *Chin Med J (Engl).* 2006 Dec 20;119(24):2075-84.
74. Inada S, Hancox JC, Zhang H, Boyett MR. One-dimensional mathematical model of the atrioventricular node including atrio-nodal, nodal, and nodal-his cells. *Biophys J.* 2009 Oct 21;97(8):2117-27.
75. Yoo S, Dobrzynski H, Fedorov VV, Xu SZ, Yamanushi TT, Jones SA, et al. Localization of Na<sup>+</sup> channel isoforms at the atrioventricular junction and atrioventricular node in the rat. *Circulation.* 2006 Sep 26;114(13):1360-71.
76. Greener ID, Tellez JO, Dobrzynski H, Yamamoto M, Graham GM, Billeter R, et al. Ion channel transcript expression at the rabbit atrioventricular conduction axis. *Circ Arrhythm Electrophysiol.* 2009 Jun;2(3):305-15.
77. Hancox JC, Mitcheson JS. Ion channel and exchange currents in single myocytes isolated from the rabbit atrioventricular node. *Can J Cardiol.* 1997 Dec;13(12):1175-82.
78. Hancox JC, Mitcheson JS. Inhibition of L-type calcium current by propafenone in single myocytes isolated from the rabbit atrioventricular node. *Br J Pharmacol.* 1997 May;121(1):7-14.
79. Marger L, Mesirca P, Alig J, Torrente A, Dubel S, Engeland B, et al. Functional roles of Ca<sub>v</sub>1.3, Ca<sub>v</sub>3.1 and HCN channels in automaticity of mouse atrioventricular cells: insights into the atrioventricular pacemaker mechanism. *Channels (Austin).* 2011 May-Jun;5(3):251-61.
80. Zhang Q, Timofeyev V, Qiu H, Lu L, Li N, Singapuri A, et al. Expression and roles of Ca<sub>v</sub>1.3 (α<sub>1D</sub>) L-type Ca<sup>2+</sup> channel in atrioventricular node automaticity. *J Mol Cell Cardiol.* 2011 Jan;50(1):194-202.
81. Marger L, Mesirca P, Alig J, Torrente A, Dubel S, Engeland B, et al. Pacemaker activity and ionic currents in mouse atrioventricular node cells. *Channels (Austin).* 2011 May-Jun;5(3):241-50.
82. Hancox JC, Levi AJ. L-type calcium current in rod- and spindle-shaped myocytes isolated from rabbit atrioventricular node. *Am J Physiol.* 1994 Nov;267(5 Pt 2):H1670-80.
83. Ou Y, Niu XL, Ren FX. Expression of key ion channels in the rat cardiac conduction system by laser capture microdissection and quantitative real-time PCR. *Exp Physiol.* 2010 Sep;95(9):938-45.

84. Baruscotti M, Bucchi A, Viscomi C, Mandelli G, Consalez G, Gneccchi-Rusconi T, et al. Deep bradycardia and heart block caused by inducible cardiac-specific knockout of the pacemaker channel gene *Hcn4*. *Proc Natl Acad Sci U S A*. 2011 Jan 25;108(4):1705-10.
85. Liu J, Noble PJ, Xiao G, Abdelrahman M, Dobrzynski H, Boyett MR, et al. Role of pacemaking current in cardiac nodes: insights from a comparative study of sinoatrial node and atrioventricular node. *Prog Biophys Mol Biol*. 2008 Jan-Apr;96(1-3):294-304.
86. Dobrzynski H, Nikolski VP, Sambelashvili AT, Greener ID, Yamamoto M, Boyett MR, et al. Site of origin and molecular substrate of atrioventricular junctional rhythm in the rabbit heart. *Circ Res*. 2003 Nov 28;93(11):1102-10.
87. Herrmann S, Layh B, Ludwig A. Novel insights into the distribution of cardiac HCN channels: an expression study in the mouse heart. *J Mol Cell Cardiol*. 2011 Dec;51(6):997-1006.
88. Ren FX, Niu XL, Han ZH, Ou Y, Ling FD, Zhou SS, et al. [Electrophysiologic characteristics of Ito in myocytes from cardiac Koch triangle]. *Sichuan Da Xue Xue Bao Yi Xue Ban*. 2009 Nov;40(6):988-93.
89. Ye Sheng X, Qu Y, Dan P, Lin E, Korthout L, Bradford A, et al. Isolation and characterization of atrioventricular nodal cells from neonate rabbit heart. *Circ Arrhythm Electrophysiol*. 2011 Dec;4(6):936-46.
90. Choisy SC, Cheng H, Smith GL, James AF, Hancox JC. Modulation by endothelin-1 of spontaneous activity and membrane currents of atrioventricular node myocytes from the rabbit heart. *PLoS One*. 2012;7(3):e33448.
91. Howarth FC, Levi AJ, Hancox JC. Characteristics of the delayed rectifier  $K^+$  current compared in myocytes isolated from the atrioventricular node and ventricle of the rabbit heart. *Pflugers Arch*. 1996 Mar;431(5):713-22.
92. Regan CP, Cresswell HK, Zhang R, Lynch JJ. Novel method to assess cardiac electrophysiology in the rat: characterization of standard ion channel blockers. *J Cardiovasc Pharmacol*. 2005 Jul;46(1):68-75.
93. Guo W, Li H, London B, Nerbonne JM. Functional consequences of elimination of  $i_{(to,f)}$  and  $i_{(to,s)}$ : early afterdepolarizations, atrioventricular block, and ventricular arrhythmias in mice lacking *Kv1.4* and expressing a dominant-negative *Kv4* alpha subunit. *Circ Res*. 2000 Jul 7;87(1):73-9.
94. Choisy SC, James AF, Hancox JC. Acute desensitization of acetylcholine and endothelin-1 activated inward rectifier  $K^+$  current in myocytes from the cardiac atrioventricular node. *Biochem Biophys Res Commun*. 2012 Jul 6;423(3):496-502.
95. Li J, Greener ID, Inada S, Nikolski VP, Yamamoto M, Hancox JC, et al. Computer three-dimensional reconstruction of the atrioventricular node. *Circ Res*. 2008 Apr 25;102(8):975-85.
96. Hucker WJ, McCain ML, Laughner JI, Iaizzo PA, Efimov IR. Connexin 43 expression delineates two discrete pathways in the human atrioventricular junction. *Anat Rec (Hoboken)*. 2008 Feb;291(2):204-15.

97. Davis LM, Rodefeld ME, Green K, Beyer EC, Saffitz JE. Gap junction protein phenotypes of the human heart and conduction system. *J Cardiovasc Electrophysiol*. 1995 Oct;6(10 Pt 1):813-22.
98. Ko YS, Yeh HI, Ko YL, Hsu YC, Chen CF, Wu S, et al. Three-dimensional reconstruction of the rabbit atrioventricular conduction axis by combining histological, desmin, and connexin mapping data. *Circulation*. 2004 Mar 9;109(9):1172-9.
99. van Rijen HV, van Veen TA, van Kempen MJ, Wilms-Schopman FJ, Potse M, Krueger O, et al. Impaired conduction in the bundle branches of mouse hearts lacking the gap junction protein connexin40. *Circulation*. 2001 Mar 20;103(11):1591-8.
100. Jansen JA, van Veen TA, de Bakker JM, van Rijen HV. Cardiac connexins and impulse propagation. *J Mol Cell Cardiol*. 2010 Jan;48(1):76-82.
101. Nishii K, Kumai M, Egashira K, Miwa T, Hashizume K, Miyano Y, et al. Mice lacking connexin45 conditionally in cardiac myocytes display embryonic lethality similar to that of germline knockout mice without endocardial cushion defect. *Cell Commun Adhes*. 2003 Jul-Dec;10(4-6):365-9.
102. Morley GE, Vaidya D, Jalife J. Characterization of conduction in the ventricles of normal and heterozygous Cx43 knockout mice using optical mapping. *J Cardiovasc Electrophysiol*. 2000 Mar;11(3):375-7.
103. VanderBrink BA, Sellitto C, Saba S, Link MS, Zhu W, Homoud MK, et al. Connexin40-deficient mice exhibit atrioventricular nodal and infra-Hisian conduction abnormalities. *J Cardiovasc Electrophysiol*. 2000 Nov;11(11):1270-6.
104. Simon AM, Goodenough DA, Paul DL. Mice lacking connexin40 have cardiac conduction abnormalities characteristic of atrioventricular block and bundle branch block. *Curr Biol*. 1998 Feb 26;8(5):295-8.
105. Schrickel JW, Kreuzberg MM, Ghanem A, Kim JS, Linhart M, Andrie R, et al. Normal impulse propagation in the atrioventricular conduction system of Cx30.2/Cx40 double deficient mice. *J Mol Cell Cardiol*. 2009 May;46(5):644-52.
106. Kreuzberg MM, Liebermann M, Segschneider S, Dobrowolski R, Dobrzynski H, Kaba R, et al. Human connexin31.9, unlike its orthologous protein connexin30.2 in the mouse, is not detectable in the human cardiac conduction system. *J Mol Cell Cardiol*. 2009 Apr;46(4):553-9.
107. Kruger O, Maxeiner S, Kim JS, van Rijen HV, de Bakker JM, Eckardt D, et al. Cardiac morphogenetic defects and conduction abnormalities in mice homozygously deficient for connexin40 and heterozygously deficient for connexin45. *J Mol Cell Cardiol*. 2006 Nov;41(5):787-97.
108. Nikolski VP, Jones SA, Lancaster MK, Boyett MR, Efimov IR. Cx43 and dual-pathway electrophysiology of the atrioventricular node and atrioventricular nodal reentry. *Circ Res*. 2003 Mar 7;92(4):469-75.
109. Loh P, Ho SY, Kawara T, Hauer RN, Janse MJ, Breithardt G, et al. Reentrant circuits in the canine atrioventricular node during atrial and ventricular echoes: electrophysiological and histological correlation. *Circulation*. 2003 Jul 15;108(2):231-8.

110. Mazgalev TN, Ho SY, Anderson RH. Anatomic-electrophysiological correlations concerning the pathways for atrioventricular conduction. *Circulation*. 2001 Jun 5;103(22):2660-7.
111. Upshaw CB, Jr., Silverman ME. The Wenckebach phenomenon: a salute and comment on the centennial of its original description. *Ann Intern Med*. 1999 Jan 5;130(1):58-63.
112. Delmar M, Michaels DC, Jalife J. Slow recovery of excitability and the Wenckebach phenomenon in the single guinea pig ventricular myocyte. *Circ Res*. 1989 Sep;65(3):761-74.
113. Hoshino K, Anumonwo J, Delmar M, Jalife J. Wenckebach periodicity in single atrioventricular nodal cells from the rabbit heart. *Circulation*. 1990 Dec;82(6):2201-16.
114. Zhang Y, Mazgalev TN. AV nodal dual pathway electrophysiology and Wenckebach periodicity. *J Cardiovasc Electrophysiol*. 2011 Nov;22(11):1256-62.
115. Shrier A, Dubarsky H, Rosengarten M, Guevara MR, Nattel S, Glass L. Prediction of complex atrioventricular conduction rhythms in humans with use of the atrioventricular nodal recovery curve. *Circulation*. 1987 Dec;76(6):1196-205.
116. Antzelevitch C, Burashnikov A. Overview of Basic Mechanisms of Cardiac Arrhythmia. *Card Electrophysiol Clin*. 2011 Mar 1;3(1):23-45.
117. Yan CAaG-X. Ionic and Cellular Basis for Arrhythmogenesis. In: Gan-Xin Yan PRK, editor. *Contemporary Cardiology: Management of Cardiac Arrhythmias*: Springer Science+Business Media; 2003. p. 41-64.
118. Weiss JN, Garfinkel A, Karagueuzian HS, Chen PS, Qu Z. Early afterdepolarizations and cardiac arrhythmias. *Heart Rhythm*. 2010 Dec;7(12):1891-9.
119. Allesie MA, Bonke FI, Schopman FJ. Circus movement in rabbit atrial muscle as a mechanism of tachycardia. II. The role of nonuniform recovery of excitability in the occurrence of unidirectional block, as studied with multiple microelectrodes. *Circ Res*. 1976 Aug;39(2):168-77.
120. Nattel S, Maguy A, Le Bouter S, Yeh YH. Arrhythmogenic ion-channel remodeling in the heart: heart failure, myocardial infarction, and atrial fibrillation. *Physiol Rev*. 2007 Apr;87(2):425-56.
121. Tellez JO, McZewski M, Yanni J, Sutyagin P, Mackiewicz U, Atkinson A, et al. Ageing-dependent remodelling of ion channel and Ca<sup>2+</sup> clock genes underlying sino-atrial node pacemaking. *Exp Physiol*. 2011 Nov;96(11):1163-78.
122. Yanni J, Tellez JO, Maczewski M, Mackiewicz U, Beresewicz A, Billeter R, et al. Changes in ion channel gene expression underlying heart failure-induced sinoatrial node dysfunction. *Circ Heart Fail*. 2011 Jul;4(4):496-508.
123. Daicho T, Yagi T, Takano S, Marunouchi T, Abe Y, Ohara M, et al. Alterations in pharmacological action of the right ventricle of monocrotaline-induced pulmonary hypertensive rats. *Biol Pharm Bull*. 2009 Aug;32(8):1378-84.

124. Koyama T, Ono K, Watanabe H, Ohba T, Murakami M, Iino K, et al. Molecular and electrical remodeling of L- and T-type  $\text{Ca}^{2+}$  channels in rat right atrium with monocrotaline-induced pulmonary hypertension. *Circ J*. 2009 Feb;73(2):256-63.
125. Sanyal SN, Ono K. Derangement of autonomic nerve control in rat with right ventricular failure. *Pathophysiology*. 2002 Jun;8(3):197-203.
126. Bruner LH, Hilliker KS, Roth RA. Pulmonary hypertension and ECG changes from monocrotaline pyrrole in the rat. *Am J Physiol*. 1983 Aug;245(2):H300-6.
127. Henkens IR, Mouchaers KT, Vliegen HW, van der Laarse WJ, Swenne CA, Maan AC, et al. Early changes in rat hearts with developing pulmonary arterial hypertension can be detected with three-dimensional electrocardiography. *Am J Physiol Heart Circ Physiol*. 2007 Aug;293(2):H1300-7.
128. Lee JK, Nishiyama A, Kambe F, Seo H, Takeuchi S, Kamiya K, et al. Downregulation of voltage-gated  $\text{K}^{+}$  channels in rat heart with right ventricular hypertrophy. *Am J Physiol*. 1999 Nov;277(5 Pt 2):H1725-31.
129. Umar S, Lee JH, de Lange E, Iorga A, Partow-Navid R, Bapat A, et al. Spontaneous ventricular fibrillation in right ventricular failure secondary to chronic pulmonary hypertension. *Circ Arrhythm Electrophysiol*. 2012 Feb;5(1):181-90.
130. Benoist D, Stones R, Drinkhill MJ, Benson AP, Yang Z, Cassan C, et al. Cardiac arrhythmia mechanisms in rats with heart failure induced by pulmonary hypertension. *Am J Physiol Heart Circ Physiol*. 2012 Jun 1;302(11):H2381-95.
131. Uzzaman M, Honjo H, Takagishi Y, Emdad L, Magee AI, Severs NJ, et al. Remodeling of gap junctional coupling in hypertrophied right ventricles of rats with monocrotaline-induced pulmonary hypertension. *Circ Res*. 2000 Apr 28;86(8):871-8.
132. Hardziyenka M, Campian ME, Verkerk AO, Surie S, van Ginneken AC, Hakim S, et al. Electrophysiologic remodeling of the left ventricle in pressure overload-induced right ventricular failure. *J Am Coll Cardiol*. 2012 Jun 12;59(24):2193-202.
133. Lourenco AP, Roncon-Albuquerque R, Jr., Bras-Silva C, Faria B, Wieland J, Henriques-Coelho T, et al. Myocardial dysfunction and neurohumoral activation without remodeling in left ventricle of monocrotaline-induced pulmonary hypertensive rats. *Am J Physiol Heart Circ Physiol*. 2006 Oct;291(4):H1587-94.
134. Burstein B, Nattel S. Atrial fibrosis: mechanisms and clinical relevance in atrial fibrillation. *J Am Coll Cardiol*. 2008 Feb 26;51(8):802-9.
135. Hadi AM, Mouchaers KT, Schaliq I, Grunberg K, Meijer GA, Vonk-Noordegraaf A, et al. Rapid quantification of myocardial fibrosis: A new macro-based automated analysis. *Anal Cell Pathol (Amst)*. 2010;33(5):257-69.
136. Lee JK, Kodama I, Honjo H, Anno T, Kamiya K, Toyama J. Stage-dependent changes in membrane currents in rats with monocrotaline-induced right ventricular hypertrophy. *Am J Physiol*. 1997 Jun;272(6 Pt 2):H2833-42.
137. Benoist D, Stones R, Drinkhill M, Bernus O, White E. Arrhythmogenic Substrate in Hearts of Rats with Monocrotaline-Induced Pulmonary Hypertension and Right Ventricular Hypertrophy. *Am J Physiol Heart Circ Physiol*. 2011 Mar 11.

138. Liguó C, John L, Maria A, Jason O, Arvinder D, Luiz B. Direct Evidence Of Unprovoked Arrhythmias In Telemetered, Conscious Rats With Chronic Pulmonary Artery Hypertension. C64 EXPERIMENTAL MODELS OF PULMONARY VASCULAR DISEASE II: American Thoracic Society; 2013. p. A4648-A.
139. Watkinson WP, Campen MJ, Costa DL. Cardiac arrhythmia induction after exposure to residual oil fly ash particles in a rodent model of pulmonary hypertension. *Toxicol Sci.* 1998 Feb;41(2):209-16.
140. Tan XY, He JG. The remodeling of connexin in the hypertrophied right ventricular in pulmonary arterial hypertension and the effect of a dual ET receptor antagonist (bosentan). *Pathol Res Pract.* 2009;205(7):473-82.
141. Tanaka Y, Takase B, Yao T, Ishihara M. Right ventricular electrical remodeling and arrhythmogenic substrate in rat pulmonary hypertension. *Am J Respir Cell Mol Biol.* 2013 Sep;49(3):426-36.
142. Xie YP, Chen B, Sanders P, Guo A, Li Y, Zimmerman K, et al. Sildenafil prevents and reverses transverse-tubule remodeling and Ca<sup>2+</sup> handling dysfunction in right ventricle failure induced by pulmonary artery hypertension. *Hypertension.* 2012 Feb;59(2):355-62.
143. Schnader J, Schloo BL, Anderson W, Stephenson LW, Fishman AP. Chronic pulmonary hypertension in sheep: temporal progression of lesions. *J Surg Res.* 1996 May;62(2):243-50.
144. Rondelet B, Kerbaul F, Motte S, van Beneden R, Rummelink M, Brimiouille S, et al. Bosentan for the prevention of overcirculation-induced experimental pulmonary arterial hypertension. *Circulation.* 2003 Mar 11;107(9):1329-35.
145. Qi J, Du J, Tang X, Li J, Wei B, Tang C. The upregulation of endothelial nitric oxide synthase and urotensin-II is associated with pulmonary hypertension and vascular diseases in rats produced by aortocaval shunting. *Heart and Vessels.* 2004 Mar;19(2):81-8.
146. Pak O, Janssen W, Ghofrani HA, Seeger W, Grimminger F, Schermuly RT, et al. Animal models of pulmonary hypertension: role in translational research. *Drug Discovery Today: Disease Models.* 2011.
147. Kay JM, Harris P, Heath D. Pulmonary hypertension produced in rats by ingestion of *Crotalaria spectabilis* seeds. *Thorax.* 1967 Mar;22(2):176-9.
148. Wilson DW, Segall HJ, Pan LC, Dunston SK. Progressive inflammatory and structural changes in the pulmonary vasculature of monocrotaline-treated rats. *Microvasc Res.* 1989 Jul;38(1):57-80.
149. Clozel M, Hess P, Rey M, Iglarz M, Binkert C, Qiu C. Bosentan, sildenafil, and their combination in the monocrotaline model of pulmonary hypertension in rats. *Exp Biol Med (Maywood).* 2006 Jun;231(6):967-73.
150. Koskenvuo JW, Mirsky R, Zhang Y, Angeli FS, Jahn S, Alastalo TP, et al. A comparison of echocardiography to invasive measurement in the evaluation of pulmonary arterial hypertension in a rat model. *Int J Cardiovasc Imaging.* 2010 Jun;26(5):509-18.
151. White RJ, Meoli DF, Swarthout RF, Kallop DY, Galaria, II, Harvey JL, et al. Plexiform-like lesions and increased tissue factor expression in a rat model of severe

- pulmonary arterial hypertension. *Am J Physiol Lung Cell Mol Physiol*. 2007 Sep;293(3):L583-90.
152. Abe K, Toba M, Alzoubi A, Ito M, Fagan KA, Cool CD, et al. Formation of plexiform lesions in experimental severe pulmonary arterial hypertension. *Circulation*. 2010 Jun 29;121(25):2747-54.
153. Taraseviciene-Stewart L, Kasahara Y, Alger L, Hirth P, Mc Mahon G, Waltenberger J, et al. Inhibition of the VEGF receptor 2 combined with chronic hypoxia causes cell death-dependent pulmonary endothelial cell proliferation and severe pulmonary hypertension. *FASEB J*. 2001 Feb;15(2):427-38.
154. Archer SL, Fang YH, Ryan JJ, Piao L. Metabolism and bioenergetics in the right ventricle and pulmonary vasculature in pulmonary hypertension. *Pulm Circ*. 2013 Jan;3(1):144-52.
155. Akhavein F, St-Michel EJ, Seifert E, Rohlicek CV. Decreased left ventricular function, myocarditis, and coronary arteriolar medial thickening following monocrotaline administration in adult rats. *J Appl Physiol* (1985). 2007 Jul;103(1):287-95.
156. Campian ME, Hardziyenka M, de Bruin K, van Eck-Smit BL, de Bakker JM, Verberne HJ, et al. Early inflammatory response during the development of right ventricular heart failure in a rat model. *Eur J Heart Fail*. 2010 Jul;12(7):653-8.
157. Watts JA, Zagorski J, Gellar MA, Stevinson BG, Kline JA. Cardiac inflammation contributes to right ventricular dysfunction following experimental pulmonary embolism in rats. *J Mol Cell Cardiol*. 2006 Aug;41(2):296-307.
158. Allanore Y, Meune C. Primary myocardial involvement in systemic sclerosis: evidence for a microvascular origin. *Clin Exp Rheumatol*. 2010 Sep-Oct;28(5 Suppl 62):S48-53.
159. Mu H, Chai H, Lin PH, Yao Q, Chen C. Current update on HIV-associated vascular disease and endothelial dysfunction. *World J Surg*. 2007 Apr;31(4):632-43.
160. Patten RD, Hall-Porter MR. Small animal models of heart failure: development of novel therapies, past and present. *Circ Heart Fail*. 2009 Mar;2(2):138-44.
161. Apkon M, Nerbonne JM. Characterization of two distinct depolarization-activated  $K^+$  currents in isolated adult rat ventricular myocytes. *J Gen Physiol*. 1991 May;97(5):973-1011.
162. Barry DM, Nerbonne JM. Myocardial potassium channels: electrophysiological and molecular diversity. *Annu Rev Physiol*. 1996;58:363-94.
163. Farraj AK, Hazari MS, Cascio WE. The utility of the small rodent electrocardiogram in toxicology. *Toxicol Sci*. 2011 May;121(1):11-30.
164. Nerbonne JM. Regulation of voltage-gated  $K^+$  channel expression in the developing mammalian myocardium. *J Neurobiol*. 1998 Oct;37(1):37-59.
165. Pond AL, Scheve BK, Benedict AT, Petrecca K, Van Wagoner DR, Shrier A, et al. Expression of distinct ERG proteins in rat, mouse, and human heart. Relation to functional I(Kr) channels. *J Biol Chem*. 2000 Feb 25;275(8):5997-6006.

166. Bers DM. Calcium fluxes involved in control of cardiac myocyte contraction. *Circ Res.* 2000 Aug 18;87(4):275-81.
167. Linz KW, Meyer R. Profile and kinetics of L-type calcium current during the cardiac ventricular action potential compared in guinea-pigs, rats and rabbits. *Pflugers Arch.* 2000 Mar;439(5):588-99.
168. Clark RB, Bouchard RA, Salinas-Stefanon E, Sanchez-Chapula J, Giles WR. Heterogeneity of action potential waveforms and potassium currents in rat ventricle. *Cardiovasc Res.* 1993 Oct;27(10):1795-9.
169. Seaman RL, Jauchem JR. Rat electrocardiogram during acute exposure to synchronized bursts of ultra-wideband pulses. *IEEE Trans Plasma Sci.* 2004;32(4):1644-52.
170. Urboniene D, Haber I, Fang YH, Thenappan T, Archer SL. Validation of high-resolution echocardiography and magnetic resonance imaging vs. high-fidelity catheterization in experimental pulmonary hypertension. *Am J Physiol Lung Cell Mol Physiol.* 2010 Sep;299(3):L401-12.
171. Quigly G. *Inflammation of the Heart in Heart Disease.* Manchester: The University of Manchester; 2013.
172. Eid BG. *KCNQ Channels As Novel Drug Targets For The Treatment of Pulmonary Hypertension.* Manchester: The University of Manchester; 2003.
173. Bell RM, Mocanu MM, Yellon DM. Retrograde heart perfusion: the Langendorff technique of isolated heart perfusion. *J Mol Cell Cardiol.* 2011 Jun;50(6):940-50.
174. Hucker WJ, Sharma V, Nikolski VP, Efimov IR. Atrioventricular conduction with and without AV nodal delay: two pathways to the bundle of His in the rabbit heart. *Am J Physiol Heart Circ Physiol.* 2007 Aug;293(2):H1122-30.
175. Gervais R, Leclercq C, Shankar A, Jacobs S, Eiskjaer H, Johannessen A, et al. Surface electrocardiogram to predict outcome in candidates for cardiac resynchronization therapy: a sub-analysis of the CARE-HF trial. *Eur J Heart Fail.* 2009 Jul;11(7):699-705.
176. Choi BR, Salama G. Simultaneous maps of optical action potentials and calcium transients in guinea-pig hearts: mechanisms underlying concordant alternans. *J Physiol.* 2000 Nov 15;529 Pt 1:171-88.
177. Olgin JE, Kalman JM, Fitzpatrick AP, Lesh MD. Role of right atrial endocardial structures as barriers to conduction during human type I atrial flutter. Activation and entrainment mapping guided by intracardiac echocardiography. *Circulation.* 1995 Oct 1;92(7):1839-48.
178. Fedorov VV, Schuessler RB, Hemphill M, Ambrosi CM, Chang R, Voloshina AS, et al. Structural and functional evidence for discrete exit pathways that connect the canine sinoatrial node and atria. *Circ Res.* 2009 Apr 10;104(7):915-23.
179. Morris GM, Boyett MR, Yanni J, Billeter R, Dobrzynski H. Detection and Measurement of Cardiac Ion Channels. *Cardiac Electrophysiology Methods and Models:* Springer; 2010. p. 187-212.

180. Yanni J, Boyett MR, Anderson RH, Dobrzynski H. The extent of the specialized atrioventricular ring tissues. *Heart Rhythm*. 2009 May;6(5):672-80.
181. Clément-Ziza M, Munnich A, Lyonnet S, Jaubert F, Besmond C. Stabilization of RNA during laser capture microdissection by performing experiments under argon atmosphere or using ethanol as a solvent in staining solutions. *Rna*. 2008;14(12):2698-704.
182. Aranda IV R, Dineen SM, Craig RL, Guerrieri RA, Robertson JM. Comparison and evaluation of RNA quantification methods using viral, prokaryotic, and eukaryotic RNA over a  $10^4$  concentration range. *Anal Biochem*. 2009;387(1):122-7.
183. Deben C, Zwaenepoel K, Boeckx C, Wouters A, Pauwels P, Peeters M, et al. Expression Analysis on Archival Material Revisited: Isolation and Quantification of RNA Extracted From FFPE Samples. *Diag Mol Pathol*. 2013;22(1):59-64.
184. Bustin SA, Benes V, Garson JA, Hellemans J, Huggett J, Kubista M, et al. The MIQE guidelines: minimum information for publication of quantitative real-time PCR experiments. *Clin Chem*. 2009;55(4):611-22.
185. Saiki RK, Gelfand DH, Stoffel S, Scharf SJ, Higuchi R, Horn GT, et al. Primer-directed enzymatic amplification of DNA with a thermostable DNA polymerase. *Science*. 1988;239(4839):487-91.
186. Steg A, Wang W, Blanquicett C, Grunda JM, Eltoum IA, Wang K, et al. Multiple gene expression analyses in paraffin-embedded tissues by TaqMan low-density array: Application to hedgehog and Wnt pathway analysis in ovarian endometrioid adenocarcinoma. *J Mol Diagn*. 2006;8(1):76-83.
187. Vandesompele J, De Preter K, Pattyn F, Poppe B, Van Roy N, De Paepe A, et al. Accurate normalization of real-time quantitative RT-PCR data by geometric averaging of multiple internal control genes. *Genome Biol*. 2002;3(7):research0034.
188. Demarest TG, Murugesan N, Shrestha B, Pachter JS. Rapid expression profiling of brain microvascular endothelial cells by immuno-laser capture microdissection coupled to TaqMan<sup>®</sup> Low Density Array. *J Neurosci Methods*. 2012;206(2):200-4.
189. Ishii S, Segawa T, Okabe S. Simultaneous Quantification of Multiple Food-and Waterborne Pathogens by Use of Microfluidic Quantitative PCR. *Appl Environl Microbiol*. 2013;79(9):2891-8.
190. Lei M, Jones SA, Liu J, Lancaster MK, Fung SS, Dobrzynski H, et al. Requirement of neuronal- and cardiac-type sodium channels for murine sinoatrial node pacemaking. *J Physiol*. 2004 Sep 15;559(Pt 3):835-48.
191. Duan D. Phenomics of cardiac chloride channels: the systematic study of chloride channel function in the heart. *J Physiol*. 2009;587(10):2163-77.
192. Huang ZM, Prasad C, Britton FC, Ye LL, Hatton WJ, Duan D. Functional role of CLC-2 chloride inward rectifier channels in cardiac sinoatrial nodal pacemaker cells. *J Mol Cell Cardiol*. 2009 Jul;47(1):121-32.
193. Hund TJ, Mohler PJ. Differential roles for SUR subunits in  $K_{ATP}$  channel membrane targeting and regulation. *Am J Physiol Heart Circ Physiol*. 2011;300(1):H33-H5.

194. Lesage F, Lazdunski M. Molecular and functional properties of two-pore-domain potassium channels. *Am J Physiol Renal Physiol*. 2000;279(5):F793-F801.
195. Petric S, Clasen L, van Wessel C, Geduldig N, Ding Z, Schullenberg M, et al. In vivo electrophysiological characterization of TASK-1 deficient mice. *Cell Physiol Biochem*. 2012;30(3):523-37.
196. Shimura M, Minamisawa S, Yokoyama U, Umemura S, Ishikawa Y. Mechanical stress-dependent transcriptional regulation of sarcolipin gene in the rodent atrium. *Biochem Biophys Res Commun*. 2005;334(3):861-6.
197. Smyth GK. *Limma: linear models for microarray data*. *Bioinformatics and computational biology solutions using R and Bioconductor*: Springer; 2005. p. 397-420.
198. Jeanmougin M, De Reynies A, Marisa L, Paccard C, Nuel G, Guedj M. Should we abandon the t-test in the analysis of gene expression microarray data: a comparison of variance modeling strategies. *PLoS One*. 2010;5(9):e12336.
199. Matthes J, Yildirim L, Wietzorrek G, Reimer D, Striessnig J, Herzig S. Disturbed atrio-ventricular conduction and normal contractile function in isolated hearts from  $Ca_v1.3$ -knockout mice. *Naunyn Schmiedeberg's Arch Pharmacol*. 2004 Jun;369(6):554-62.
200. Olcese R. I(KACh) at the whim of a capricious M2R. *J Physiol*. 2011 Apr 15;589(Pt 8):1869-70.
201. Piao L, Fang YH, Parikh KS, Ryan JJ, D'Souza KM, Theccanat T, et al. GRK2-mediated inhibition of adrenergic and dopaminergic signaling in right ventricular hypertrophy: therapeutic implications in pulmonary hypertension. *Circulation*. 2012 Dec 11;126(24):2859-69.
202. Camm AJ, Lau CP. Electrophysiological effects of a single intravenous administration of ivabradine (S 16257) in adult patients with normal baseline electrophysiology. *Drugs R D*. 2003;4(2):83-9.
203. Fox K, Ford I, Steg PG, Tendera M, Ferrari R. Ivabradine for patients with stable coronary artery disease and left-ventricular systolic dysfunction (BEAUTIFUL): a randomised, double-blind, placebo-controlled trial. *Lancet*. 2008 Sep 6;372(9641):807-16.
204. Swedberg K, Komajda M, Bohm M, Borer JS, Ford I, Tavazzi L. Rationale and design of a randomized, double-blind, placebo-controlled outcome trial of ivabradine in chronic heart failure: the Systolic Heart Failure Treatment with the I(f) Inhibitor Ivabradine Trial (SHIFT). *Eur J Heart Fail*. 2010 Jan;12(1):75-81.
205. Verrier RL, Sobrado MF, Pagotto VP, Kanas AF, Machado AD, Varone BB, et al. Inhibition of If in the atrioventricular node as a mechanism for dronedarone's reduction in ventricular rate during atrial fibrillation. *Heart Rhythm*. 2013 Nov;10(11):1692-7.
206. Hamidi SA, Lin RZ, Szema AM, Lyubsky S, Jiang YP, Said SI. VIP and endothelin receptor antagonist: an effective combination against experimental pulmonary arterial hypertension. *Respir Res*. 2011;12:141.
207. Iglarz M, Binkert C, Morrison K, Fischli W, Gatfield J, Treiber A, et al. Pharmacology of macitentan, an orally active tissue-targeting dual endothelin receptor antagonist. *J Pharmacol Exp Ther*. 2008 Dec;327(3):736-45.

208. McMurtry MS, Bonnet S, Michelakis ED, Haromy A, Archer SL. Statin therapy, alone or with rapamycin, does not reverse monocrotaline pulmonary arterial hypertension: the rapamycin-atorvastatin-simvastatin study. *Am J Physiol Lung Cell Mol Physiol*. 2007 Oct;293(4):L933-40.
209. Mouchaers KT, Schalij I, Versteilen AM, Hadi AM, van Nieuw Amerongen GP, van Hinsbergh VW, et al. Endothelin receptor blockade combined with phosphodiesterase-5 inhibition increases right ventricular mitochondrial capacity in pulmonary arterial hypertension. *Am J Physiol Heart Circ Physiol*. 2009 Jul;297(1):H200-7.
210. Galie N, Manes A, Branzi A. The endothelin system in pulmonary arterial hypertension. *Cardiovasc Res*. 2004 Feb 1;61(2):227-37.
211. McLaughlin VV, Sitbon O, Badesch DB, Barst RJ, Black C, Galie N, et al. Survival with first-line bosentan in patients with primary pulmonary hypertension. *Eur Respir J*. 2005 Feb;25(2):244-9.
212. Rubin LJ, Badesch DB, Barst RJ, Galie N, Black CM, Keogh A, et al. Bosentan therapy for pulmonary arterial hypertension. *N Engl J Med*. 2002 Mar 21;346(12):896-903.
213. Monfredi O, Griffiths L, Clarke B, Mahadevan VS. Efficacy and safety of bosentan for pulmonary arterial hypertension in adults with congenital heart disease. *Am J Cardiol*. 2011 Nov 15;108(10):1483-8.
214. Pulido T, Adzerikho I, Channick RN, Delcroix M, Galie N, Ghofrani HA, et al. Macitentan and morbidity and mortality in pulmonary arterial hypertension. *N Engl J Med*. 2013 Aug 29;369(9):809-18.
215. Hill NS, Warburton RR, Pietras L, Klinger JR. Nonspecific endothelin-receptor antagonist blunts monocrotaline-induced pulmonary hypertension in rats. *J Appl Physiol*. 1997 Oct;83(4):1209-15.
216. Galie N, Rubin L, Hoeper M, Jansa P, Al-Hiti H, Meyer G, et al. Treatment of patients with mildly symptomatic pulmonary arterial hypertension with bosentan (EARLY study): a double-blind, randomised controlled trial. *Lancet*. 2008 Jun 21;371(9630):2093-100.
217. Hess P, Clozel M, Clozel JP. Telemetry monitoring of pulmonary arterial pressure in freely moving rats. *J Appl Physiol*. 1996 Aug;81(2):1027-32.
218. Huang J, Wolk JH, Gewitz MH, Mathew R. Caveolin-1 expression during the progression of pulmonary hypertension. *Exp Biol Med (Maywood)*. 2012 Aug 1;237(8):956-65.
219. Prie S, Leung TK, Cernacek P, Ryan JW, Dupuis J. The orally active ET(A) receptor antagonist (+)-(S)-2-(4,6-dimethoxy-pyrimidin-2-yl-oxy)-3-methoxy-3,3-diphenyl-propionic acid (LU 135252) prevents the development of pulmonary hypertension and endothelial metabolic dysfunction in monocrotaline-treated rats. *J Pharmacol Exp Ther*. 1997 Sep;282(3):1312-8.
220. Dupuis J, Prie S. The ET(A)-Receptor Antagonist LU 135252 Prevents the Progression of Established Pulmonary Hypertension Induced by Monocrotaline in Rats. *J Cardiovasc Pharmacol Ther*. 1999 Jan;4(1):33-9.

221. Prie S, Stewart DJ, Dupuis J. EndothelinA receptor blockade improves nitric oxide-mediated vasodilation in monocrotaline-induced pulmonary hypertension. *Circulation*. 1998 Jun 2;97(21):2169-74.
222. Lim KA, Kim KC, Cho MS, Lee BE, Kim HS, Hong YM. Gene expression of endothelin-1 and endothelin receptor a on monocrotaline-induced pulmonary hypertension in rats after bosentan treatment. *Korean Circ J*. 2010 Sep;40(9):459-64.
223. Uslan DZ, Tleyjeh IM, Baddour LM, Friedman PA, Jenkins SM, St Sauver JL, et al. Temporal trends in permanent pacemaker implantation: a population-based study. *Am Heart J*. 2008 May;155(5):896-903.
224. Marti-Almor J, Cladellas M, Bazan V, Delclos J, Altaba C, Guijo MA, et al. [Novel predictors of progression of atrioventricular block in patients with chronic bifascicular block]. *Rev Esp Cardiol*. 2010 Apr;63(4):400-8.
225. Barold SS, Hayes DL. Second-degree atrioventricular block: a reappraisal. *Mayo Clin Proc*. 2001 Jan;76(1):44-57.
226. Coumbe AG, Naksuk N, Newell MC, Somasundaram PE, Benditt DG, Adabag S. Long-term follow-up of older patients with Mobitz type I second degree atrioventricular block. *Heart*. 2013 Mar;99(5):334-8.
227. Shaw DB, Gowers JI, Kekwick CA, New KH, Whistance AW. Is Mobitz type I atrioventricular block benign in adults? *Heart*. 2004 Feb;90(2):169-74.
228. Pfeufer A, van Noord C, Marcianti KD, Arking DE, Larson MG, Smith AV, et al. Genome-wide association study of PR interval. *Nat Genet*. 2010 Feb;42(2):153-9.
229. Li J, Logantha SJ, Yanni J, Cai X, Zhang H, Dobrzynski H, et al., editors. Computer simulation of Purkinje fibres from a rabbit model of congestive heart failure. *Computing in Cardiology Conference (CinC)*, 2013; 2013: IEEE.

## A. Appendix

---

Gene name	Protein encoded
18S-Hs99999901_s1	18S
B2m-Rn00560865_m1	$\beta$ -2 microglobulin
Gapdh-Rn99999916_s1	GAPDH
Hprt1-Rn01527840_m1	hypoxanthine-guanine phosphoribosyltransferase
Pgk1-Rn00821429_g1	phosphoglycerate kinase 1
Scn5a-Rn00565502_m1	Nav1.5
Scn1a-Rn00578439_m1	Nav1.1
Scn10a-Rn00568393_m1	Nav1.8
Scn1b-Rn00441210_m1	Nav $\beta$ 1
Cacna1c-Rn00709287_m1	Cav1.2
Cacna1d-Rn00568820_m1	Cav1.3
Cacna1g-Rn00581051_m1	Cav3.1
Cacna1h-Rn01460348_m1	Cav3.2
Cacna2d1-Rn01442580_m1	Cav $\alpha$ 2 $\delta$ 1
Cacna2d2-Rn00457825_m1	Cav2 $\delta$ 2
Cacnb2-Rn00587789_m1	Cav $\beta$ 2
Clcn2-Rn00567553_m1	chloride channel 2
Clcn3-Rn01535195_m1	chloride channel 3
Hcn1-Rn00670384_m1	HCN1
Hcn2-Rn01408572_mH	HCN2
Hcn4-Rn00572232_m1	HCN4
Kcna2-Rn02769834_s1	Kv1.2
Kcna4-Rn02532059_s1	Kv1.4
Kcna5-Rn00564245_s1	Kv1.5
Kcnb1-Rn00755102_m1	Kv2.1
Kcnd2-Rn00581941_m1	Kv4.2
Kcnd3-Rn00709608_m1	Kv4.3
Kcne1-Rn02094595_s1	MinK
Kcnh2-Rn00588515_m1	ERG1
Kcnip2-Rn01411451_m1	KCHIP2
Kcnj8-Rn01492857_m1	K <sub>ir</sub> 6.1
Kcnj11-Rn01764077_s1	K <sub>ir</sub> 6.2
Abcc8-Rn00564778_m1	SUR1
Abcc9-Rn00564842_m1	SUR2
Kcnq1-Rn00583376_m1	K <sub>v</sub> LQT1
Kcnj2-Rn00568808_s1	K <sub>ir</sub> 2.1
Kcnj12-Rn02533449_s1	K <sub>ir</sub> 2.2

<b>Gene name</b>	<b>Protein encoded</b>
Kcnj14-Rn00821873_m1	K <sub>ir</sub> 2.4
Kcnj3-Rn00434617_m1	K <sub>ir</sub> 3.1
Kcnj5-Rn01789221_mH	K <sub>ir</sub> 3.4
KCNK1-Hs00158428_m1	TWIK1
Kcnk3-Rn00583727_m1	TASK1
Casq2-Rn00567508_m1	Calsequestrin 2
Ryr2-Rn01470303_m1	RyR2
Ryr3-Rn01328415_g1	RyR3
Pln-Rn01434045_m1	Phospholamban
Slc8a1-Rn00570527_m1	NCX1
Atp2a2-Rn00568762_m1	SERCA2a
Atp2b1-Rn01502902_m1	PMCA1
Gja1-Rn01433957_m1	Cx43
Gja5-Rn00570632_m1	Cx40
Gja7-Rn01750705_m1	Cx45
Gjd3-Rn01771737_s1	Cx30.2
Atp1a1-Rn01533986_m1	Na <sup>+</sup> /K <sup>+</sup> ATPase $\alpha$ -1 subunit
Atp1a2-Rn00560789_m1	Na <sup>+</sup> /K <sup>+</sup> ATPase $\alpha$ -2 subunit
Atp1a3-Rn00560813_m1	Na <sup>+</sup> /K <sup>+</sup> ATPase $\alpha$ -3 subunit
Atp1b1-Rn00565405_m1	Na <sup>+</sup> /K <sup>+</sup> ATPase $\beta$ 1 subunit
Slc9a1-Rn00561924_m1	Na <sup>+</sup> /H <sup>+</sup> transporter
Chrm2-Rn02532311_s1	muscarinic acetylcholine receptor M2
Adora1-Rn00567668_m1	adenosine A1 receptor
Adra1a-Rn00567876_m1	adrenergic receptor, 1a/1c
Adra1b-Rn01471343_m1	adrenergic receptor, $\alpha$ -1b
Adrb1-Rn00824536_s1	adrenergic receptor, $\beta$ 1
Adrb2-Rn00560650_s1	adrenergic receptor, $\beta$ -2
Sln-Rn02769377_s1	sarcolipin
Mef2c-Rn01494046_m1	myocyte enhancer factor 2C
Bmp2-Rn00567818_m1	bone morphogenetic protein 2
Nfkb1-Rn01399583_m1	nuclear factor of kappa light polypeptide gene enhancer in B-cells 1
Nkx2-5-Rn00586428_m1	Nkx2-5
Rest-Rn01413148_m1	RE1-silencing transcription factor
Sp1-Rn00561953_m1	Sp1 transcription factor
Tbx3-Rn00710902_m1	TbX3
Tbx5-Rn01481891_m1	TbX5
Ctgf-Rn01537279_g1	connective tissue growth factor
Il1b-Rn00580432_m1	interleukin 1 $\beta$
Tnf-Rn01525859_g1	tumor necrosis factor
<td>fibronectin 1</td>	fibronectin 1
Vim-Rn00579738_m1	vimentin
Tgfb1-Rn00572010_m1	Transforming growth factor, $\beta$ 1

<b>Gene name</b>	<b>Protein encoded</b>
Col1a1-Rn01463848_m1	Collagen type 1 $\alpha$
Col3a1-Rn01437681_m1	Collagen type 3 $\alpha$
Mmp2-Rn01538170_m1	matrix metalloproteinase 2
Mmp9-Rn00579162_m1	matrix metalloproteinase 9
Eln-Rn01499782_m1	elastin
Timp1-Rn01430875_g1	Timp 1
Timp2-Rn00573232_m1	Timp 2
Timp3-Rn00441826_m1	Timp 3
Timp4-Rn01459160_m1	Timp 4
Myh6-Rn00691721_g1	myosin heavy chain 6
Myh7-Rn01488777_g1	myosin heavy chain 7
Nppa-Rn00561661_m1	Atrial natriuretic peptide precursor
Nppb-Rn00676450_g1	Brain natriuretic peptide
Edn1-Rn00561129_m1	endothelin 1
Ednra-Rn00561137_m1	endothelin receptor type A
Ednrb-	endothelin receptor type B
Trpc1-Rn00585625_m1	Transient receptor potential channel 1

**Table A-1. Full list of targets included on TLDA qPCR card.**

	Control								
Atrium	20.4	42.6	44.8	37.3	24.6	*	28.8	26.4	4.4
Transitional tissue	2.8	2.1	2.8	3.6	2.5	1.1	3.8	3.6	<b>too low to measure</b>
Inferior nodal extension	1.1	<b>0.5</b>	<b>0.8</b>	<b>0.4</b>	1.0	<b>0.3</b>	<b>0.5</b>	<b>0.5</b>	<b>too low to measure</b>
Compact node	<b>0.6</b>	2.5	<b>0.8</b>	1.5	<b>0.8</b>	1.0	2.0	1.4	<b>too low to measure</b>
Penetrating bundle	1.5	<b>0.8</b>	<b>0.8</b>	1.5	1.5	<b>0.4</b>	1.3	<b>0.9</b>	<b>too low to measure</b>
Ventricle	52.0	62.8	67.6	46.2	89.8	67.2	50.0	62.2	6.1
	MCT								
Atrium	19.8	44.9	39.0	42.6	13.2	26.0	40.4	76.4	
Transitional tissue	*	4.2	5.6	1.0	2.5	9.3	3.7	6.8	
Inferior nodal extension	3.0	2.3	1.7	3.6	1.1	3.1	1.8	1.1	
Compact node	*	2.7	<b>0.7</b>	4.1	1.3	1.9	1.8	1.8	
Penetrating bundle	*	<b>0.6</b>	2.1	1.7	<b>0.6</b>	1.6	<b>0.5</b>	<b>0.6</b>	
Ventricle	69.2	65.0	50.0	112.0	27.4	75.0	16.6	94.2	

**Table A-2. RNA concentrations of all samples (in ng/μl). For all samples with concentrations of greater than 1 were reverse transcribed using a total of 16ng of RNA. For samples with a concentration of less than 1ng/μl a total of 16 x sample concentration was used for reverse transcription (because the maximum volume for the reaction was 16μl).**

Atrium									
Current	Proteins	Control	$d_{ion}^i$	MCT	$d_{ion}^i$	Significant	MCT/Control (%)	% test (p5)	scaling factor for current (percent)
$I_f$	HCN1		97		142		147	13.3	50
	HCN2		58		46		80	<b>34.6</b>	
	HCN4		1014		391 *		39	16.9	
$I_{Na}$	Na <sub>v</sub> 1.1		351		214		61	17.0	162
	Na <sub>v</sub> 1.5		4660		7881		169	17.3	
	Na <sub>v</sub> β1		1201		1335		111 -		
	Na <sub>v</sub> 1.8		3		1 *		47 -		
$I_{Ca,L}$	Ca <sub>v</sub> 1.2		309		141 *		46	19.0	46
	Ca <sub>v</sub> 1.3		3		0		16	21.0	
$I_{Ca,T}$	Ca <sub>v</sub> 3.1		546		208		38 -		42
	Ca <sub>v</sub> 3.2		1109		495		45 -		
$I_{Kur}$	K <sub>v</sub> 1.5		533		393		74		74
$I_{Kr}$	ERG1		201		78 *		39		39
$I_{Ks}$	K <sub>v</sub> LQT1		691		573		83		83
	MinK		2		16		1060 *		
$I_{Kslow}$	K <sub>v</sub> 1.2		450		41 *		9 -		9
$I_{Kss}$	K <sub>v</sub> 1.4		254		91 *		36 -		36
$I_{Kfast}$	K <sub>v</sub> 4.2		49		7 *		14	18.3	
	K <sub>v</sub> 4.3		1192		583 *		49	4.0	
	KCHIP2		2184		525 *		24 -		
$I_{K1}$	K <sub>v</sub> 2.1		475		227 *		48	23.8	38
	K <sub>v</sub> 2.2		611		203		33	34.0	
	K <sub>v</sub> 2.4		8		10		117 -		
SERCA	SERCA2a		202744		113405		56		56
RyR	RyR2		21577		9232		43 -		43
	RyR3		134		114 *		85 -		
$I_{NaCa}$	NCX1		5853		4257		73 -		73
$I_{NaK}$	α1 Na <sup>+</sup> -K <sup>+</sup> pump		16412		11570		71 -		68
	α2 Na <sup>+</sup> -K <sup>+</sup> pump		1912		758 *		40 -		
	α3 Na <sup>+</sup> -K <sup>+</sup> pump		99		128		129 -		
	β1 Na <sup>+</sup> -K <sup>+</sup> pump		18042		26353		146 -		
Electrical coupling	Cx30.2		0		0		47	9.0	59
	Cx40		159		269		170	200.0	
	Cx43		5780		2866		50	80.0	
	Cx45		812		806		99	30.0	
$I_{CaP}$ (sarcolemmal calcium pump)	PMCA1		488		504		103		103

Table A-3. Data used to model ion channel conductance and electrical coupling used in the computer modelling of the atrial cells in the MCT model of the AV node. Data is taken from the mRNA expression from the atrium. \* p<0.05 for difference in control and MCT mRNA expression assessed by limma test.

Inferior nodal extension							
Current	Proteins	Control $d_{ion}^i$	MCT $d_{ion}^i$	Significant	MCT/Control (%)	$\gamma_{ion}$ (pS)	scaling factor for current (percent)
$I_f$	HCN1	411	230		56	13.3	19
	HCN2	16	9		58	34.6	
	HCN4	8112	1446 *		18	16.9	
$I_{Na}$	Na <sub>v</sub> 1.1	171	55		32	17.0	122
	Na <sub>v</sub> 1.5	632	802		151	17.3	
	Na <sub>v</sub> β1	330	527		160 -		
	Na <sub>v</sub> 1.8	0	2 *		948 -		
$I_{CaL}$	Ca <sub>v</sub> 1.2	288	148 *		52	19.0	51
	Ca <sub>v</sub> 1.3	1	0		1	21.0	
$I_{CaT}$	Ca <sub>v</sub> 3.1	216	50		23 -		15
	Ca <sub>v</sub> 3.2	240	17		7 -		
$I_{Kur}$	K <sub>v</sub> 1.5	954	269		28		28
$I_{Kr}$	ERG1	27	10 *		38		38
$I_{Ks}$	K <sub>v</sub> LQT1	112	95		85		85
	MinK	1	0		8 *		
$I_{Kslow}$	K <sub>v</sub> 1.2	39	1 *		1 -		1
$I_{Kss}$	K <sub>v</sub> 1.4	21	7 *		35 -		35
$I_{Kfast}$	K <sub>v</sub> 4.2	5	1 *		22	18.3	
	K <sub>v</sub> 4.3	631	259 *		49	4.0	
	KCHIP2	2635	245 *		9 -		
$I_{Ks}$	K <sub>v</sub> 2.1	96	99 *		103	23.8	40
	K <sub>v</sub> 2.2	115	3		3	34.0	
	K <sub>v</sub> 2.4	2	0		7 -		
SERCA	SERCA2a	93494	38967		42		42
RyR	RyR2	1882	134		7 -		8
	RyR3	18	22 *		117 -		
$I_{NaCa}$	NCX1	1772	452		26 -		26
$I_{NaK}$	α1 Na <sup>+</sup> -K <sup>+</sup> pump	10767	9867		92 -		78
	α2 Na <sup>+</sup> -K <sup>+</sup> pump	1975	704 *		36 -		
	α3 Na <sup>+</sup> -K <sup>+</sup> pump	888	96		11 -		
	β1 Na <sup>+</sup> -K <sup>+</sup> pump	2941	4681		156 -		
Electrical coupling	Cx30.2	2	0		1	9.0	62
	Cx40	68	39		58	200.0	
	Cx43	314	129		41	80.0	
	Cx45	1030	843		82	30.0	
$I_{CaP}$ (sarcolemmal calcium pump)	PMCA1	410	281		69		69

Table A-4. Data used to model ion channel conductance and electrical coupling used in the computer modelling of the AN cells in the MCT model of the AV node. Data is taken from the mRNA expression from the inferior nodal extension. \*  $p < 0.05$  for difference in control and MCT mRNA expression assessed by limma test.

Compact node							
Current	Proteins	Control $d_{ion}^i$	MCT $d_{ion}^i$	Significant	MCT/Control (%)	$\gamma_{ion}$ (pS)	scaling factor for current (percent)
$I_f$	HCN1	411	359		87	13.3	31
	HCN2	12	15		126	<b>34.6</b>	
	HCN4	11775	3474 *		29	16.9	
$I_{Na}$	Na <sub>v</sub> 1.1	234	115		49	17.0	176
	Na <sub>v</sub> 1.5	401	996		248	17.3	
	Na <sub>v</sub> β1	522	551		106	-	
	Na <sub>v</sub> 1.8	0	1 *		894	-	
$I_{Ca,L}$	Ca <sub>v</sub> 1.2	246	112 *		46	19.0	46
	Ca <sub>v</sub> 1.3	1	0		44	21.0	
$I_{Ca,T}$	Ca <sub>v</sub> 3.1	248	252		102	-	71
	Ca <sub>v</sub> 3.2	298	137		46	-	
$I_{Kur}$	K <sub>v</sub> 1.5	1022	831		81		81
$I_{Kr}$	ERG1	25	26 *		102		102
$I_{Ks}$	K <sub>v</sub> LQT1	183	119		65		65
	MinK	4	2		52 *		
$I_{Kslow}$	K <sub>v</sub> 1.2	15	11 *		73		73
$I_{Kss}$	K <sub>v</sub> 1.4	29	25 *		84		84
$I_{Kfast}$	K <sub>v</sub> 4.2	0	0 *		143	18.3	
	K <sub>v</sub> 4.3	451	299 *		66	4.0	
	KChIP2	451	81 *		18	-	
$I_{K1}$	K <sub>v</sub> 2.1	128	114 *		89	23.8	67
	K <sub>v</sub> 2.2	65	24		37	34.0	
	K <sub>v</sub> 2.4	2	2		129	-	
SERCA	SERCA2a	70401	62299		88		88
RyR	RyR2	4403	1670		38	-	38
	RyR3	24	28 *		116	-	
$I_{hace}$	NCX1	2836	1996		70	-	70
$I_{hck}$	α1 Na <sup>+</sup> -K <sup>+</sup> pump	17540	13922		79	-	76
	α2 Na <sup>+</sup> -K <sup>+</sup> pump	1546	1031 *		67	-	
	α3 Na <sup>+</sup> -K <sup>+</sup> pump	1069	281		26	-	
	β1 Na <sup>+</sup> -K <sup>+</sup> pump	3990	7378		185	-	
Electrical coupling	Cx30.2	2	1		47	9.0	102
	Cx40	66	57		101	200.0	
	Cx43	154	247		160	80.0	
	Cx45	1284	1076		84	30.0	
$I_{csp}$ (sarcolemmal calcium pump)	PMCA1	375	333		89		89

Table A-5. Data used to model ion channel conductance and electrical coupling used in the computer modelling of the N cells in the MCT model of the AV node. Data is taken from the mRNA expression from compact node. \* p<0.05 for difference in control and MCT mRNA expression assessed by limma test.

Penetrating Bundle										
Current	Proteins	Control	$d_{ion}^i$	MCT	$d_{ion}^i$	Significant	MCT/Control (%)	$\chi^2_{lim}$ (p5)	scaling factor for current (percent)	
$I_f$	HCN1		138		227		165		13.3	36
	HCN2		10		86		649		34.6	
	HCN4		24605		8650 *		35		16.9	
$I_{Na}$	Na <sub>v</sub> 1.1		70		79		113		17.0	169
	Na <sub>v</sub> 1.5		1546		2656		172		17.3	
	Na <sub>v</sub> β1		266		382		144 -			
	Na <sub>v</sub> 1.8		17		9 *		51 -			
$I_{Ca,L}$	Ca <sub>v</sub> 1.2		278		188 *		61		19.0	60
	Ca <sub>v</sub> 1.3		1		0		6		21.0	
$I_{Ca,T}$	Ca <sub>v</sub> 3.1		163		30		18 -			66
	Ca <sub>v</sub> 3.2		200		210		105 -			
$I_{K,ur}$	K <sub>v</sub> 1.5		723		490		68			68
$I_{K,r}$	ERG1		29		28 *		96			96
$I_{K,s}$	K <sub>v</sub> LQT1		140		185		118			118
	MinK		2		1		50 *			
$I_{K,slow}$	K <sub>v</sub> 1.2		67		10 *		14 -			14
$I_{K,ss}$	K <sub>v</sub> 1.4		22		18 *		84 -			84
$I_{K,fast}$	K <sub>v</sub> 4.2		0		4 *		882		18.3	111
	K <sub>v</sub> 4.3		369		170 *		46		4.0	
	KChIP2		842		509 *		60 -			
$I_{K,1}$	K <sub>v</sub> 2.1		352		380 *		108		23.8	111
	K <sub>v</sub> 2.2		32		42		134		34.0	
	K <sub>v</sub> 2.4		2		2		115 -			
SERCA	SERCA2a		24420		26945		110			110
RyR	RyR2		1678		3005		179 -			180
	RyR3		12		28 *		237 -			
$I_{NaCa}$	NCX1		3283		1313		40 -			40
$I_{NaK}$	α1 Na <sup>+</sup> -K <sup>+</sup> pump		13448		15316		114 -			106
	α2 Na <sup>+</sup> -K <sup>+</sup> pump		2169		1659 *		72 -			
	α3 Na <sup>+</sup> -K <sup>+</sup> pump		402		97		24 -			
	β1 Na <sup>+</sup> -K <sup>+</sup> pump		3781		3187		84 -			
Electrical coupling	Cx30.2		1		0		5		9.0	88
	Cx40		988		535		54		200.0	
	Cx43		139		1022		733		80.0	
	Cx45		2530		2006		79		30.0	
$I_{CaP}$ (sarcolemmal calcium pump)	PMCA1		388		401		103			103

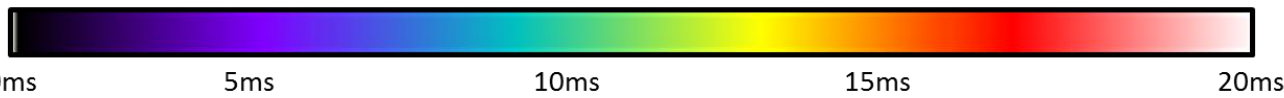
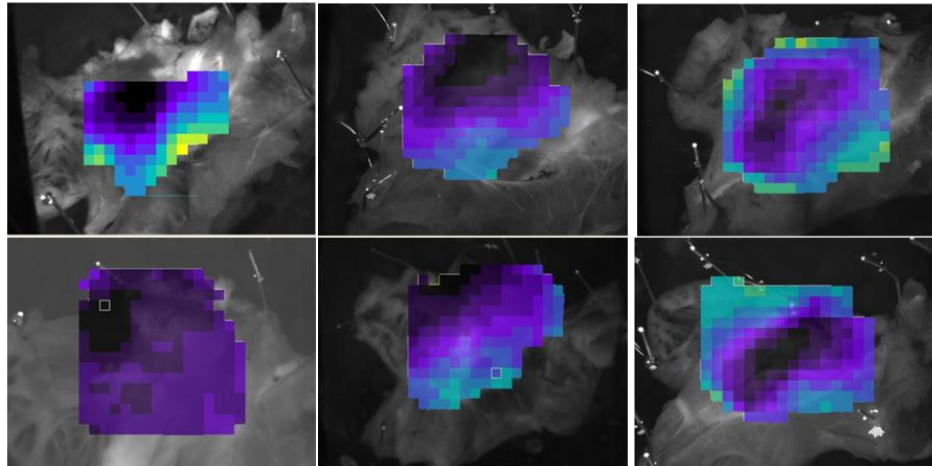
Table A-6. Data used to model ion channel conductance and electrical coupling used in the computer modelling of the NH cells in the MCT model of the AV node. Data is taken from the mRNA expression from the penetrating bundle. \* p<0.05 for difference in control and MCT mRNA expression assessed by limma test.

Ventricle							
Current	Proteins	Control $d_{ion}^i$	MCT $d_{ion}^i$	Significant	MCT/Control (%)	$\gamma_{100}$ (pS)	scaling factor for current (percent)
$I_f$	HCN1	1	7		639	13.3	72
	HCN2	750	222		30	<b>34.6</b>	
	HCN4	795	1211 *		152	16.9	
$I_{Na}$	Na <sub>v</sub> 1.1	187	272		146	17.0	63
	Na <sub>v</sub> 1.5	7765	4776		62	17.3	
	Na <sub>v</sub> β1	1346	1450		108 -		
	Na <sub>v</sub> 1.8	0	0 *		240 -		
$I_{Ca,L}$	Ca <sub>v</sub> 1.2	193	310 *		161	19.0	161
	Ca <sub>v</sub> 1.3	0	0		44	21.0	
$I_{Ca,T}$	Ca <sub>v</sub> 3.1	78	67		73 -		78
	Ca <sub>v</sub> 3.2	476	373		78 -		
$I_{K,ur}$	K <sub>v</sub> 1.5	301	254		84		84
$I_{K,r}$	ERG1	109	84 *		59		59
$I_{K,s}$	K <sub>v</sub> LQT1	753	579		77		77
	MinK	5	11		196 *		
$I_{K,slow}$	K <sub>v</sub> 1.2	89	34 *		38 -		38
$I_{K,ss}$	K <sub>v</sub> 1.4	63	65 *		103 -		103
$I_{K,fast}$	K <sub>v</sub> 4.2	47	19 *		40	18.3	
	K <sub>v</sub> 4.3	444	182 *		41	4.0	
	KCHIP2	5897	3721 *		63 -		
$I_{K,s}$	K <sub>v</sub> 2.1	708	753 *		106	23.8	87
	K <sub>v</sub> 2.2	262	132		50	34.0	
	K <sub>v</sub> 2.4	30	6		20 -		
SERCA	SERCA2a	61344	164649		268		268
RyR	RyR2	16797	13525		72 -		72
	RyR3	56	64 *		114 -		
$I_{NaCa}$	NCX1	3811	3025		79 -		79
$I_{NaK}$	α1 Na <sup>+</sup> -K <sup>+</sup> pump	5604	8289		148 -		112
	α2 Na <sup>+</sup> -K <sup>+</sup> pump	3326	1942 *		58 -		
	α3 Na <sup>+</sup> -K <sup>+</sup> pump	208	34		16 -		
	β1 Na <sup>+</sup> -K <sup>+</sup> pump	12331	7948		64 -		
Electrical coupling	Cx30.2	0	0		63	9.0	80
	Cx40	298	456		153	200.0	
	Cx43	4978	3214		65	80.0	
	Cx45	449	900		200	30.0	
$I_{CaP}$ (sarcolemmal calcium pump)	PMCA1	444	338		76		76

Table A-7. Data used to model ion channel conductance and electrical coupling used in the computer modelling of the ventricular cells in the MCT model of the AV node. Data is taken from the mRNA expression from the ventricle. \* p<0.05 for difference in control and MCT mRNA expression assessed by limma test.

A

Control



B

MCT

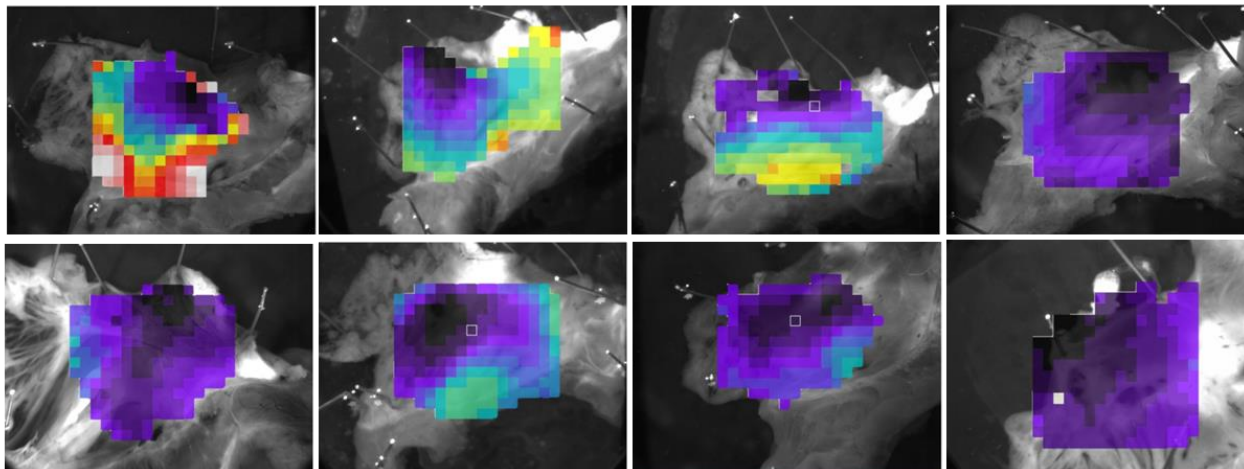


**Figure A-1. Optical activation maps in the SA/AV node preparation. The activation map was created in Optiq using the time at which the optical signal was 90% from baseline to peak (Tact90\_Basic). All sequences are shown with a 20ms colour scale. A) Control rats. Conduction velocity in the atrium was rapid in all preparations. B) MCT treated rats. Some preparations showed slowed conduction velocity but others showed preserved conduction velocity.**